# New Methods for Detecting Dynamic and Thermodynamic Characteristics of Sea Ice from Radar Remote Sensing

by

Alexander Sergeyevich Komarov

A Thesis Submitted to the Faculty of Graduate Studies of

The University of Manitoba

in Partial Fulfillment of the Requirements of the Degree of

Doctor of Philosophy

Department of Electrical and Computer Engineering
University of Manitoba
Winnipeg, Manitoba, Canada

# ABSTRACT

This dissertation presents new methods for detecting dynamic and thermodynamic characteristics of Arctic sea ice using radar remote sensing. Such methods are important to better understand the the impact of ongoing reduction of Arctic sea ice on physical, chemical and biological processes in the Arctic marine ecosystem.

A new technique for ice motion detection from sequential satellite synthetic aperture radar (SAR) images was developed and thoroughly validated. This method is more robust and accurate compared to the previous ones. The accuracy of the system is 0.43 km obtained from a comparison between SAR-derived ice motion vectors and in-situ sea ice beacon trajectories. For the first time, we evaluated ice motion tracking results derived from HH and HV polarization channels of RADARSAT-2 ScanSAR imagery and formulated a condition where the HV channel is more reliable than the HH channel for ice motion tracking. Furthermore, we found that the ice motion tracking from the HV channel is not affected by noise floor stripes (due to inhomogeneity of the antenna pattern across the satellite track), which are prominent in the cross-polarization RADARSAT-2 ScanSAR images.

Sea ice motion is substantially controlled by surface winds. Two new models for ocean surface wind speed retrieval from C-band SAR data have been developed and validated based on a large body of statistics on buoy observations collocated and coincided with RADARSAT-1 and -2 ScanSAR images. The proposed models without wind direction input demonstrated a better accuracy than conventionally used CMOD_IFR2 and CMOD5.N models in combination with the SAD co-polarization ratio (VV/HH), which require wind direction input. Root-mean square error (RMSE) for our HH-HV wind speed retrieval model is 1.59 m/s while RMSE of

CMOD5.N+SAD model (which requires wind direction) is 2.19 m/s. As a combination of the developed methods we designed a wind speed-ice motion product which can be a useful tool for studying sea ice dynamics processes in the marginal ice zone.

To effectively asses the thermodynamic properties of sea ice advanced tools for modeling electromagnetic (EM) wave scattering from rough natural surfaces are required. In this dissertation a new analytical formulation for EM wave scattering from rough boundaries interfacing inhomogeneous media is presented based on the first-order approximation of the small perturbation method. This solution operates with physically meaningful reflection and transmission coefficients associated with certain geophysical media (e.g. snow and ice) which makes it practical for geophysical remote sensing applications. Available solutions in the literature represent special cases of our general solution.

The developed scattering theory was applied to experimental data collected at three stations (with different snow thicknesses) during the Circumpolar Flaw Lead system study in the Beaufort Sea from the research icebreaker Amundsen. Good agreement between the model and experimental data were observed for all three case studies. The model results revealed that the scattering at the snow-ice rough interface is usually stronger than at the air-snow interface. Furthermore, both model and experimental normalized radar cross-section (NRCS) values were considerably higher for thin snow cover (4 cm) compared to the thick snow cover case (16 cm). This effect is associated with the lower attenuation of the propagated wave within the thin snow in comparison to the thick snow pack. Different brine content in snow covers with close thicknesses (4 cm and 3 cm) significantly affected the backscatter components from the air-snow and snow-ice interfaces; however, the total backscattering coefficients for VV polarization (at all incidence angles) and HH polarization (at incidence angles below 35°) did not change

considerably. These findings provide the physical basis for, and suggest that, winter snow thickness retrieval may be possible from radar observations under surface scattering conditions.

# ACKNOWLEDGMENTS

I would like to thank my advisors Professor David Barber and Professor Lotfollah Shafai for their guidance throughout my Ph.D. research. I would also like to thank my graduate committee members Professor Puyan Mojabi and Professor Jens Ehn for academic support.

I would like to thank all the graduate students and staff at the Centre for Earth Observation Science for creating great research atmosphere. In particular, I am thankful to Dr. Dustin Isleifson (now with the Magellan Aerospace), Dr. Randall Scharien (now with the University of Victoria), Jack Landy, Nariman Firoozy, Kerri Warner, David Babb, Dr. Mukesh Gupta, and Dr. Ryan Galley for helpful discussions.

I would like to thank the Canadian Ice Service and the Meteorological Service of Canada for support in this research. In particular, I am grateful to Dr. Vladimir Zabeline, Dr. Roger DeAbreu, and Matt Arkett.

My research was funded from multiple sources. I received financial support from a Natural Sciences and Engineering Research Council of Canada Alexander Graham Bell Canada Graduate Scholarship, a University of Manitoba Graduate Fellowship, and a Manitoba Graduate Scholarship. I am also thankful to Prof. Barber, the V.E. Barber Memorial Fellowships in Arctic Research, and the Edward R. Toporeck Graduate Fellowship in Engineering for funding my research.

During my Ph.D. study I presented results at several international conferences which were held in Europe and North America. I would like to thank Prof. Barber and the University of Manitoba for making these trips possible.

Finally, I would like to thank my family for their support throughout my Ph.D. study.

# TABLE OF CONTENTS

# LIST OF TABLES

# LIST OF FIGURES

# USE OF COPYRIGHTED MATERIAL

Chapter 3 of this dissertation is reproduced with minor modifications from Komarov and Barber **[**Sea ice motion tracking from sequential dual-polarization RADARSAT-2 images, *IEEE Trans. Geosci. Remote Sens.*, vol. 52, no. 1, pp. 121-136, Jan. 2014], with permission from the Institute of Electrical and Electronics Engineers**.**

Chapter 4 of this dissertation is reproduced with minor modifications from Komarov et al. [Ocean surface wind speed retrieval from C-band SAR images without wind direction input, *IEEE Trans. Geosci. Remote Sens*., vol. 52, no. 2, pp. 980-990, Feb. 2014], with permission from the Institute of Electrical and Electronics Engineers**.**

Chapter 5 of this dissertation is reproduced with minor modifications from Komarov et al. [Electromagnetic wave scattering from rough boundaries interfacing inhomogeneous media and application to snow-covered sea ice, *Progress in Electromagnetic Research*, vol. 144, pp. 201-219, 2014], with permission from the Electromagnetics Academy.

Chapter 6 of this dissertation is reproduced with minor modifications from Komarov et al. [Modeling and measurement of C-band radar backscatter from snow-covered first-year sea ice, *IEEE Trans. Geosci. Remote Sens.*, in press, 2015].

# CHAPTER 1. INTRODUCTION

## 1.1. Motivation

Arctic sea ice extent has been drastically declining over the past three decades [1]. The low record minimum in summer sea ice extent of 3.41 million sq. km. (which is 49% less than 1979 to 2000 average) was captured by passive microwave spaceborne radiometers in September 2012 [2]. Correspondingly, there is strong evidence that the Arctic Ocean multi-year (MY) sea ice has been rapidly disappearing at a rate of 15.1% per decade [3], [4]. During this, the MY sea ice is being replaced by seasonal first-year (FY) sea ice as the maximum extent (in winter) has not changed appreciably [5]. The Arctic ice thickness also decreased by 42% and 21% for fall (October-November) and winter (February-March) respectively during the 2003-2008 period [6]. Decrease of the Arctic ice volume leads to increasing ice mobility. On average, the Arctic sea ice drift speed increased by 10.6% per decade for the period 1992-2009, which is much larger than the wind speed increase (~1.5% per decade) [7].

The observed decline in sea ice volume significantly impacts physical, chemical and biological processes in the Arctic marine ecosystem. These changes also facilitate industrial developments in the Arctic Ocean. However, hazardous ice features (i.e. hummocked MY ice floes, MY and FY pressure ridges, and ice islands) remain a threat to stationary and mobile infrastructure in the southern Beaufort Sea [8]. Therefore, reliable detection of dynamic and thermodynamic characteristics of sea ice is becoming increasingly important.

Spaceborne Synthetic Aperture Radar (SAR) observations with very high resolution have been extensively used to monitor of changes in sea ice. SAR sensors are (generally) independent of

clouds and can operate during day and night times as opposed to optical instruments. To date, SAR observations provide the most reliable information on sea ice cover for national Ice Centers (to map and forecast sea ice conditions), icebreakers, and off-shore industry. High temporal resolution and large spatial coverage of SAR imagery are desirable for more accurate monitoring of rapid dynamic and thermodynamic changes in sea ice over the entire Arctic Ocean. Canadian RADARSAT-2 [9] launched in 2007 increased the temporal and geographical coverage of the circumpolar zone by airborne SAR platforms. Among other new technical features, RADARSAT-2 has the cross-polarization channel in the ScanSAR mode (compared to its predecessor RADARSAT-1). In the future, Canadian RADARSAT Constellation mission (RCM) [10] will be equipped with three independent SAR platforms analogous to RADARSAT-2. Also, the European Space Agency (ESA) Sentinel-1 two satellite constellation mission is currently replacing ESA Envisat platform. These new missions will lead to a significant growth in satellite radar observations over the Arctic Ocean.

The new capabilities of SAR sensors and the increasing volume of SAR imagery over the Arctic Ocean require improved methods for retrieving key parameters of sea ice from SAR. Interpretation of radar signatures is not often straightforward and requires advanced signal processing algorithms and advanced modeling techniques for electromagnetic wave scattering from snow-covered sea ice. The retrieval/detection methods should also take into account new technical capabilities of microwave satellite platforms (e.g. availability of the cross-polarization channel and improved noise floor characteristics).

This Ph.D. research is dedicated to the development of new methods for detecting dynamic and thermodynamic characteristics of sea ice from radar remote sensing.

## 1.2. Thesis Objectives

The overall goal of this research is to develop new methods for detecting both dynamic and thermodynamic characteristics of sea ice using radar remote sensing. We highlight four sets of objectives which contribute to the main goal as follows. The first two sets of objectives (Set 1 and Set 2) are devoted to the development of new techniques for sea ice motion and ocean surface wind speed retrieval from SAR imagery. The second two sets of objectives (Set 3 and Set 4) are devoted to the development of a new model for electromagnetic wave scattering from rough interfaces separating layered media and application of this theory to experimental physical and scatterometer data collected over snow-covered FY sea ice for different snow thicknesses. These four sets of objectives are stated as follows:

Set of Objectives 1

1.1. To develop and validate a new sea ice motion tracking system operating with sequential SAR images.

1.2. To evaluate capabilities of the co- and cross-polarization images of RADARSAT-2 ScanSAR data for ice motion tracking.

Set of Objectives 2

2.1. To develop and validate a wind speed retrieval model free of input wind direction for RADARSAT-1 HH ScanSAR imagery.

2.2. To develop and validate a wind speed retrieval model free of input wind direction for RADARSAT-2 HH-HV ScanSAR imagery, and to evaluate different options for wind speed imaging.

2.3. To explore the possibility of merging wind speeds over the ocean surface and ice motion over the sea ice (Objective 1.1) from SAR for improved monitoring of sea ice dynamics in the marginal ice zone (MIZ).

Set of Objectives 3

3.1. To derive a general analytical formulation for electromagnetic wave scattering from an arbitrary number of rough interfaces separating layered media with the use of the first-order approximation of the small perturbation theory. The solution must be expressed through complex reflection and transmission coefficients associated with the inhomogeneous media.

3.2. To validate the obtained solution by treating special cases available in the literature and comparing numerical results with those available in the literature.

3.3. To present an analytical formulation for electromagnetic wave scattering from snow-covered sea ice as a special case of the general solution.

Set of Objectives 4

4.1. To model normalized radar cross-sections (NRCS) in C-band from snow-covered FY sea ice for different snow thickness conditions over smooth first-year sea ice using our wave scattering theory (Objective 3.1).

4.2. To validate the numerical results against winter ship-based scatterometer observations of snow-covered FY sea ice collected in the Canadian Arctic.

4.3. Investigate the influence of snow cover on radar signatures using model and experimental data.

## 1.3. Thesis Outline

In Chapter 2 we discuss physical fundamentals of dynamic and thermodynamic processes occurring in snow-covered sea ice and also describe existing radar remote sensing methods for detecting these processes.

The core of this dissertation is composed of four peer-reviewed journal publications which constitute Chapters 3, 4, 5 and 6 respectively. Chapters 3 and 4 are devoted to the new methods for assessing the dynamic state of sea ice from SAR images. Chapters 5 and 6 are devoted to the development of new methods for assessing the thermodynamic state of sea ice using microwave scattering modelling. Chapters 3, 4, 5, and 6 address Sets of Objectives 1, 2, 3, and 4 respectively.

In Chapter 3 we present and validate a new sea ice motion tracking system operating with sequential SAR images. We also evaluate capabilities of co- and cross-polarization channels of RADARSAT-2 ScanSAR mode for ice motion detection. This work has been published in *IEEE Transactions on Geoscience and Remote Sensing* journal [11]:

**A. S. Komarov** and D. G. Barber, "Sea ice motion tracking from sequential dual-polarization RADARSAT-2 images *IEEE Transactions on Geoscience and Remote Sensing*, vol. 52, no. 1, pp. 121-136, Jan. 2014.

In Chapter 4 we present and validate two new models for ocean surface wind speed retrieval from RADARSAT-2 images which do not require input wind direction (as opposed to conventionally used CMOD type models). Furthermore, a new tool combining ice motion and ocean surface wind speed in the marginal ice zone (MIZ) is proposed. This work has been published in *IEEE Transactions on Geoscience and Remote Sensing* journal [12]:

**A. S. Komarov**, V. Zabeline, and D. G. Barber, "Ocean surface wind speed retrieval from C-band SAR images without wind direction input," *IEEE Transactions on Geoscience and Remote Sensing*, vol. 52, no. 2, pp. 980-990, Feb. 2014.

In Chapter 5 we derive and validate a theoretical model for electromagnetic wave scattering from rough surfaces separating arbitrary layered media using the first-order approximation of the small perturbation theory. We further adapt this model for snow-covered sea ice. This work has been published in *Progress in Electromagnetic Research* journal [13]:

**A. S. Komarov**, L. Shafai, and D. G. Barber, "Electromagnetic wave scattering from rough boundaries interfacing inhomogeneous media and application to snow-covered sea ice," *Progress in Electromagnetic Research*, vol. 144, pp. 201-219, 2014.

In Chapter 6 we validate the wave scattering model (developed in Chapter 5) against C-band scatterometer measurements collected in the Canadian Arctic (from the CCGS Amundsen) for different snow thickness conditions. In this chapter we also evaluate the influence of snow cover on C-band radar backscatter. This work is in press of *IEEE Transactions on Geoscience and Remote Sensing* journal [14]:

**A. S. Komarov**, D. Isleifson, D. G. Barber, and L. Shafai, "Modeling and measurement of C-band radar backscatter from snow-covered first-year sea ice," *IEEE Transactions on Geoscience and Remote Sensing*, in press, 2015.

In Chapter 7 the results are summarizes and future directions of this research are suggested.

# CHAPTER 2. BACKGROUND

In this chapter we present relevant information on physics of sea ice dynamic and thermodynamic processes as well as existing radar remote sensing methods for detecting dynamic and thermodynamic states of sea ice.

This chapter is substantially based on my Ph.D. Candidacy exam essay responding to the following question: "Describe the physical processes giving rise to dynamic and thermodynamic characteristics of snow covered sea ice. Assess the ability of active microwave remote sensing and microwave scattering models to develop effective tools to assess both the dynamic and thermodynamic states of snow-covered sea ice."

This chapter is organized as follows. In Section 2.1 we introduce the momentum balance equation for sea ice motion and describe its individual forces. In Section 2.2 we focus on algorithms for assessing the sea ice dynamic state from synthetic aperture radar (SAR) imagery. First, a concept of ice motion tracking from SAR along with area-based and feature-based image matching techniques are introduced. Second, calculation of various kinematic parameters of sea ice is presented. Third, existing methods to ocean surface wind speed retrieval from SAR imagery are evaluated. In Section 2.3 we describe properties of snow and sea ice and present the heat transfer equation for snow-covered sea ice with corresponding boundary conditions at the air-snow, ice-snow and ice-water interfaces. Following this, the thermal properties of sea ice and energy fluxes are discussed. In Section 2.4 we describe how modeling of electromagnetic wave interaction with snow-covered sea ice can be used for assessing the thermodynamic state. First, we present Maxwell's equations and define the complex dielectric constant. Second, we discuss the

linkage between the dielectric properties of snow and sea ice and corresponding physical characteristics. Third, we discuss microwave scattering modelling focusing on the first-order approximation of the small perturbation theory.

## 2.1. Physics of Sea Ice Dynamics

Sea ice moves in response to winds and ocean currents, Coriolis force, the internal stress in the ice, and sea surface tilt. Sea ice dynamic processes cause different phenomena such as ice leads and ice pressure ridges formation (through divergence and convergence). These phenomena change drag properties of sea ice and thus substantially influence ice dynamics. In this section we consider sea ice dynamics in terms of physical causes and consequences of sea ice motion.

### 2.1.1. Sea Ice Motion Equation

The momentum balance equation is written according to Newton's Second Law [15]-[17]:

$$m\mathbf{a} = \boldsymbol{\tau}_a + \boldsymbol{\tau}_w + \boldsymbol{\tau}_c + \boldsymbol{\tau}_i + \boldsymbol{\tau}_t \tag{2.1}$$

$m$ - ice mass per unit area, $\mathrm{kg/m^2}$; $\mathbf{a}$ - ice acceleration, $\mathrm{m/s^2}$; $\boldsymbol{\tau}_a$ - air stress, $\mathrm{N/m^2}$; $\boldsymbol{\tau}_w$ - water stress, $\mathrm{N/m^2}$; $\boldsymbol{\tau}_c$ - Coriolis force, $\mathrm{N/m^2}$; $\boldsymbol{\tau}_i$ - internal stress in the ice, $\mathrm{N/m^2}$; $\boldsymbol{\tau}_t$ - force due to sea surface tilt, $\mathrm{N/m^2}$.

2.1.2. Air Stress and Water Stress

The air stress at the atmospheric boundary layer is a force exerted by the wind on the ice surface. It is proportional to the square of the wind speed relative to the surface. Often, the air stress is expressed through the geostrophic winds as follows [16]:

$$\boldsymbol{\tau}_{\mathbf{a}} = \rho_a C_{ag} U_{ag} \left( \mathbf{U}_{\mathbf{ag}} \cos\theta_a + \hat{z}_0 \times \mathbf{U}_{\mathbf{ag}} \sin\theta_a \right), \tag{2.2}$$

where $\rho_a$ is air density, $C_{ag}$ is air drag coefficient with respect to the geostrophic wind $\mathbf{U}_{\mathbf{ag}}$ at the top of the atmospheric boundary layer. The geostrophic wind results from a balance between the atmospheric pressure gradient and the Coriolis force (which is discussed in section 2.3). $\hat{z}_0$ is a unit vector normal to the surface, $\theta_a$ is a turning angle between the geostrophic and the surface wind due to the Ekman effect. Wind velocity rotates counterclockwise down from the geostrophic wind to the surface (in the Northern hemisphere). In [18] and [19] it was found by observation that the air stress vector is rotated by $\theta_a = 25^o$ relative to the geostrophic winds. However, this angle may depend on surface roughness and atmospheric stability. Equation (2.2) ignores the ice velocity which is usually much smaller than the wind speed.

Typically the air drag coefficient is measured with respect to the surface wind. The measured drag coefficient $C_a$ is larger than $C_{ag}$. These two drag coefficients can be linked through the magnitudes of the surface and geostrophic winds. The drag coefficient $C_a$ is a function of the ice surface roughness (small and large scale), and it significantly varies for different types of sea ice between $0.7\times10^{-3}$ (grease ice) and $8.0\times10^{-3}$ (extremely rough ice) [20], [21]. Since the roughness

may have small and large scales, the drag coefficient can be split into two components: skin friction drag and form drag. Banke et al. [22] proposed a simple relationship between the drag coefficient and measurable physical parameters as follows:

$$C_a = C_{10} + \frac{1}{2} C_f H_r N_r , \tag{2.3}$$

where $C_{10}$ is the skin friction drag coefficient, $C_f$ is the form drag coefficient for a single ridge sail, $H_r$ is the mean height of ridges, $N_r$ is concentration of ridges (a number of ridges per unit downwind distance). In the same study the following empirical relationships between both drag coefficients and ice surface parameters were found:

$$\left.\begin{aligned} C_{10} &= \left(1.10 + 0.072\sigma_s\right)10^{-3} \\ C_f &= 0.012 + 0.012\varphi_s \end{aligned}\right\}, \tag{2.4}$$

where $\sigma_s$ is the root-mean square (RMS) height of the rough surface (changing from 3.5 cm to 13 cm), and $\alpha_r$ is the ridge slope (ranging from 15° to 50°). In [22] the skin friction drag coefficient varied from $1\times10^{-3}$ to $2\times10^{-3}$ while the form drag coefficient lied in the range between 0.1 and 0.6 depending on whether the ridges are mostly first-year (higher values) or multiyear (lower values).

In a similar way, the water stress is defined through the geostrophic currents taking into account the Ekman effect [16]:

$$\boldsymbol{\tau}_{\mathbf{w}} = \rho_w C_{wg} \left| \mathbf{U}_{\mathbf{wg}} - \mathbf{U}_{\mathbf{i}} \right| \left[ \left( \mathbf{U}_{\mathbf{wg}} - \mathbf{U}_{\mathbf{i}} \right) \cos\theta_w + \hat{z}_0 \times \left( \mathbf{U}_{\mathbf{wg}} - \mathbf{U}_{\mathbf{i}} \right) \sin\theta_w \right], \tag{2.5}$$

where $\rho_w$ is the water density, $C_{wg}$ is the water drag coefficient with respect to the geostrophic current, $\mathbf{U}_{\mathbf{i}}$ is the ice velocity. The water drag coefficient is normally measured with respect to the surface current. A typical value of the water drag coefficient $C_w$ with respect to the surface current is about 0.004; however, $C_w$ is a function of the physical roughness of the ice underside. $\mathbf{U}_{\mathbf{wg}}$ is the geostrophic current at the bottom of the oceanic boundary layer (~30 m). The geostrophic current results from an equilibrium between the force due to the sea surface tilt and the Coriolis force. $\theta_w$ is the turning angle between the geostrophic current at the bottom of the ocean boundary layer and the ice underside current. This angle is also about 25° and positive for the Northern hemisphere (counting counterclockwise).

In the most elementary case where internal stress and surface tilt are not significant, the ice moves along the geostrophic wind. This case represents Zubov's law [23] which stated that ice drifts parallel to the isobars. Zubov's rule is in agreement with the Nansen-Ekman ice drift rule (1902), which stated that ice moves at 2% of the wind speed at 30° to the right of the surface wind in the Northern hemisphere.

Mean sea ice velocity in the Arctic Ocean as function of long-term sea level pressure distribution was studied by Colony and Thorndike [24]. They demonstrated that the general sea ice circulation pattern (including the Beaufort Gyre and Transpolar Drift) follows the mean annual surface atmospheric pressure field and the geometry of the basin.

2.1.3 Coriolis Force

The next term in the momentum balance equation (2.1) is the Coriolis force which arises because all geophysical observations on the Earth are made relative to the coordinate system associated with the Earth itself. The Earth is a non-inertial frame of reference, and this is why in order to use Newton's laws of motion an additional term which takes into account the fact that the body is being accelerated by the Earth rotation must be introduced. This force is called the Coriolis force and it is expressed (per a unit area) as follows:

$$\boldsymbol{\tau}_{\mathbf{c}} = -2m\left(\boldsymbol{\Omega} \times \mathbf{U}_{\mathbf{i}}\right), \tag{2.6}$$

where $\boldsymbol{\Omega}$ is the Earth angular velocity, $\mathbf{U}_{\mathbf{i}}$ is the ice velocity. Components of the Earth's angular velocity at certain latitude are demonstrated in Figure 2.1. If we consider two-dimensional motion of sea ice which has the northern and eastern components only, then (2.6) can be rewritten as follows:

$$\boldsymbol{\tau}_{\mathbf{c}} = 2\Omega m\left(U_N \sin\varphi \hat{e}_E - U_E \sin\varphi \hat{e}_N + U_E \cos\varphi \hat{e}_U\right), \tag{2.7}$$

where $\left(U_E, U_N\right)$ are the eastern and northern components of the ice velocity, $\left(\hat{e}_E, \hat{e}_N, \hat{e}_U\right)$ are unit orthogonal vectors for eastern, upward and northern directions. Since the upward component is much smaller than the Earth's gravitation, the last expression can be reduced to:

$$\boldsymbol{\tau}_{\mathbf{c}} = f_c m\left(U_N \hat{e}_E - U_E \hat{e}_N\right), \ \left|\boldsymbol{\tau}_{\mathbf{c}}\right| = f_c m U_i, \tag{2.8}$$

where $f_c = 2\Omega \sin\varphi$ is the Coriolis parameter. At high latitudes the Coriolis force is higher than at low latitudes. At the equator the upward component of the Earth's angular velocity is equal to zero and thus, the Coriolis force is zero.

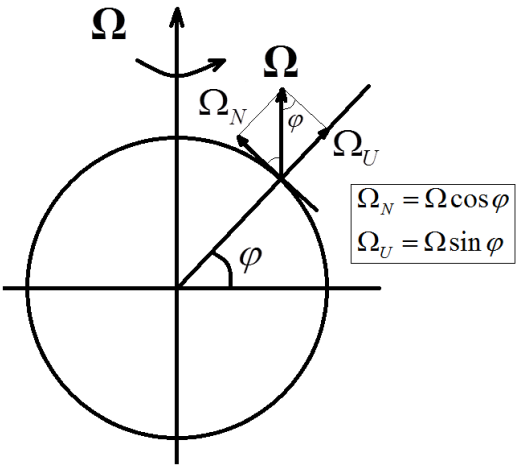


Figure 2.1. Northern $\Omega_N$ and upward $\Omega_U$ components of the Earth's angular velocity at latitude $\varphi$.

2.1.4. Sea Surface Tilt

Term $\boldsymbol{\tau}_{\mathbf{t}}$ in (2.1) is caused by sea surface tilt which occurs because the sea surface does not necessarily follow the geoid. The tilt of sea surface relative to the geoid causes a horizontal pressure gradient force which is expressed as follows [16]:

$$\boldsymbol{\tau}_{\mathbf{t}} = -mg \cdot \nabla H_s, \tag{2.9}$$

where $H_s$ is the elevation of the sea surface with respect to the geoid, and $g$ is the gravitational acceleration.

### 2.1.5. Internal Stress

The internal stress $\boldsymbol{\tau}_i$ is the total force which acts on a unit area of ice cover embedded in a sea ice sheet due to stress transmitted through the ice from the adjacent parts of the ice sheet. This force must be accounted for if the ice concentration is higher than 80% [15]. The internal stress is a function of several factors such as the rheology, strength of the ice cover and the existing ice thickness distribution.

The motion of an ice continuum can be decomposed into rigid translation, rigid rotation, and strain. Strain represents the physical deformation of single volume elements in the continuum including extension/contraction, shear and rotation. Strain and rotation are tensor quantities [25].

Strain rate denotes how fast ice deforms in different directions while vorticity shows how fast ice rotates. Strain rate and vorticity are important kinematic characteristics of sea ice motion and their components are defined as follows for ice velocity $\mathbf{U_i} = \{u(x,y),\ v(x,y)\}$ [25]:

$$\left.\begin{aligned} \dot{\varepsilon}_{xx} &= \frac{\partial u}{\partial x} \\ \dot{\varepsilon}_{xy} &= \dot{\varepsilon}_{yx} = \frac{1}{2}\left(\frac{\partial u}{\partial y} + \frac{\partial v}{\partial x}\right) \\ \dot{\varepsilon}_{yy} &= \frac{\partial v}{\partial y} \end{aligned}\right\} \qquad \left.\begin{aligned} \dot{\omega}_{xx} &= \dot{\omega}_{yy} = 0 \\ \dot{\omega}_{xy} &= \frac{1}{2}\left(\frac{\partial v}{\partial x} - \frac{\partial u}{\partial y}\right) = -\dot{\omega}_{yx} \end{aligned}\right\}, \tag{2.10}$$

where $\dot{\varepsilon}$ and $\dot{\omega}$ are strain rate and vorticity respectively. Two principal components of the strain rate tensor can be found from the eigenvalue equation. Typically, the sum and the difference of the eigenvalues are introduced for the analysis of a strain-rate tensor as follows:

$$\dot{\varepsilon}_1 = \frac{\partial u}{\partial x} + \frac{\partial v}{\partial y},\ \dot{\varepsilon}_2 = \left[ \left( \frac{\partial u}{\partial x} - \frac{\partial v}{\partial y} \right)^2 + \left( \frac{\partial u}{\partial y} + \frac{\partial v}{\partial x} \right)^2 \right]^{1/2} \tag{2.11}$$

Here, $\dot{\varepsilon}_1$ quantifies the divergence or convergence of the ice field, with a positive value indicating a divergent motion field and a negative value a convergent field. $\dot{\varepsilon}_2$ defines the magnitude of the shearing. They depict different aspects of the deformation rate and are invariant with translation and rotation. We also introduce a new strain-rate vector with $\dot{\varepsilon}_1$ and $\dot{\varepsilon}_2$ components with the magnitude

$$\left\| \dot{\varepsilon} \right\| = \sqrt{\dot{\varepsilon}_1^2 + \dot{\varepsilon}_2^2}\,, \tag{2.12}$$

and azimuth

$$\psi = \text{atan}\left( \frac{\dot{\varepsilon}_2}{\dot{\varepsilon}_1} \right) \tag{2.13}$$

of the strain-rate vector which define the total deformation rate and the ratio of shearing and divergence, respectively. In particular, $\psi = 0, \pi/2$, and $\pi$ correspond to pure divergence, pure shear and pure convergence, respectively.

To take into account the internal ice stress $\boldsymbol{\tau}_i$, a constitutive law, which relates the strain rate of the ice cover to the applied stress is required. Several sea ice rheologies were proposed by Hibler in [16] and [26]. If sea ice rheology is defined then stress tensor components $\sigma_{xx}, \sigma_{xy}, \sigma_{yx}, \sigma_{yy}$ are known and the internal stress components can be determined as follows:

$$\tau_{ix} = \frac{\partial \sigma_{xx}}{\partial x} + \frac{\partial \sigma_{xy}}{\partial y},\ \tau_{iy} = \frac{\partial \sigma_{yx}}{\partial x} + \frac{\partial \sigma_{yy}}{\partial y}. \tag{2.14}$$

2.1.6. Pressure Ridges

A pressure ridge is a linear deformation of sea ice which is formed under convergent forces excerted by wind and/or the ocean. The youngest ice is the weakest part in the ice cover and is the first portion to be crushed. In sea ice dynamics, ridging is the main sink of kinetic energy in deformation due to friction and production of potential energy.

On the other hand, ridges are important aero- and hydrodynamic form drag elements at the air-ice and water-ice interfaces. The above water part of a ridge is the sail while the below water part (more extensive) is called the keel. Keels in the Arctic can reach down to 50 m, although most are about 10-25 m deep or less. In the sail and lower keel the ice blocks are loose or weekly frozen together. A simple structural model of ridges consists of a triangular keel and sail (Figure 2.2) described by the keel depth $h_k$, sail height $h_s$, slope keel angle $\varphi_k$ and slope sail angle $\varphi_s$.

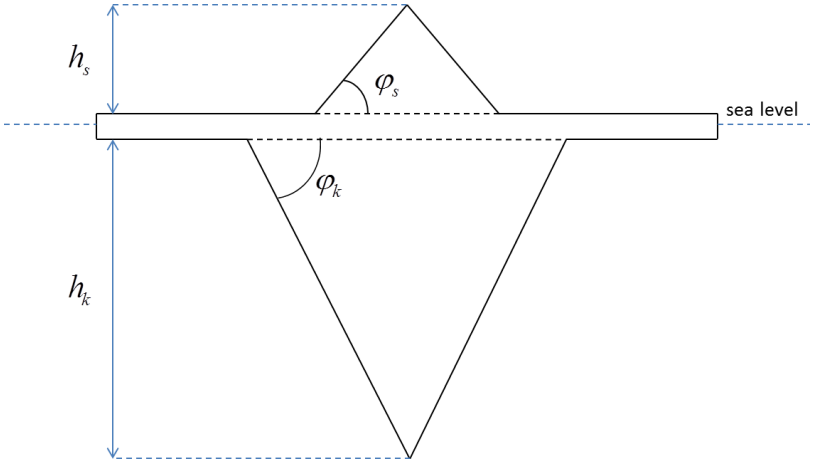


Figure 2.2. Schematic diagram of an ice ridge.

The relationship between the keel and sail heights can be estimated from the Archimedes law which can be written for our simple case as follows [25]:

$$(\rho_w - \rho_i)h_k^2 \cot\varphi_k = \rho_i h_s^2 \cot\varphi_s , \tag{2.15}$$

where $\rho_w, \rho_i$ are water and ice densities respectively. If $\varphi_k = \varphi_s$ the ratio of keel depth to sail height is estimated as $r_{ks} = h_k / h_s = 2.8$. If $\varphi_k = 30^o$ and $\varphi_s = 20^o$ then $r_{ks} = 3.5$ (from (2.15)). For multiyear ridges $r_{ks} \approx 3$ and for the first year ice ridges $r_{ks} \approx 4-5$ [25].

The spatial distribution of ridging is described in terms of their size and occurrence. Sail heights or keel depths distribution was proposed by [15] for the Arctic Ocean as follows:

$$n(h) = b \cdot \exp\left[-b(h - h_0)\right],\ h > h_0 , \tag{2.16}$$

where $n$ is the number of sails/keels per unit distance of track, $h_0$ is the low level cut-off. Parameter $b$ is defined through the mean keel depth/sail height $h_m$ as follows:

$$b = \left(h_m - h_0\right)^{-1}, \tag{2.17}$$

The exponential distribution (2.16) comes from the fact assuming all height arrangements yielding the same total sum are equally probable. Representative values for the mean sail height and keel depth $h_m$ in the central Arctic Ocean are $\langle h_s \rangle \approx 1.2 - 1.4\,\text{m}$ (cut-off is 0.9 m) and $\langle h_k \rangle \approx 8 - 14$ m (cut-off is 1.6 m). Therefore, parameter $b^{-1}$ is 0.3-0.5 m for sails and 2-5 m for keels.

According to [25] spacing between ridges is described by a logarithmic normal distribution. Representative values for mean ridge spacing are 5-10 km in the central Arctic Ocean, but with the cutoff sail heights of 0.4 m. The ridge size and spacing distributions are combined to form a measure of ridging intensity.

Ice topography also plays an important role in snow catchment hydrology over the first-year and multi-year sea ice. Snow distribution is substantially controlled by sea ice ridging. Generally, greater variability in snow depth was observed over ridged ice compared to smooth first-year ice [28], [29]. In addition, snow depth over the ridged ice was higher than on the smooth ice [28], [29].

## 2.2. Detection of Sea Ice Dynamics from SAR Imagery

SAR imagery acquired by satellite platforms (e.g. Canadian RADARSAT-1 and 2) is currently the most reliable source of information for routine detection of changes in sea ice cover at the regional and local scales [30]. Among other modes RADARSAT-2 ScanSAR Wide mode provides 500×500 km single-polarization (HH or VV) or dual-polarization (HH-HV or VV-VH) scenes with 50 m resolution [9]. In this section we describe how SAR imagery can be used for retrieval of sea ice motion, sea ice kinematic parameters and ocean surface wind speed.

### 2.2.1. Sea Ice Motion Tracking from SAR Images

Sea ice motion can be automatically detected from sequential SAR images taken over the same geographical area and separated by a time interval of a few days (usually 1 – 3 days). The statement of problem is fairly simple - to detect similar ice floes/features in both SAR images evenly distributed over the area of interest with the accuracy of 1 pixel. Even though the human eye is the best tool for such image matching, enormous amount of time and effort would be required to process even one image pair. This is why various automated image processing algorithms have been designed. It is worthwhile to note though that for verification of any automated ice motion tracking algorithm visual thorough inspection is still very important. In addition, in-situ ice motion beacons can be used for verification.

Existing ice motion tracking techniques contain many phases which may include a preprocessing step, image matching and error filtering steps. Within the preprocessing step, quite often a pyramid representation of input images is performed. The idea of image pyramids introduced in [31] was built on the fact that the direct matching process applied to the original

images would take massive computational resources (because the entire second image would serve as a search area). Having a few pyramid levels makes it possible to start ice tracking at the lowest resolution level, and then to refine the ice motion vector field at a higher resolution level using vectors found at the previous resolution level. Efficient identification of search areas at the next resolution level based on the ice motion derived from the previous resolution level is a separate problem.

Image pyramid levels can be generated through a recursive application of a low-pass filter and simple 2×2 pixel averaging starting with the original image [32], [33]. The low-pass filter is required to supress the coherent fading affect (distinctive in SAR imagery). Then the output image becomes an input to this routine to produce a set of pyramid images. At each resolution level a set of distinctive ice features suitable for tracking must be automatically identified. An error filtering step is necessary to eliminate false matches (i.e. ice tracking vectors). Often, simple thresholding of some measure of similarity between two subimages is applied [33]. However, in addition to this, an adaptive error filtering technique might be required.

Even though there are many steps in any ice motion tracking algorithm, the image matching component is the main one. Below we consider existing image matching approaches suitable for ice motion tracking pointing out their advantages and disadvantages. The methods can be divided into area-based and feature-based methods.

1) Area-based methods

The area based methods operate with subimages and are applicable best to the ice pack with medium and high ice concentrations.

Cross-correlation matching technique

This classical matching approach has been used in many ice tracking algorithms (e.g. [31], [33], [34]). A cross-correlation coefficient between the reference subimage $a$ with $N \times N$ pixels (from image 1) and a candidate subimage $b$ with $N \times N$ pixels (from image 2) is calculated as follows:

$$c = \frac{\sum_{i,j=1}^{N} \left(a_{ij} - \bar{a}\right)\left(b_{ij} - \bar{b}\right)}{\sqrt{\sum_{i,j=1}^{N} \left(a_{ij} - \bar{a}\right)^2 \sum_{i,j=1}^{N} \left(b_{ij} - \bar{b}\right)^2}}. \tag{2.18}$$

The cross-correlation coefficient $c$ varies from -1 to 1 and indicates the measure of similarity between two subimages $a$ and $b$. If the reference subimage $a$ is fixed and the subimage $b$ is a moving window within some search area in the second image then a cross-correlation matrix can be formed based on equation (2.18). Coordinates of the maximum value in this matrix would correspond to the motion vector of the reference subimage $a$.

The cross-correlation approach is very simple, straightforward and easy to code; however, there are two significant disadvantages of this approach: (1) it is computationally expensive for large images; (2) it does not capture the rotational component of ice motion.

Phase-correlation matching technique

This approach relies on the property of the Fourier transform that a shift in a spatial domain transforms into a phase shift in the frequency domain [32], [35]-[37]. Suppose function $f(\mathbf{r})$ has Fourier transform $F_1(\mathbf{u})$. Then the shifted function $f(\mathbf{r}-\mathbf{r_0})$ has Fourier transform

$F_2(\mathbf{u}) = e^{-i\mathbf{u}\mathbf{r}_0} F_1(\mathbf{u})$, where $\mathbf{r_0}$ denotes the shift vector. The translational component is found through the maximum value coordinates of the following phase-correlation function:

$$C = \mathcal{F}^{-1}\left( \frac{F_1^* \cdot F_2}{\left|F_1^*\right| \cdot \left|F_2\right|} \right), \tag{2.19}$$

where $\mathcal{F}^{-1}$ is the inverse Fourier transform operator; asterisk denotes complex conjugation. In this simple example the phase-correlation function is the delta-function of the argument $(\mathbf{r} - \mathbf{r_0})$. In practice, the inverse Fast Fourier Transform (FFT) transform is applied, and the maximum value of the phase-correlation matrix is linked with the shift vector coordinates. The phase correlation technique works significantly faster compared to the cross-correlation one due to the availability of the FFT routine. Also, a step of the moving window in the search area could be selected larger than one pixel. Furthermore, the phase-correlation approach can be extended to detection of the rotational component through the use of the Fourier shift and rotation theorem [38]. If $f_2(x, y)$ is a translated and rotated replica of $f_1(x, y)$ then from the Fourier transform properties we obtain:

$$\left.\begin{aligned} F_1(\xi,\eta) &= \mathcal{F}\{f_1(x,y)\} = \int_{-\infty-\infty}^{+\infty+\infty} f_1(x,y) e^{-i\xi x - i\eta y}\, dxdy \\ F_2(\xi,\eta) &= \mathcal{F}\{f_2(x,y)\} = e^{-i\xi x_0 - i\eta y_0} F_1(\xi\cos\theta_0 + \eta\sin\theta_0, -\xi\sin\theta_0 + \eta\cos\theta_0) \end{aligned}\right\}, \tag{2.20}$$

where $\mathcal{F}$ denotes the Fourier transform operator; $\theta_0$ is angle of rotation; $(x_0, y_0)$ are components of the shift vector. System of equations (2.20) indicates that the magnitude or the spectrum $F_2(\xi, \eta)$ is rotated as well. In polar coordinate this rotation is transformed into a shift which can be detected using the original phase-correlation technique given by (2.19).

A general disadvantage of the phase-correlation approach is that the peak value in the phase-correlation matrix does not provide a clear measure of similarity between two subimages.

Binary matching

If we operate with two binary images, it is convenient to use a binary matching approach [39]. For template matching, a metric that measures the degree of mismatch between the template $f$ and an unknown target pattern $g$ is defined as follows:

$$m = \sum_{R_p} XOR(f, g), \tag{2.21}$$

where $R_p$ is the size of the template pattern. A small value of $m$ indicates that two patterns are similar and a large value indicates that they are different. Only logical XOR operation on the pairs of pixel values (which gives 0 when they are of the same value, otherwise 1) needs to be performed, and therefore this method is very efficient computationally.

2) Feature-based methods

The feature-based methods operate with separate ice floes and could be more efficient in automated tracking of low-concentrated sea ice.

Ψ-S correlation

Ψ-S correlation approach has been developed by Kwok et al. [34] for tracking of features that have translated and rotated. The main idea of this method is to create a specific representation of the floe boundaries using Ψ-S coordinates as shown in Figure 2.3. The direction of the tangent to a shape is plotted as a function of arc length around the curve.

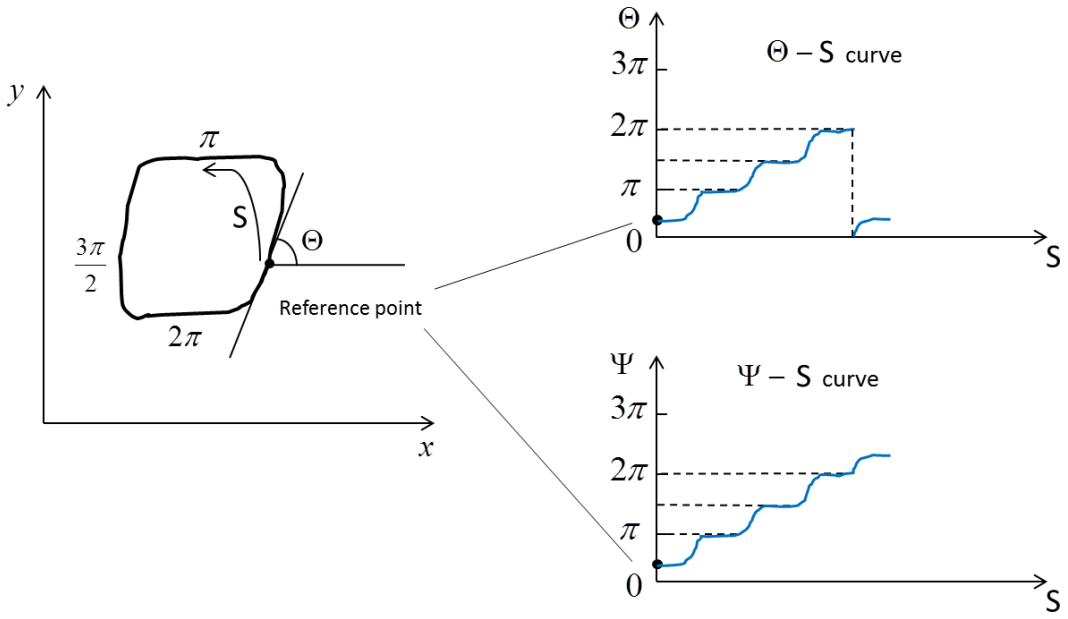


Figure 2.3. Concept of Ψ-S curve.

The matching between two Ψ-S curves is done by the one-dimensional cross-correlation of the Ψ-S segments:

$$r(k) = \frac{\sum_{j=1}^{n_s} \Psi_1(j)\Psi_2(j+k) - \mu_1\mu_2}{q_1 q_2}, \tag{2.22}$$

where $\mu_1, \mu_2$ are the means of Ψ-S segments; $q_1, q_2$ are the standards of deviation of Ψ-S segments and $n_s$ is the length of the segment. The value of $k$ that maximizes this expression gives the index of the beginning of the best match segment in $\Psi_2$.

The computational advantage of this approach comes from the fact that the correlation is linear rather than two-dimensional. A match is evaluated at each point along a boundary, rather than at each point in a region. In addition, this method is unaffected by rotation of features. The rotation of a feature adds a constant to its Ψ-S curve, which does not affect the correlation measure. The relative rotation $\theta$ of the features is obtained directly as

$$\theta = \mu_1 - \mu_2. \tag{2.23}$$

Dynamic programming approach

McConnel et al. [40] extended the Ψ-S correlation method to the possibility of detection of deformed floes using dynamic programming. This approach allows to identify the best matching between two sequences $s_1(1..M)$ and $s_2(1..N)$. A mapping between two sequences contains $P$ possible pairings, where $P \geq \max(M, N)$. Amongst these pairs one has the smallest "cost measure":

$$c(i,j)=\sum_{k}\left|s_{1i(k)}-s_{2j(k)}\right|,\ k=1..P\,. \tag{2.24}$$

The distance between two sequences is $D(s_1,s_2)=\min[c(i,j)]$ over all possible pair combinations.

For tracking ice floes, however, the objective is to locate the feature in one image that best matches a given feature in the other image. This can be accomplished by selecting a subinterval of the Ψ-S curve of a floe boundary from one image, and finding the subinterval of the Ψ-S curves of the other image most similar to it.

### 2.2.2. Sea Ice Kinematic Parameters from SAR

Having a dense ice motion vector field derived from two sequential SAR images makes it possible to directly calculate a number important ice kinematic parameters such as divergence, shearing and vorticity according to formulations (2.10) - (2.11) presented in Section 2.1. It is also possible to define a type of deformation through the deformation angle given by (2.13) [41]-[43].

The partial derivatives of the ice velocity field can be calculated on a rectangular mesh. An example of deformed grids on a SAR image over the ice can be found in [42]. Furthermore, having numerous SAR image pairs, cumulative kinematic parameters can be estimated almost all over the entire Arctic as shown in [44].

Sea ice area flux is another very important kinematic parameter of sea ice which can be calculated directly from SAR-derived ice motion vector fields. This value quantifies what area of ice moves through a certain gate in the Arctic Ocean (located e.g. in the Canadian Arctic Archipelago) per time unit. The sea ice area flux is typically estimated as follows [45], [46]:

$$F_g = \sum_k c_k \, u_{k\perp} \Delta x_k \,, \tag{2.25}$$

where $\Delta x_k$ is the spacing along the gate, [m]; $u_{k\perp}$ is the ice velocity component normal to the gate of the $k$-th ice motion vector, [m/s], and $c_k$ is the ice concentration in vicinity of the $k$-th vector.

### 2.2.3. Ocean Surface Wind Speed Retrieval from SAR

As discussed previously in Section 2.1 wind is one of the major factors affecting sea ice motion. Unfortunately, it is impossible to estimate surface wind speed directly over the sea ice from SAR or any other remote sensing satellite instrument. However, wind speed over the ocean surface can be mapped from SAR imagery to better monitor sea ice dynamics [47]. This additional piece of information is especially beneficial in MIZ where large areas of open water are found. In this section we discuss existing models for ocean surface wind speed retrieval from SAR and some of their deficiencies.

Winds over the ocean significantly affect sea surface roughness which in turn governs the backscatter normalized radar-cross section (NRCS) measured by a SAR instrument. Wind retrieval models which are based on the physical theory of electromagnetic waves interaction with the ocean surface are quite complex and computationally expensive. Furthermore, they do not agree well with experimental data in a wide range of wind speeds [48]-[53]. This is why empirical wind retrieval models are used in practical applications. A series of C-band geophysical model functions (CMODs) [54]-[56] have been extensively used for ocean surface wind speed retrieval from SAR. They have been built based on a large statistics of measurements taken by the European

spaceborne scatterometers ERS-1 and 2 (C-band, VV-polarization) collocated and coincided with in-situ ocean buoy observations. A general CMOD geophysical function can be expressed as follows:

$$\sigma_{VV}^{0}(\theta,\varphi,V) = a_0(\theta,V)\left[1 + a_1(\theta,V)\cos\varphi + a_2(\theta,V)\cos 2\varphi\right]^p, \tag{2.26}$$

where $\sigma_{VV}^{0}$ is C-band VV NRCS in linear units, $\theta$ is the antenna incidence angle, $V$ is the wind speed at 10 m height in m/s, $\varphi$ is the wind direction relative to the antenna look, $a_0(\theta,V)$, $a_1(\theta,V)$ and $a_2(\theta,V)$ are empirically determined functions of the incidence angle and wind speed, $p$ is a constant. All CMODs have the same general formulation (2.26), but they differ by the empirical constant $p$ and the appearances of functions $a_0$, $a_1$ and $a_2$. If $\sigma_{VV}^{0}$, $\theta$ and $\varphi$ are known, then equation (2.26) can be easily inverted relative to the wind speed $V$. It is important to note that the wind direction $\varphi$ is typically provided by numerical weather prediction (NWP) models which are often unreliable especially dealing with the Arctic region (mainly due to the presence of sea ice) [57]. Inaccuracy in the input wind direction may lead to an error in the retrieved wind speed (especially at high winds).

CMOD geophysical functions have been widely applied to SAR imagery which have a much higher resolution (~100 m) compared to the space borne scatterometers (~25 km). With the launch of Canadian RADARSAT-1 in 1995 the problem of wind speed retrieval from HH polarization images arose. To address this issue, various approximations of C-band co-polarization ratios (VV/HH) over the open water have been applied to the HH signal [58], [59]. For instance, in [59]

it was shown that the Kirchhoff co-polarization ration in conjunction with CMOD_IFR2 is suitable for wind speed retrieval from RADARSAT-1. However, existing approximations of the co-polarization ratio are still not accurate enough (as shown in [59]); hence, this inaccuracy may result in a significant error in wind speed estimation using CMODs.

Figure 2.4 shows dependences of VV NRCS calculated according to the latest CMOD5.N [55] on wind speed at various incidence angles. It is seen that the CMOD curves tend to saturate at high wind speed. This effect may also produce a large error in high wind speed retrievals [60].

With the launch of Canadian RADARSAT-2 in 2007 the new cross-polarization channel (HV) became available. In [61] there was shown an effect that the cross-polarization signal does not saturate at high wind speeds and does not depend on wind direction. Moreover, the following linear relationship between the wind speed and the cross-polarization signal was derived based on a large statistics of RADARSAT-2 Fine Quad images [61] and corresponding buoy measurements:

$$\sigma_{HV}^{0} = 0.596V - 35.6\ [\mathrm{dB}], \tag{2.27}$$

However, this simple model cannot be applied to RADARSAT-2 ScanSAR dual-polarization mode (HH-HV) due to the fact that the ScanSAR images have a significantly higher level of noise floor compared to the Fine Quad, which means that the cross-polarization signal at low and moderate wind speeds cannot be taken full advantage of. Nevertheless, results in [61] indicate that the cross-polarization channel in the wide ScanSAR mode could be an additional useful input to wind retrieval from SAR.

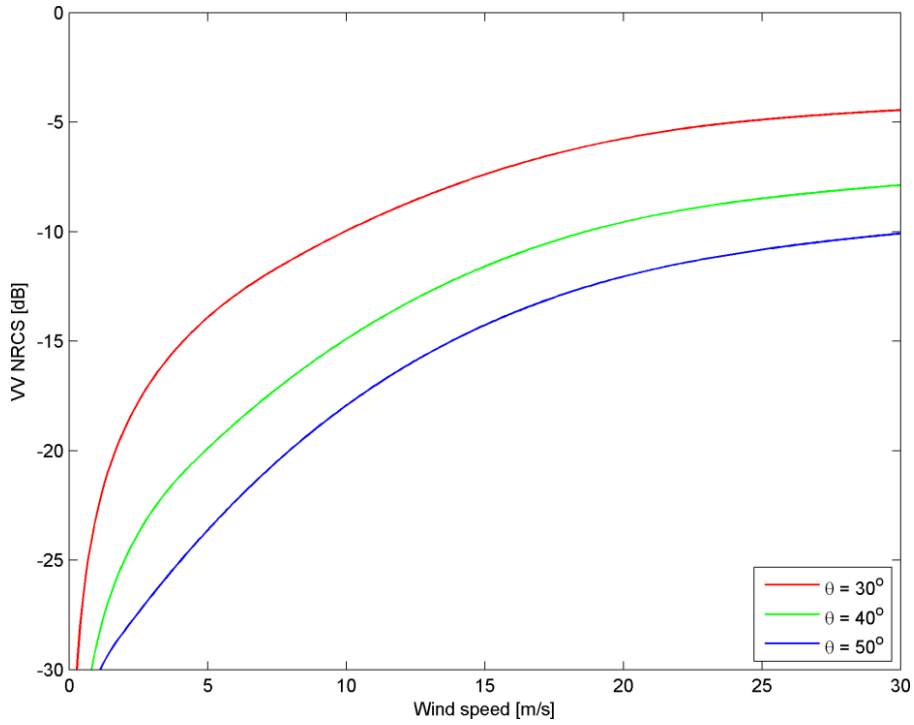


Figure 2.4. Dependence of VV radar backscatter on wind speed calculated according to CMOD5.N, wind direction is 45$^{o}$ relative to the antenna look.

## 2.3. Physics of Sea Ice Thermodynamics

In this section we review physical processes which govern thermodynamic characteristics of snow-covered sea ice. Interestingly enough, while physics of ice dynamics is described by the momentum balance equation (see equation (2.1) in Section 2.1), the physics of ice thermodynamics is described by the heat transfer equation with boundary conditions given by the energy flux balance. Similar to the dynamics part of this chapter, in this section we discuss the main equation of sea ice thermodynamics and its individual components. First, we discuss properties of sea ice and snow. Following this, we introduce a one-dimensional thermodynamic model for snow-covered sea ice. Then we discuss thermal properties of snow and sea ice which

control heat transfer. Finally, energy heat fluxes at the air-snow and ice-ocean interfaces are described.

### 2.3.1. Sea Ice Formation and Structure

Sea ice is formed when the sea water temperature reaches the freezing point (-1.86 $^{o}$C at 34 ppt). A decrease in the surface temperature causes instability of the upper layer because the density of cold sea water at the surface is higher than the density of warmer water underneath it. This results in mixing of water in the upper ocean layer followed by the heat transfer. Once the mixed layer is super-cooled, tiny discs and needles begin to form floating towards the surface. As freezing progresses a layer of frazil ice is formed, which later becomes grease ice. In the absence of wind the grease ice turns into a layer of thin smooth ice called nilas. Under wind conditions the frazil ice consolidates into rounded discs collectively called pancake ice. Pancakes are surrounded by elevated rims which are formed due to ice motion and collisions. The congelation growth begins once the ice is consolidated [62]. The upper 1-10 cm layer of sea ice called frazil layer consists of randomly oriented ice crystals. This random orientation is caused by the initial turbulent formation of ice. Beneath the frazil layer there is a transition layer. Within this layer ice has grown according to the geometric selection, i.e. the ice crystals with crystallographic c-axis oriented perpendicular to the temperature gradient had a preference while the crystals with a different orientation of c-axis are cut off. In the columnar ice layer (which is below the transition layer) all the crystals has horizontally oriented c-axes. During the ice growth brine is rejected from the ice and trapped in interstices of ice crystals and platelet substructure. The brine is concentrated in brine pockets and brine channels which have different sizes and shapes (depending on temperature). Brine dynamics

within the ice is driven by various mechanisms: brine pocket migration, brine expulsion, gravity drainage, or melt water flushing. The salinity profile of first-year sea ice is typically C-shaped due to the formation mechanism and brine dynamics. The brine volume within the ice varies with depth and represents a function of temperature and bulk salinity. Below the columnar layer there is a skeleton layer (1-3 cm thick) facing the ocean. It consists of lamellar platelets directed towards the water. The structure of the columnar layer is driven by changes in the skeletal layer [62].

### 2.3.2. Snow

A snow layer on sea ice consists of a combination of air and ice. Under melting conditions, liquid water occurs in the snow matrix. If brine is expelled from the upper ice volume into the snow, it has to be considered as an additional component. Snow substantially regulates heat transfer between the atmosphere and sea ice. Since the snow is a good insulator, in winter the ice-snow interface is stably warmer than the air-snow interface. In spring, the temperature gradient within the snow is changing according to the diurnal variations [63].

Snow is composed of ice crystals with various sizes and shapes which undergo a series of metamorphisms [64]. In a dry snowpack a high temperature gradient causes vapor transport from the bottom of the snow upwards. This results in high vapor pressure and fast kinetic growth of snow grains. Wet snow metamorphism is classified into the pendular and funicular regimes. In the pendular regime the snow moisture is less than 7% and the liquid water can stay between the snow grains. In this regime the clusters of grains form quickly. In the funicular regime the wetness exceeds 7% and the water begins to drain. In this regime the pore spaces are filled with water and individual grains obtain a spherical form.

2.3.3. Thermodynamic Model for Snow-Covered Sea Ice

A one-dimensional thermodynamic model for snow-covered sea ice developed by Maykut and Untersteiner [65] predicts the thermodynamic state of the snow and ice layers. It is assumed that the snow-covered sea ice is an infinite horizontally homogeneous slab which is impinged by various energy fluxes at the air-snow and ice-ocean interfaces as shown in Figure 2.5. The core mathematical formulation of the model consists of two heat transfer differential equations (in snow and ice) with respect to the temperature, which is a function of the vertical coordinate and time.

1) Heat transfer equations in snow and ice

In the snow cover the heat transfer equation with respect to temperature $T(z,t)$ as a function of the vertical coordinate $z$ and time $t$ is given as follows [65]:

$$\rho_s c_s \frac{\partial T}{\partial t} = k_s \frac{\partial^2 T}{\partial z^2} + I_0 \kappa_s e^{-\kappa_s z}, \tag{2.28}$$

where $\rho_s$ is the snow density, [kg/m$^3$]; $c_s$ is the specific heat of the snow, [J/kgK]; $k_s$ is the thermal conductivity of the snow, [W/mK], which is in the simplest case assumed to be a constant over depth. $I_0$ is the transmitted radiation into the medium, [W/m$^2$] (which is a function of physical properties of material, incidence angle and wavelength) and $\kappa_s$ is the bulk radiation extinction coefficient (integrated over all wavelengths and solid angles). The first term in the right hand side of equation (2.28) represents heat conduction while the second term represents penetration and extinction of short-wave radiation within the snow layer.

Given that thermal properties of sea ice depend on the temperature and salinity (as shown further), the heat transfer equation for sea ice becomes nonlinear. However, some of the nonlinear terms are three orders of magnitude smaller than the major terms, and, thus, the heat transfer equation within the sea ice (accounting for the snow layer on top) can be written as follows [65]:

$$\rho_i(S,T)c_i(S,T)\frac{\partial T}{\partial t} = k_i(S,T)\frac{\partial^2 T}{\partial z^2} + I_0\kappa_i e^{-\kappa_i z-\kappa_s h_s}, \tag{2.29}$$

where $\rho_i(S,T)$ is the density of sea ice, $c_i(S,T)$ is the specific heat of sea ice and $k_i(S,T)$ is the thermal conductivity of sea ice. All are functions of temperature and salinity. $\kappa_i$ is the radiation extinction coefficient of the ice; $h_s$ is snow thickness.

2) Boundary conditions

The heat transfer within snow-covered sea ice is partially controlled by energy fluxes at the air-snow and ice-ocean interfaces. To unambiguously solve differential equations (2.28) and (2.29) a set of boundary conditions must be formulated based on the energy balance at the interfaces.

Energy balance at the air-snow interface:

At the snow surface the following balance of heat fluxes is held:

$$(1-\alpha)F_r - I_0 + F_L - F_{EL} + F_s + F_l + F_c = \begin{cases} 0, & T_s < 273.15K \\ -q_s\rho_s\dfrac{dh_s}{dt}, & T_s = 273.15K \end{cases}, \tag{2.30}$$

where positive sign denotes fluxes going towards the surface. In the left hand side of equation (2.30) all the fluxes are time dependent input parameters. The major energy fluxes include $F_r$ is incoming short wave radiation, which basically follows the sun and varies throughout the year; $\alpha F_r$ is outgoing short wave radiation; $\alpha$ is the surface bulk albedo; $F_L$ is incoming long-wave radiation from the atmosphere and clouds; $F_{EL}$ is outgoing long-wave radiation. All fluxes are in [W/m$^2$].

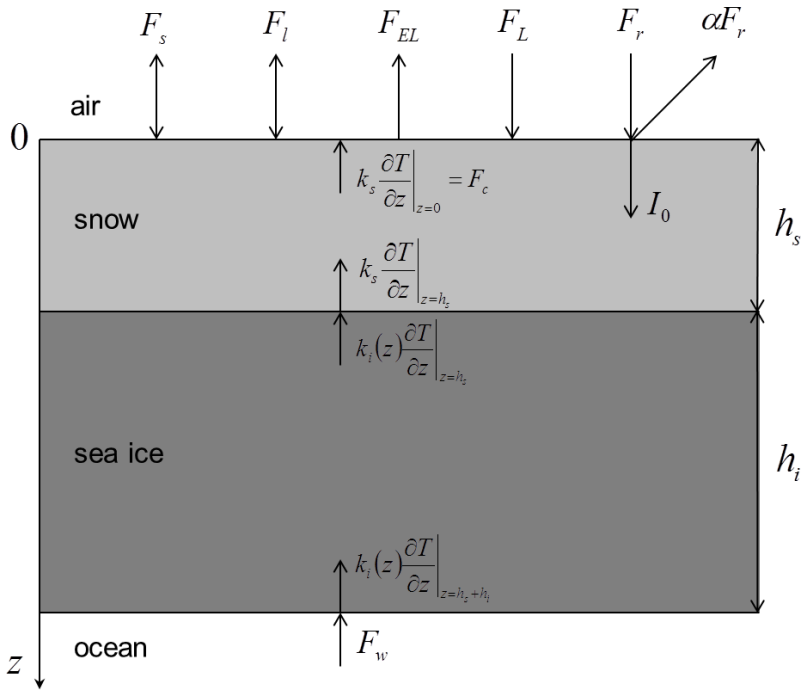


Figure 2.5. Illustration of heat transfer within snow-covered sea ice

The smaller fluxes include $F_s$, $F_l$, and $F_c$ are sensible, latent and conduction heat fluxes respectively between the snow surface and the adjacent air. The right hand side of equation (2.30)

accounts for two options: (1) if the surface temperature is below freezing point; (2) if the surface temperature is at the freezing point and some portion of snow melts. $q_s$ is the latent heat of fusion of the snow surface and $\rho_s$ is the snow density.

Equation (2.30) can be resolved with respect to the surface temperature at a certain point in time, using, for instance, the Newton-Raphson iteration method. The obtained result would provide the boundary temperature value for the numerical scheme.

Boundary condition at the snow-ice interface:

At the snow-ice interface it is assumed that the temperature and heat flux functions are continues:

$$\left.\begin{aligned} T(h_s+0) &= T(h_s-0) \\ k_i\left(\frac{\partial T}{\partial z}\right)_{h_s+0} &= k_s\left(\frac{\partial T}{\partial z}\right)_{h_s-0} \end{aligned}\right\}. \tag{2.31}$$

Boundary condition at the ice-water interface:

At the ice bottom the energy balance can be written as follows:

$$k_i\left(\frac{\partial T}{\partial z}\right)_{h_s+h_i} - F_w = q_i\rho_i\frac{dh_i}{dt}, \tag{2.32}$$

where the first term represents the conductive heat flux at the ice bottom, and the second term $F_w$ is the ocean heat flux. The right hand side indicates ice melt or growth as a result of these two

fluxes acting at the ice-water interface; $q_i$ is the latent heat of fusion at the ice bottom, $\rho_i$ is the ice density, and $h_i$ is the ice thickness which depends on time.

From equation (2.32) the temperature gradient at the bottom for a certain time can be derived. This provides a boundary value to the numerical scheme.

### 2.3.4. Thermal Properties of Snow

Thermal conductivity of snow is an order of magnitude smaller than that of sea ice. This means that the snow layer acts as a good insulator between sea ice and the atmosphere. In the heat transfer equation (2.28) the snow thermal conductivity was put a constant; however, this parameter depends on snow density $\rho_s$ (in $\mathrm{kg/m}^3$) and temperature $T$ (in K) as follows [66]:

$$k_s = 2.845\times10^{-6}\rho_s^2 + 2.7\times10^{-4}\cdot 2^{(T-233)/5}, \tag{2.33}$$

where snow density and temperature typically depend on depth. Equation (2.33) accounts for direct thermal conduction (first term) and water vapor diffusion (second term). However, this formulation does not account for brine/liquid content in snow.

Specific heat of snow (in [J/kgK]) can be represented as a linear function of temperature (in [K]) [66]:

$$c_s = 92.88 + 7.364T\,. \tag{2.34}$$

2.3.5. Thermal Properties of Sea Ice

Thermal conductivity of sea water is about 25% of the conductivity of fresh ice [15]. Therefore, conduction of heat in the sea ice is substantially influenced by brine pockets trapped in the ice during bottom accretion. The brine and surrounding ice are in phase equilibrium at a certain freezing temperature. If the temperature rises, then some portion of ice around the brine pockets melts. This process decreases salinity of brine and increases the freezing point. Therefore, the brine pockets are able to retard the heating or cooling of the ice. Thus, bulk thermal properties of the ice (thermal conductivity and specific heat) are functions of temperature and salinity. The thermal conductivity of sea ice can be expressed as a function of temperature (in K) and salinity (in parts per thousand) as follows [67]:

$$k_i = k_{pi} + \frac{\beta S}{T - 273.15}, \tag{2.35}$$

where $\beta = 0.117$ W/(m·ppt), and $k_{pi}$ is the thermal conductivity of pure (fresh) ice defined by [68] as a function of temperature (in K) only:

$$k_{pi} = 9.828 \exp(-0.0057\, T). \tag{2.36}$$

The volumetric heat capacity (product of density and specific heat) can be described as a function of temperature and salinity as follows [65]:

$$\rho_i c_i = \rho_{pi} c_{pi} + \frac{\gamma S}{(T - 273.15)^2}, \tag{2.37}$$

where $\rho_{pi} = 916$ kg/m$^3$ and $c_{pi} = 2113$ J/kgK are density and specific heat of pure ice respectively, $\gamma = 1.715 \times 10^7$ J·K/(m$^3$ppt).

The concept of latent heat for sea ice is not straightforward because ice and brine can coexist at any temperature. Ono [69] proposed an equation for latent heat of fusion (J/kg) of sea ice for temperatures above -8$^o$C:

$$q_i = 333394 - 2113(T - 273.15) - 114.2S + \frac{18040S}{T - 273.15}. \tag{2.38}$$

Figure 2.6 demonstrates dependencies of three thermal parameters of sea ice (calculated according to equations (2.35), (2.37) and (2.38)) on temperature and salinity. It is seen that the thermal conductivity and latent heat of fusion of warm very saline ice (e.g. young ice or melting first-year ice) become lower while the volumetric heat capacity gets higher compared to those of cold low salinity ice.

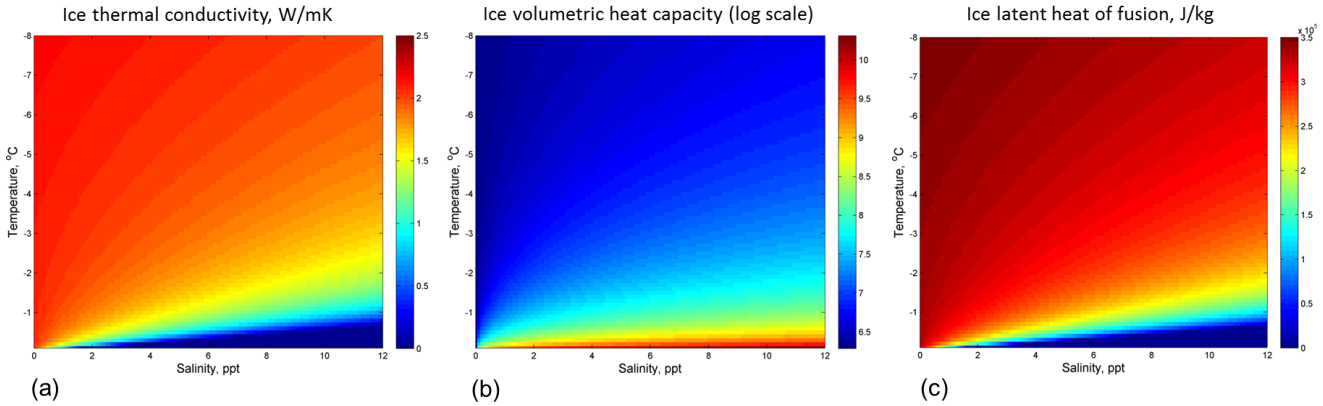


Figure 2.6. Thermal properties of sea ice versus temperature and salinity: (a) thermal conductivity, (b) volumetric heat capacity; (c) latent heat of fusion.

### 2.3.6. Energy Fluxes

The solar short-wave radiation of clear sky $F_r$ is a function of the solar zenith angle and vapor pressure [70]. Clouds reduce the incoming short-wave radiation reaching the surface by the factor depending on the cloud coverage [70]. The bulk albedo (i.e. ratio of reflected and incident solar radiation) is an integrated characteristic across the short-wave spectrum. This parameter is very important to the thermodynamic model since it is sensitive to ice thickness and brine volume in young ice. Table 2.1 shows changes in albedo for different types of ice (from 0.52 for bare first-year ice to 0.87 for snow-covered ice). Furthermore, in summer (when the short-wave radiation reaches its peak) there is a spatial variability of the albedo across the sea ice due to the presence of melt ponds, snow, and bare ice.

Table 2.1. Range of observed bulk albedo for various surfaces.

| Surface type | Albedo |
|---|---|
| Open water | 0.06 |
| Old melt pond | 0.15 |
| Ponded FY ice | 0.21 |
| Mature pond | 0.29 |
| Refrozen melt pond | 0.4 |
| Bare FY ice | 0.52 |
| Melting white ice | 0.56 – 0.68 |
| Frozen white ice | 0.7 |
| Melting snow | 0.77 |
| Wind packed snow | 0.81 |
| New snow | 0.87 |

The part of the shortwave radiation that passes through the snow and ice is parameterized by Beer's law as follows [70]:

$$I(z) = (1-\alpha)F_r e^{-\kappa z}, \tag{2.39}$$

where $\kappa$ is the bulk extinction coefficient (integrated over the spectral range of the shortwave radiation) of snow or ice.

The emitted long-wave radiation $F_{EL}$ by the surface is defined by the Stefan-Boltzmann law:

$$F_L = e_L \sigma T_0^4 , \tag{2.40}$$

where $e_L$ is the long wave emissivity of the surface (~0.96), $T_0$ is the surface temperature (in K), and $\sigma$ is the Stefan-Boltzmann constant. Emissivity of the incoming long-wave radiation $F_L$ from the atmosphere and clouds heavily depends on the air temperature, and cloud coverage [70]. In winter, in the absence of solar radiation, the long-wave radiation is particularly important in the surface energy balance.

The turbulent sensible ($F_s$) and latent heat fluxes ($F_l$) are functions of wind speed, temperature and humidity differences between the surface and the atmosphere [70].

In the model [65] the ocean heat flux $F_w$ is assumed to be a constant equal to 2 W/m$^2$. However, it can highly vary throughout the year [71] and therefore it is challenging to model this parameter. The ocean heat flux can be estimated indirectly using long term ice mass balance buoy (IMB) observations [72].

## 2.4. Microwave Scattering Models

Radar microwave remote sensing has been widely used to assess the thermodynamic state of snow-covered sea ice. Radar signatures are sensitive to the system configurations (frequency, polarization, incidence angle) and the properties of the sea ice (dielectrics of snow and ice, air and brine inclusions, topography) [73]. In turn, the dielectric constants of snow and ice are controlled by their geophysical properties.

Modeling of electromagnetic waves scattering by snow-covered sea ice is a crucial component in understanding the linkage between observed radar response and corresponding geophysical properties of snow-covered sea ice. We focus on the modeling of surface scattering from winter first-year snow-covered sea ice where the contribution from volume scattering can be neglected in C- and L-bands.

We begin this section with Maxwell's equations and the definition of the normalized radar cross-section (NRCS). Then we introduce the concept of the complex dielectric constant (CDC) and present mixture models for estimating CDCs of snow and sea ice. Finally, we present the framework of the small perturbation theory applied to Maxwell's equation and discuss existing solutions and their limitations.

### 2.4.1. Maxwell's Equations

Electromagnetic fields at any point of space and time must satisfy Maxwell's equations [74], [75]:

$$\left.\begin{aligned}
&\nabla \times \mathbf{H} = \frac{\partial \mathbf{D}}{\partial t} + \mathbf{j} + \mathbf{j}^{\mathbf{ext}} \\
&\nabla \times \mathbf{E} = -\frac{\partial \mathbf{B}}{\partial t} \\
&\nabla \cdot \mathbf{D} = \rho + \rho^{ext} \\
&\nabla \cdot \mathbf{B} = 0 \\
&\mathbf{j} = \sigma \mathbf{E} \\
&\frac{\partial \rho}{\partial t} + \nabla \cdot \mathbf{j} = 0 \\
&\frac{\partial \rho^{ext}}{\partial t} + \nabla \cdot \mathbf{j}^{\mathbf{ext}} = 0
\end{aligned}\right\}, \tag{2.41}$$

where $\mathbf{E}$ and $\mathbf{H}$ are total electric and magnetic fields, $\rho$ is the charge density, $\mathbf{j}$ is the current density, $\rho^{ext}$ is the charge density of external sources, $\mathbf{j}^{\mathbf{ext}}$ is the current density of external sources, $\sigma$ is conductivity of the medium, $\mathbf{D}$ and $\mathbf{B}$ are electric and magnetic flux densities respectively which are linked with electric and magnetic fields as follows [75]:

$$\left.\begin{aligned}\mathbf{D} &= \varepsilon_0\mathbf{E} + \mathbf{P}\\ \mathbf{B} &= \mu_0\mathbf{H} + \mathbf{M}\end{aligned}\right\}, \tag{2.42}$$

where $\mathbf{P}$ is the electric polarization in the medium, and $\mathbf{M}$ is the magnetic polarization of the medium (magnetization); $\varepsilon_0$ and $\mu_0$ are electric permittivity and magnetic permeability of vacuum respectively.

In our microwave remote sensing problem a monochromatic electromagnetic plane wave with arbitrary polarization is incident upon the snow-covered sea ice structure. The incidence angle relative to the vertical axis is $0 \le \Theta_0 < \pi/2$. The wave is scattered by the rough air-snow and snow-ice interfaces and also propagates within the media. Our problem is monochromatic and a time dependence of the electric and magnetic fields is accepted to be $e^{-i\omega t}$, where $\omega$ is the angular frequency. Since the incident field is a plane wave then sources are absent, i.e. $\mathbf{j}^{\mathbf{ext}} = 0$, $\rho^{ext} = 0$. Then, Maxwell's equations (2.41) can be rewritten as follows:

$$\left.\begin{aligned} \nabla \times \mathbf{H} &= -i\omega\mathbf{D} + \sigma\mathbf{E} \\ \nabla \times \mathbf{E} &= i\omega\mathbf{B} \\ \nabla \cdot \mathbf{D} &= \frac{1}{i\omega}\nabla \cdot (\sigma\mathbf{E}) \\ \nabla \cdot \mathbf{B} &= 0 \end{aligned}\right\}. \tag{2.43}$$

2.4.2. Normalized Radar Cross-Section

Suppose the electric and magnetic fields are found in far zone. Then, the normalized radar-cross-section (NRCS) in the bistatic case is a function of the elevation angle $\theta$ and azimuth angle $\varphi$ and it can be defined as follows [49]:

$$\sigma_{pq}(\theta,\varphi;\Theta_0,\Phi_0) = 4\pi r^2 \frac{\left\langle S_{pq}(\theta,\varphi;\Theta_0,\Phi_0)\right\rangle}{S_{0p}A}, \tag{2.44}$$

where the direction of the incident wave is given by $\Theta_0$ (elevation angle) and $\Phi_0$ (azimuth angle). In the last equation $\left\langle S_{pq}(\theta,\varphi;\Theta_0,\Phi_0)\right\rangle$ is the average value of the Poynting vector (energy flux density) at the observation point $(\theta,\varphi)$ in far zone from a unit area of the surface; $A$ is the surface area; $r$ is the distance between the scattering surface and the observation point; $S_{0p}$ is the energy flux density of the incident plane wave. At the same time, the NRCS also depends on polarization of the incident electromagnetic wave $(p)$ and polarization of the received wave $(q)$.

In the monostatic (backscatter) case the receiver point coincides with the transmitter i.e. we assume $\theta = \Theta_0$ and $\varphi = \Phi_0 + \pi$.

2.4.3. Complex Dielectric Constant

We consider fields with the harmonic time dependence. Many natural media (e.g. containing water) has the property of frequency dispersion. Charged particles in the medium move due to the external electric field $\mathbf{E}$. They gain torque and the medium becomes polarized. Since the charged particles are inertial, this process cannot be done instantly. This mechanism causes energy loss. Furthermore, electric flux density $\mathbf{D}$ at some point in time is determined by the electric field at the previous moments of time. This phenomenon is called frequency dispersion [75]. CDC of such media depends on the frequency $\omega$. Then, in Maxwell's equations (2.41) for linear isotropic media with frequency dispersion the electric field and electric induction can be linked through the following constitutive relation:

$$\mathbf{D} = \varepsilon_0 \varepsilon_r(\omega)\mathbf{E}, \tag{2.45}$$

where $\varepsilon_r$ is the relative permittivity of the medium as a function of frequency. If the magnetic permeability of all media is 1 then the constitutive relationship for magnetic field is the following:

$$\mathbf{B} = \mu_0 \mathbf{H}. \tag{2.46}$$

Also, from Maxwell's equations:

$$-i\omega\mathbf{D} + \sigma\mathbf{E} = -i\omega\varepsilon_0\left(\varepsilon_r + i\frac{\sigma}{\omega\varepsilon_0}\right)\mathbf{E} = -i\omega\varepsilon_0\varepsilon(\omega)\mathbf{E}, \tag{2.47}$$

where $\varepsilon$ is the CDC of the medium which includes ohmic loss (in the presence of free charges in the medium).

CDCs of snow and sea ice govern wave propagation through the medium. Therefore, the accurate description of CDC of these media is very important in electromagnetic modeling.

### 2.4.4. Dielectric Properties of Sea Ice

Sea ice is a complex medium which consists of pure ice, brine pockets, and air bubbles. A two-phase medium with a host material (pure ice) and inclusions (brine pockets) can be applied to first-year sea ice (with no air bubbles). Even though the dielectric constants of individual components (brine and pure ice) are well known, modelling CDC of their mixture (i.e. sea ice) is challenging.

One of the possible approaches is the refractive dielectric mixture model:

$$\sqrt{\varepsilon_i} = \sqrt{\varepsilon_{pi}}\left(1 - V_b\right) + \sqrt{\varepsilon_{bi}} V_b \tag{2.48}$$

Where $\varepsilon_{pi}$ is the dielectrics of the host medium (pure ice), $\varepsilon_{bi}$ is the dielectrics of inclusions (brine pockets), $V_b$ is the volumetric brine content in sea ice. In [76] the refractive model showed a good agreement with dielectric measurements reported in [77].

The brine volume $V_b$ can be derived according to Frankenstein and Garner formulations [78] through measured temperatures and bulk salinities:

$$V_b = \begin{cases} 10^{-3} S\left(-\dfrac{52.56}{t} - 2.28\right), & -2.06^{\circ}\mathrm{C} \le t \le -0.5^{\circ}\mathrm{C} \\ 10^{-3} S\left(-\dfrac{45.917}{t} + 0.930\right), & -8.2^{\circ}\mathrm{C} \le t \le -2.06^{\circ}\mathrm{C} \\ 10^{-3} S\left(-\dfrac{43.795}{t} + 1.189\right), & -22.9^{\circ}\mathrm{C} \le t \le -8.2^{\circ}\mathrm{C} \end{cases}, \tag{2.49}$$

Where $S$ is bulk salinity of sea ice (in ppt), $t$ is temperature of sea ice (in $^{\circ}\mathrm{C}$). Note that Frankenstein and Garner equations [78] assume constant sea ice density of 0.926 g/cm$^3$.

1) Dielectric constant of pure ice

The dielectrics of the host material $\varepsilon_{pi}$ (pure ice) is nearly a constant (~3.17) with a slight dependence on temperature ($t, ^{\circ}\mathrm{C}$) [79]:

$$\varepsilon_{pi} = 3.1884 + 0.00091\, t\,. \tag{2.50}$$

The imaginary part in microwave band is quite small (~$10^{-3}$) and often can be neglected.

2) Dielectric constant of pure water and brine

The frequency dependence of the dielectrics of pure water is described by the well-known Debye equation [80]:

$$\varepsilon_w = \varepsilon_{w\infty} + \frac{\varepsilon_{ws} - \varepsilon_{w\infty}}{1 - i\omega\tau_w}, \tag{2.51}$$

where $\varepsilon_{w\infty}$ is the high frequency (or optical) limit which is 4.9, $\varepsilon_{ws}$ is the static dielectric constant of water (for $\omega = 0$) which depends on temperature, $\tau_w$ is the relaxation time which is also temperature dependent [80]. Relaxation time is the time interval required for water dipoles to return to the initial position after the externally applied electric field is turned off. The corresponding relaxation frequency (obtained from $2\pi f_w \tau_w = 1$) indicates the maximum of the dispersion loss in the frequency dependencies.

If there are dissolved salts in water, then free charges are present, and an additional ohmic loss term is introduced in the Debye equation as follows:

$$\varepsilon_{bi} = \varepsilon_{b\infty} + \frac{\varepsilon_{bs} - \varepsilon_{b\infty}}{1 - i\omega\tau_b} + i\frac{\sigma_b}{\omega\varepsilon_0}, \tag{2.52}$$

where $\varepsilon_{b\infty}$ is the limiting high frequency dielectrics of brine (4.9), $\varepsilon_{bs}$ is the limiting static dielectrics of brine, $\sigma_b$ is the conductivity of brine, $\tau_b$ is the relaxation time of brine. The real parts of dielectrics for fresh and salty water are very similar; however, the imaginary parts are very different at the frequencies lower than the relaxation frequency (corresponding to the curve peak) due to the ohmic loss term in equation (2.52) [80].

The Debye parameters for the brine in equilibrium with ice were determined by Stogryn and Desargant [81]:

$$\varepsilon_{b\infty} = \frac{82.79 + 8.19t^2}{15.68 + t^2} \tag{2.53}$$

$$\varepsilon_{bs} = \frac{939.66 - 19.068t}{10.37 - t} \tag{2.54}$$

$$2\pi\tau_b = 10^{-9}\left(0.10990 + 0.13603 \cdot 10^{-2} t + 0.20894 \cdot 10^{-3} t^2 + 0.28167 \cdot 10^{-5} t^3\right) \tag{2.55}$$

$$\sigma_b = \begin{cases} -t \exp\left(0.5193 + 0.8755 \cdot 10^{-1} t\right), & t \geq -22.9^{\circ}\text{ C} \\ -t \exp\left(1.0334 + 0.1100\, t\right), & t < -22.9^{\circ}\text{ C} \end{cases} \tag{2.56}$$

In equations (2.53) – (2.56), which fit experimental data in the temperature range from 0 to -25$^{o}$C, $t$ is the brine temperature (in $^{o}$C).

2.4.5. Dielectric Properties of Snow

Snow on sea ice is a mixture of air, pure ice grains, fresh water, and brine. While an electromagnetic wave is moderately sensitive to the mixture of air and pure ice, it is extremely sensitive to even small fractions of liquid (brine or fresh water) in the snow. Therefore, the CDC of the snow (mixture) is substantially governed by the liquid phase in the snow. Unfortunately, a reliable formulation for snow CDC which would take into account the presence of brine and fresh water in snow does not exist.

Dielectric constant of dry snow is well studied and can be accurately predicted as a function of snow density $\rho_d$ $\left(0.09\ \text{g/cm}^3 \leq \rho_d \leq 0.38\ \text{g/cm}^3\right)$ in the range of frequencies $3\ \text{GHz} \leq f \leq 37\ \text{GHz}$ [82]:

$$\varepsilon_d = 1.0 + 1.832\ \rho_d . \tag{2.57}$$

The CDC of wet snow is mostly controlled by liquid water content. One of the models for describing the CDC of wet snow (with no brine) was proposed by Hallikainen [82]. His Debye-like model is given as follows:

$$\varepsilon_s = \varepsilon_d + AW^{\alpha} + \frac{B}{1 - if\ /\ f_0} W^{\beta} . \tag{2.58}$$

In the last equation, $f$ is a frequency in the range between 3 and 37 GHz; $W$ is volumetric moisture content $m^3/m^3$ that may vary from 0 to 12%; $A = 2.14$, $B = 30.43$, $\alpha = 1.015$, $\beta = 1.31$, and $f_0 = 9.07$ GHz are empirical constants.

The presence of brine in snow on top of sea ice substantially influences the imaginary part of the dielectric constant due to the ohmic loss (particularly at lower frequencies). The brine volume content in snow (in the absence of fresh water) can be found using Drinkwater and Crocker formulations [83] through snow density, temperature and bulk salinity. Then, the dielectric constant of brine wetted snow can be estimated using a dielectric mixture model (such as the refractive dielectric mixture model).

### 2.4.6. Modelling of Electromagnetic Wave Scattering

Dielectric mixture models provide a link between geophysical properties of snow-covered sea ice and dielectric constants of the media. The dielectric constants serve as an important input to any

microwave scattering model. In this section we focus on the case of snow-covered first year sea ice where the dominant scattering occurs at the air-snow and snow-ice rough interfaces. There are various approaches for modelling of electromagnetic waves scattering by snow-covered sea ice. A review of various scattering models which account for volume or surface scattering in sea ice is given by [84].

Semi-empirical models [80], [85] based on the radiative transfer theory [86] naturally account for volume scattering within snow and sea ice; however, the surface scattering components in these models must be determined separately from physical or empirical scattering models.

The physical based models rely on exact (numerical) or approximate solutions of Maxwell's equations.

Numerical finite-difference time-domain (FDTD) [87], [88] and finite-volume time-domain (FVTD) [89] methods are directly applied to Maxwell's equations and provide a solution within a certain approximation. In these methods surface and subsurface roughness/deformations and an arbitrary behaviour of the dielectric constant within the snow and sea ice can be accounted for. However, the numerical methods require significant computational resources due to the facts that (1) numerous realizations of the random rough surface must be simulated, and (2) extremely fine mesh in the situations where absorption is very high (e.g. sea water under the ice) is required. These constraints make the numerical methods barely applicable to satellite remote sensing problems (e.g. analysis of temporal changes of SAR signatures). Since the numerical methods do not have a closed form solution, there is not a clear linkage between the scattering characteristics and the physical properties of the media (e.g. roughness and dielectrics).

Analytical methods are aimed to derive a closed-form solution of Maxwell's equation under certain approximations. The small perturbation method (SPM) was introduced for analytical formulation of waves scattering from slightly rough surfaces by Rice [90] in 1951. Since then the SPM theory has been extended onto solving more complex scattering problems. The SPM final formulations are expressed in a closed form and demonstrate a clear linkage between the scattering coefficients and the physical properties of the media. Furthermore, the SPM theory can be generalized for a few rough interfaces embedded in media. The SPM solution can also be extended to the case when the small-scale roughness is modulated by a large-scale topography (e.g. typical for multiyear ice). An idea of such an extension to the two-scale geometry can be found in [49]. Since the forward solver does not require heavy computational recourses, it can be run multiple times for different incidence angles, polarizations and physical properties of the media which would facilitate the problem of inversion. Thus, they seem more applicable to geophysical problems.

Below we introduce a concept of the SPM formalism including boundary conditions for electromagnetic fields at the rough interface. We also describe available SPM solutions for different scattering geometries.

1) The underlying theory of SPM

Suppose we have a rough air-snow or snow-ice interface $\zeta(\boldsymbol{\rho})$ which sets a random deviation from a plane at $z = z_r$, where $\boldsymbol{\rho} = \{x, y\}$ - position vector in the horizontal plane. The SPM formalism applies to surfaces $\zeta(\boldsymbol{\rho})$ with a small surface height variation and small surface slopes [91]:

$$kL_\zeta < 3, \quad k\sigma_\zeta < 0.3, \ \frac{\sigma_\zeta}{L_\zeta} < 0.3, \tag{2.59}$$

where $k$ is the wave number in the medium, $L_\zeta$ is the correlation length of the rough surface, $\sigma_\zeta = \left\langle \zeta^2 \right\rangle$ is the standard deviation of the rough surface. For the first-year sea ice these conditions are valid for wavelengths in C-band (5.5 GHz) and L-band (1.4 GHz).

In the presence of the random rough interface the solution of Maxwell's equations should contain a random component. Therefore, Maxwell's equations do not have an exact analytical solution. According to the first-order approximation of the SPM method, the electric and magnetic fields are expanded in a perturbation series as follows [49], [50]:

$$\left.\begin{aligned} \mathbf{E}(\boldsymbol{\rho}, z) &\approx \mathbf{E}^{(0)}(\boldsymbol{\rho}, z) + \mathbf{E}^{(1)}(\boldsymbol{\rho}, z) \\ \mathbf{H}(\boldsymbol{\rho}, z) &\approx \mathbf{H}^{(0)}(\boldsymbol{\rho}, z) + \mathbf{H}^{(1)}(\boldsymbol{\rho}, z) \end{aligned}\right\}, \tag{2.60}$$

where $\mathbf{E}^{(0)}$, $\mathbf{H}^{(0)}$ are exact solutions of Maxwell's equations (zero-order fields) in the absence of the small-scale roughness, and $\mathbf{E}^{(1)}$, $\mathbf{H}^{(1)}$ are first-order fields which depend on the amplitude of the roughness [48]. The first-order fields represent a random component of the electromagnetic field due to the rough interface. Hence, the roughness' impact is taken into account by a random additive component (first-order fields).

2) Boundary conditions for SPM

Both zero-order and first-order fields must satisfy regular boundary conditions at smooth interfaces i.e. the tangential components must be continuous. At the mean level of the rough interface $z = z_r$ it is possible to demonstrate that within the first-order approximation of SPM the following boundary conditions are valid [48]:

$$\left.\begin{aligned}
&\mathbf{E}_t^{(1)}(\boldsymbol{\rho}, z_r + 0) - \mathbf{E}_t^{(1)}(\boldsymbol{\rho}, z_r - 0) = \\
&= -\zeta(\boldsymbol{\rho})\left[\left(\frac{\partial \mathbf{E}_t^{(0)}}{\partial z}\right)_{z=z_r+0} - \left(\frac{\partial \mathbf{E}_t^{(0)}}{\partial z}\right)_{z=z_r-0}\right] - \nabla_\perp \zeta(\boldsymbol{\rho})\left[E_z^{(0)}(\boldsymbol{\rho}, z_r + 0) - E_z^{(0)}(\boldsymbol{\rho}, z_r - 0)\right] \\
&\mathbf{H}_t^{(1)}(\boldsymbol{\rho}, z_r + 0) - \mathbf{H}_t^{(1)}(\boldsymbol{\rho}, z_r - 0) = \\
&= -\zeta(\boldsymbol{\rho})\left[\left(\frac{\partial \mathbf{H}_t^{(0)}}{\partial z}\right)_{z=z_r+0} - \left(\frac{\partial \mathbf{H}_t^{(0)}}{\partial z}\right)_{z=z_r-0}\right] - \nabla_\perp \zeta(\boldsymbol{\rho})\left[H_z^{(0)}(\boldsymbol{\rho}, z_r + 0) - H_z^{(0)}(\boldsymbol{\rho}, z_r - 0)\right]
\end{aligned}\right\}, \quad (2.61)$$

where $\mathbf{E}_t^{(1)}$, $\mathbf{H}_t^{(1)}$ are tangential components of the first-order fields, $\mathbf{E}_t^{(0)}$, $\mathbf{H}_t^{(0)}$ are tangential components of the zero-order fields, $E_z^{(0)}$, $H_z^{(0)}$ are normal components of the zero-order fields, $\nabla_\perp$ is the gradient operator in the horizontal plane ( $x - y$ ).

The right hand side of (2.61) is not zero opposed to the smooth boundary case. Therefore, the zero-order fields must be found first in order to be substituted into the boundary conditions (2.61). Note that for the sake of symmetry, boundary conditions (2.61) are written here for a general case when both electric permittivity and magnetic permeability of the medium are not unity.

3) Main steps of SPM

A solution within the first-order approximation of the SPM method can be built as follows [48]. First zero-order fields are derived directly from Maxwell's equations. If the CDC of media varies over depth then the exact analytical solution does not exist; however, a closed-form solution can still be expressed through particular solutions of wave equations in a nonhomogeneous medium. The zero-order fields must satisfy boundary conditions and conditions at infinity.

Second, the first-order fields are presented as a superposition of infinite number of plane waves outgoing from the rough interface in multiple directions through the Fourier integral.

Third, the zero-order and first order fields are substituted into the boundary conditions (2.61) at the mean level of the rough interface, and the spectral magnitudes of the scattered field can be derived.

Finally, the first-order fields can be estimated in far zone using the method of stationary phase [74] and the scattering characteristics can be found through the Poynting vector. The cross-polarized backscatter return within the first-order approximation is zero. However, it is non-zero in the bi-static case.

2.4.7. Existing SPM Solutions and Their Limitations

The simplest SPM solution was developed for the case where the wave is scattered by a rough surface on top of a homogeneous half-space [49]. Radar backscatters (VV and HH) for this case are the following:

$$\sigma_{HH}^{0} = \frac{4k_0^4}{\pi}\left|\frac{\varepsilon - 1}{\left(\cos\Theta_0 + \sqrt{\varepsilon - \sin^2\Theta_0}\right)^2}\right|^2 \tilde{K}(-2\mathbf{q_0})\cos^4\Theta_0, \qquad (2.62)$$

$$\sigma_{VV}^0 = \frac{4k_0^4}{\pi}\left|(\varepsilon-1)\frac{(\varepsilon-1)\sin^2\Theta_0+\varepsilon}{\left(\varepsilon\cos\Theta_0+\sqrt{\varepsilon-\sin^2\Theta_0}\right)^2}\right|^2 \tilde{K}(-2\mathbf{q_0})\cos^4\Theta_0, \tag{2.63}$$

where $\varepsilon$ is the CDC of the half-space, $\mathbf{q_0}$ is the longitudinal wave number of the incident wave, $k_0$ is the wave number in vacuum, $\hat{K}$ is the spatial power spectral density of the rough surface which is defined as a spectrum of the autocorrelation function as follows:

$$\tilde{K}(\boldsymbol{\alpha}) = \int_{-\infty}^{\infty} K(\boldsymbol{\rho}) e^{-i\boldsymbol{\alpha}\boldsymbol{\rho}} d\boldsymbol{\rho}, \tag{2.64}$$

where $K(\boldsymbol{\rho})$ is the autocorrelation function of the rough surface.

It is worth noting from (2.62) - (2.63) that the co-polarization ratio $\sigma_{VV}^0/\sigma_{HH}^0$ is independent of the surface roughness while it depends only on the CDC $\varepsilon$ and incidence angle $\Theta_0$.

Yarovoy derived an SPM solution [92] for wave scattering from a rough surface embedded in a three layered structure shown in Figure 2.7(a). An alternative formulation in terms of reflection and transmission coefficients was proposed in [93]:

$$\sigma_{HH}^0 = \frac{k_0^4}{4\pi}\left|(\varepsilon_2-\varepsilon_1)\left(\frac{\tau_{a1H}e^{iw_1d_1}}{1+r_Hr_{a1H}e^{2iw_1d_1}}\right)^2(1+r_H)^2\right|^2 \tilde{K}(-2\mathbf{q_0}) \tag{2.65}$$

$$\sigma_{VV}^0 = \frac{k_0^4}{4\pi}\left|\frac{\varepsilon_2-\varepsilon_1}{\varepsilon_1}\left(\frac{\tau_{a1V}e^{iw_1d_1}}{1+r_Vr_{a1V}e^{2iw_1d_1}}\right)^2\left\{\frac{\sin^2\Theta_0}{\varepsilon_2}(1+r_V)^2+\frac{\varepsilon_1-\sin^2\Theta_0}{\varepsilon_1}(1-r_V)^2\right\}\right|^2 \tilde{K}(-2\mathbf{q_0}), \tag{2.66}$$

where $d_1$ is the thickness of the upper layer with CDC $\varepsilon_1$, $w_1 = k_0\sqrt{\varepsilon_1 - \sin^2\Theta_0}$ is the transverse wave number in medium 1, $\tau_{a1H}$, $\tau_{a1V}$ are ordinary Fresnel transmission coefficients through the interface between air and medium 1 at horizontal and vertical polarizations respectively. $r_{a1H}$, $r_{a1V}$ are ordinary Fresnel reflection coefficients from the boundary between air and medium 1 at horizontal and vertical polarizations respectively; $r_H$ and $r_V$ are reflection coefficients from the two-layered structure (medium 2 and medium 3) for horizontal and vertical polarizations respectively.

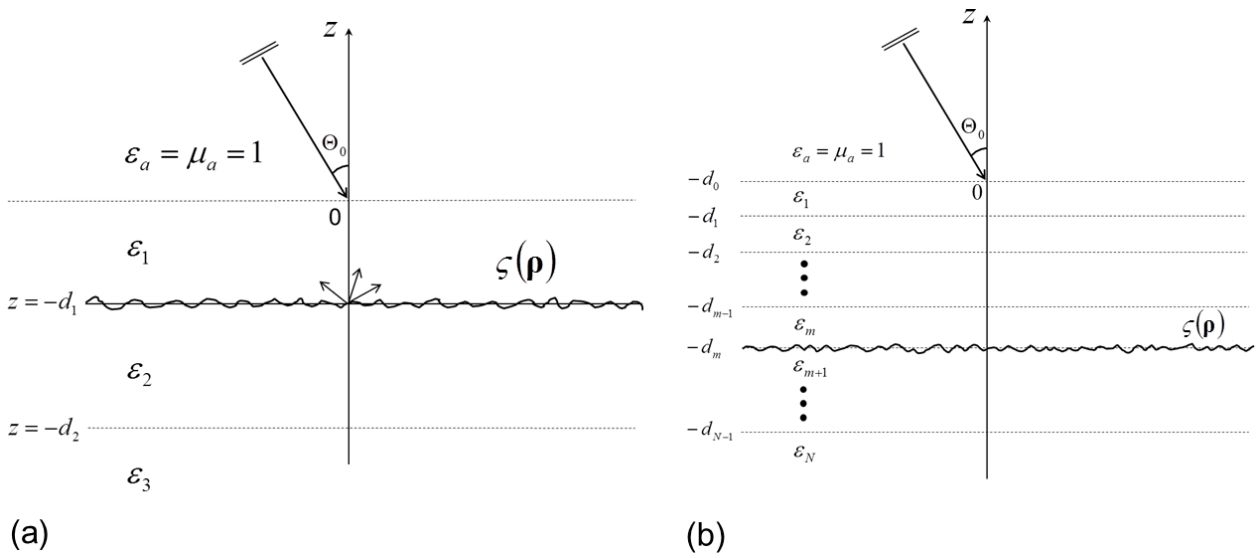


Figure 2.7. (a) Yarovoy's scattering geometry [92], (b) Imperatore's scattering geometry [96].

Interestingly enough, if CDC's of medium 1 and medium 2 are equal (i.e. the dielectric contrast between medium 1 and medium 2 is zero) then the roughness is absent and the solution (2.65) - (2.66) naturally goes to zero.

Scattering from a layered structure with a rough upper boundary was considered in [94]. Then the SPM solution was extended to the problem of scattering from two [95] and more rough interfaces [96] embedded in a layered medium. Imperatore et al. [96] presented an SPM solution for waves scattering from a rough surface embedded in a medium containing a number of homogeneous discrete layers as shown in Figure 2.7(b). His solution for the backscattering case in our notations can be written as follows:

$$\sigma_{HH}^0 = \frac{k_0^4}{4\pi}\left|\left(\varepsilon_{m+1}-\varepsilon_m\right)\frac{k_0^2\cos^2\Theta_0}{w_m^2}\left(1+r_{mH}\right)^2\frac{\left(T_H^{m-1}\right)^2\exp\left(2iw_m\Delta_m\right)}{\left[1-r_{mH}R_H^{m-1}\exp\left(2iw_m\Delta_m\right)\right]^2}\right|^2\tilde{K}(-2\mathbf{q_0}) \tag{2.67}$$

$$\sigma_{VV}^0 = \frac{k_0^4}{4\pi}\left|\left(\varepsilon_{m+1}-\varepsilon_m\right)\frac{\cos^2\Theta_0\left(T_V^{m-1}\right)^2\exp\left(2iw_m\Delta_m\right)}{\left[1-r_{mV}R_V^{m-1}\exp\left(2iw_m\Delta_m\right)\right]^2}\left\{\frac{k_0^2\varepsilon_m}{w_m^2\varepsilon_{m+1}}\left(1+r_{mV}\right)^2-\left(1-r_{mV}\right)^2\right\}\right|^2\tilde{K}(-2\mathbf{q_0}), \tag{2.68}$$

where $w_m = k_0\sqrt{\varepsilon_m-\sin^2\Theta_0}$ is the transverse wave number in layer $m$ which is just above the rough surface, $\Delta_m$ is the thickness of layer $m$. $T_H^{m-1}$ and $T_V^{m-1}$ are transmission coefficients through the upper $m-1$ layers above the rough surface for horizontal and vertical polarizations respectively. $R_H^{m-1}$ and $R_V^{m-1}$ are reflections coefficients from the upper $m-1$ layers for horizontal and vertical polarizations respectively. $r_{mH}$ and $r_{mV}$ are reflections coefficients from the lower half-space beneath the rough interface for horizontal and vertical polarizations respectively.

Similar to the previous case, if the dielectric contrast between $m$ and $m+1$ layers is zero, then there is no surface scattering and backscatter coefficients become zero.

We would like to note that dielectrics of snow and sea ice can be described as a piece-wise continuous function of the vertical coordinate. To this point an SPM solution for waves scattering from rough interfaces separating media with continuous dielectric profiles has not been derived.

## 2.5. Conclusion

In this chapter we defined main physical processes and interactions which are giving rise to the dynamic and thermodynamic characteristics of snow-covered sea ice. We also evaluated existing active microwave remote sensing methods for retrieving dynamic state of sea ice and described the ability of the microwave scattering models to assess the thermodynamic state of snow-covered sea ice.

The existing and future advanced SAR space borne platforms in combination with efficient processing algorithms would enable us to reliably detect and quantify sea ice dynamic characteristics all over the Arctic Ocean with very high resolution. Moreover, operational implementation of these methods is being conducted at Ice Centers. At the same time, accurate detection of certain thermodynamic characteristics of sea ice from SAR platforms is more challenging. This is due to (1) complexity of sea ice structure; (2) difficulties in modelling dielectric properties of snow and sea ice; (3) challenges in modelling microwave scattering characteristics.

# CHAPTER 3. SEA ICE MOTION TRACKING FROM SEQUENTIAL DUAL-POLARIZATION RADARSAT-2 IMAGES

**A. S. Komarov** and D. G. Barber, "Sea ice motion tracking from sequential dual-polarization RADARSAT-2 images," *IEEE Trans. Geosci. Remote Sens.*, vol. 52, no. 1, pp. 121-136, Jan. 2014.

## 3.1. Introduction

Arctic sea ice has significantly changed over the past three decades. Comiso et al. in [1] demonstrated that the trend for the entire Arctic ice area (seasonal and perennial ice) has shifted from -3.0% per decade in 1979-1996 to -10.7% per decade for 1996-2007. Over these periods, first-year (FY) ice replaced much of the multi-year (MY) ice. For the 2004-2008 period the winter cover of MY ice shrank by 1.5 million $km^2$ and currently covers one-third of the Arctic Basin [97]. Furthermore, the Arctic ice thickness decreased by 42% and 21% for fall (October - November) and winter (February - March) respectively during the 2003-2008 period [6]. Decrease of the Arctic ice volume leads to increasing ice mobility. On average, the Arctic sea ice drift speed increased by 10.6% per decade for the period 1992-2009, which is much larger than the wind speed increase (~1.5% per decade) as shown in [7].

Information on sea ice motion is required to quantify changes in sea ice at the regional scale including (1) ice volume exchange between the Canadian Arctic Archipelago (CAA) and the Arctic Ocean, (2) formation of ice leads and ridges and (3) development and maintenance of polynya regions. For example, Kwok in [45] estimated that a mean annual volume flux of ~100 $km^3$ is exported from the CAA into the Canada Basin for the 1997-2002 period. Since sea ice dynamics affects sea ice morphology [25], a number of publications (e.g. [41], [42]) were devoted

to studying formation of leads and pressure zones in the regions with a high concentration of sea ice based on divergence and shear of the ice velocity vector field. Finally, sea ice motion detection in polynya regions was used to understand mechanisms of formation and maintenance of polynyas [35], [98]. In [98] it was shown that ice export is a dominant process in maintaining the North Water Polynya during spring 1998.

At the local scale, tracking of potentially unmanageable ice features such as ice islands and MY ice is required to prevent hazards to shipping and damaging oil platforms in the Arctic Ocean. In addition, operational information on local ice motion is necessary for conducting field work in the Beaufort Sea in compliance with the United Nations Convention on the Law of the Sea (UNCLOS).

Spaceborne synthetic aperture radar (SAR) observations with very high resolution (100 m and smaller) have been extensively used to monitor of changes in sea ice. High temporal resolution and large spatial coverage of SAR imagery are desirable for more reliable monitoring of rapid dynamic and thermodynamic changes in sea ice over the entire Arctic. Canadian RADARSAT-2 [9] launched in December 2007 increased the temporal and geographical coverage of the circumpolar zone by airborne SAR platforms. Among other new technical features, RADARSAT-2 has the cross-polarization channel in the ScanSAR mode (compared to its predecessor RADARSAT-1). Currently, the RADARSAT-1 and 2 (operating in C-band) together provide frequent and reliable operational information on changes in sea ice. In the future, Canadian RADARSAT Constellation mission (RCM) [10] will be equipped with three independent SAR platforms analogous to RADARSAT-2, which will lead to a significant growth in satellite radar observations over the Arctic Ocean. Thus, the new capabilities of SAR sensors and the increasing volume of SAR

imagery over the Arctic Ocean require improved methods for retrieving key parameters of sea ice from SAR.

Ice motion is one of the crucial dynamic characteristics of sea ice cover. An ice velocity field with a high spatial resolution can be extracted from SAR sequential images over a wide geographical area (up to 500×500 km), while in-situ ice tracking beacons are able to provide ice velocity of only one geographical point. In this study we focus on ice motion tracking from ScanSAR dual-polarization RADARSAT-2 imagery.

In the literature, various automated ice motion tracking algorithms can be found [31]-[36]. The classical cross-correlation matching approach [31], [33] is widely applied to various image registration problems. This cross-correlation technique is based on direct calculation of the correlation coefficient that is a measure of similarity between two subimages. Coordinates of the maximum correlation coefficient in the correlation matrix are connected to the shift vector coordinates. However, there are two disadvantages to this approach. The first disadvantage is computational inefficiency, especially for situations where the search area is much larger than the reference subimage. The second disadvantage of this method is that it cannot capture the rotational component of sea ice motion. Modifications of the cross-correlation method to embrace the rotation component such as preliminary rotation of the reference subimage at a number of discrete angles lead to dramatic increasing of calculation time. An efficient approach to reduce the computational load is the method of nested correlations described in [31]. Meanwhile, the cross-correlation approach used in [31] does not capture rotated ice features.

Another image registration technique is the phase-correlation method based on the Fourier transform shift theorem [37]. With the availability of the Fast Fourier Transform (FFT) this

method works several times faster than the cross-correlation approach. Additionally, the phase-correlation approach is modified to include the rotation effect [38]. However, a disadvantage to this method is that the peak value in the phase-correlation matrix does not provide an evident measure of similarity between two subimages.

Besides the image matching technique, there are several other important steps in ice motion tracking algorithms. One of them is selecting initial control points in the first image. Some studies suggest using a set of points located on a regular grid [31], [34]. This approach is convenient for certain tasks such as deformation analysis of sea ice. However, some control points can be located in featureless areas making it harder to find corresponding matches in the second image. Another important step of the ice tracking algorithm is the error filtering step which is necessary to eliminate erroneous ice drift vectors. Many studies (e.g. [33]) suggest thresholding of the cross-correlation coefficients. Occasionally, false matches may remain if their cross-correlation coefficients exceed the threshold. Thus, prior to the thresholding procedure some adaptive filtering approach is recommended.

The existing ice motion tracking algorithms have been applied to co-polarization SAR images only; however, ice motion can be also extracted from cross-polarization data if it is available. The cross-polarization channel of RADARSAT-2 ScanSAR imagery is extensively used for operational monitoring of sea ice at the Canadian Ice Service (CIS). The cross-polarization image provides various ice features invisible in the co-polarization image [100], [101]. Thereby, we expect that ice motion information obtained from the cross-polarization images may enhance the ice motion product derived from the co-polarization images. Evaluation of ice motion tracking from co- and cross-polarization images requires a special treatment.

In this study we pursue two main objectives. (1) To develop a new sea ice motion tracking system operating with sequential RADARSAT-2 ScanSAR images. (2) To evaluate capabilities of the co- and cross-polarization images of RADARSAT-2 ScanSAR mode for ice motion tracking.

## 3.2. Preprocessing of SAR Images for Ice Motion Tracking

For ice motion tracking we use RADARSAT-2 ScanSAR Wide a (SCWA) mode which allows for imaging of an area of around 500×500 km with 50 m resolution [9]. The image is covering the full incidence angle range of 20° to 49°. The SCWA mode provides the images with one of the following four polarization options: HH-HV, VV-VH, HH or VV. We employ the HH-HV dual-polarization images for ice motion tracking.

Two overlapping sequential raw RADARSAT-2 images are converted to the normalized radar cross-section (NRCS) units according to the procedure described in [9]. The resolution is reduced from 50 m to 100 m by a simple averaging. Then, the images are reprojected into the Lambert Conformal Conic (LCC) projection [102] using the georeference information given in the auxiliary product files. The gradient search method described in [103] is implemented to reproject raw SAR data into the LCC projection. The overlapping area between two sequential images is extracted from the reprojected data. Finally, a land/data/no data mask is generated for the obtained image pair.

An ultimate goal of the sea ice tracking algorithm is to recognize similar areas in two sequential georeferenced SAR images. A direct search for matching features in the input image pair requires a significant computational load due to a large size of original SAR imagery. One possible option

to improve computational efficiency is through the use of image pyramids [31]-[33], [36]. This method reduces computational time by tracking ice features at different scales.

The preprocessing steps include pyramid data representation of the georeferenced SAR images and selection of control points defining ice features at each resolution level.

### 3.2.1. Pyramid Image Representation

In order to generate a hierarchical data structure containing several image levels, we applied a recursive process of the median filtering with a 3×3 pixel window and a simple 2×2 pixel averaging over an image beginning with the original image. The median filter effectively removes coherent fading, preserving the edges. The output image then becomes the input to produce a set of images with decreased resolution and size. Multi-resolution images are generated for both scenes and the lowest resolution image serves as the initial input for the image matching procedure. The number of pyramid levels could vary. In our study, four resolution levels with 800 m, 400 m, 200 m, and 100 m resolutions are generated.

Prior to the ice motion tracking procedure, the Gaussian filter with the window size of 3×3 pixel and the Laplace operator are sequentially applied to each resolution level in order to highlight the edges and other heterogeneities. Also, the Laplacian reduces the trend across the satellite track which occurs due to the dependence of the co-polarization NRCS on the incidence angle.

### 3.2.2. Selection of Control Points

A procedure for an automated selection of control points was specifically developed to identify those image features that are potentially suitable for the matching step. The idea behind it is to

generate a set of evenly spread control points over each pyramid level in a way that the following two conditions are met:

a) All points should be located in some distinctive areas that have relatively high variance.

b) Vertical and horizontal components of the distance between any two points should not be lower than a prescribed value.

The proposed procedure for selecting control points includes two steps: (1) Calculation of the variance matrix and (2) Selection of control points based on the obtained variance matrix.

1) Variance Matrix Calculation

An illustration of the variance matrix calculation is presented in Figure 3.1. Each element of the matrix is calculated from a window $w \times w$ as follows:

$$V = \frac{1}{w^2} \sum_{i,j=1}^{w} \left( a_{ij} - \bar{a} \right)^2 , \tag{3.1}$$

where $w$ is a window size, $a_{ij}$ are elements of the window $w \times w$, $\bar{a}$ is the average value within this window.

If the original image has $m$ columns and $n$ rows, then the variance matrix has $\left[ \frac{m-w}{h} \right] + 1$ columns and $\left[ \frac{n-w}{h} \right] + 1$ rows, where the square brackets denote the integer part of a number, and $h$ is the step size. The generated variance matrix is the input for the selection process.

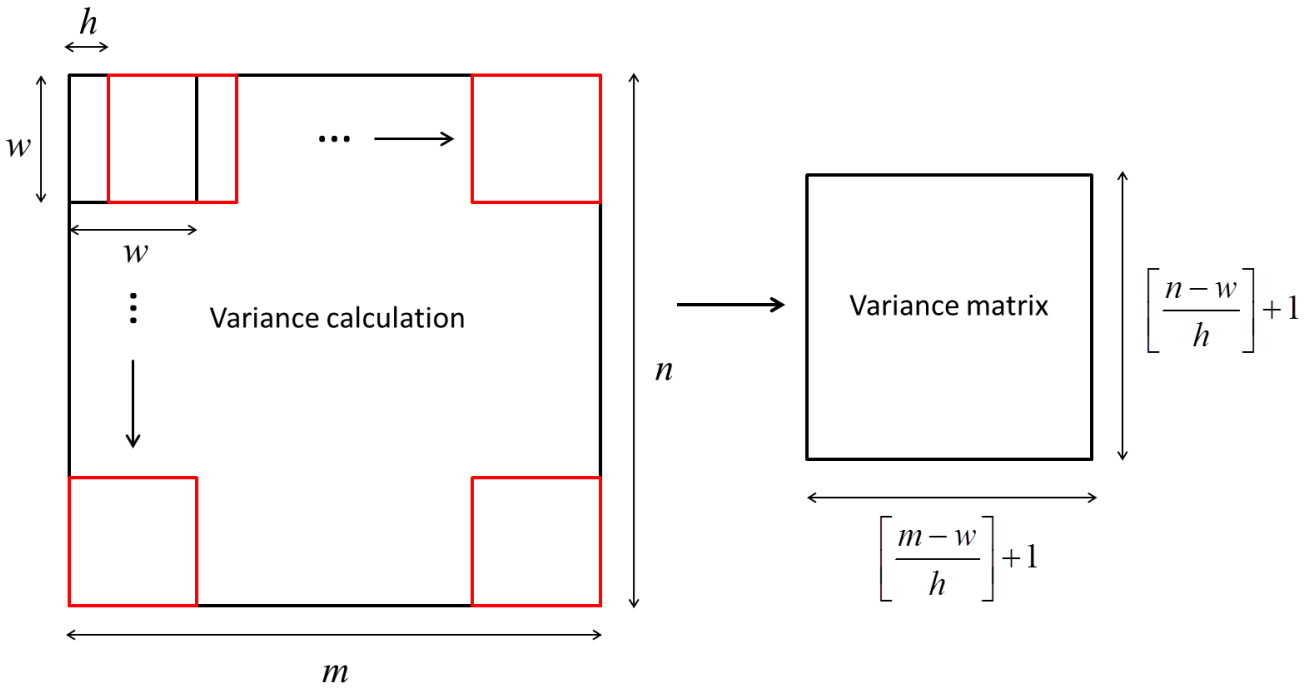


Figure 3.1. Variance matrix calculation.

2) Selection Process

In addition to the variance matrix, the selection routine requires one input parameter *R*, which must be such a value that each control point with coordinates $(x_c, y_c)$ does not have any neighbour point within the following area in the variance image: $\{x_c - R : x_c + R, y_c - R : y_c + R\}$.

The selection process consists of three sequential passes as shown in Figure 3.2. The first pass is preliminary sifting of elements in the variance matrix. The second pass defines those points which are local maximums in surrounding $(2R+1)\times(2R+1)$ regions. After the second pass, the areas where local maximums do not exist may remain. In these areas variance monotonically changes. The third pass is designed to add points with sufficiently high variances in such regions.

In the first pass the variance matrix is divided into 3×3 non-overlapping squares. Inside each square the point with the maximum variance remains, while the other eight points are removed. The obtained subset of points ***S1*** serves as input for the next pass. In the second pass we establish a square area $A=\{x_c-R:x_c+R, y_c-R:y_c+R\}$ by surrounding each point from the set ***S1***. Then the reference variance of the central point $(x_c, y_c)$ is compared with the variance of each point lying inside the area ***A***. If the variance of the reference point is lower than the variance of a current point from ***A***, then the reference point is removed and the variance of the next point from the initial set ***S1*** is analyzed. Otherwise, we discard the current point and go to the next point in ***A***. As a result of this sifting process, we obtain a new subset of points ***S2*** which contains only several points from ***S1***. For the third pass two sets of points ***S1*** and ***S2*** from the previous two passes are inputs. In the areas where there are no points from ***S2*** a few points from ***S1*** with sufficiently high variances are added as follows. A square $\boldsymbol{A}=\{x_c-R:x_c+R, y_c-R:y_c+R\}$ around each of the points from ***S1*** is analyzed. If inside this square there exists at least one point from the set ***S2*** then we proceed to the next point from ***S1***. Otherwise, if the variance of the current point from ***S1*** exceeds a threshold then this point is added to the set ***S2***. The threshold is calculated as $T = mean + (\max - mean)/5$, where *mean* and *max* are average and maximum values of the variance subimage within the square ***A***; the coefficient 5 was selected heuristically.

In consequence of the described selection processes, ***S2*** is the output set of control points in the variance image. Finally, the coordinates of the control points from ***S2*** are converted into the original image coordinates as follows:

$$\left.\begin{aligned} x &= (x_c - 1)h + w/2 \\ y &= (y_c - 1)h + w/2 \end{aligned}\right\}, \tag{3.2}$$

where $(x_c, y_c)$ denote coordinates of a control point in the variance matrix, while $(x, y)$ are coordinates of the control point in the original image coordinates. The described routine for selecting control points is applied to each resolution level for generating a set of evenly spread points located at various heterogeneities.

Figure 3.3 demonstrates an example of four pyramid image levels as well as control points on each resolution level shown in red. The parameter *R* is chosen to be 3 pixels for all the resolution levels, while the window size ($w$) and the step size ($h$) are different for each resolution level and their values are presented in Figure 3.3.

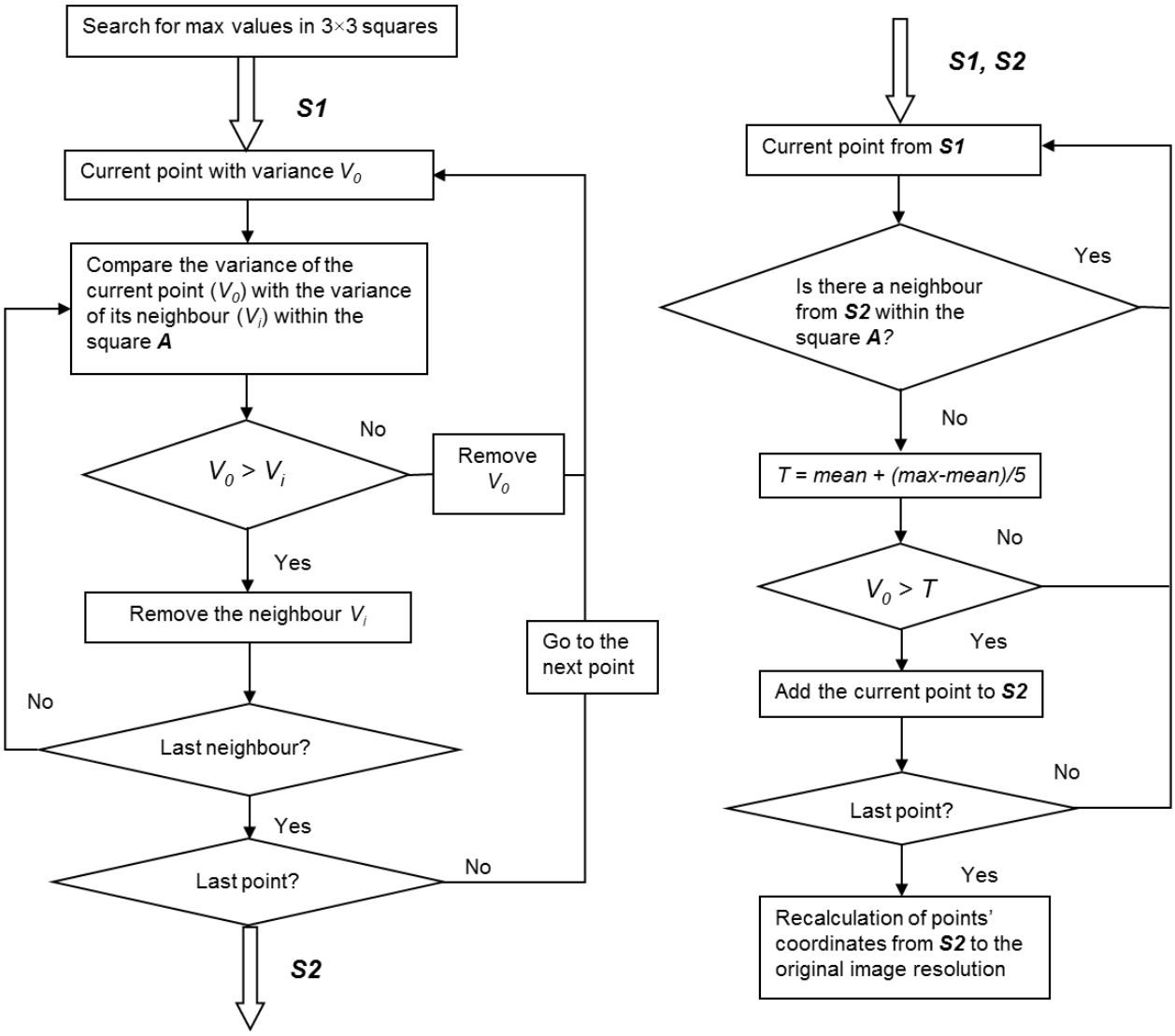


Figure 3.2. Selection of control points flowchart.

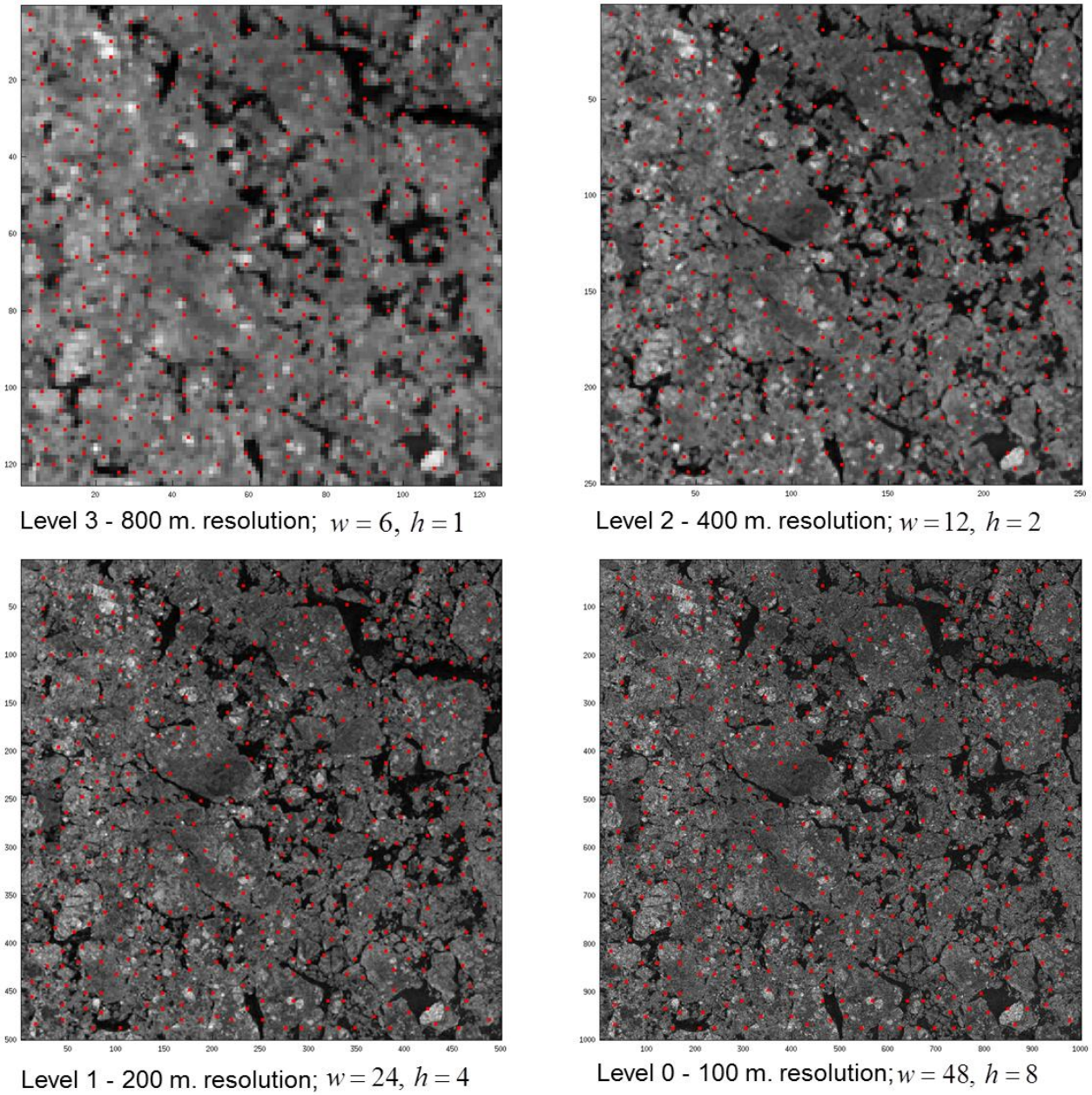


Figure 3.3. An example of four resolution levels and sets of control points on each of them; $w$ and $h$ are the window size and step size respectively in pixels. The original image was taken on April 22, 2009 (RARARSAT-2 ScanSAR Wide mode, HH-polarization), southeast of Baffin Island, Canada.

## 3.3. Ice Motion Tracking

The ice motion tracking procedure follows the selection of control points routine at each resolution level. In this section we introduce the cross- and phase-correlation matching approaches and put forward a matching technique which is based on a combination of these two methods. Then we describe the proposed strategy for ice motion detection at different resolution levels. Finally, we discuss thresholding and quality assessment of output vectors at each resolution level.

### 3.3.1. Cross- and Phase-Correlation

The cross- and phase-correlation matching techniques are known methods for registering similar features in two images. The cross-correlation technique is based on direct calculation of the correlation coefficient, which is a measure of the similarity between two data sets [31], [33]. The shift vector is obtained from coordinates of a maximum correlation coefficient in the correlation matrix. However, the cross-correlation method does not capture the rotational component of ice motion. The phase correlation technique is based on the property of the fourier transform that a shift in the spatial domain transforms into a phase shift in the frequency domain [32], [35]-[37]. For instance, if a 2D function $f(\mathbf{r})$ has Fourier transform $F_1(\mathbf{u})$, then the shifted function $f(\mathbf{r}-\mathbf{r_0})$ will have Fourier transform $F_2(\mathbf{u})=e^{-i\mathbf{u}\mathbf{r}_0}F_1(\mathbf{u})$, where $\mathbf{r_0}$ denotes the shift vector. This translational component can be retrieved by finding maximum value coordinates of the following phase-correlation function:

$$C=\mathcal{F}^{-1}\left(\frac{F_1^{*}\cdot F_2}{\left|F_1^{*}\right|\cdot\left|F_2\right|}\right), \tag{3.3}$$

where $\mathcal{F}^{-1}$ is the inverse Fourier transform operator; asterisk denotes complex conjugation. In this simple example the phase-correlation function is the delta-function of the argument $(\mathbf{r}-\mathbf{r}_0)$. In practice, the phase correlation matrix is found by applying the discrete inverse FFT to the cross-power spectrum. Peak coordinates in this matrix are recalculated to the shift vector coordinates.

The phase-correlation approach works several times faster than the cross-correlation due to the availability of the Fast Fourier Transform (FFT). In addition, the phase-correlation approach can be expanded for detection of the rotational component based on the Fourier shift and rotation theorem [38]. Suppose $f_2(x,y)$ is a translated and rotated replica of $f_1(x,y)$ then according to the Fourier transform properties we obtain:

$$\begin{aligned} F_1(\xi,\eta) &= \mathcal{F}\{f_1(x,y)\} = \int_{-\infty-\infty}^{+\infty+\infty} f_1(x,y)e^{-i\xi x - i\eta y}\,dxdy \\ F_2(\xi,\eta) &= \mathcal{F}\{f_2(x,y)\} = e^{-i\xi x_0 - i\eta y_0} F_1(\xi\cos\theta_0 + \eta\sin\theta_0, -\xi\sin\theta_0 + \eta\cos\theta_0) \end{aligned}, \quad (3.4)$$

where $\mathcal{F}$ denotes the Fourier transform operator; $\theta_0$ is angle of rotation; $(x_0, y_0)$ are components of the shift vector.

Equations (3.4) indicate that the magnitude or the spectrum $F_2(\xi,\eta)$ is rotated as well:

$$|F_2(\xi,\eta)| = |F_1(\xi\cos\theta_0 + \eta\sin\theta_0, -\xi\sin\theta_0 + \eta\cos\theta_0)|. \quad (3.5)$$

After transition to polar coordinates $(\rho,\theta)$ the last expression can be rewritten as follows:

$$P_2(\rho,\theta) = P_1(\rho,\theta-\theta_0), \tag{3.6}$$

where $P_1$ and $P_2$ are magnitudes of the spectra represented in polar coordinates:

$$\begin{aligned} P_2(\rho,\theta) &= \left|F_2(\xi_0 + \rho\cos\theta, \eta_0 + \rho\sin\theta)\right| \\ P_1(\rho,\theta-\theta_0) &= \left|F_1(\xi_0\cos\theta_0 + \eta_0\sin\theta_0 + \rho\cos(\theta-\theta_0), -\xi_0\sin\theta_0 + \eta_0\cos\theta_0 + \rho\sin(\theta-\theta_0))\right|. \end{aligned} \tag{3.7}$$

From (3.6) and (3.7) it is seen that in polar coordinates the rotation transforms to a simple shift along axis $\theta$. Therefore, the same phase-correlation technique can be applied to the magnitudes of the spectra $P_1$ and $P_2$ to find the angular shift $\theta_0$. The phase-correlation matrix in this case is calculated as follows:

$$C_\theta = \mathcal{F}^{-1}\left(\frac{\mathcal{F}(P_1)^* \cdot \mathcal{F}(P_2)}{\left|\mathcal{F}(P_1)^*\right| \cdot \left|\mathcal{F}(P_2)\right|}\right), \tag{3.8}$$

where $\mathcal{F}$ denotes the Fourier transform applied to functions $P_1$ and $P_2$. The peak coordinates in matrix $C_\theta$ indicate the angular shift $\theta_0$. However, $\pi$ angular ambiguity occurs because the 2D Fourier spectrum is conjugate symmetric for real images. This ambiguity is avoided if we rotate the image by two angles: $\theta_0$ and $\theta_0 + \pi$. Having the rotated first subimage in these two angles and the second subimage, we are able to determine a translational component by applying the phase-correlation technique analogous to (3.3) [38]. The maximum value of peak strengths corresponds

to the correct angle $\theta_0$ or $\theta_0 + \pi$. The polar representation and rotation of images are performed using the bilinear interpolation.

A disadvantage of the phase-correlation approach is that the peak value in the phase correlation matrix does not provide a clear measure of similarity between two subimages.

### 3.3.2. Matching Procedure by Combining Phase- and Cross-Correlation Techniques

We propose a combination of the phase- and cross- correlation matching techniques for detecting a match of the reference feature in the second image. The reference subimage is defined as a window $w \times w$ surrounding a control point which corresponds to some feature in the first image. An illustration and a flowchart of this matching routine are presented in Figure 3.4. We divide the search area into several overlapping windows with the same size as the reference subimage. Gaussian windowing is applied to input subimages prior to the phase-correlation routine. The windowing step attenuates the signal towards the image edges in order to reduce the influence of boundary pixels on the Fourier transform. The overlapping step $h$ in the search area must not exceed half the width of the Gaussian curve:

$$h \le \frac{w\sigma}{2}, \tag{3.9}$$

where $w$ is the window size, $\sigma$ is the relative half width of the Gaussian curve. Typically, $\sigma = 0.5$, which corresponds to the maximum overlapping step $h = w/4$. The window size $w$ is

chosen to be 64 pixels. The size of the search area varies depending on the stage of our ice motion tracking algorithm as discussed in the next section.

Condition given by (3.9) allows for involving the entire search area in the matching process without any gaps. We conduct the phase-correlation image registration technique between the reference window and every window from the search area. As a result of this process, a set of possible displacements of the reference window is obtained. It is necessary to choose among them the most reliable match. Since the phase-correlation technique does not provide the measure of similarity between two subimages, some independent estimation should be applied. We suggest the cross-correlation coefficient is calculated for all potential displacements of the first subimage found by the phase-correlation routine. The cross-correlation coefficient for each matching between the first subimage and a second subimage from the search area is found as follows:

$$c = \frac{\sum_{i,j}\left(a_{ij} - \bar{a}\right)\left(b_{ij} - \bar{b}\right)}{\sqrt{\sum_{i,j}\left(a_{ij} - \bar{a}\right)^2 \sum_{i,j}\left(b_{ij} - \bar{b}\right)^2}}, \tag{3.10}$$

where $a$ is a window surrounding a control point from the first image; $b$ is a rotated matching subimage from the second image. The angle of rotation $\theta_0$ and the matching subimage itself are known from the phase-correlation matching procedure. The size of the square windows $a$ and $b$ is equal to the full width of the Gaussian curve i.e. $w \cdot \sigma$ or 32×32 pixel for our initial parameters $w = 64$ and $\sigma = 0.5$. $\bar{a}$ and $\bar{b}$ are average values of windows $a$ and $b$ respectively. The maximum value of the cross-correlation coefficient corresponds to the best match for the first

subimage. In addition, the cross-correlation coefficient is used for setting a level of confidence for the obtained drift vector.

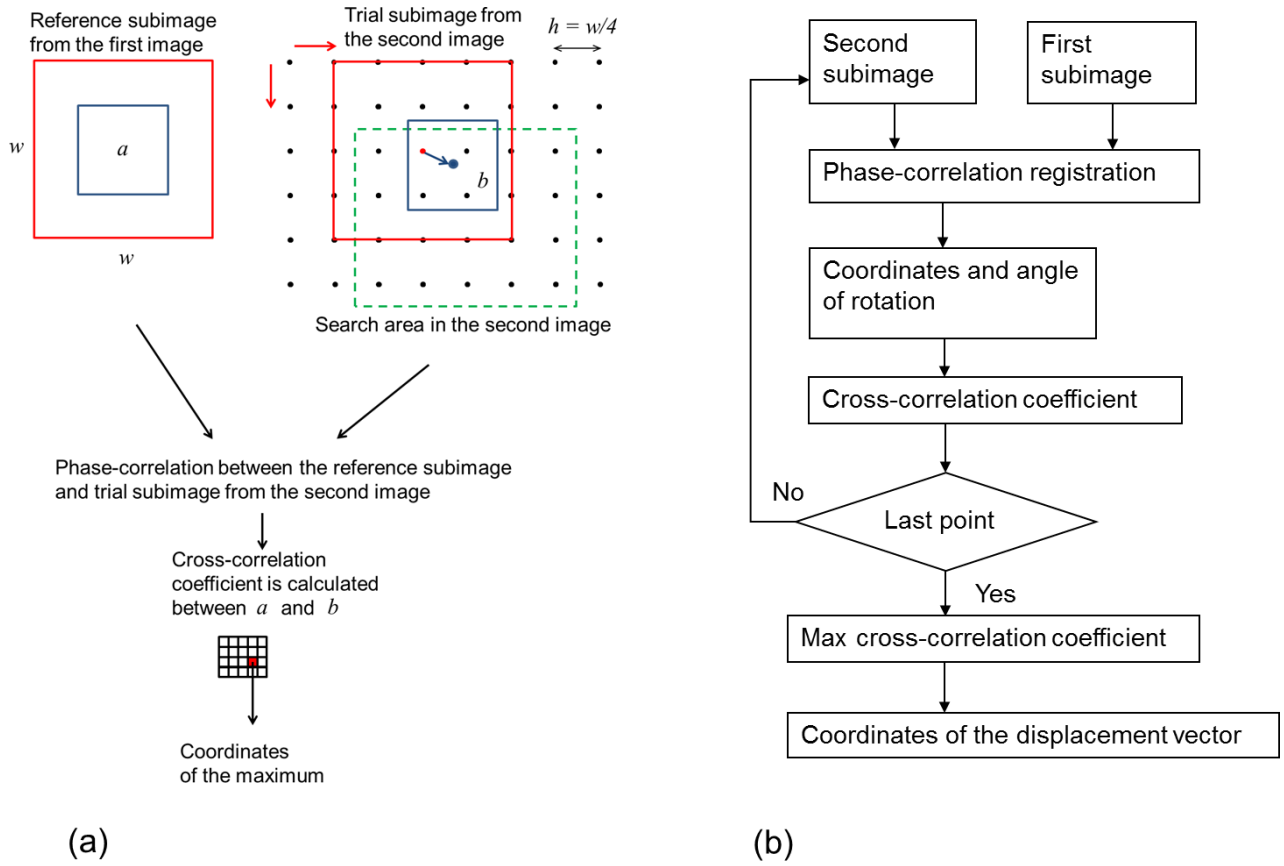


Figure 3.4. Illustration (a) and flowchart (b) of the matching technique.

The use of the cross-correlation coefficient for selecting the best candidate found by the phase-correlation matching technique was also proposed in [36]. However, in our study the angle of rotation is taken into account prior to calculating the cross-correlation coefficient.

### 3.3.3. Ice Tracking Strategy

The ice tracking strategy consists of ice motion detection at the lowest resolution level, ice motion detection at higher levels, and filtering erroneous vectors at each resolution level.

Below we separately discuss the tracking strategy for the lowest resolution level with the coarsest resolution and higher resolution levels.

#### 1) The Lowest Resolution Level

At the lowest resolution level the entire second image serves as a search area for all control points in the first image. The matching routine described in the previous section is applied to each control point. Thereby, for each control point there is a certain vector of displacement assigned.

After this step, an elimination of erroneous vectors is required. We propose a new filtering approach which is based on combining the forward pass (ice tracking from the first image to the second one) and backward pass (ice tracking from the second image to the first one). Since a displacement vector is assigned to each control point in the first image, the coordinates of all control points in the second image are determined. Consequently, a set of points in the second image is obtained. Now it is possible to apply exactly the same matching routine to the obtained control points in the second image. Ideally, all these points from the second image should come back to the original control points in the first image. In other words, the absolute value of the sum of forward and backward vectors should not exceed the chosen 1 pixel threshold as shown in Figure 3.5(a). Those vectors which do not satisfy this criterion are removed. The rest of the vectors are additionally classified by thresholding of their cross-correlation coefficients as discussed in Section 3.3.4.

2) Higher Resolution Levels

Vectors found at the previous resolution level serve as guide vectors at the present resolution level. For example, at the second resolution level the ice motion vectors found at the lowest (third) resolution level are involved where numbering of the resolution levels is shown in Figure 3.3. The guide vectors provide information about potential search areas in the second image. If a control point is located within a relatively small region (typically 48×48 pixel) surrounding the beginning point of the nearest guide vector then the search area is small (32×32 pixel) and its center is determined by the end of this guide vector as illustrated in Figure 3.5(b). Otherwise, the search process must be conducted within a larger search window. The size of this window is estimated based on the maximum length of a guide vector within a square 128×128 pixel around the control point as demonstrated in Figure 3.5(c). It is worthwhile to note that the sizes of the search areas (32×32 pixel and $3 \cdot MaxDisp \times 3 \cdot MaxDisp$ pixel) and the area surrounding a guide vector (48×48 pixel) were defined empirically based on numerous tests of the ice tracking system. In the conducted experiments the search areas were established as small as possible while the area surrounding a guide vector was chosen as large as possible to decrease the computational load. During these tests the quality of derived vectors was controlled by comparing the output results obtained for different sizes of the search areas and the area surrounding a guide vector. The matching routine is applied to the reference subimage and the established search area in the second image in order to determine the displacement of the control point. All the control points are processed using the same technique. The filtering of error vectors procedure is performed using the same "forward-backward" approach as for the lowest resolution level, except that guide vectors from the previous level are involved in the backward matching routine.

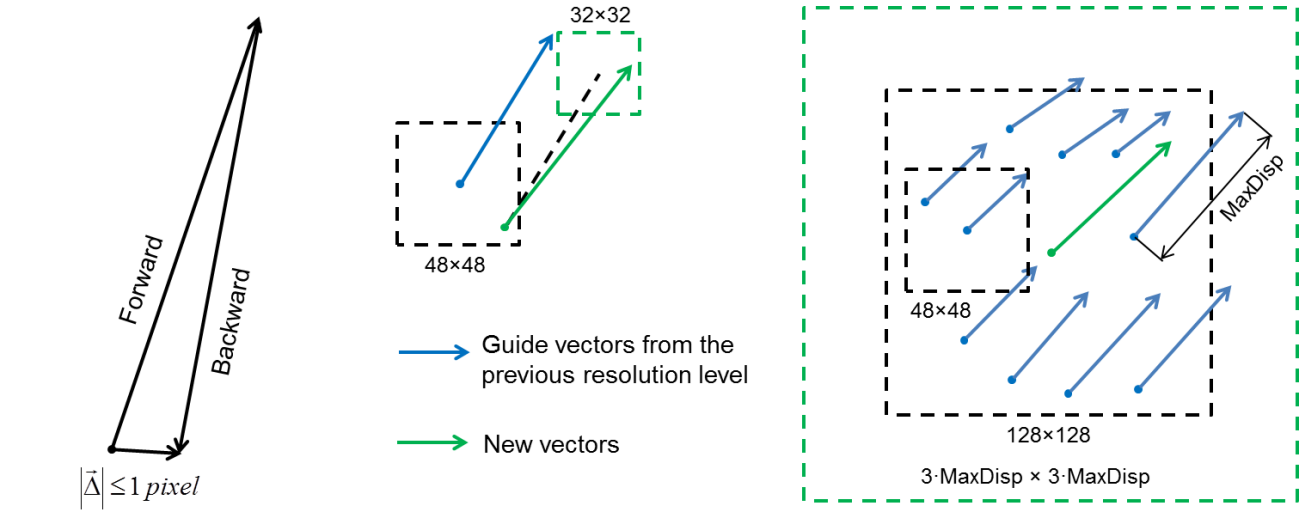


Figure 3.5. (a) Filtering of erroneous vectors based on forward and backward passes of ice tracking; (b) and (c) illustrate transitions from a lower resolution level to the following upper level for small and large search areas (green dashed squares) respectively.

### 3.3.4. Thresholding and Quality Assessment of Output Vectors

Thresholding and quality assessment follows forward and backward passes at each resolution level. The vectors are divided into four groups based on their cross-correlation coefficients as shown in Table 3.1. Very low confidence vectors are discarded.

Table 3.1. Cross-correlation threshold coefficients for different resolution levels.

| **Resolution** / **Confidence Level** | **Level 0 (100 m)** | **Level 1 (200 m)** | **Level 2 (400 m)** | **Level 3 (800 m)** |
|---|---|---|---|---|
| **Very Low (Removed)** | < 0.1 | < 0.2 | < 0.3 | < 0.4 |
| **Low** | 0.1 - 0.2 | 0.2 – 0.3 | 0.3 - 0.4 | 0.4 – 0.5 |
| **Medium** | 0.2 – 0.3 | 0.3 – 0.4 | 0.4 – 0.5 | 0.5 – 0.6 |
| **High** | > 0.3 | > 0.4 | > 0.5 | > 0.6 |

The thresholds for cross-correlation coefficients in Table 3.1 were found empirically based on numerous tests of the algorithm on different ice conditions and geographical areas. One may observe that the cross-correlation threshold decreases when the resolution increases. This is associated with the fact that, in general, the correlation between matching features in two images decreases when transiting from a lower resolution level to the following upper level. From a statistical analysis of cross-correlation coefficients derived for several image pairs we found that the cross-correlation coefficient decrease rate is $\sim -0.1/resolution\,level$. This means that the cross-correlation coefficient 0.1 obtained at the highest resolution level corresponds to 0.4 at the lowest resolution level which is sufficiently high to admit the similarity between two subimages.

Accuracy of output ice drift vectors was assessed visually on several image pairs as a human eye is the most reliable tool for detecting similar features in two images. Majority of the output vectors indicated correct matches; however, outliers may occur. The erroneous displacements belong to the low-confidence set of vectors. If an ice motion vector is missing for a particular control point, then the algorithm has not been able to determine a matching subimage in the second image. These situations typically occur in featureless areas such as sea ice covered by wet snow or melt ponds.

## 3.4. Performance of Sea Ice Tracking System

### 3.4.1. Comparison between SAR Ice Motion and Ice Beacon Data

To compare ice motion derived from SAR images against ice beacon data we ran our ice motion tracking algorithm for 10 RADARSAT-2 ScanSAR image pairs acquired for the period of time from September 25, 2009 to October 19, 2009 over the southern Beaufort Sea. The time interval

between sequential images varied from one to three days. We used data from 10 Global Positioning System (GPS) ice beacons deployed by the University of Manitoba as part of our ongoing ArcticNet Networks of Centres of Excellence partnership with Imperial Oil and British Petroleum in the southern Beaufort Sea. The beacons transmitted data every two hours. Their positional error did not exceed 100 m. For each image pair we identified ice beacon trajectories corresponding to the time interval between the two images. Ice beacon locations at the image acquisition times were determined using the linear interpolation for two neighbour beacon positions. For a given ice beacon trajectory we assigned the nearest ice tracking vector such that the distance between the start positions of the beacon trajectory and the nearest tracking vector was smaller than 3 km. We collected 36 coincided and collocated satellite and beacon ice motion vectors. Figure 3.6 demonstrates a very good agreement between ice motion tracking and ice beacon data.

The root mean square error (RMSE) indicated in Figure 3.6 was calculated as follows:

$$\mathrm{RMSE} = \sqrt{\frac{\sum_{i=1}^{N}\left(x_i^t - x_i^b\right)^2 + \left(y_i^t - y_i^b\right)^2}{N}} = 0.428\,\mathrm{km}, \qquad (3.11)$$

where

$N$ is the total number of ice tracking – ice beacon vector pairs

$\left(x_i^t, y_i^t\right)$ are horizontal and vertical components of $i$ th ice tracking vector;

$\left(x_i^b, y_i^b\right)$ are horizontal and vertical components of $i$ th ice beacon vector;

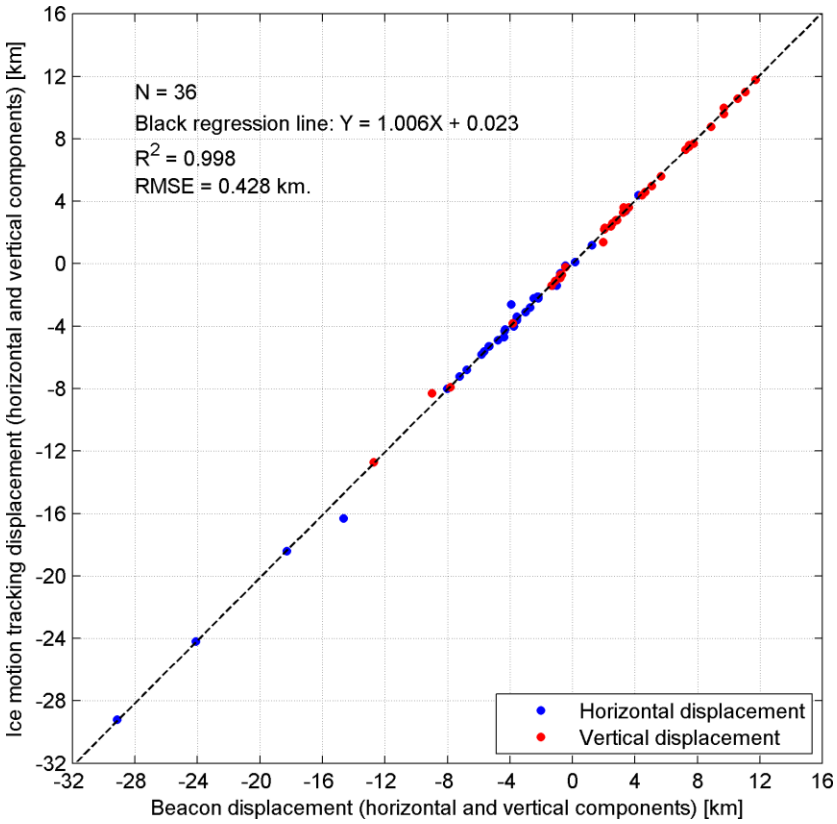


Figure 3.6. Comparison between ice motion vectors derived by our algorithm from SAR images and ice beacon data. Blue and red dots denote horizontal and vertical displacements respectively.

The obtained RMSE is slightly lower than the error of 0.6 km reported in the recent study [104].

In the comparisons shown in Figure 3.6 we employed ice motion tracking vectors with all the levels of confidence (low, medium and high). Table 3.2 shows RMSEs specifically calculated for ice motion vectors with low, medium and high levels of confidence. One may observe that the smallest RMSE between the ice tracking and ice beacon data is obtained for vectors with a high level of confidence while the largest RMSE is found for vectors with a low level of confidence.

Table 3.2. RMSE between SAR ice motion and ice beacon data for three levels of confidence of ice tracking vectors

| Level of confidence | Number of comparisons | RMSE [km] |
|---|---|---|
| **Low** | 6 | 0.672 |
| **Medium** | 17 | 0.456 |
| **High** | 13 | 0.164 |

3.4.2. Sea Ice Motion Fields Derived from SAR

Two ice motion fields produced by the sea ice tracking system are presented in this section. Resolution of all input images is 100 m.

Figure 3.7(a) and Figure 3.7(b) show two sequential HV images separated by one day time interval. Figure 3.7(c) shows the output ice motion vectors found by the algorithm. Red, yellow and green vectors indicate low, medium and high levels of confidence respectively.

The presented example contains several rotated floes which are registered by the tracking procedure. Two rotated floes in Figure 3.7(c) are marked by white rectangles.

The level of deformation experienced by these floes is manually assessed. An area from Image 1 containing the floe of interest and an area from Image 2 embracing the same floe are selected. Then the floe from Image 2 is manually rotated and merged with the matching floe from Image 1. The obtained merged images for Floe 1 and Floe 2 are displayed in Figure 3.8(a) and (b) respectively. The conducted visual analysis of the merged images indicates that there is a slight deformation of Floe 1 and there is no deformation of Floe 2.

The absence of deformation means that the distance between any two points on the floes should be a constant over time. This condition of rigidity for one floe can be formulated as follows:

$$\delta = \frac{\sqrt{\sum_{i>j} \left( d_{ij}(t_1) - d_{ij}(t_2) \right)^2}}{n} < 1\,\text{pixel}, \tag{3.12}$$

where $d_{ij}(t)$ denotes a distance (in pixels) between control points $i$ and $j$ at the moment of time $t$ ; $t_1$ and $t_2$ are acquisition times of the images; $n$ is the number of segments on the floe. Floe 1 has six motion vectors and 15 segments, and Floe 2 has five motion vectors and 10 segments as Figure 3.8(c) and (d) show.

From (3.12) the deviation from rigidity for the first floe is $\delta = 0.41$ pixel while for the second floe $\delta = 0.19$ pixel. In both cases the obtained values are less than one pixel. However, the deformation of the first floe is slightly higher compared to the second floe which is consistent with the manual analysis. It is worthwhile to point out, that such an assessment of accuracy is possible only if floes are rigid. In conditions where ice floes are significantly deformed or broken the accuracy cannot be estimated through the criterion (3.12). Therefore, the detection accuracy of non-rigid motion of sea ice was assessed visually on a large number of image pairs.

Figure 3.9 presents another example of ice motion tracking. Figure 3.9(a) and Figure 3.9(b) show two sequential SAR images acquired over the southeast of Baffin Island. Figure 3.9(c) demonstrates output displacement vectors. A rotated floe is marked by a white rectangular box in all three images. The rotation angle of this floe determined by the algorithm is 20°.

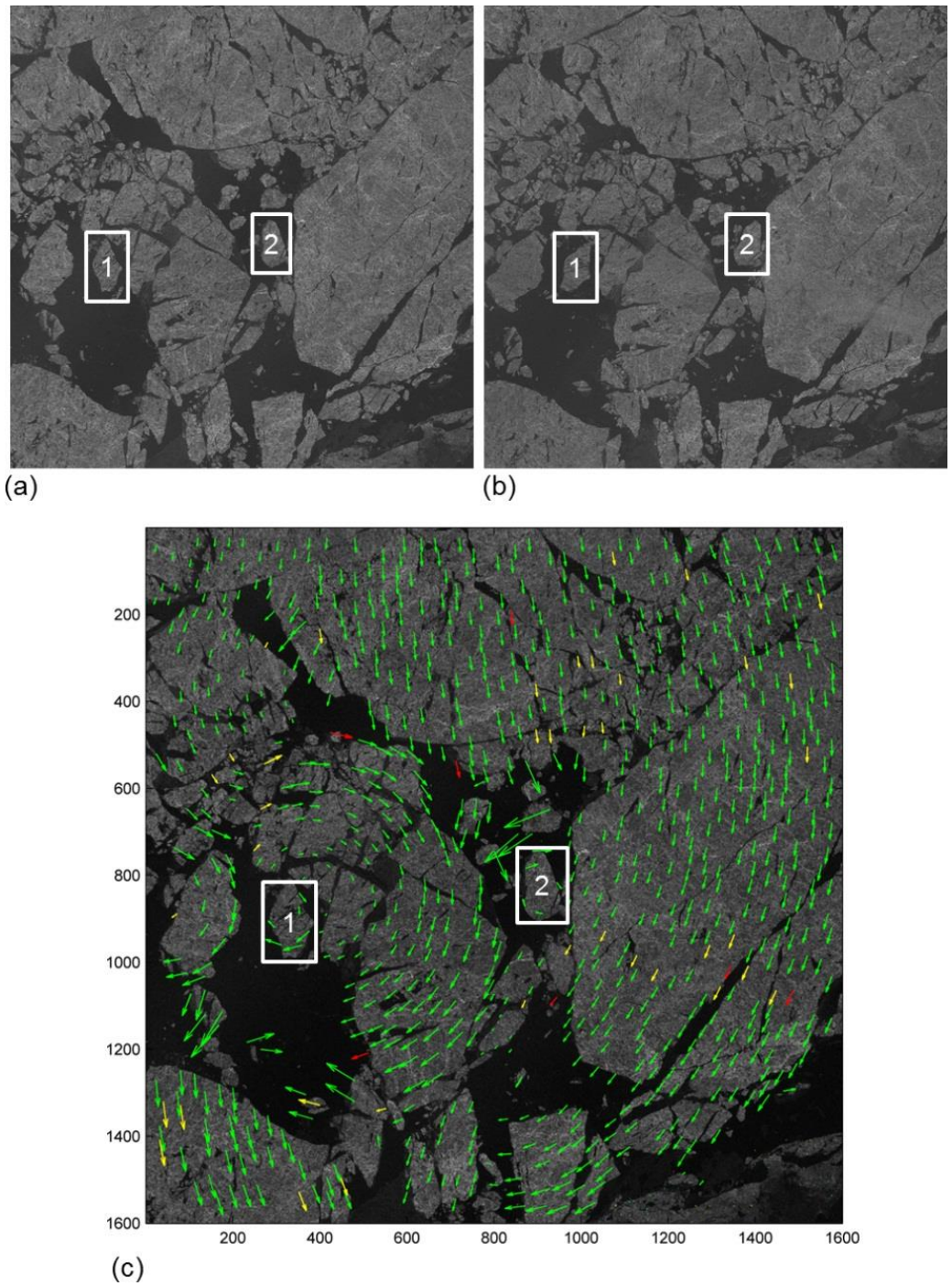


Figure 3.7. (a) and (b) are input sequential RADARSAT-2 images, HV-polarization. The images were taken on May 24, 2008, 15:32 and on May 25, 2008, 15:03 respectively to the west of Ellesmere Island; two examples of rotated floes are marked by white rectangles; (c) represents output ice drift vectors plotted on the first SAR image. Green: high level of confidence, yellow: medium level of confidence, red: low level of confidence.

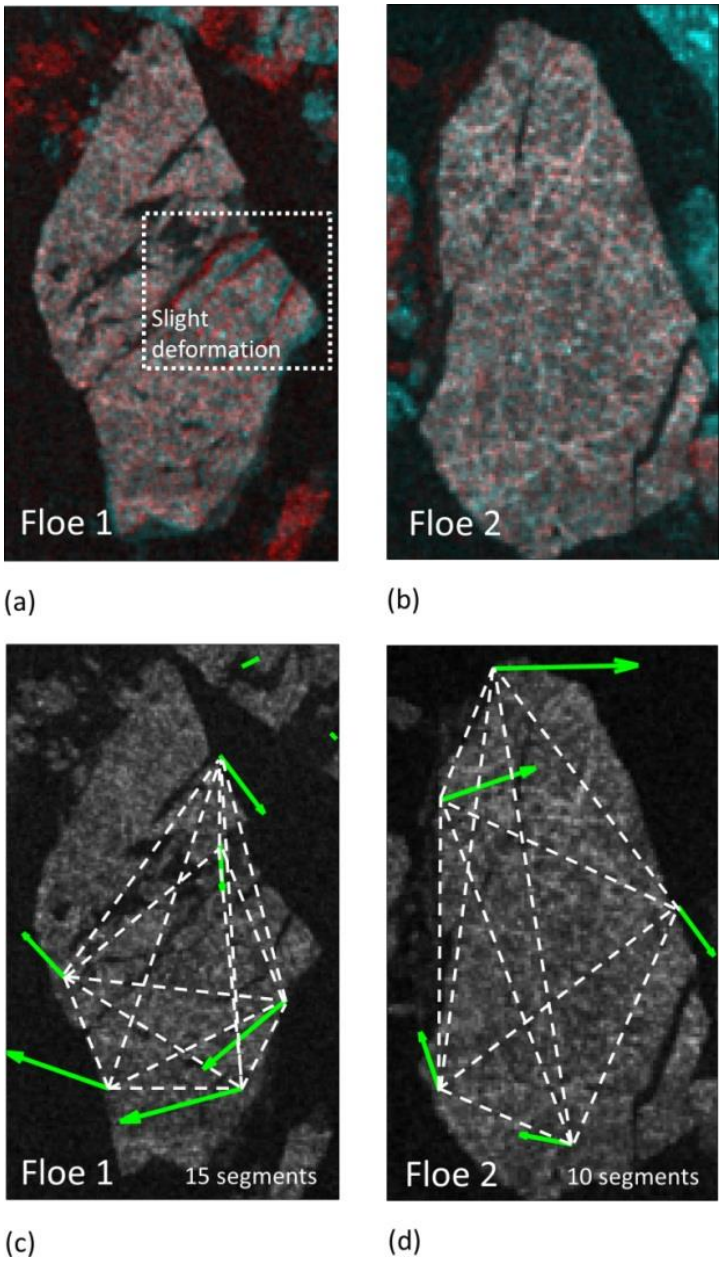


Figure 3.8. Deformation assessment of Floe 1 and Floe 2 indicated in Figure 3.7(c). (a) Floe 1 represented as a manual combination of two sequential subimages. Red: Image 1, green: Image 2, blue: Image 2. Slight deformation of the floe can be observed; (b) Floe 2 represented as a manual combination of two sequential subimages. Red: Image 1, green: Image 2, blue: Image 2; (c) Floe 1 has 15 segments. Estimated deviation from rigidity is $\delta = 0.41$; (d) Floe 2 has 10 segments. Estimated deviation from rigidity is $\delta = 0.19$.

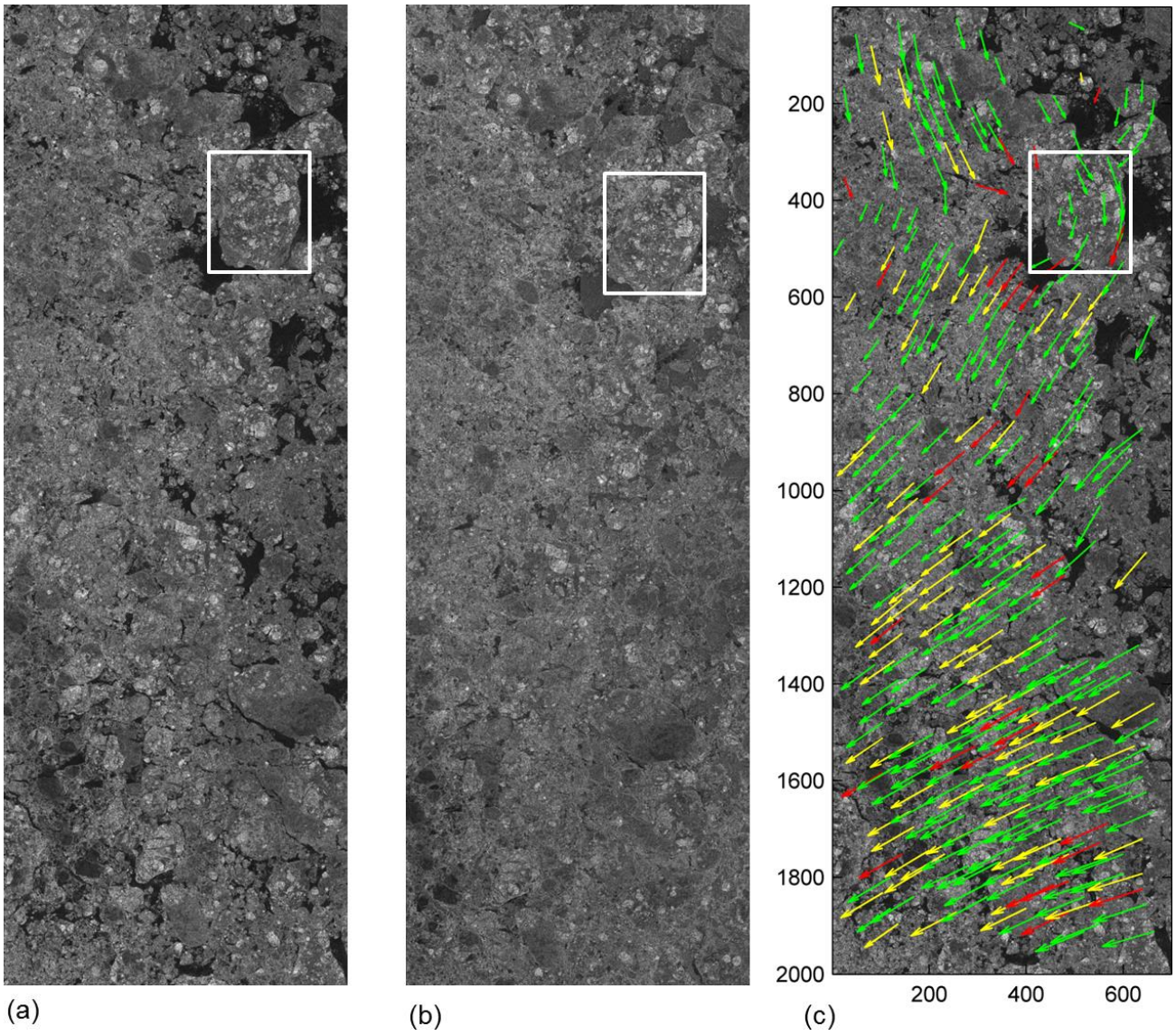


Figure 3.9. (a) and (b) are input sequential RADARSAT-2 images, HH-polarization. The images were taken on April 22, 2009, 10:22 and on April 22, 2009, 21:52 respectively over the southeast of Baffin Island; a rotated floe is marked by a white rectangle; (c) represents output ice drift vectors plotted on the first SAR image. Green: high level of confidence, yellow: medium level of confidence, red: low level of confidence.

Numerous tests show that the developed ice tracking algorithm demonstrates best performance for high and medium ice concentrations. In case of low-concentrated summer sea ice, the system shows low-confidence drift vectors or no vectors at all. Often times the open water has different

signatures in sequential SAR images due to different wind speeds. Thus, variability of the signal in SAR imagery over the sea surface negatively influences the matching procedure. For low ice concentration different floe based tracking algorithms such as [39], [40], [105] might be more efficient.

## 3.5. Evaluation of Ice Motion Tracking from Co- and Cross-Polarization Images

### 3.5.1. Cross-Polarization Channel of RADARSAT-2

Both co- and cross-polarization channels of RADARSAT-2 ScanSAR Wide/Narrow imagery are suitable for extracting ice motion. The co-polarization signal is sensitive to small scale roughness of sea ice compared to the cross-polarization signal which is primarily generated on large scale changes in ice topography. In addition, the cross-polarization image makes it possible to distinguish ice features significantly better in the near range of incidence angles compared to the co-polarization image. According to [100], [101] the cross-polarization data (HV) facilitates the following tasks:

1) ice-water separation;
2) estimation of floe size;
3) identification of first year and multiyear ice;
4) identification of large scale deformation features.

While the co-polarization channel is very sensitive to small-scale roughness, the depolarization effect is negligible over smooth ice (e.g. new ice). Therefore, the cross-polarization provides minimal improvement in detection of new ice.

Together, HH and HV data provide more accurate information on the state of sea ice cover; therefore, this combination is beneficial for ice charting by operational ice services.

In terms of automated ice motion tracking, the cross-polarization channel may provide stable features undetectable by the co-polarization image. Thus, we expect that the combination of ice motion vectors extracted from the both channels should provide more reliable ice motion fields.

Figure 3.10(a) demonstrates an example of a cross-polarization image, and Figure 3.10(b) shows changes of the HH NRCS $\sigma^0_{HH}$, the HV NRCS $\sigma^0_{HV}$ and the noise-equivalent sigma zero (NESZ) $\sigma^0_{NE}$ across the satellite track (line number is 3000). The NESZ values are available in the RADARSAT-2 ScanSAR Wide product. The original image was converted to 100 m resolution. The most identifiable negative structure in cross-polarization images is several stripes parallel to the satellite track marked in Figure 3.10(a) with blue dashed lines. From Figure 3.10(b) it can be noticed that the HV signal (red) is closer to the noise floor (i.e. NESZ) than the HH signal. The stripes appear in the image because the noise floor of the sensor modulates the low cross-polarization signal. The NESZ varies in the across track direction, while it is a constant in the along track direction. The stripes are especially pronounced over the calm ocean, where the cross-polarization signal is close to the noise floor. Furthermore, the noise floor stripes can become apparent over the sea ice, where the cross-polarization signal is quite low (e.g. new ice). Since the co-polarization signal is significantly above the noise floor, the noise floor stripes are not prominent in co-polarization images.

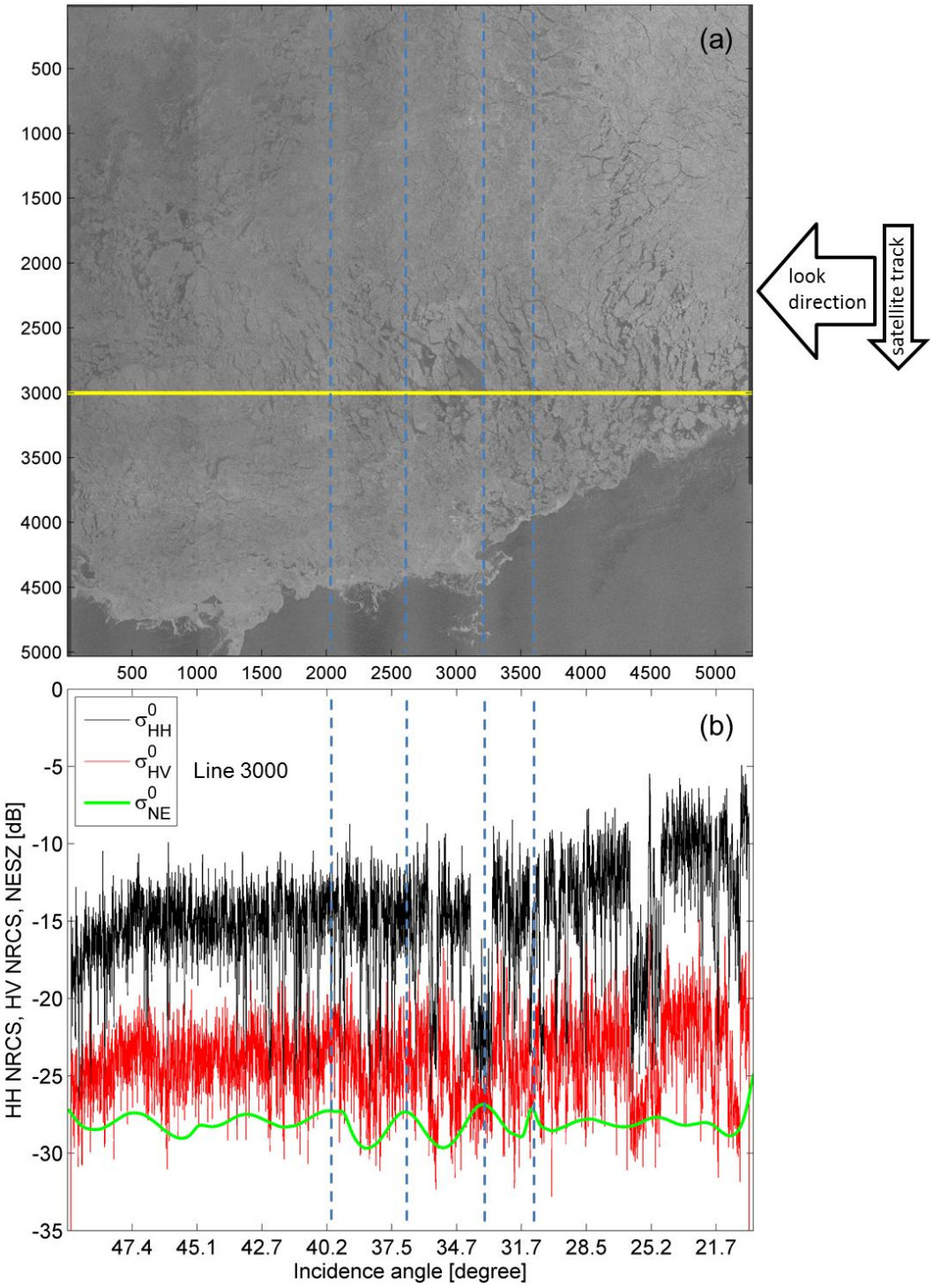


Figure 3.10. (a) Example of a cross-polarization image over the Beaufort Sea (October 16, 2009), descending orbit; (b) HH and HV signals as well as the noise floor versus pixel number/incidence angle at line number 3000. The incidence angle depends nonlinearly on the pixel number. Blue dashed lines indicate several stripes parallel to the satellite track.

3.5.2. Correction of Noise Floor Stripes in Cross-Polarization Images

In order to examine how the noise floor stripes in the cross-polarization image affect the ice motion tracking we developed a technique for reducing the impact of the noise on cross-polarization imagery.

The proposed procedure for image correction contains the following steps.

a) The raw image is calibrated (converted to NRCS units in dB).

b) The centered noise floor is calculated as follows:

$$\eta(i,j) = \sigma^0_{NE}(i,j) - \overline{\sigma^0_{NE}}(j), \tag{3.13}$$

where $\overline{\sigma^0_{NE}}(j)$ is the mean value of the noise floor at line $j = 1..N_{lin}$, $N_{lin}$ is the number of lines in the image, $i = 1..N_{pix}$, $N_{pix}$ is the number of pixels across the satellite track. $\sigma^0_{NE}$ is the NESZ taken in dB units

c) The image is divided into non-overlapping square windows. The window size is chosen to be $20 \times 20$ pixel for 100 m resolution. For each pixel within a given window the difference between the cross-polarization signal and the NESZ is calculated as follows:

$$\Delta\sigma = \sigma^0_{HV} - \sigma^0_{NE}, \tag{3.14}$$

where $\sigma^0_{HV}$ is the HV NRCS taken in dB units. If this difference does not exceed a threshold level, then the pixel is assigned as a "bad" pixel, otherwise it is assigned as "good". The threshold is chosen to be 4 dB which provides a sufficient level of signal over the noise floor.

d) A ratio between the number of "bad" pixels and the total number of pixels within each window is calculated. The obtained concentration of "bad" pixels is assigned to each pixel in a given window. Thus, a new image $C_b$ (concentration of "bad" pixels) is formed.

e) Finally, each pixel in the initial image is corrected as follows:

$$\tilde{\sigma}_{HV}(i,j) = \sigma^0_{HV}(i,j) - C_b(i,j)\eta(i,j), \tag{3.15}$$

where $(i,j)$ is pixel coordinates; $C_b(i,j)$ is the concentration of "bad" pixels within the window $(i,j)$ it belongs to. The proposed approach corrects a cross-polarization image based on local differences between the signal and noise floor. The concentration of "bad" pixels $C_b$ varies from 0 to 1. For instance, if the cross-polarization signal is significantly higher than the NESZ, than the concentration of "bad" pixels $C_b = 0$ and the correction procedure is not performed:

$$\tilde{\sigma}_{HV}(i,j) = \sigma^0_{HV}(i,j). \tag{3.16}$$

On the other hand, if the signal is close to the NESZ, then the concentration of "bad" pixels $C_b = 1$, and a significant correction is conducted as follows:

$$\tilde{\sigma}_{HV}(i,j) = \sigma^{0}_{HV}(i,j) - \eta(i,j). \tag{3.17}$$

We tested the technique for noise stripes correction on several HV images taken over sea ice and open water. Figure 3.11 shows an example of HV image (a) over sea ice and the same image after the correction technique is applied (b).

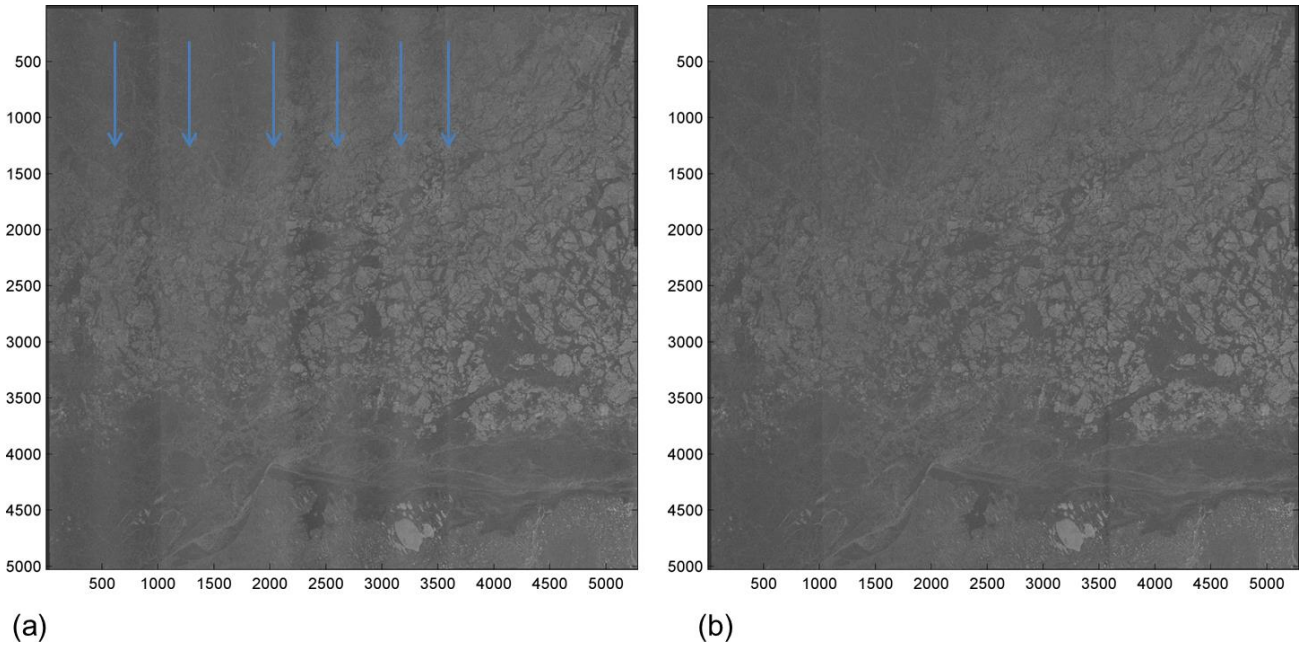


Figure 3.11. Cross-polarization (HV) image over the Beaufort Sea (December 18, 2009), descending orbit before (a) and after (b) applying the noise removal procedure. Blue arrows indicate stripes parallel to the satellite track.

The technique for filtering noise floor stripes in cross-polarization imagery is also valuable for expert visual analysis of sea ice cover (e.g. for producing ice charts at operational ice centers such as the CIS).

### 3.5.3. Ice Motion Tracking From Co- and Cross-Polarization Images

Since the ice motion detection from satellite data relies on recognition of similar features into two sequential images, the presence of stable features in both images is essential for accurate tracking. As mentioned in Section 3.5.1, the co- and cross-polarization channels indicate different ice features. Therefore, potential benefits of ice tracking from cross-polarization images are derived from the cross-polarization channel's advantageous capability to detect various ice features (which are not visible in the co-polarization channel). For instance, an ability of the cross-polarization channel to delineate ice floes and separate the multiyear ice is helpful in ice tracking. On the other hand, we do not expect any benefit of using the cross-polarization images over new ice where SAR signatures are featureless, and the signal level is close to the noise floor.

Figure 3.12 demonstrates ice motion tracking results derived from two sequential dual-polarization (HH-HV) images separated by a three-day time interval. One can observe that in the image subset $s_1$ a larger number of motion vectors were derived from the HH channel compared to the HV one. At the same time, for the image subset $s_2$ the HV channel provides a significantly better result than the HH channel. This means that it is not feasible to unambiguously judge whether the HH or HV channel is preferable for ice motion tracking: in certain conditions HH is preferable to HV and vice versa.

To further evaluate the difference between ice motion tracking from co- and cross-polarization channels, 10 dual-polarization ScanSAR Wide image pairs (HH-HV) over the Beaufort Sea were selected for the period of time from September 25, 2009 to October 19, 2009. The time interval between sequential images varied from one to three days. We conducted three

ice tracking runs for each image pair with the following inputs: (1) two HH images; (2) two HV images; (3) two HV images preprocessed by the noise floor filtering algorithm described above.

Output tracking results for each image pair were analyzed into non-overlapping square windows. The total number of ice motion vectors derived from HH and HV channels was computed for each window. In addition, the difference between the average HV signal and the NESZ was also computed. The described statistics were calculated for all the ten image pairs.

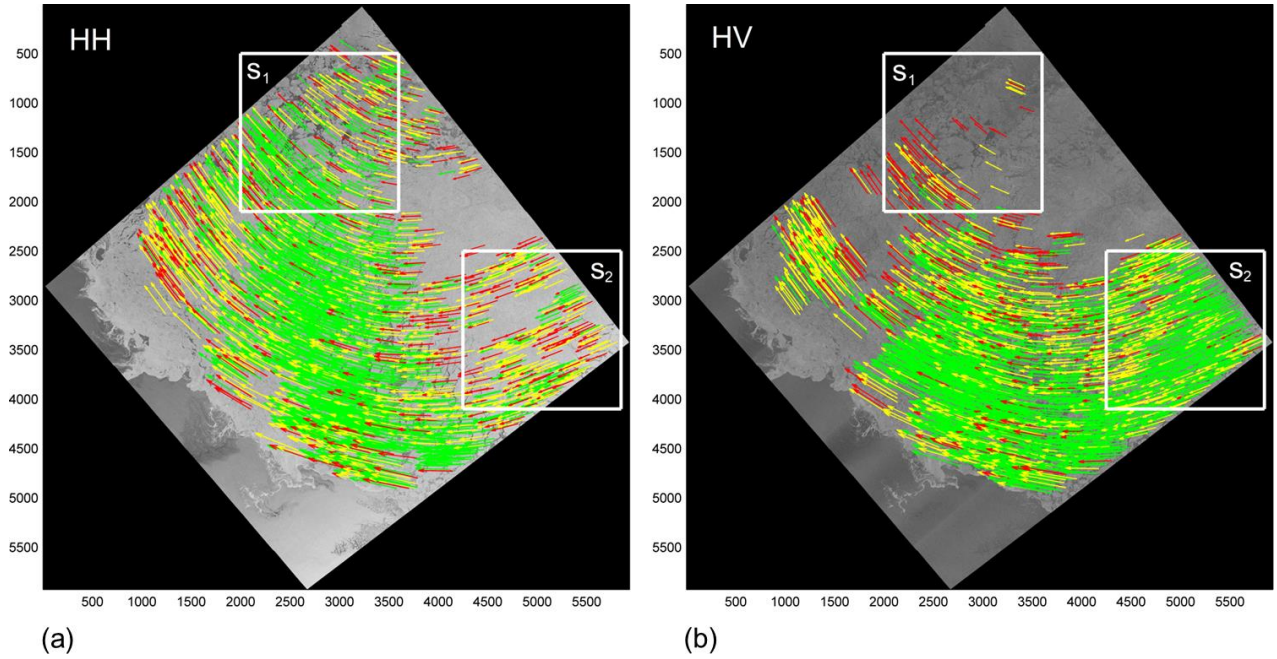


Figure 3.12. Ice motion tracking results from HH (a) and HV (b) channels. Two sequential images were taken on October 16, 2009, 15:59 and October 19, 2009, 16:12 over the southern Beaufort Sea. Vectors are plotted on the first SAR image. Green: high level of confidence, yellow: medium level of confidence, red: low level of confidence. For the image subset $s_1$ a larger number of ice motion vectors were derived from the HH channel compared to the HV one, while for $s_2$ more ice motion vectors were derived from the HV channel compared to the HH one.

Figure 3.13(a) shows a dependence of the difference between the number of motion vectors derived from HV ( $N_{HV}$ ) and HH ( $N_{HH}$ ) channels on the difference between the HV NRCS ( $\sigma^0_{HV}$ )

and the NESZ ($\sigma^0_{NE}$) taken in linear units for a window size of 400 pixels. The green points indicate the same dependence as the black points but for noise floor corrected HV images.

If the HV signal is close to the noise floor, then the difference $N_{HV} - N_{HH}$ becomes negative which means that the number of motion vectors extracted from the HH channel is larger than the number of vectors extracted from HV. This indicates that the tracking algorithm produces a better result from the HH channel than from the HV channel. If the HV signal is significantly higher than the noise floor, then the difference $N_{HV} - N_{HH}$ is positive. This implies that the number of motion vectors extracted from the HV channel is larger than the number of vectors extracted from the HH channel. For high HV signals the ice motion tracking from the HV channel is beneficial compared to the HH channel.

From Figure 3.13(a) it is also seen that the difference $N_{HV} - N_{HH}$ for filtered HV images is approximately the same as for the original HV images. This fact suggests that the developed ice motion tracking algorithm is not sensitive to the noise floor stripes along the satellite track.

The intersection point between the black/green regression line and the zero level in Figure 3.13(a) specifies a threshold for the difference between the HV signal and the noise floor. The found threshold indicates that the HV channel provides a more detailed ice motion field compared to the HH channel if the difference between the HV signal and the noise floor exceeds 0.003. At the same time, if the difference between the HV signal and the noise floor is lower than 0.003, then the HV channel is not as beneficial for ice motion tracking as the HH channel. Thus, from this analysis the following rule is formulated:

If $\sigma^0_{HV} - \sigma^0_{NE} > 0.003$ (linear units), then for ice tracking HV is preferable to HH;

If $\sigma^0_{HV} - \sigma^0_{NE} < 0.003$ (linear units), then for ice tracking HH is preferable to HV.

The same analysis was conducted for a larger window. The dependence of $N_{HV} - N_{HH}$ on $\sigma^0_{HV} - \sigma^0_{NE}$ (linear units) for the twice larger window size (800 pixels) is presented in Figure 3.13(b). Despite the smaller number of points due to the larger window size, we observe similar results as for the window size of 400 pixels.

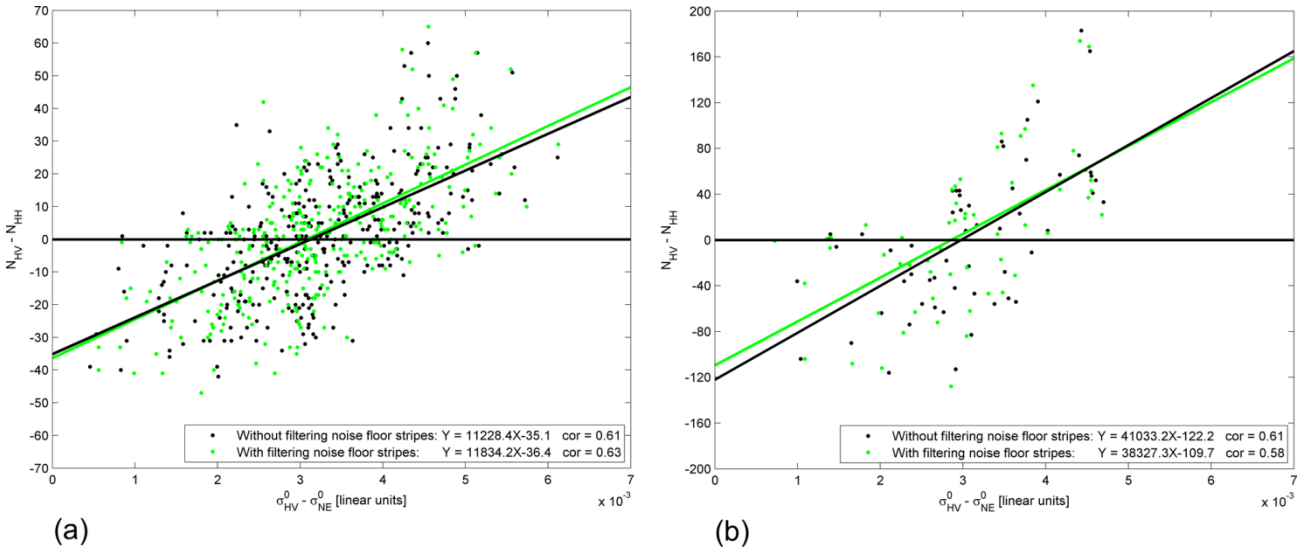


Figure 3.13. Difference between the number of ice motion vectors derived from HH and HV channels. (a) window size is 400 pixels; (b) window size is 800 pixels.

We conducted the same assessment for different levels of confidence of ice motion tracking vectors. The window size was selected to be 400 pixels and the noise floor correction procedure was not applied. Figure 3.14 shows a dependence of $N_{HV} - N_{HH}$ versus $\sigma^0_{HV} - \sigma^0_{NE}$ (linear units) for low, medium and high levels of confidence. The correlation coefficients for each of the three groups of points were calculated. It may be observed that the correlation coefficient is negative (-0.22) for the low confidence vectors (red points), while it is the largest (0.55) for the high

confidence vectors (green points). Thus, $N_{HV} - N_{HH}$ of low confidence vectors slightly decreases when $\sigma^0_{HV} - \sigma^0_{NE}$ increases while $N_{HV} - N_{HH}$ of medium and high confidence vectors increases when $\sigma^0_{HV} - \sigma^0_{NE}$ increases. Therefore, the additional vectors derived from the cross-polarization imagery primarily have medium or high level of confidence. In other words, plugging in the cross-polarization channel leads to increasing the number of vectors with medium and high levels of confidence.

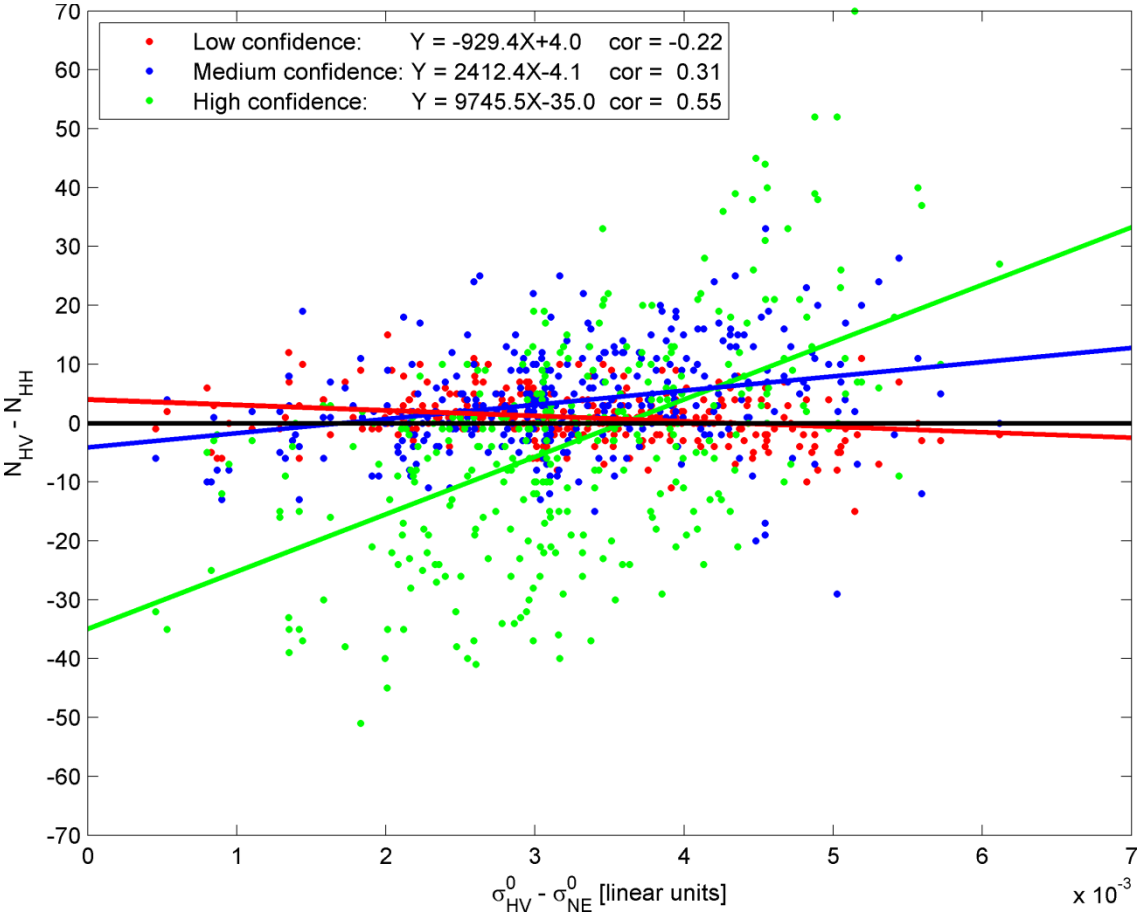


Figure 3.14. Difference between the number of ice motion vectors derived from HH and HV channels for low, medium and high levels of confidence. Window size is 400 pixels.

Our results suggest that the ice motion field derived from the HV images is able to significantly enhance the ice motion product derived from the HH images if the HV signal is sufficiently high. If the HV signal is low, then the produced ice motion field from the HV images will primarily contain low-confidence output vectors or no vectors at all. In this case, more complete ice motion information is derived from the HH channel. The level of the HV signal may vary significantly within one image. Consequently, in the areas where the HV signal is sufficiently high, a more comprehensive ice motion vector field is extracted from the HV channel compared to the HH channel. In the areas where the HV signal is low there is no supplementary ice motion vectors extracted from the HV channel. Therefore, a combination of the ice motion vector fields extracted from the HH and HV channels provides a more complete result than the ice motion information obtained from the HH or HV channels separately.

## 3.6. Conclusion

In this study we pursued two main objectives. (1) The first objective was to develop a sea ice motion tracking system operating with sequential RADARSAT-2 ScanSAR images and (2) to evaluate capabilities of the co- and cross-polarization images of RADARSAT-2 ScanSAR data for ice motion tracking.

To address the first objective, we arranged the ice tracking system to include three major steps: preprocessing, matching, and error filtering. Each of these steps combines specifically developed new approaches and existing methods.

As part of the preprocessing step we use an idea introduced in [31] of multiresolution representation of input images to decrease the computational load. At each resolution level, control

points in the first image are assigned. For control points selection we propose a new algorithm which automatically selects features associated with different ice heterogeneities (leads, cracks, ridges). Such a technique makes the probability of finding matches for these control points in the second image higher compared to the regular grid approach [31], [34], where some points may fall in featureless areas.

For the matching step of the ice tracking system we combine the phase-correlation [38] and cross-correlation techniques [31], [33]. This approach makes it possible to derive the translational and rotational components of ice motion from the phase-correlation technique as well as to quantitatively estimate the similarity between two subimages and to set different levels of confidence to output ice drift vectors based on the cross-correlation coefficients.

For filtering of erroneous vectors at each resolution level we suggest a new technique which is based on a comparison of ice drift vectors obtained from the forward (ice tracking from the first image to the second one) and backward (ice tracking from the second image to the first one) passes of ice motion detection. If the absolute value of the sum between the forward and backward drift vectors exceeds a threshold (1 pixel) then the vector is eliminated. After this procedure additional filtering is performed by thresholding the cross-correlation coefficients. For the rest of the vectors, a confidence level (low, medium, high) is set up for each output drift vector based on its cross-correlation coefficient.

We observed a very good agreement between the ice motion derived from SAR images and ice beacon data. RMSE was 0.428 km for 36 comparison points. Furthermore, the ice tracking algorithm's accuracy was assessed visually for a large number of image pairs, and the error of

found vectors did not exceed one pixel. Also, an error within one pixel was found for absolutely rigid ice motion based on the condition of rigidity of a floe.

To address the second objective we ran the developed ice motion tracking system on 10 dual-polarization RADARSAT-2 ScanSAR image pairs taken over the southern Beaufort Sea in September - October 2009. Our statistical analysis of output ice tracking results revealed that if the difference between the HV signal and the noise floor in linear units exceeds 0.003, then the HV channel is beneficial for ice motion tracking compared to the HH channel. Accordingly, if the difference between the HV signal and the noise floor in linear units is lower than 0.003, then for ice motion tracking the HH channel is preferable to the HV channel. We also examined how the noise floor stripes in the cross-polarization image affect the ice motion tracking. First, we developed a technique for filtering noise floor stripes in HV imagery, which is also useful for visual expert analysis of sea ice cover. Second, we demonstrated that the ice motion tracking algorithm is not sensitive to the noise floor stripes along the satellite track.

We found that ice motion information extracted from the HV images is able to enhance the ice motion vector field derived from the HH images in the areas where the HV signal is sufficiently high. Furthermore, the additional vectors derived from the HV images have primarily medium or high levels of confidence. We recommend a simple superposition of the ice drift vector fields obtained independently from the HH and HV channels as a final ice motion result derived from sequential dual-polarization RADARSAT-2 ScanSAR images.

The developed sea ice motion tracking system has been implemented for operational use at the CIS, Environment Canada. It has been proven to be an instrumental tool for verifying sea ice

forecasting models, estimating sea ice exchange between the CAA and the Arctic Ocean, and supporting field work in the Arctic Ocean conducted in compliance with the UNCLOS.

In light of the upcoming RCM mission [10], high resolution ice motion vector fields would be derived more frequently, almost all over the Arctic Ocean from both co- and cross-polarization images. Given the increased industrial activity in the Arctic Ocean the need for ice motion information has never been as acute as it is now. To be able to safely operate in the marginal ice zones surrounding the Arctic Ocean, timely and precise information on ice motion will be required.

# CHAPTER 4. OCEAN SURFACE WIND SPEED RETRIEVAL FROM C-BAND SAR IMAGES WITHOUT WIND DIRECTION INPUT

**A. S. Komarov**, V. Zabeline, and D. G. Barber, "Ocean surface wind speed retrieval from C-band SAR images without wind direction input," *IEEE Trans. Geosci. Remote Sens*, vol. 52, no. 2, pp. 980-990, Feb. 2014.

## 4.1. Introduction

Changes in wind speed play an important role in the Earth's climate. Wind dominates mixing of the ocean surface mixed layer and controls exchange of gas, mass and momentum across this interface [106]. An overall trend of increasing values of wind speed over the past two decades has been recently discovered. According to satellite altimeter measurements, wind speeds over the majority of the world's oceans have increased by 2.5–5% per decade [107]. However, analysis of long-term passive microwave SSM/I observations suggested that this global trend is around 1% per decade [108]. The latter appears more realistic in light of consequences that wind trends would have on global evaporation and precipitation [108]. Hence, more accurate satellite-based wind records with higher resolution are essential for specifying trends in global winds.

At the regional and local scales, information on wind speed is required for a number of operational applications. For instance, detailed mapping of wind speeds over the water surface could improve short-range forecasts and extreme events warnings in Canadian coastal zones and on the Great Lakes. It could also provide important information for tracking and forecasting oil slick displacements as well as search and rescue operations.

Since wind is one of the major factors affecting sea ice dynamics, wind speed mapping over the open water is required in the marginal ice zone (MIZ) of the Arctic Ocean. Existing numerical

weather prediction (NWP) models with a coarse resolution are not reliable in the Arctic region, particularly due to the presence of sea ice. For example, in a recent evaluation study of the Weather Research and Forecasting (WRF) model [57], near-surface wind speed was the poorest of all the predicted surface variables. The coarse 60-km resolution introduced a large amount of error due to inadequate modelling of local wind effects and local flow field distortions.

Spaceborne synthetic aperture radar (SAR) platforms have been extensively used to monitor winds at the ocean surface. Wind speed can be mapped over a wide geographical area (500 × 500 km), with very high resolution (smaller than 500 m). Physical models of electromagnetic waves interaction with sea surface [48]-[53] are quite complex and do not agree well with experimental data, and therefore, in practice, various empirical formulations are applied. A series of C-band geophysical model functions (CMODs) [54]-[56] are widely used to derive wind speeds from C-band SAR images.

Initial CMOD wind speed retrieval models were developed for VV polarization C-band data acquired by wind scatterometers aboard European satellites ERS-1 and ERS-2. A wide swath and relatively coarse resolution (25 km) of satellite scatterometers make them applicable to large-scale weather forecasting. However, the coarse scatterometer resolution does not allow for capturing wind behavior in the coastal zone. At the same time, high resolution of SAR measurements compared to scatterometers and NWP models enables us to observe small-scale changes in surface winds and to improve forecasts in the coastal zones.

CMOD models were extended to HH polarization SAR images [58], [59] through applying various approximations of co-polarization ratios (VV/HH) over the water surface. It was found [59] that the CMOD_IFR2 model, in conjunction with the Kirchhoff approximation of the co-

polarization ratio dependent on incidence angle, is suitable to derive wind speeds from RADARSAT-1 ScanSAR images. The most recent geophysical function CMOD5.N was proposed in [56] and a more accurate co-polarization ratio dependent not only on incidence angle but also on wind speed (called SAD) was introduced in [109]. However, approximations of the co-polarization ratio may still introduce significant error into wind speed estimation through the CMOD models. In addition, wind direction input is required to run CMOD-type models. Normally, wind direction is provided by NWP models, which are often not accurate (especially in the Arctic Ocean).

With the launch of Canadian RADARSAT-2, new cross-polarization channels became available [9]. It was shown [61] that the cross-polarization return from the ocean surface is independent of wind direction. In the same study, a strong linear relationship between wind speed and the cross-polarization signal (which is sometimes referred to as the C-2PO model) was demonstrated for fully-polarization RADARSAT-2 Fine Quad imagery. However, this simple relationship cannot be applied to dual-polarization RADARSAT-2 ScanSAR imagery (suitable for operational needs) where the noise floor values are significantly higher compared to the Fine Quad mode. Two new wind speed retrieval models applicable to RADARSAT-2 VV-VH ScanSAR imagery were proposed in [110]. Unlike CMOD models, these models use the additional cross-polarization variable as input. One of the models introduced in [110] does not require input wind direction, while demonstrating a better accuracy than the CMOD_IFR2. However, such a model has not been developed for RADARSAT-2 horizontal polarization HH-HV ScanSAR mode. At the same time, primarily this beam mode of RADARSAT-2 imagery is being currently ordered by the Canadian Ice Service (CIS) for operational monitoring of the Canadian Arctic. This is associated with the fact that HH polarization provides greater differentiation between open water and ice than

VV polarization [111], [112]. The additional HV channel of RADARSAT-2 further facilitates a number of tasks, such as estimation of floe size and identification of first-year and multi-year sea ice [100].

In this study, we pursue three major objectives: (1) to develop and validate a wind speed retrieval model free of input wind direction for RADARSAT-1 HH ScanSAR imagery; (2) to develop and validate a wind speed retrieval model free of input wind direction for RADARSAT-2 HH-HV ScanSAR imagery, and to evaluate different options for wind speed imaging; and (3) to explore how SAR wind speed retrieval without wind directions can be beneficial for studying various processes in the Arctic Ocean Marginal Ice Zone (MIZ).

## 4.2. Data

### 4.2.1. SAR Imagery

To build the HH wind speed retrieval model, we used 347 RADARSAT-1 ScanSAR Wide (SCW) and ScanSAR Narrow (SCN) images acquired over the Canadian west and east coasts for the period May 2008 to May 2010. For development of the HH-HV–type model, we used 84 RADARSAT-2 dual-polarization (HH-HV) SCW and SCN images acquired over the Canadian west and east coasts for the period November 2010 to March 2011.

### 4.2.2. Buoy Data

We employed buoy measurements collected on the west and east Canadian coasts. The buoy observations are available through the Environment Canada (EC) Thetis database [113]. All buoy instruments measure and average wind speed and wind direction within 10-minute intervals on an

hourly basis. Hourly observations of wave height and period were observed and averaged over 40-minute intervals. Note that the Thetis database provides buoy transmission times only; actual wind speed observation times are not reported. Therefore, in order to obtain real observation times, it is necessary to know the time lags between transmission and observation. Time lags are different for every Eastern buoy, while they equal 20 minutes for the western buoys. For example, if buoy 46004 (West) transmits data at 1:35, the actual observation of wind speed and direction is taken between 1:05 and 1:25. We used data from 17 buoys on the Canadian west coast and 9 on the east coast. Figure 4.1 shows the geographical anchor locations of the western and eastern buoys. All buoy wind speed observations were converted to equivalent neutral wind speeds at a reference height of 10 m above the ocean surface using a NASA algorithm described in [114]. This method reduces the influence of atmospheric stability based on the measured air and sea temperatures as well as heights of the anemometer and the air temperature sensor.

## 4.3. Methods

### 4.3.1. Processing SAR Data by the Wind Information Processing System (WIPS)

The Wind Information Processing System (WIPS) for the routine retrieval of surface wind speed over Canada's coastal waters has been implemented at the Meteorological Service of Canada, EC, as part of a two-year pilot project. The quasi-operational system derives wind speed from a co-polarization channel (HH or VV) of RADARSAT-1 and -2 satellite imagery using the CMOD_IFR2 algorithm [54], [59]. Wind directions required by the CMOD algorithms are provided by the Global Environmental Multiscale Regional (GEM REG) model [115] run by the Canadian Meteorological Centre (CMC). The output resolution of wind speed maps and processed

SAR images (incidence angle, normalized radar cross-section) is 500 m If a cross-polarization channel is available in the input SAR imagery, then WIPS additionally provides a noise-equivalent sigma zero (NESZ) and calibrated cross-polarization normalized radar cross-section (NRCS) image with 500-m resolution. However, this information has not been used by WIPS for wind speed retrieval.

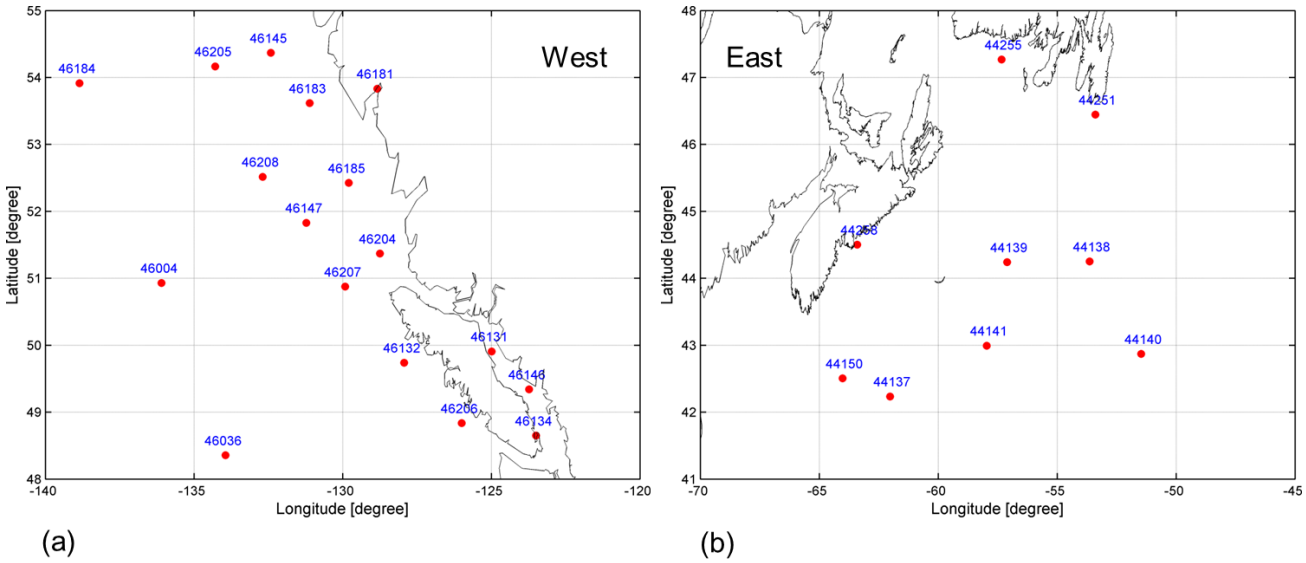


Figure 4.1. Geographical locations of ocean buoys (EC Thetis database) on Canadian (a) west and (b) east coasts.

4.3.2. Creation of Wind Speed Databases

A general flowchart of the proposed algorithm is shown in Figure 4.2 and described in this section. All available SAR images noted in Section 4.2 are preprocessed by WIPS. For each wind field, we identify buoys that are located inside the corresponding SAR scene. Usually, the number of buoys inside one SAR scene varies from one to five. The buoy data corresponding to a particular SAR scene can be extracted directly from the Thetis database [113]. The time difference between a SAR

scene and the nearest buoy measurement does not exceed 30 minutes. To find the buoy location coordinates within a scene (pixel, line), we implemented a gradient search method described in [103]. This approach is efficient for searching a specific geographical point (latitude/longitude) of interest in a satellite swath. To obtain the incidence angle, HH NRCS, NESZ and HV NRCS (if available), precisely over the buoy location, we used bilinear interpolation.

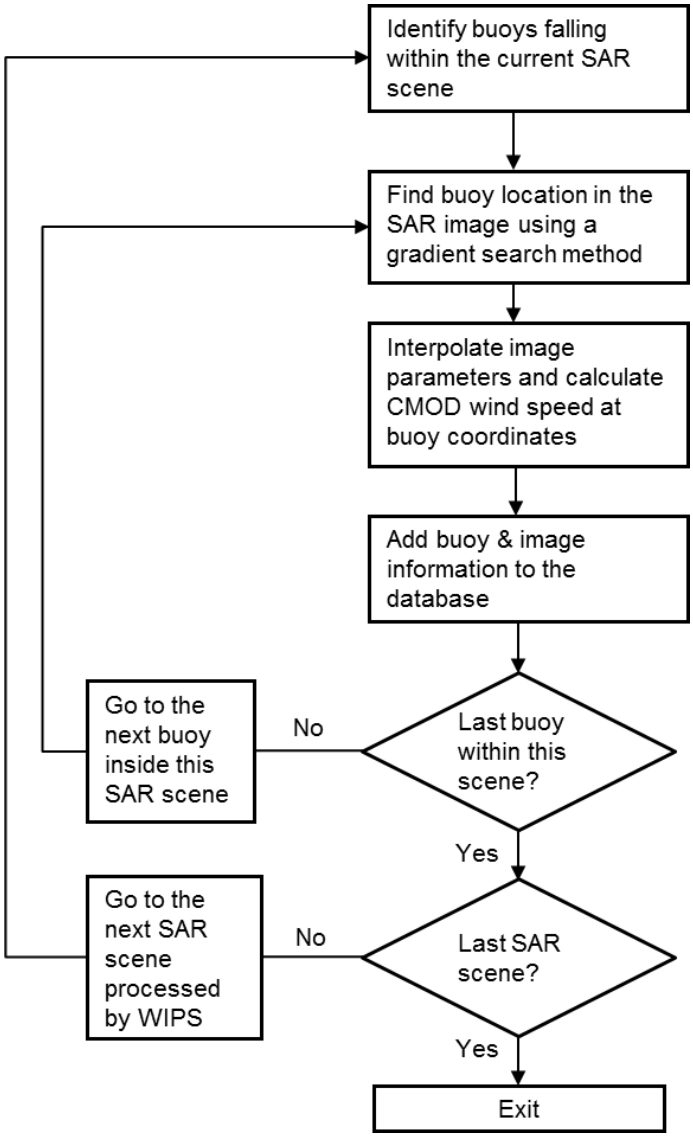


Figure 4.2. Flowchart of building a database for developing wind speed retrieval models

As a result, we created two wind speed databases for two types of SAR data: RADARSAT-1 (HH) and RADARSAT-2 (HH-HV). The first database contains 755 samples and the second contains 248 samples. Created databases are suitable for further analysis and regression modelling of wind speed through SAR parameters.

## 4.4. HH Model without Wind Direction

To build the HH wind speed retrieval model, the initial HH database containing 755 samples was divided into two subsets: (1) 500 samples (a training subset) and (2) 255 samples (a testing subset).

The first subset was used for training the model. We propose a quadratic relationship in a regression model between buoy wind speed as a dependent variable and HH NRCS along with incidence angle as independent variables (there is no wind direction as an independent variable):

$$V = a_0 + a_1\sigma^0_{HH} + a_2\theta + a_3\left(\sigma^0_{HH}\right)^2 + a_4\theta^2 + a_5\sigma^0_{HH}\theta\,, \tag{4.1}$$

where $V$ is the wind speed, m/s; $\theta$ is the incidence angle, degree; and $\sigma^0_{HH}$ is the HH NRCS, dB. Table 4.1 presents coefficients $a_0, a_1, ..., a_5$, which were determined through the regression analysis of the training dataset. Figure 4.3 shows buoy measurements (black points) and a fitted surface given by equation (4.1).

Table 4.1. Regression coefficients for the HH model (4.1)

| | |
|---|---|
| $a_0$ | -16.50189 |
| $a_1$ | 0.81709 |
| $a_2$ | 1.65899 |
| $a_3$ | 0.06022 |
| $a_4$ | 0.00333 |
| $a_5$ | 0.06981 |

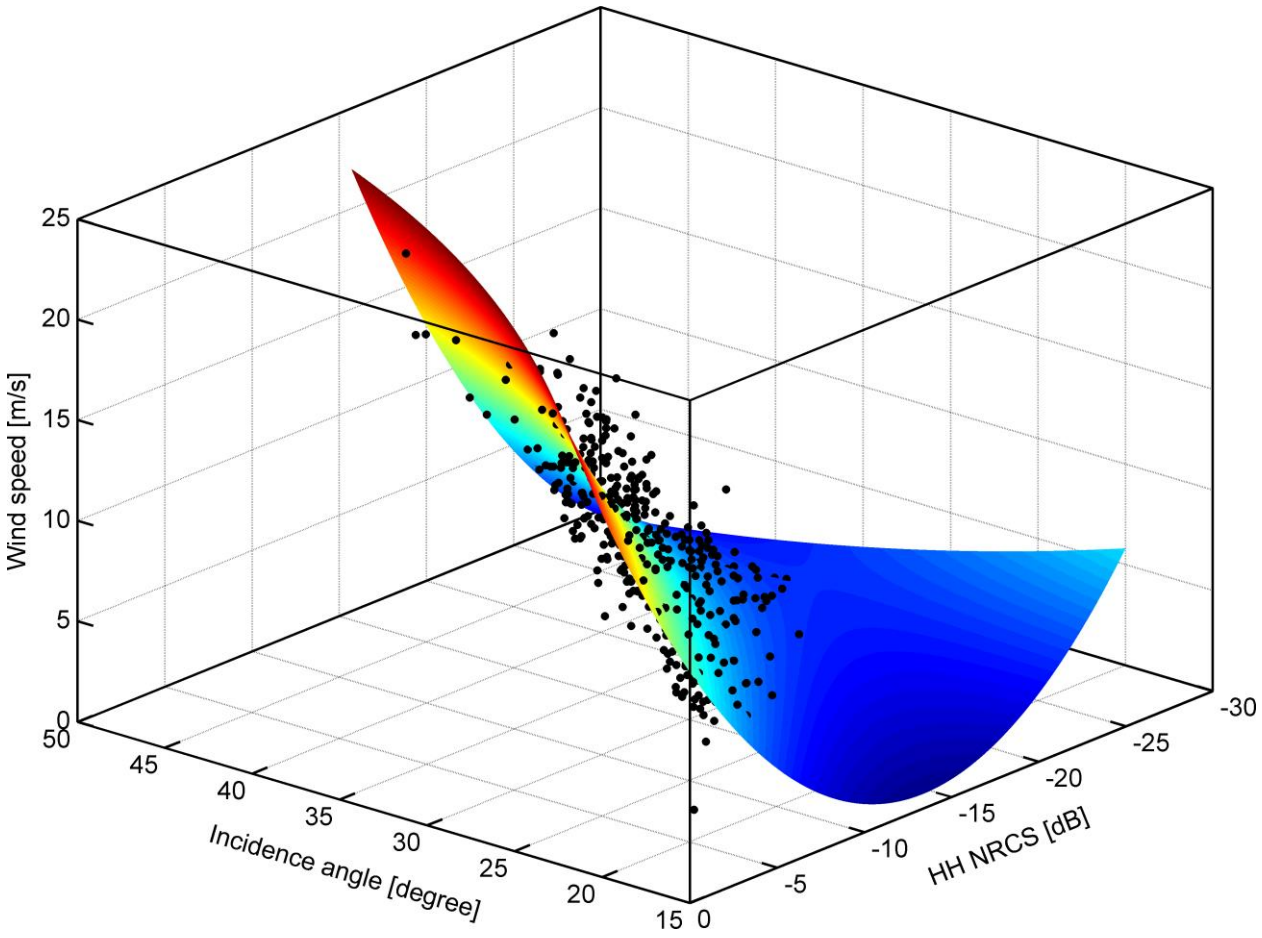


Figure 4.3. Fitting surface of buoy measurements for the HH model (4.1).

The model developed on the first subset (training) was tested on the second subset (testing). Figure 4.4 demonstrates the performance of the regression model on training and testing subsets, and for comparing the performance of the CMOD_IFR2 [54] and CMOD5.N [56] models with the SAD co-polarization ratio [109] on the same datasets. Figure 4.4(b), (d) and (f) illustrates that our regression model performs better on the testing data subset (RMSE = 1.77 m/s) compared to the CMOD5.N (RMSE = 1.95 m/s) and CMOD_IFR2 (RMSE = 2.23 m/s) with the SAD co-polarization ratio. This result suggests that the error coming from the SAD approximation of the co-polarization ratio [109] is greater than the error resulting from the omission of wind direction in a regression model. Thus, our model without wind direction has a higher accuracy than the CMOD_IFR2 and CMOD5.N models with the SAD co-polarization ratio.

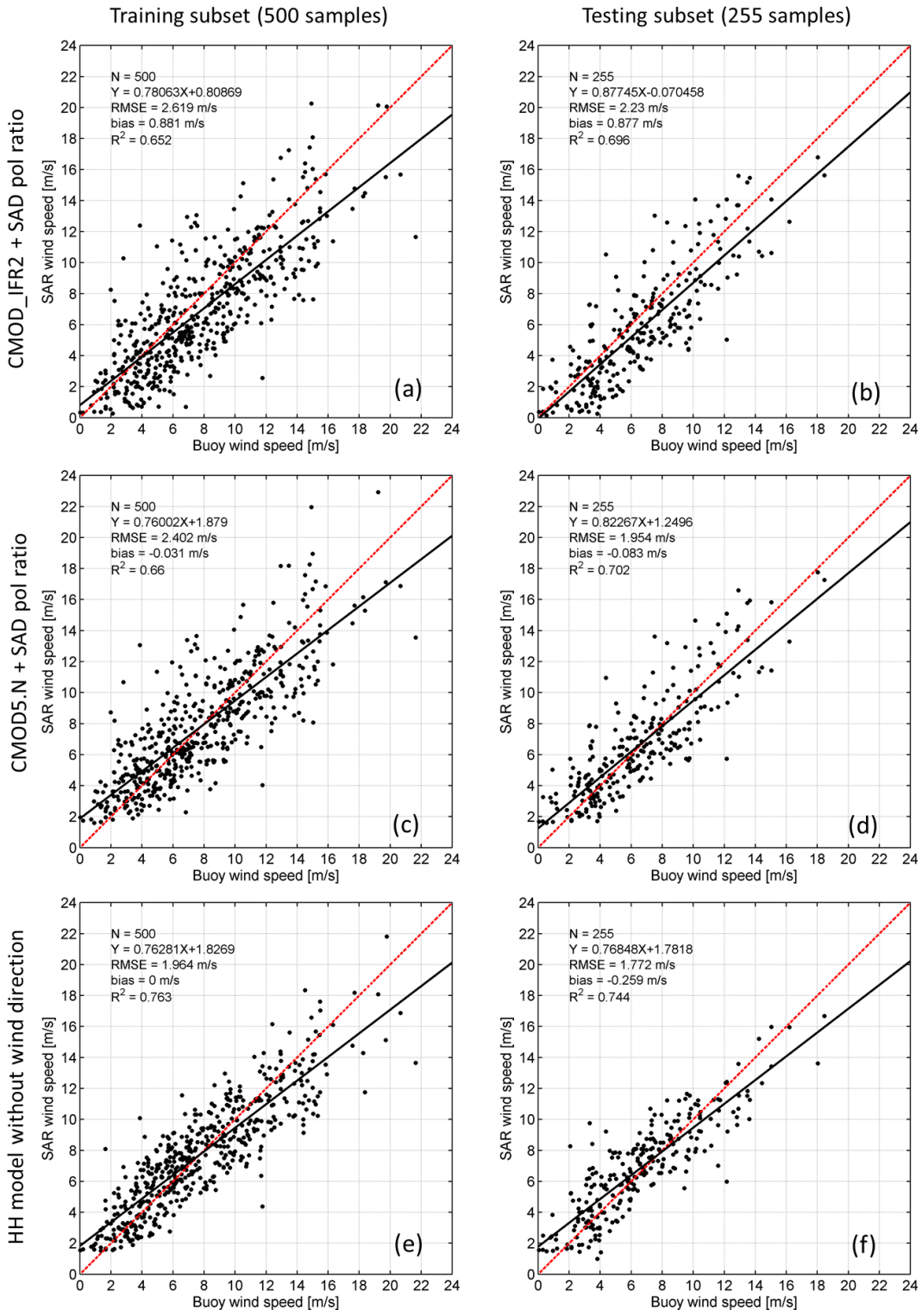


Figure 4.4. HH wind speed retrieval algorithm without wind direction versus the CMOD_IFR2 and CMOD5.N with the SAD co-polarization ratio wind speed retrieval models. (a) wind speeds

calculated according to the CMOD_IFR2 with the SAD co-polarization ratio versus buoy data for the training subset; (b) wind speeds calculated according to the CMOD_IFR2 with the SAD co-polarization ratio versus buoy data for the testing subset; (c) wind speeds calculated according to the CMOD5.N with the SAD co-polarization ratio versus buoy data for the training subset; (d) wind speeds calculated according to the CMOD5.N with the SAD co-polarization ratio versus buoy data for the testing subset; (e) wind speeds calculated according to our HH model without wind direction versus buoy data for the training subset; (d) wind speeds calculated according to our HH model without wind direction versus buoy data for the testing subset.

To ensure that the proposed regression model is not biased towards a few wind directions we examined distributions of relative wind directions within the studied datasets. Figure 4.5 demonstrates two distributions of absolute values of relative wind directions measured by buoys for both training and testing subsets. The wind direction relative to the antenna look is defined as follows:

$$\varphi = \varphi_t - \varphi_b + \frac{\pi}{2}, \tag{4.2}$$

where $\varphi_t$ is the satellite track angle; $\varphi_b$ is the angle of buoy wind direction counting clockwise from the North. We considered the distributions of the absolute value of wind directions (from 0 to $\pi$) because CMOD geophysical functions are even with respect to the relative wind direction $\varphi \in [-\pi, \pi]$. Figure 4.5 reveals that the distributions of wind directions in both subsets are close to uniform; therefore, no preferred wind directions can be identified in our subsets. This result indicates that the proposed HH model (4.1) does not have any preference in wind direction.

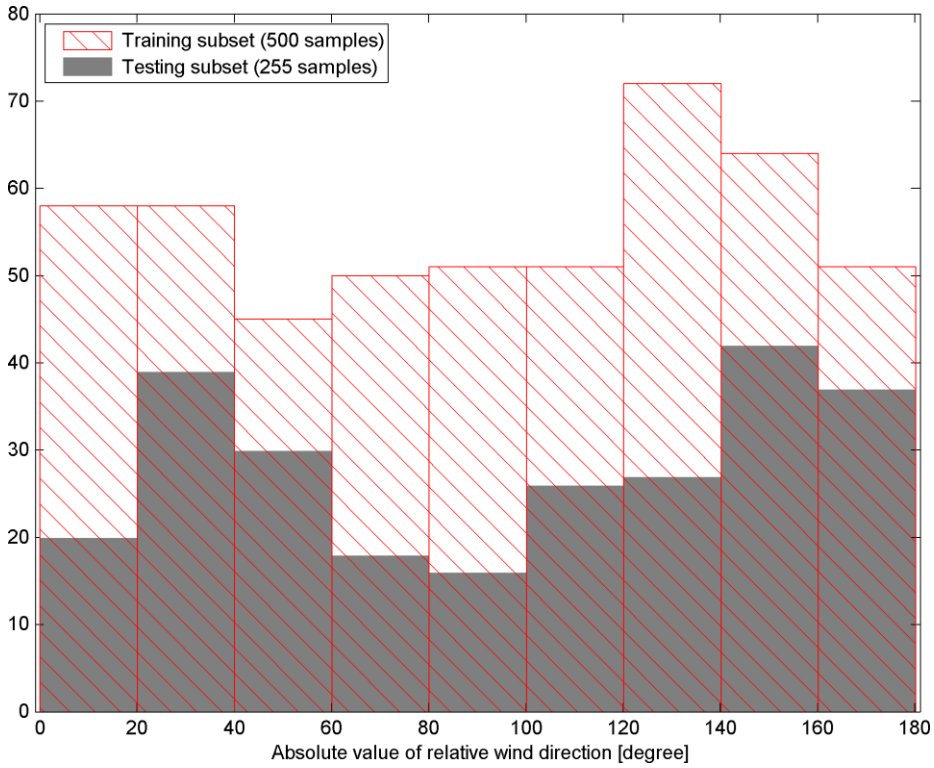


Figure 4.5. Distribution of absolute values of relative wind directions measured by buoys of the HH model.

## 4.5. HH-HV Model without Wind Direction

### 4.5.1. Analysis of the HH-HV Database

It is well known that the co-polarization signal tends to saturate with increasing wind speed over the open water [60], [116]. This effect can also be observed in Figure 4.6(a), which shows a dependence of the HH NRCS on the buoy wind speed for three groups of incidence angles. Contrary to the HH signal, the HV signal does not saturate with increasing the wind speed as demonstrated in Figure 4.6(b). Also, Figure 4.6 shows a weaker dependence of HV NRCS on incidence angle in the range of $20^{o} \le \theta \le 50^{o}$ compared to the HH NRCS. Hence, introducing the

HV NRCS into a regression analysis may improve the accuracy of the wind speed retrieval especially for strong winds. Figure 4.6 shows that the HV signal is significantly lower than the HH signal, and that the HV signal is close to the noise floor for low and moderate wind speeds. Therefore, the noise floor must be taken into consideration in the wind speed retrieval algorithms.

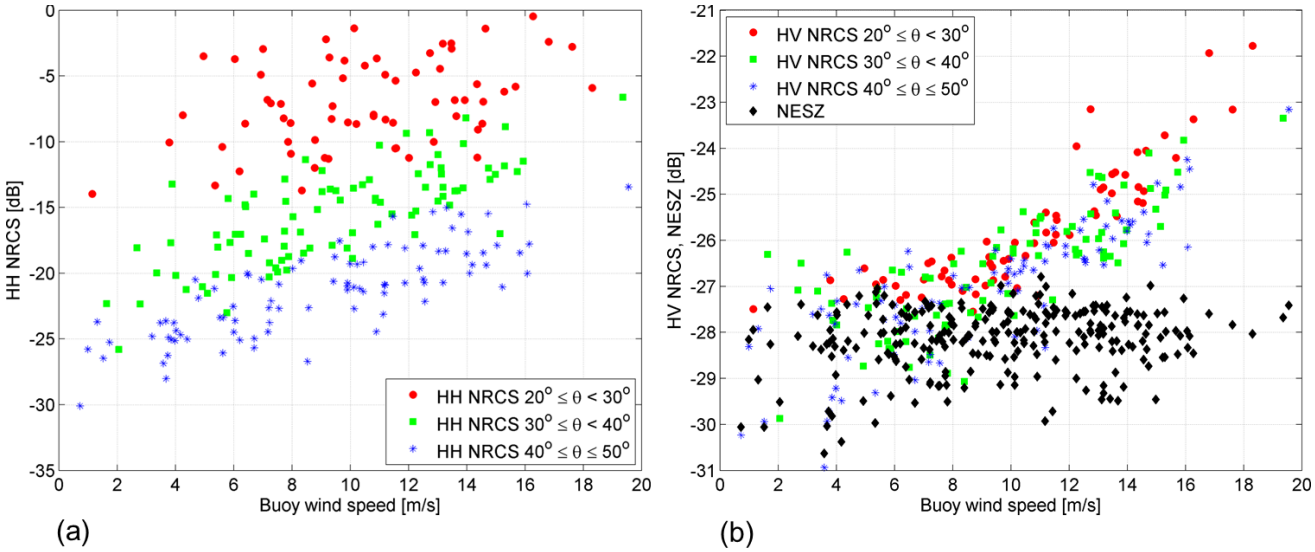


Figure 4.6. Dependence of (a) HH NRCS and (b) HV NRCS and NESZ on the buoy wind speed for three ranges of incidence angles; 248 samples.

For further analysis, the HH NRCS $\sigma^0_{HH}$, HV NRCS $\sigma^0_{HV}$ and NESZ $\sigma^0_{NE}$ are converted to linear units as follows:

$$\sigma^0_{HH\,lin} = 10^{\frac{\sigma^0_{HH}}{10}},\ \sigma^0_{HV\,lin} = 10^{\frac{\sigma^0_{HV}}{10}},\ \sigma^0_{NE\,lin} = 10^{\frac{\sigma^0_{NE}}{10}}. \quad (4.3)$$

Figure 4.7(a) shows the noise floor dependence on the incidence angle. The behaviour of the NESZ across the satellite track is caused by the irregular antenna elevation pattern. In our datasets

the NESZ level for HH-HV ScanSAR images over the ocean surface varied from -30.6 to -26.8 dB. Relatively high levels of the NESZ in RADARSAT-2 ScanSAR products (compared to the fully-polarization mode) may control the cross-polarization signal. Therefore, a careful consideration of cross-polarization NRCS with respect to the NESZ is required for wind retrieval.

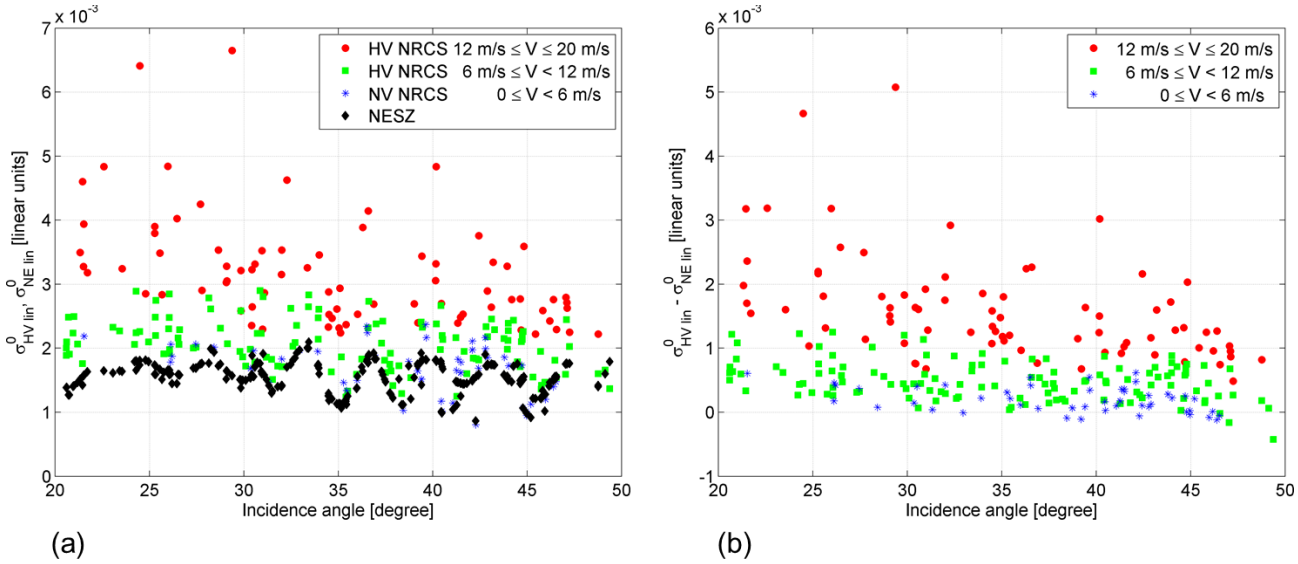


Figure 4.7. Dependence of (a) HV NRCS and NESZ in linear units and (b) HV NRCS minus NESZ in linear units on the incidence angle for three ranges of buoy wind speeds; 248 samples.

Figure 4.7(a) also demonstrates a dependence of the HV NRCS and NESZ taken in linear units on the incidence angle for three ranges of buoy wind speeds. The points with wind speeds higher than 12 m/s are well above the noise floor, while points with wind speeds lower than 6 m/s lie closer to the NESZ pattern. Thus, for low wind speeds, the HV signal is substantially governed by the noise floor. To reduce this effect we introduce the difference between the HV NRCS and the NESZ $\sigma^0_{HVlin} - \sigma^0_{NElin}$ taken in linear units. A dependence of this difference on the incidence

angle is displayed in Figure 4.7(b). Furthermore, similar to [110], we introduce a new HV cross-polarization variable expressed in dB units as follows:

$$\eta_{HV} = \begin{cases} 10\log_{10}\left(\dfrac{\sigma^0_{HV\,lin} - \sigma^0_{NE\,lin}}{\varepsilon}\right) & \sigma^0_{HV\,lin} - \sigma^0_{NE\,lin} > \varepsilon \\ 0 & \sigma^0_{HV\,lin} - \sigma^0_{NE\,lin} \le \varepsilon \end{cases}, \tag{4.4}$$

where $\varepsilon$ denotes a threshold that cuts the HV signal in the vicinity of the noise floor. Selection of the threshold $\varepsilon$ was based on the following considerations. Excessively high thresholds essentially exclude the cross-polarization channel from the wind speed retrieval model (as can be seen in the next section), which decreases the accuracy of retrieved wind speeds. Very low threshold values lead to appearance of noise floor stripes parallel to the satellite track in wind speed maps. Visual examination of numerous wind speed images produced by the HH-HV model enabled us to establish a useful threshold value at $\varepsilon = 4 \cdot 10^{-4}$.

Figure 4.8 shows a strong dependence of the HV cross-polarization variable (4.4) on the wind speed for three ranges of incidence angles. A slight dependence of $\eta_{HV}$ on the incidence angle can also be observed.

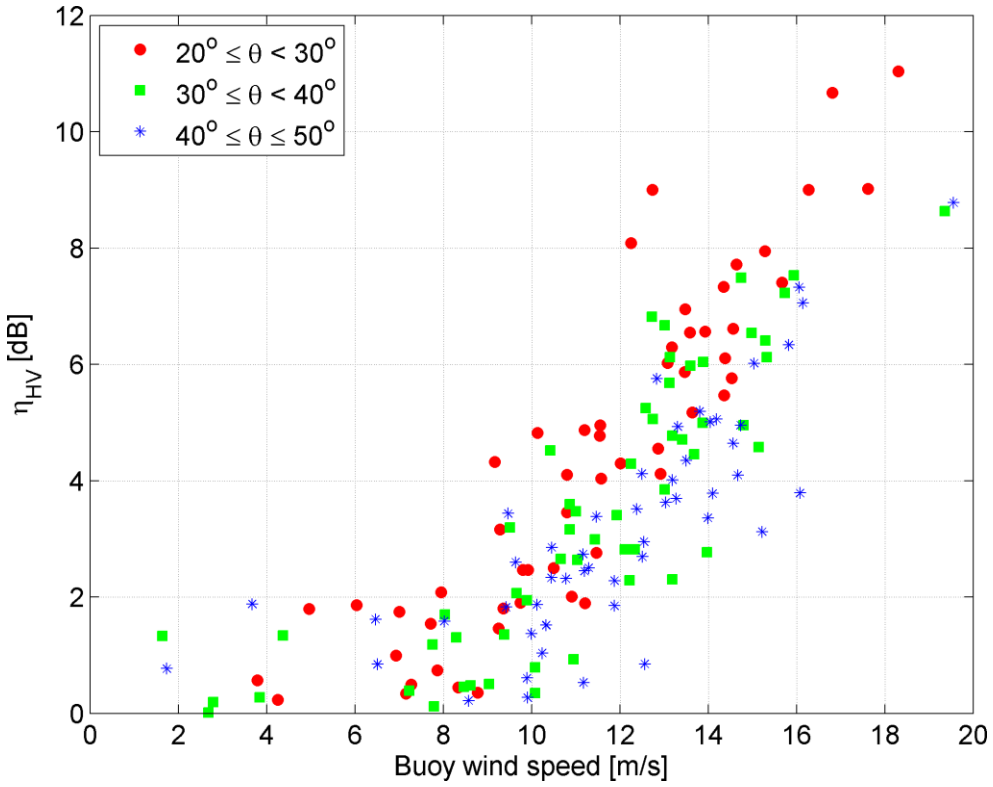


Figure 4.8. Dependence of the HV cross-polarization variable on the buoy wind speed for three ranges of incidence angles, $\varepsilon = 4 \cdot 10^{-4}$; 162 out of 248 samples which fulfil the condition $\sigma^0_{HV\,lin} - \sigma^0_{NE\,lin} > \varepsilon$.

4.5.2. HH-HV Wind Speed Retrieval Model

Our initial HH-HV database containing 248 samples was divided into two subsets: (1) 130 samples (a training subset) and (2) 118 samples (a testing subset). The following relationship between wind speed and HH-HV image parameters is proposed:

$$V = \begin{cases} c_0 + c_1\sigma^0_{HH} + c_2\theta + c_3\eta_{HV} + c_4(\sigma^0_{HH})^2 + c_5\theta^2 + c_6(\eta_{HV})^2 + c_7\sigma^0_{HH}\eta_{HV} + c_8\sigma^0_{HH}\theta & \sigma^0_{HV\,lin} - \sigma^0_{NElin} > \varepsilon \\ p_0 + p_1\sigma^0_{HH} + p_2\theta + p_3(\sigma^0_{HH})^2 + p_4\theta^2 + p_5\sigma^0_{HH}\theta & \sigma^0_{HV\,lin} - \sigma^0_{NElin} \le \varepsilon \end{cases}, \quad (4.5)$$

where $V$ is the wind speed, m/s; $\theta$ is the incidence angle, degree; $\sigma^0_{HH}$ is the HH NRCS, dB; and $\eta_{HV}$ is the new cross-polarization variable. Two sets of coefficients, $c_0, c_1, ..., c_8$ and $p_0, p_1, ..., p_5$ (displayed in Table 4.2), were determined through a regression analysis applied to the training subset.

Table 4.2. Regression coefficients for the HH-HV model (4.5).

| | | | |
|---|---|---|---|
| $c_0$ | 5.87419 | $p_0$ | -6.92202 |
| $c_1$ | 0.80594 | $p_1$ | 1.61996 |
| $c_2$ | 0.27113 | $p_2$ | 1.36301 |
| $c_3$ | 1.38335 | $p_3$ | -0.02644 |
| $c_4$ | -0.10676 | $p_4$ | -0.02272 |
| $c_5$ | -0.02097 | $p_5$ | -0.0487 |
| $c_6$ | -0.0022 | - | - |
| $c_7$ | 0.02593 | - | - |
| $c_8$ | -0.10327 | - | - |

Figure 4.9 demonstrates the performance of the HH-HV regression model (4.5) on the training and testing subsets as well as the performance of the CMOD_IFR2 [54] and CMOD5.N [55] models with the SAD co-polarization ratio [109] on the same datasets. From Figure 4.9(b), (d) and (f) it is seen that our HH-HV regression model performs better on the testing data subset (RMSE = 1.59 m/s), compared to the CMOD5.N (RMSE = 2.19 m/s) and CMOD_IFR2 (RMSE = 2.03 m/s) with the SAD co-polarization ratio. Thus, the proposed HH-HV model without the wind direction has a better accuracy than the CMOD_IFR2 and CMOD5.N models with the SAD approximation of the co-polarization ratio.

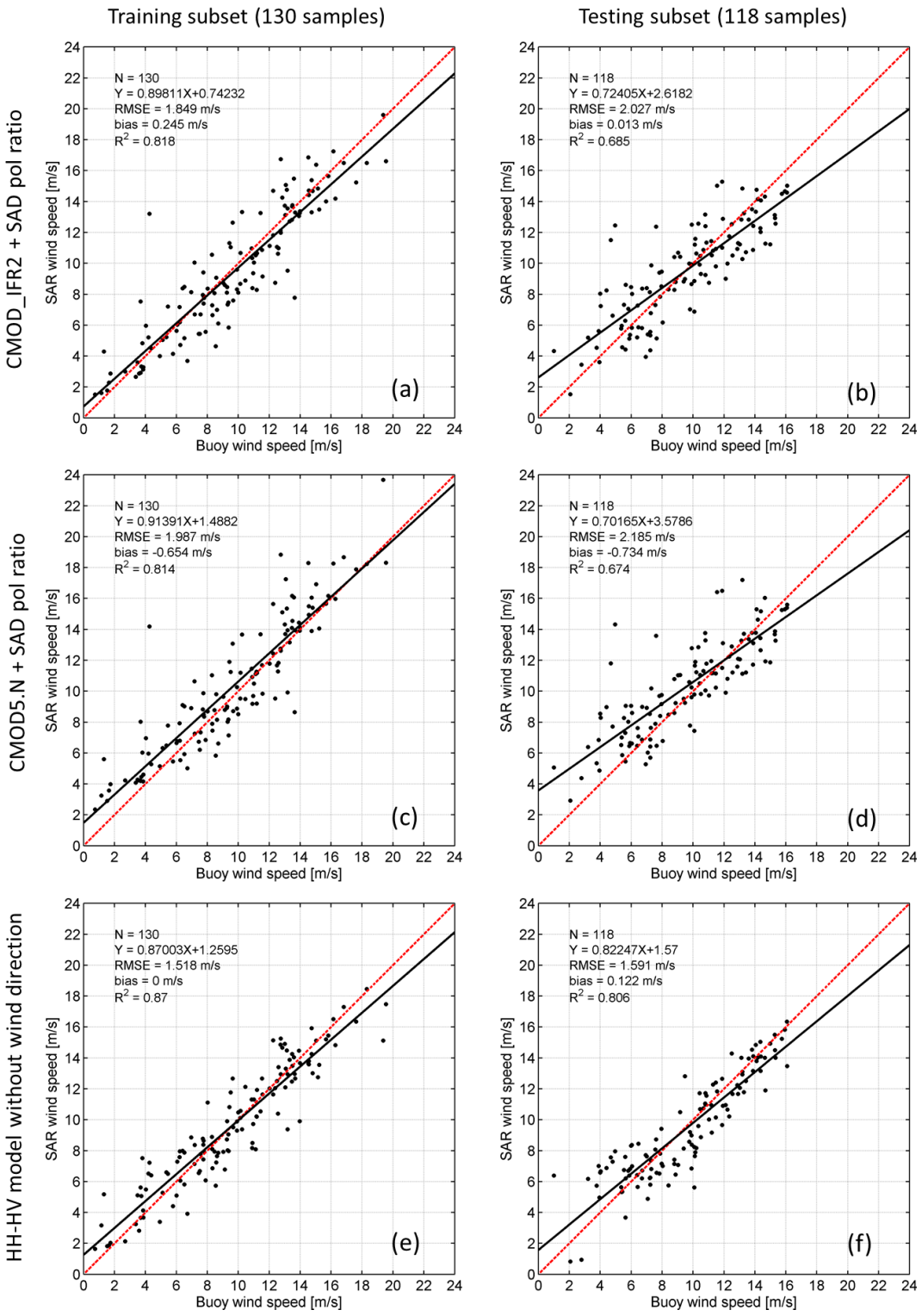


Figure 4.9. HH-HV wind speed retrieval algorithm without wind direction versus the CMOD_IFR2 and CMOD5.N with the SAD co-polarization ratio wind speed retrieval models. (a)

wind speeds calculated according to the CMOD_IFR2 with the SAD co-polarization ratio versus buoy data for the training subset; (b) wind speeds calculated according to the CMOD_IFR2 with the SAD co-polarization ratio versus buoy data for the testing subset; (c) wind speeds calculated according to the CMOD5.N with the SAD co-polarization ratio versus buoy data for the training subset; (d) wind speeds calculated according to the CMOD5.N with the SAD co-polarization ratio versus buoy data for the testing subset; (e) wind speeds calculated according to our HH model without wind direction versus buoy data for the training subset; (d) wind speeds calculated according to our HH model without wind direction versus buoy data for the testing subset.

Analogous to Figure 4.5 for the HH model, Figure 4.10 demonstrates distributions of buoy wind directions relative to the antenna look for both training and testing subsets. From the presented histograms no preferred wind direction can be identified. This indicates that the proposed HH-HV model is not biased towards any wind direction.

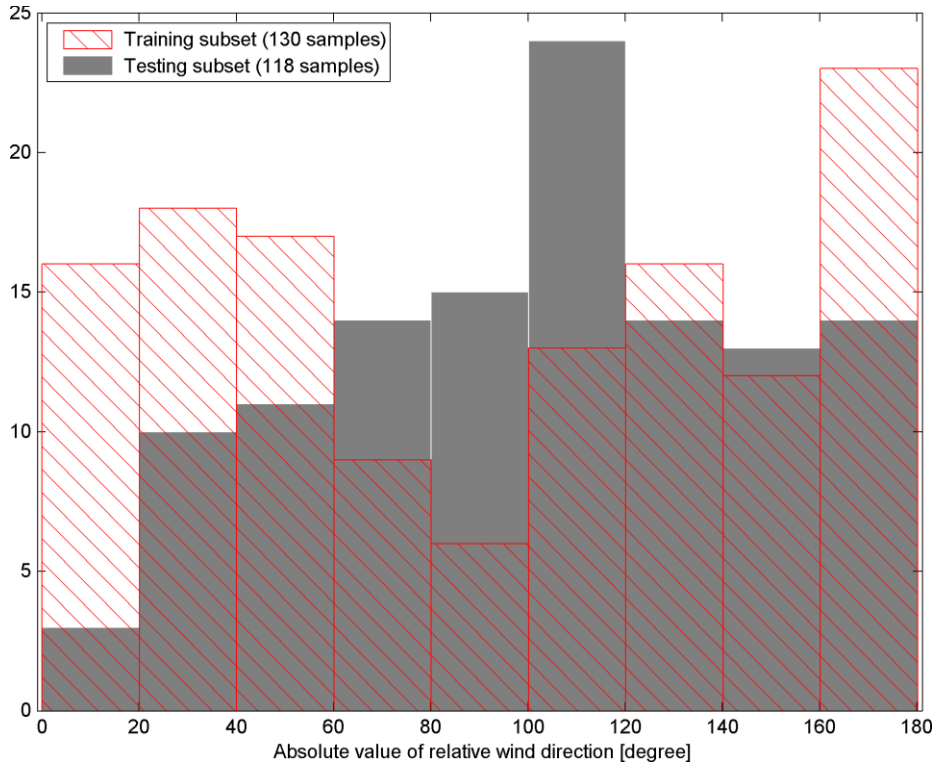


Figure 4.10. Distribution of absolute values of relative wind directions measured by buoys for the HH-HV model.

4.5.3. Wind Speed Imaging Using HH-HV Model

The original resolution of RADARSAT-2 ScanSAR Wide imagery is 50 m [9]. Direct calculation of wind speed from the original image would lead to a noisy pattern due to the presence of speckle noise in the raw SAR image. Therefore, a degraded wind speed image is generated. We examined two options to derive a wind speed product with a lower resolution compared to the initial SAR image:

Option 1:

(a) the calibrated 50-m resolution image is degraded to a 500-m resolution image;

(b) wind speed is derived from the obtained degraded image.

Option 2:

(a) wind speed is derived from the calibrated 50-m resolution RADARSAT-2 ScanSAR HH-HV image;

(b) the obtained 50-m resolution wind field is degraded to a 500-m resolution product.

We found that these two options provide almost identical wind speed maps computed by the HH model (4.1) or CMOD models. However, in the case of the HH-HV model (4.5), the results can be different due to the piecewise nature of this model. Figure 4.11(a) shows an example of the wind speed product with a 500-m resolution derived from a RADARSAT-2 HH-HV image using Option 1. A grainy pattern can be observed in a subset of 100 × 100 pixels demonstrated in Figure 4.11(b). This effect is associated with the switching between two modes of the HH-HV model (4.5).

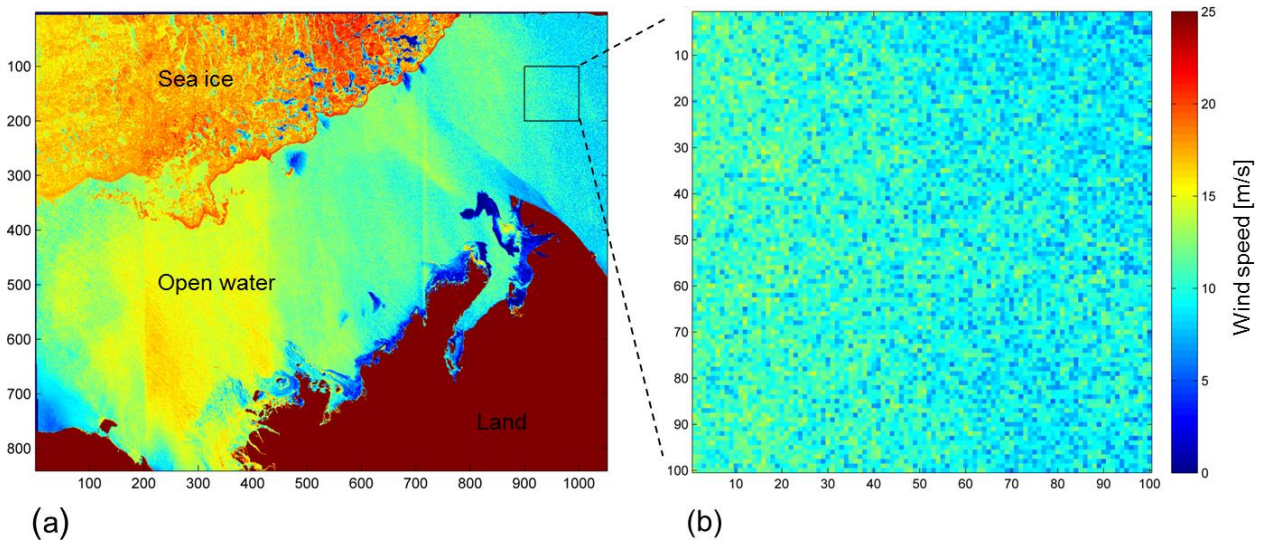


Figure 4.11. Wind speed mapping from a RADARSAT-2 ScanSAR HH-HV image through the following steps: (1) the calibrated 50-m resolution image is degraded to a 500-m resolution image; and (2) wind speed is derived from the obtained degraded image. Wind speed is valid only over the open water. (a) 500-m resolution wind speed map; (b) 100×100 pixel subset from this wind field. The RADARSAT-2 image was acquired over the southern Beaufort Sea on October 10, 2009, at 15:35.

To overcome this issue, we introduced Option 2 for processing HH-HV RADARSAT-2 images. A wind speed map generated through Option 2 is shown in Figure 4.12(a) and a 100 × 100 pixel subset is shown in Figure 4.12(b). The wind speed subset displayed in Figure 4.12(b) is significantly less grainy than the corresponding subset shown in Figure 4.11(b). This can be explained by the fact that in Option 2 we simultaneously average out the speckle noise and the noise introduced by the switching effect in the HH-HV model, while in Option 1 we reduce speckle effect only. Thus, Option 2 is better than Option 1 for wind speed mapping through the use of the HH-HV model.

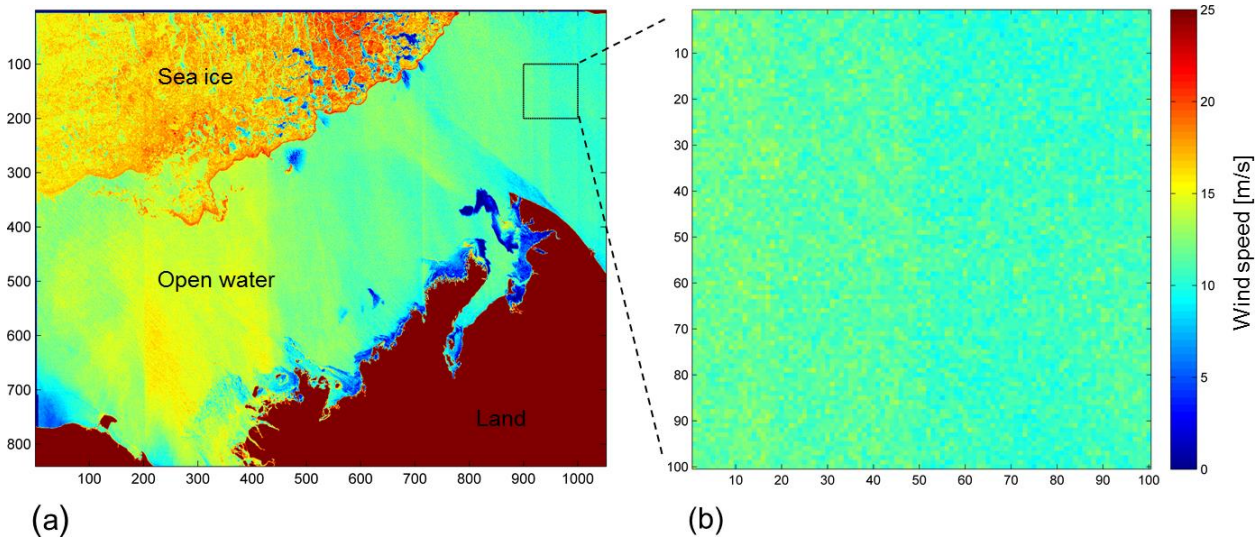


Figure 4.12. Wind speed mapping from a RADARSAT-2 ScanSAR HH-HV image through the following steps: (1) wind speed is derived from the calibrated 50-m resolution RADARSAT-2 ScanSAR HH-HV image; (2) the obtained 50-m resolution wind field is degraded to a 500-m resolution product. (a) 500-m resolution wind speed map; (b) 100×100 pixel subset from this wind field. Wind speed is valid only over the open water. The RADARSAT-2 image was acquired over the southern Beaufort Sea on October 10, 2009, at 15:35.

## 4.6. Wind Speed Mapping in the Marginal Ice Zone

Ocean surface wind speed distribution in the vicinity of sea ice is complex and is difficult to predict with NWP models. Therefore, wind speed retrieval without wind direction input is particularly important in the Arctic region where NWP models are not reliable. In this section we demonstrate how SAR wind retrieval can be beneficial for studying various processes in the MIZ given that winds substantially affect ice motion and ice concentration.

To illustrate different options for wind speed imaging, which are presented in Figure 4.11 and Figure 4.12, we employed a RADARSAT-2 image acquired on October 10, 2009 over the southern Beaufort Sea MIZ. It is worthwhile to note that the wind speed calculation is valid only

over the open water, while over the sea ice the colour is meaningless. At the same time, the sea ice motion field over the sea ice can be extracted if a supplemental sequential SAR image is available. We added an image taken on October 13, 2009, and derived ice displacements for the time period from October 10 to October 13, 2009, using our sea ice motion tracking algorithm presented in [11]. Thus, from RADARSAT-2 ScanSAR images, it is possible to extract wind speed over the open water and a sea ice motion vector field over the sea ice. An example of such an ice motion – wind speed product is shown in Figure 4.13.

Figure 4.13 shows that higher wind speeds (derived over the open water) cause higher sea ice velocities, whereas lower wind speeds correspond to shorter ice motion vectors. Furthermore, wind speeds in openings in sea ice (e.g., leads and cracks) are lower than over the ocean, due to the effect of wind shadowing by floes, described for example in [111]. This indicates that the developed tool is useful for studying various dynamic phenomena in the Arctic Ocean, such as the relationship between the wind speed, sea ice velocity and ice concentration in the Arctic Ocean MIZ. Moreover, SAR-derived wind speed and ice motion in the MIZ can provide reliable initial conditions for ice forecasting models. Data such as this will also find utility in studies of the exchange of CO2 across the ocean-sea ice-atmosphere (OSA) interface helping to determine the overall role of the MIZ as a source or sink for greenhouse gases [106].

Another example of merging ice motion and ocean surface wind speed in the MIZ, is shown in Figure 4.14. This case demonstrates ice dynamics under low wind speed conditions (< 6 m/s). An enlarged fragment in Figure 4.14 shows that two multi-year ice floes move in opposite directions. This is associated with the fact that, in the absence of strong and moderate wind, the main factors affecting ice motion are ocean currents and the Coriolis force [25]. Therefore, these floes might

move in different directions because they experience different oceanographic forcing [8]. Thus, the developed ice motion-wind speed tool can be useful in separating wind and oceanographic forcing in the MIZ. The enlarged fragment demonstrates that two multi-year ice floes move in opposite directions under low wind speed conditions.

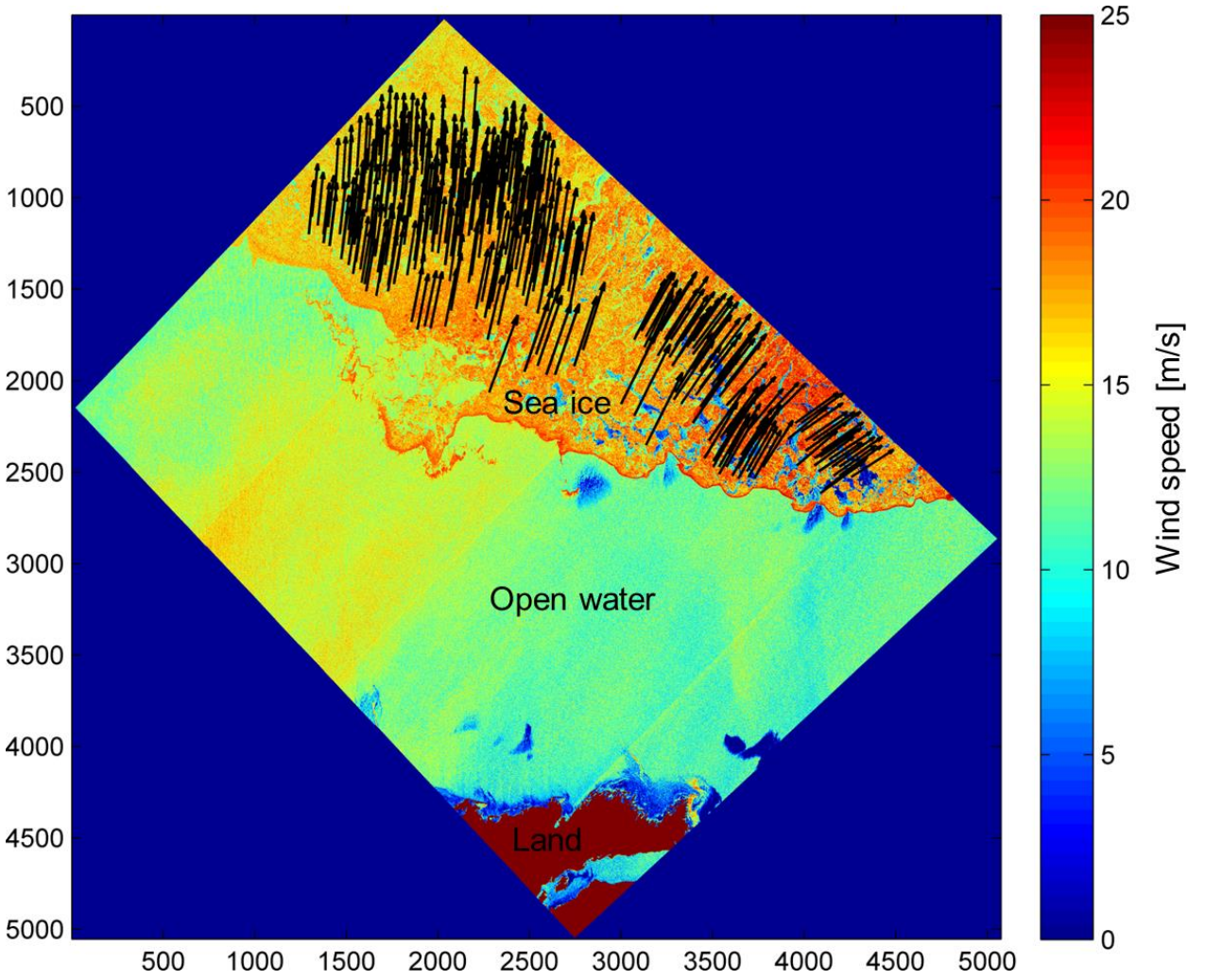


Figure 4.13. An example of ice motion – wind speed product. 1 pixel is 100 m. Sea ice motion is derived from two sequential RADARSAT-2 ScanSAR HH-HV images using the ice motion tracking algorithm proposed in [11]. The first image was acquired on October 10, 2009, at 15:35, and the second image was acquired on October 13, 2009, at 15:47. Each vector indicates the total displacement of ice for the three-day time interval. Wind speed is derived from the first SAR image using the HH-HV model (4.5), and is valid only over the open water.

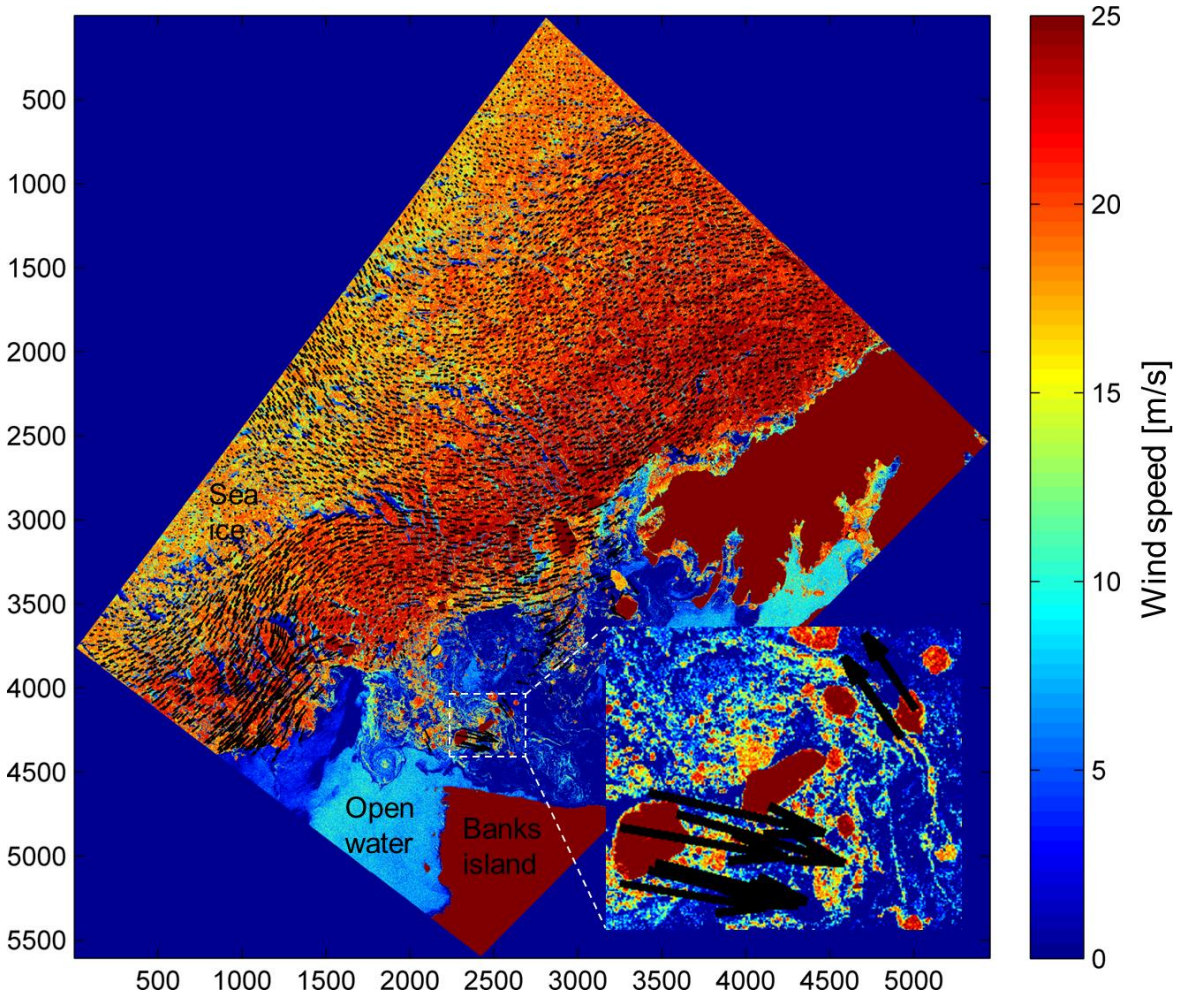


Figure 4.14. An example of ice motion – wind speed product. 1 pixel is 100 m. Sea ice motion is derived from two sequential RADARSAT-2 ScanSAR HH-HV images using the ice motion tracking algorithm proposed in [11]. The first image was acquired on September 28, 2010, at 15:37, and the second image was acquired on September 29, 2010, at 15:08. Each vector indicates the total displacement of ice for the three-day time interval. Wind speed is derived from the first SAR image using the HH-HV model (4.5), and is valid only over the open water.

## 4.7. Conclusion

In this study we pursued three main objectives: (1) to develop and validate a wind speed retrieval model free of input wind direction for RADARSAT-1 HH ScanSAR imagery; (2) to develop and validate a wind speed retrieval model free of input wind direction for RADARSAT-2 HH-HV ScanSAR imagery, and to evaluate different options for wind speed imaging; and (3) to explore how SAR wind speed retrieval without wind directions can be beneficial for studying various processes in the Arctic Ocean MIZ.

To address the first objective, we collected 755 coincided and collocated RADARSAT-1 HH measurements and buoy observations. This database was divided into training (500 samples) and testing subsets (255 samples). The independent variables of this regression model are HH NRCS and incidence angle. The developed HH model showed better performance (RMSE = 1.77 m/s) than the CMOD5.N (RMSE = 1.95 m/s) and CMOD_IFR2 (RMSE = 2.23 m/s) with the SAD approximation of the co-polarization ratio on the independent dataset (testing subset). This result indicates that the error coming from the SAD approximation is greater than the error resulting from the omission of wind direction in a regression model.

To address the second objective, we collected 248 coincided and collocated RADARSAT-2 HH-HV measurements and buoy observations. This database was divided into training (130 samples) and testing subsets (118 samples). The independent variables of this model are HH NRCS, HV NRCS, NESZ and incidence angle. The new cross-polarization variable ($\eta_{HV}$) in the regression model was introduced through the difference between the HV signal and the noise floor. The developed HH-HV model showed better performance (RMSE = 1.59 m/s) than the CMOD5.N (RMSE = 2.19 m/s) and CMOD_IFR2 (RMSE = 2.03 m/s) with the SAD approximation of the co-

polarization ratio on the independent dataset. The introduced cross-polarization variable compensates for the absence of the wind direction, which is required by CMOD-type models. For the HH-HV model, we considered two options of wind speed mapping, and we found that in practice it is preferable to compute a wind field as follows: (a) derive the wind speed from the calibrated 50-m resolution RADARSAT-2 ScanSAR HH-HV image; and (b) degrade the obtained 50-m resolution wind field to a 500-m resolution map. This approach averages out the speckle noise and the noise introduced by the switching process in the HH-HV model (4.5).

The developed algorithms do not require input of wind directions, and can be used in the areas where wind directions provided by an NWP model are not reliable (e.g., in the Arctic Ocean). The proposed models have been integrated into a quasi-operational system at the Meteorological Service of Canada.

As a final step of this study (third objective), we proposed the ice motion-wind speed product, which appears to be promising for studying various dynamic processes in the OSA system in the Arctic Ocean MIZ. More specifically, the proposed tool can be useful for: (a) studying the relationship between wind speed, ice velocity and ice concentration; (b) assimilation of wind speed and ice motion into sea ice forecasting models; (c) estimation of momentum and heat exchange across the OSA; and (d) separating wind and oceanographic forcing for detailed analysis of ice floes' motion.

# CHAPTER 5. ELECTROMAGNETIC WAVE SCATTERING FROM ROUGH BOUNDARIES INTERFACING INHOMOGENEOUS MEDIA AND APPLICATION TO SNOW-COVERED SEA ICE

**A. S. Komarov**, L. Shafai, and D. G. Barber, "Electromagnetic wave scattering from rough boundaries interfacing inhomogeneous media and application to snow-covered sea ice," *Progress in Electromagnetic Research,* vol. 144, pp. 201-219, 2014.

## 5.1. Introduction

Accelerated decline of the Arctic sea ice extent [1] and thickness [6], [97] causes dramatic changes in the coupled ocean-sea ice-atmosphere system. Over the past three decades the ice-albedo feedback mechanism played a major role in a pervasive increase in the amount of solar energy deposited in the upper Arctic Ocean, with maximum values of 4% per year [117]. Larger heat fluxes from the ocean to the atmosphere are expected to cause significant warming of the Arctic region [118]. Furthermore, extensive solar heating led to a sharp depletion of thick multiyear (MY) ice and concomitantly increased proportion of first-year (FY) ice. Monitoring, modeling and predicting these climatic changes in the Arctic is becoming increasingly important because of the increase in development of recently accessible Arctic resources.

Microwave radar remote sensing has been extensively used for detecting dynamic [11], [104] and thermodynamic changes [119] in sea ice. However, improved algorithms for extracting key parameters of sea ice from radar observations such as synthetic aperture radar (SAR) imagery are still required. To better understand the linkage between the geophysical and thermodynamic state of sea ice and radar signatures, modeling techniques for electromagnetic wave scattering from snow-covered sea ice are particularly important. These models should reproduce scattering

characteristics in the bistatic case (when transmitter and receiver antennas are spanned in space) to anticipate future bistatic spaceborne SAR systems [120].

In the literature various approaches to modeling of electromagnetic wave scattering from rough surfaces can be found.

Semi-empirical composite scattering models [80], [85], [121] allow to naturally account for volume scattering in sea ice (based on the radiative transfer theory [86]); however, the surface scattering terms in these models need to be separately determined from empirically or physically based theories.

All other models considered are based on solution of Maxwell's equations. They can be classified into numerical and analytical (wave theory) methods. Unlike the radiative transfer models, the physical models are able to provide phase information as well.

Numerical finite-difference time-domain (FDTD) [87], [88] and finite-volume time-domain (FVTD) [89] methods exactly solve Maxwell's equations, within numerical approximation. These methods can account for surface and subsurface roughness and an arbitrary behavior of the dielectric constant within the media. However, the time domain methods require significant computational resources due to a number of reasons. Among them are (a) numerous realizations of the random rough surface, and (b) extremely fine mesh in the situations where absorption is high (e.g. sea water under the ice). Unfortunately, the computational constrains make the numerical methods difficult to apply to practical remote sensing problems such as simulation of temporal changes in SAR signatures over the sea ice.

Analytical methods are aimed to derive a closed-form solution of Maxwell's equations under various approximations. These methods are not computationally expensive and thereby more

suitable for practical geophysical applications. The small perturbation method (SPM) was introduced by Rice [90] in 1951 to analytically describe wave scattering from slightly rough surfaces. Since then the SPM theory was extended to solving more complex scattering problems. In [92] an SPM solution for wave scattering from a rough surface embedded in a three-layered structure was derived. Scattering from a layered structure with a rough upper boundary was treated in [94]. In [93] a unified formulation of perturbative solutions derived by [92] and [94] was presented. Later the SPM solution was extended to scattering from two [95] and several rough interfaces [96] embedded in a layered medium. The recent study by [96] presents an SPM solution for the medium treated as a number of homogeneous discrete layers separated by rough interfaces. Meanwhile, most natural media (e.g. snow, ice, soil) have continuous profiles of dielectric constants and a few rough interfaces separating the inhomogeneous media. Therefore, it is important to consider the SPM formalism for wave scattering from rough surfaces interfacing continuous dielectric fillings between them.

Our main goal is to build a geoscience user-oriented SPM solution expressed through physically meaningful reflection and transmission coefficients associated with the continuously layered media (e.g. snow, ice, soil). These reflection and transmission coefficients could be either modelled through discretization of the layered media, in some cases found analytically, or measured directly (in the field or laboratory).

An important application of the SPM theory is modeling of microwave scattering from the FY snow-covered sea ice. This type of ice is anticipated to prevail in the Arctic Ocean in the near future [4]. In the frequency range between 0.5 GHz (P-band) and 10 GHz (X-band) the dominant scattering mechanism for the FY ice is often the surface scattering from two rough interfaces: air-

snow and snow-ice interfaces. Both interfaces are slightly rough in these frequency bands, and thereby, the SPM theory is applicable to model microwave interactions with snow-covered FY sea ice.

Thus, in this study we pursue three main objectives. (1) To derive a general analytical formulation for electromagnetic wave scattering from an arbitrary number of rough interfaces separating continuously layered media with the use of the first-order approximation of the SPM theory. The solution must be expressed through complex reflection and transmission coefficients associated with the inhomogeneous media. (2) To validate the obtained solution by treating special cases available in the literature and comparing numerical results with those available in the literature. (3) To present an analytical formulation for electromagnetic wave scattering from snow-covered sea ice as a special case of the general solution.

## 5.2. Statement of Scattering Problem

Geometry of the general scattering problem is displayed in Figure 5.1 in cylindrical coordinates $\{\boldsymbol{\rho}, z\}$. The area $z > 0$ is a free space with relative permittivity and permeability of one. Complex dielectric constant (CDC) and complex magnetic constant (CMC) of the inhomogeneous half space $z < 0$ are described by piecewise continuous functions through a set of continuous functions $\varepsilon_n(z)$, $\mu_n(z)$ such that their derivatives are continuous within layers $-d_n < z < -d_{n-1}$. The continuously inhomogeneous media are separated by $N$ rough interfaces located at $z = -d_n$, where $n = 0,1,2,...,N-1$, and $d_0 = 0$. Suppose, that roughness of interfaces is described by stationary random functions $\zeta_n(\boldsymbol{\rho})$ with zero average value $\langle \zeta_n(\boldsymbol{\rho}) \rangle = 0$, where the sharp

brackets $\langle ... \rangle$ denote ensemble averaging. A plane electromagnetic monochromatic wave with angular frequency $\omega$, harmonic time dependence $e^{-i\omega t}$ and an arbitrary polarization is incident upon this structure. The incidence angle is $0 \le \Theta_0 < \frac{\pi}{2}$ relative to the vertical axis $z$.

Our goal is to determine electromagnetic fields in far zone in the upper half-space and to calculate the normalized radar cross-sections (NRCS) $\sigma_{VV}$, $\sigma_{HH}$, $\sigma_{HV}$ and $\sigma_{VH}$ as functions of azimuth and elevation angles in the upper half-space $z > 0$. We assume that the formulated problem is considered within the validity range of the first-order approximation of the SPM theory.

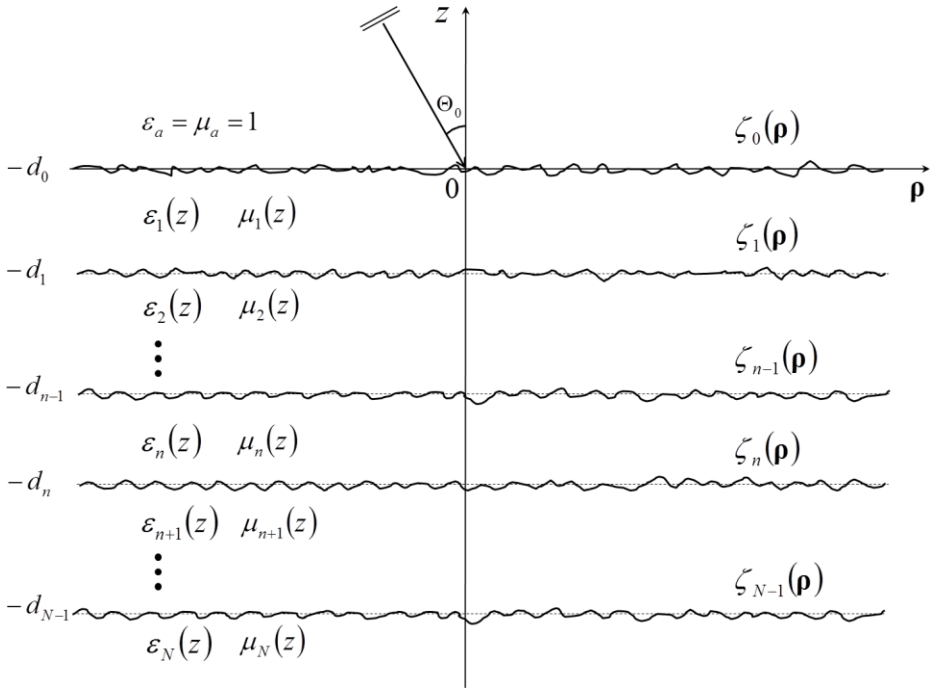


Figure 5.1. Illustration of a general problem for wave scattering from rough interfaces separating continuously layered media. Reproduced courtesy of the Electromagnetics Academy.

## 5.3. Derivation of Solution

First, we derive a formulation for a key scattering problem with a single rough interface $\zeta_n(\boldsymbol{\rho})$ located at $z=-d_n$, where $n=0,1,2,...,N-1$, and $d_0=0$. Then we generalize the obtained solution for an arbitrary number of rough boundaries. The SPM formalism applies to surfaces with a small surface height variation and small surface slopes with respect to the incident wavelength [91]:

$$kL_n<3,\quad k\sigma_n<0.3,\ \frac{\sigma_n}{L_n}<0.3, \tag{5.1}$$

where $k$ is the wave number in the medium, $L_n$ is the correlation length and $\sigma_n=\sqrt{\langle \zeta_n{}^2 \rangle}$ is the standard deviation of the rough surface $\zeta_n(\boldsymbol{\rho})$. Also, we assume that the gradient of the dielectric constant in the vicinity of the rough interface is small i.e. $\left|\frac{\varepsilon'(-d_n\pm 0)}{\varepsilon(-d_n\pm 0)}\right|\sigma_n << 1$. Following the first-order approximation of the SPM formalism the electric and magnetic fields are expanded in a perturbation series [48]-[50] as follows:

$$\begin{aligned}\mathbf{E}(\boldsymbol{\rho},z)&\approx\mathbf{E}^{(0)}(\boldsymbol{\rho},z)+\mathbf{E}^{(1)}(\boldsymbol{\rho},z)\\ \mathbf{H}(\boldsymbol{\rho},z)&\approx\mathbf{H}^{(0)}(\boldsymbol{\rho},z)+\mathbf{H}^{(1)}(\boldsymbol{\rho},z)\end{aligned}, \tag{5.2}$$

where $\mathbf{E}^{(0)}$, $\mathbf{H}^{(0)}$ are zero-order fields when the roughness is absent, and $\mathbf{E}^{(1)}$, $\mathbf{H}^{(1)}$ are first-order fields dependent on the roughness function [48]. The first-order fields represent a random component of the electromagnetic field due to the rough interface. Thus, the roughness influence is taken into account by a random additive component (first-order fields). To solve the scattering problem with only one rough interface at $z=-d_n$ zero-order and first-order fields must be defined in three regions: $z>0, -d_n<z<0$ and $z<-d_n$. Since we have the only rough interface at $z=-d_n$ we introduce the boundary conditions for zero-order and first-order fields at $z=0$ and $z=-d_n$ as follows.

Zero-order approximation:

At $z=0$:

$$\begin{aligned}\mathbf{E}_t^{(0)}(\boldsymbol{\rho},+0)-\mathbf{E}_t^{(0)}(\boldsymbol{\rho},-0)=0\\ \mathbf{H}_t^{(0)}(\boldsymbol{\rho},+0)-\mathbf{H}_t^{(0)}(\boldsymbol{\rho},-0)=0\end{aligned}. \tag{5.3}$$

At $z=-d_n$:

$$\begin{aligned}\mathbf{E}_t^{(0)}(\boldsymbol{\rho},-d_n+0)-\mathbf{E}_t^{(0)}(\boldsymbol{\rho},-d_n-0)=0\\ \mathbf{H}_t^{(0)}(\boldsymbol{\rho},-d_n+0)-\mathbf{H}_t^{(0)}(\boldsymbol{\rho},-d_n-0)=0\end{aligned}. \tag{5.4}$$

First-order approximation:

At $z=0$:

$$\begin{aligned}\mathbf{E}_t^{(1)}(\boldsymbol{\rho},+0)-\mathbf{E}_t^{(1)}(\boldsymbol{\rho},-0)=0\\ \mathbf{H}_t^{(1)}(\boldsymbol{\rho},+0)-\mathbf{H}_t^{(1)}(\boldsymbol{\rho},-0)=0\end{aligned}. \tag{5.5}$$

At the rough interface $z=-d_n$ [48]:

$$\begin{aligned}
&\mathbf{E}_t^{(1)}(\boldsymbol{\rho},-d_n+0)-\mathbf{E}_t^{(1)}(\boldsymbol{\rho},-d_n-0)=-\zeta_n(\boldsymbol{\rho})\left[\left(\frac{\partial \mathbf{E}_t^{(0)}}{\partial z}\right)_{z=-d_n+0}-\left(\frac{\partial \mathbf{E}_t^{(0)}}{\partial z}\right)_{z=-d_n-0}\right]\\
&-\nabla_\perp\zeta_n(\boldsymbol{\rho})\left[E_z^{(0)}(\boldsymbol{\rho},-d_n+0)-E_z^{(0)}(\boldsymbol{\rho},-d_n-0)\right]\\
&\mathbf{H}_t^{(1)}(\boldsymbol{\rho},-d_n+0)-\mathbf{H}_t^{(1)}(\boldsymbol{\rho},-d_n-0)=-\zeta_n(\boldsymbol{\rho})\left[\left(\frac{\partial \mathbf{H}_t^{(0)}}{\partial z}\right)_{z=-d_n+0}-\left(\frac{\partial \mathbf{H}_t^{(0)}}{\partial z}\right)_{z=-d_n-0}\right],\\
&-\nabla_\perp\zeta_n(\boldsymbol{\rho})\left[H_z^{(0)}(\boldsymbol{\rho},-d_n+0)-H_z^{(0)}(\boldsymbol{\rho},-d_n-0)\right]
\end{aligned} \tag{5.6}$$

where $\nabla_\perp$ is the gradient operator in the horizontal plane ($x-y$). Two sets of boundary conditions (5.3) (at $z=0$) and (5.4) (at $z=-d_n$) are introduced in order to express zero–order fields through reflection and transmission coefficients associated with the inhomogeneous slab $-d_n<z<0$ and the reflection coefficient from the half-space $z<-d_n$. Zero-order fields are required only to determine magnitudes of the first-order fields through boundary conditions (5.6).

Below we present formulations for zero-order and first-order fields.

### 5.3.1. Zero-Order Fields

The total zero-order fields do not contain scattering components, and they should satisfy regular boundary conditions (5.3) and (5.4) at smooth interfaces.

Electromagnetic fields in an arbitrary layered medium are described by one-dimensional wave equations (for horizontal and vertical polarizations) with nonconstant coefficients dependent on the vertical coordinate $z$. These differential equations could potentially be solved numerically with respect to the electromagnetic fields. At the same time, the general solution for fields in a finite

inhomogeneous layer can be expressed as a superposition of particular solutions of auxiliary Cauchy problems for a given wave equation. These solutions define the field distribution in the medium as well as magnitudes of reflected and transmitted waves at the interfaces.

1) Fields in the Air Half-Space $z \geq 0$

In the upper half-space zero-order fields are presented as a superposition of the incident and specularly reflected plane waves. In our problem it is convenient to represent magnitudes of electric $\mathbf{E}^{(0)}$ and magnetic $\mathbf{H}^{(0)}$ fields through an expansion over the basis vectors $\{\hat{\rho}, \hat{\varphi}, \hat{z}\}$ of the cylindrical coordinate system as our medium is homogeneous with respect to the azimuth angle and inhomogeneous with respect to the vertical coordinate only. This means that all the reflection and transmission coefficients do not depend on the azimuth angle. Also, the total field is symmetric relative to the azimuth incidence angle $\Phi_0$. The basis vectors $\{\hat{\rho}, \hat{\varphi}, \hat{z}\}$ of the cylindrical coordinate system are linked with the Cartesian unit vectors $\{\hat{x}, \hat{y}\}$ as follows:

$$\hat{\rho} = \hat{x}\cos\Phi_0 + \hat{y}\sin\Phi_0$$
$$\hat{\phi} = -\hat{x}\sin\Phi_0 + \hat{y}\cos\Phi_0 \ .$$

It is worthwhile to point out that we consider a general case $\Phi_0 \neq 0$ in order to take into account more complex problems. For example, for anisotropic rough surfaces it could be more convenient to choose the coordinate system associated with the principal direction of anisotropy (and not with the direction of wave propagation).

The zero-order fields in the upper half space can be expressed as follows:

$$\mathbf{E}^{(0)}(\boldsymbol{\rho},z)=\left\{E_H\left[e^{-iw_0(q_0)z}+\Re_H(q_0)e^{iw_0(q_0)z}\right]\hat{\phi}-E_V\frac{w_0(q_0)}{k_0}\left[e^{-iw_0(q_0)z}-\Re_V(q_0)e^{iw_0(q_0)z}\right]\hat{\rho}\right.$$
$$\left.-E_V\frac{q_0}{k_0}\left[e^{-iw_0(q_0)z}+\Re_V(q_0)e^{iw_0(q_0)z}\right]\hat{z}\right\}e^{i\mathbf{q_0}\boldsymbol{\rho}}, \qquad (5.7a)$$

$$\mathbf{H}^{(0)}(\boldsymbol{\rho},z)=\frac{1}{Z_0}\left\{E_V\left[e^{-iw_0(q_0)z}+\Re_V(q_0)e^{iw_0(q_0)z}\right]\hat{\phi}+E_H\frac{w_0(q_0)}{k_0}\left[e^{-iw_0(q_0)z}-\Re_H(q_0)e^{iw_0(q_0)z}\right]\hat{\rho}\right.$$
$$\left.+E_H\frac{q_0}{k_0}\left[e^{-iw_0(q_0)z}+\Re_H(q_0)e^{iw_0(q_0)z}\right]\hat{z}\right\}e^{i\mathbf{q_0}\boldsymbol{\rho}}. \qquad (5.7b)$$

In (5.7a) and (5.7b) $E_H$ and $E_V$ denote magnitudes of the electric field of the incident wave for horizontal and vertical polarizations respectively. $k_0=\omega\sqrt{\varepsilon_0\mu_0}$, and $Z_0=\sqrt{\mu_0/\varepsilon_0}$ are the wave number and impedance in free space respectively; $\boldsymbol{\rho}=x\hat{x}+y\hat{y}=\rho(\hat{x}\cos\varphi+\hat{y}\sin\varphi)$ is a position vector of an observation point in the horizontal plane, where $\varphi$ is an azimuth angle of the observation point. Also $\mathbf{q_0}=k_0\sin\Theta_0\left(\hat{x}\cos\Phi_0+\hat{y}\sin\Phi_0\right)=k_0\sin\Theta_0\hat{\rho}$ is the longitudinal wave vector which is a projection of the wave vector in the air onto the horizontal plane. The transverse wave number is a projection of the incident wave vector onto the axis $z$ which can be written as $w_0(q_0)=\sqrt{k_0^2-q_0^2}=k_0\cos\Theta_0$. $\Re_{H,V}(q_0)$ are reflection coefficients from the entire inhomogeneous structure $z\le 0$ for horizontal and vertical polarization with respect to electric and magnetic fields respectively. Solution (5.7a) and (5.7b) satisfy Maxwell's equations, boundary conditions at $z=0$ and the conditions at infinity.

2) Fields in the Inhomogeneous Medium $-d_n \le z \le 0$

In the inhomogeneous medium a closed-form analytical solution does not exist; however, the solution can be expressed through piecewise continuous functions $U_H(z)$ and $U_V(z)$ as follows:

$$\mathbf{E}^{(0)}(\boldsymbol{\rho}, z) = \left\{ U_H(z)\hat{\phi} + \frac{1}{ik_0\varepsilon(z)} U_V'(z)\hat{\rho} - \frac{q_0}{k_0\varepsilon(z)} U_V(z)\hat{z} \right\} e^{i\mathbf{q}_0\boldsymbol{\rho}}, \tag{5.8a}$$

$$\mathbf{H}^{(0)}(\boldsymbol{\rho}, z) = \frac{1}{Z_0}\left\{ U_V(z)\hat{\phi} - \frac{1}{ik_0\mu(z)} U_H'(z)\hat{\rho} + \frac{q_0}{k_0\mu(z)} U_H(z)\hat{z} \right\} e^{i\mathbf{q}_0\boldsymbol{\rho}}, \tag{5.8b}$$

where

$$U_{H,V}(z) = C_{1H,V} U_{1H,V}(z) + C_{2H,V} U_{2H,V}(z). \tag{5.9}$$

In equations (5.8a) and (5.8b) the stroke denotes a derivative with respect to $z$. In (5.9) $U_{1H}(z)$ and $U_{2H}(z)$ are particular solutions of one-dimensional wave equations for continuously layered media (given by equations (5.A1) and (5.A2) in Appendix 5.A). We accept that the introduced particular solutions satisfy the following initial conditions at the upper boundary $z = 0$:

$$U_{1H}(0) = 1,\ U_{1H}'(0) = 0,\ \ U_{2H}(0) = 0,\ \ U_{2H}'(0) = i\mu_1(0) w_0(q_0), \tag{5.10}$$

$$U_{1V}(0) = 1,\ U_{1V}'(0) = 0,\ \ U_{2V}(0) = 0,\ \ U_{2V}'(0) = i\varepsilon_1(0) w_0(q_0). \tag{5.11}$$

3) Fields in Half-Space $z \le -d_n$

In the lower half-space zero-order fields are given by:

$$\mathbf{E}^{(0)}(\boldsymbol{\rho}, z) = \left\{ V_H(z)\hat{\phi} + \frac{1}{ik_0\varepsilon(z)} V_V'(z)\hat{\rho} - \frac{q_0}{k_0\varepsilon(z)} V_V(z)\hat{z} \right\} e^{i\mathbf{q}_0\boldsymbol{\rho}}, \tag{5.12a}$$

$$\mathbf{H}^{(0)}(\boldsymbol{\rho}, z) = \frac{1}{Z_0}\left\{ V_V(z)\hat{\phi} - \frac{1}{ik_0\mu(z)} V_H'(z)\hat{\rho} + \frac{q_0}{k_0\mu(z)} V_H(z)\hat{z} \right\} e^{i\mathbf{q}_0\boldsymbol{\rho}}, \tag{5.12b}$$

where $V_H(z)$ and $V_V(z)$ are solutions of wave equations (5.A1) and (5.A2).

Plugging zero-order fields in boundary conditions (5.3) and (5.4) we obtain two systems of algebraic equations.

Horizontal polarization:

$$\left.\begin{aligned} C_{1H} &= E_H[1+\Re_H(q_0)] \\ C_{2H} &= -E_H[1-\Re_H(q_0)] \\ C_{1H}U_{1H}(-d_n) + C_{2H}U_{2H}(-d_n) &= V_H(-d_n) \\ C_{1H}U_{1H}'(-d_n) + C_{2H}U_{2H}'(-d_n) &= \frac{\mu_n(-d_n)}{\mu_{n+1}(-d_n)} V_H'(-d_n) \end{aligned}\right\}. \tag{5.13}$$

Vertical polarization:

$$\left.\begin{aligned} C_{1V} &= E_V[1+\Re_V(q_0)] \\ C_{2V} &= -E_V[1-\Re_V(q_0)] \\ C_{1V}U_{1V}(-d_n) + C_{2V}U_{2V}(-d_n) &= V_V(-d_n) \\ C_{1V}U_{1V}'(-d_n) + C_{2V}U_{2V}'(-d_n) &= \frac{\varepsilon_n(-d_n)}{\varepsilon_{n+1}(-d_n)} V_V'(-d_n) \end{aligned}\right\}. \tag{5.14}$$

Reflection coefficients $\Re_{H,V}(q_0)$ can be excluded from equations (5.13) and (5.14). Then using results of Appendices 5.A and 5.B, coefficients $C_{1H,V}$, $C_{2H,V}$ are derived as follows:

$$\begin{aligned} C_{1H,V} &= \frac{E_{H,V}}{iw_0(q_0)}\left[ik_0 M^n_{H,V}(q_0)U_{2H,V}(-d_n) + L^n_{H,V}(q_0)U'_{2H,V}(-d_n)\right] \\ C_{2H,V} &= -\frac{E_{H,V}}{iw_0(q_0)}\left[ik_0 M^n_{H,V}(q_0)U_{1H,V}(-d_n) + L^n_{H,V}(q_0)U'_{1H,V}(-d_n)\right] \end{aligned}, \qquad (5.15)$$

where:

$$L^n_{H,V}(q_0) = \frac{w_0(q_0)}{w_n(q_0)}\frac{T^n_{H,V}(q_0)}{1-r^n_{H,V}(q_0)R^n_{H,V}(q_0)}\left[1+r^n_{H,V}(q_0)\right], \qquad (5.16)$$

$$M^n_{H,V}(q_0) = \frac{w_0(q_0)}{k_0}\frac{T^n_{H,V}(q_0)}{1-r^n_{H,V}(q_0)R^n_{H,V}(q_0)}\left[1-r^n_{H,V}(q_0)\right]. \qquad (5.17)$$

In (5.16) and (5.17) $T^n_{H,V}(q_0)$ and $R^n_{H,V}(q_0)$ are transmission and reflection coefficients for a set of upper layers in the area $z > -d_n$, when the wave propagates from a homogeneous half-space $z < -d_n$ with CDC $\varepsilon_n(-d_n)$ and CMC $\mu_n(-d_n)$ for horizontal and vertical polarizations respectively. These transmission and reflection coefficients are derived in Appendix 5.A and given by (5.A11) and (5.A12).

In (5.16) and (5.17) $w_n(q_0) = \sqrt{k_0^2\varepsilon_n(-d_n)\mu_n(-d_n) - q_0^2}$, $\operatorname{Im} w_n \geq 0$; $r^n_{H,V}(q_0)$ are reflection coefficients in the problem where a plane wave is incident from a homogeneous area $z > -d_n$ with

CDC $\varepsilon_n(-d_n)$ and CMC $\mu_n(-d_n)$ upon the inhomogeneous half-space $z<-d_n$. To obtain (5.15) we also used relationships (5.B6) and (5.B7) between $V'_{H,V}(-d_n)$, $V_{H,V}(-d_n)$ and $r^n_{H,V}(q_0)$ derived in Appendix 5.B.

If the rough boundary is located on top of the inhomogeneous structure (i.e. $n=0$) then $T^0_{H,V}(q_0)=1$, $R^0_{H,V}(q_0)=0$, $r^0_{H,V}(q_0)=\Re_{H,V}(q_0)$. In this special case equations (5.16) and (5.17) can be reduced as follows:

$$L^0_{H,V}(q_0)=1+\Re_{H,V}(q_0), \tag{5.18}$$

$$M^0_{H,V}(q_0)=\frac{w_0(q_0)}{k_0}\left[1-\Re_{H,V}(q_0)\right]. \tag{5.19}$$

From (5.13) and (5.14) we note that $C_{1H,V}$ and $C_{2H,V}$ do not depend on the rough interface number $n$. Using expressions (5.15) for coefficients $C_{1,2H,V}$ in conjunction with equations for zero-order fields, the required expressions for boundary conditions (5.6) can be written as follows:

$$\begin{aligned}
&E_z^{(0)}(-d_n+0)-E_z^{(0)}(-d_n-0)=-\frac{\Delta\varepsilon_{n+1}q_0}{\varepsilon_{n+1}(-d_n)k_0}E_V L^n_V(q_0)e^{i\mathbf{q}_0\boldsymbol{\rho}}\\
&\left.\frac{\partial\mathbf{E}_t^{(0)}}{\partial z}\right|_{z=-d_n+0}-\left.\frac{\partial\mathbf{E}_t^{(0)}}{\partial z}\right|_{z=-d_n-0}=-ik_0\left[E_V\left(\Delta\mu_{n+1}\varepsilon_n(-d_n)+\frac{\Delta\varepsilon_{n+1}}{\varepsilon_{n+1}(-d_n)}\frac{q_0^2}{k_0^2}\right)L^n_V(q_0)\hat{\rho}-\Delta\mu_{n+1}E_H M^n_H(q_0)\hat{\phi}\right]e^{i\mathbf{q}_0\boldsymbol{\rho}}
\end{aligned} \tag{5.20}$$

$$\begin{aligned}
&H_z^{(0)}(-d_n+0)-H_z^{(0)}(-d_n-0)=\frac{1}{Z_0}\frac{\Delta\mu_{n+1}q_0}{\mu_{n+1}(-d_n)k_0}E_H L^n_H(q_0)e^{i\mathbf{q}_0\boldsymbol{\rho}}\\
&\left.\frac{\partial\mathbf{H}_t^{(0)}}{\partial z}\right|_{z=-d_n+0}-\left.\frac{\partial\mathbf{H}_t^{(0)}}{\partial z}\right|_{z=-d_n-0}=\frac{ik_0}{Z_0}\left[E_H\left(\Delta\varepsilon_{n+1}\mu_n(-d_n)+\frac{\Delta\mu_{n+1}}{\mu_{n+1}(-d_n)}\frac{q_0^2}{k_0^2}\right)L^n_H(q_0)\hat{\rho}+\Delta\varepsilon_{n+1}E_V M^n_V(q_0)\hat{\phi}\right]e^{i\mathbf{q}_0\boldsymbol{\rho}}.
\end{aligned} \tag{5.21}$$

In these expressions we introduced dielectric and magnetic contrasts at the boundary $z = -d_n$ as $\Delta\varepsilon_{n+1} = \varepsilon_{n+1}(-d_n) - \varepsilon_n(-d_n)$ and $\Delta\mu_{n+1} = \mu_{n+1}(-d_n) - \mu_n(-d_n)$ respectively. To derive (5.20) and (5.21) we found Wronskians of the particular solutions at $z = -d_n$ given by (5.C4) and (5.C5) in Appendix 5.C.

5.3.2. First-Order Fields in Integral Form

First-order approximation defines scattered fields by a rough surface. The scattered field is random and can be treated as a superposition of infinite number of plane waves outgoing in different directions from the rough interface. Therefore, it is convenient to represent the first-order fields through the Fourier integral. A Fourier transform of the rough surface is introduced as follows:

$$\tilde{\zeta}_n(\boldsymbol{\xi} - \mathbf{q}_0) = \iint \zeta_n(\boldsymbol{\rho}') e^{-i(\boldsymbol{\xi} - \mathbf{q}_0)\boldsymbol{\rho}'} d\boldsymbol{\rho}' . \tag{5.22}$$

The magnitudes of spectral functions can be found through boundary conditions for the first-order approximation. Below we provide integral representations of the first-order fields in three media.

1) Fields in the Air Half-Space $z \geq 0$

In the upper half-space the first-order fields from the $n$th rough boundary can be written as follows:

$$\mathbf{E}^{(1)}(\boldsymbol{\rho},z)=\frac{1}{(2\pi)^2}\iint\left\{a_H^n(\boldsymbol{\xi})\hat{\psi}+\frac{w_0(\xi)}{k_0}a_V^n(\boldsymbol{\xi})\hat{\xi}-\frac{\xi}{k_0}a_V^n(\boldsymbol{\xi})\hat{z}\right\}\tilde{\zeta}_n(\boldsymbol{\xi}-\mathbf{q_0})e^{iw_0(\xi)z+i\boldsymbol{\xi}\boldsymbol{\rho}}d\boldsymbol{\xi}\,, \tag{5.23a}$$

$$\mathbf{H}^{(1)}(\boldsymbol{\rho},z)=\frac{1}{Z_0(2\pi)^2}\iint\left\{a_V^n(\boldsymbol{\xi})\hat{\psi}-\frac{w_0(\xi)}{k_0}a_H^n(\boldsymbol{\xi})\hat{\xi}+\frac{\xi}{k_0}a_H^n(\boldsymbol{\xi})\hat{z}\right\}\tilde{\zeta}_n(\boldsymbol{\xi}-\mathbf{q_0})e^{iw_0(\xi)z+i\boldsymbol{\xi}\boldsymbol{\rho}}d\boldsymbol{\xi}\,. \tag{5.23b}$$

where $a_{H,V}^n(\boldsymbol{\xi})$ are magnitudes of the scattered field. The functions under the integral sign are represented as expansions over a basis in the cylindrical coordinate system $\{\xi,\psi,z\}$ in the wave numbers' space. $\hat{\psi}$ and $\hat{\xi}$ are the azimuth and radial unit vectors associated with the floating coordinate system in the wave numbers' space. In (5.23) $d\boldsymbol{\xi}=\xi d\xi d\psi$ and the vertical component of the wave number of partial plane waves in free space is given by $w_0(\xi)=\sqrt{k_0^2-\xi^2}$, $\operatorname{Im}w_0(\xi)\geq 0$.

2) Fields in the Medium $-d_n\leq z\leq 0$

In the inhomogeneous medium the first-order fields can be given by:

$$\mathbf{E}^{(1)}(\boldsymbol{\rho},z)=\frac{1}{(2\pi)^2}\iint\left\{u_H(\boldsymbol{\xi},z)\hat{\psi}+\frac{1}{ik_0\varepsilon(z)}u_V'(\boldsymbol{\xi},z)\hat{\xi}-\frac{\xi}{k_0\varepsilon(z)}u_V(\boldsymbol{\xi},z)\hat{z}\right\}\tilde{\zeta}_n(\boldsymbol{\xi}-\mathbf{q}_0)e^{i\boldsymbol{\xi}\boldsymbol{\rho}}d\boldsymbol{\xi}\,, \tag{5.24a}$$

$$\mathbf{H}^{(1)}(\boldsymbol{\rho},z)=\frac{1}{Z_0(2\pi)^2}\iint\left\{u_V(\boldsymbol{\xi},z)\hat{\psi}-\frac{1}{ik_0\mu(z)}u_H'(\boldsymbol{\xi},z)\hat{\xi}+\frac{\xi}{k_0\mu(z)}u_H(\boldsymbol{\xi},z)\hat{z}\right\}\tilde{\zeta}_n(\boldsymbol{\xi}-\mathbf{q}_0)e^{i\boldsymbol{\xi}\boldsymbol{\rho}}d\boldsymbol{\xi}\,, \tag{5.24b}$$

where

$$u_{H,V}(\boldsymbol{\xi},z)=c^{n}_{1H,V}(\boldsymbol{\xi})u_{1H,V}(\xi,z)+c^{n}_{2H,V}(\boldsymbol{\xi})u_{2H,V}(\xi,z)\,. \tag{5.25}$$

In (5.25) $u_{1,2H}(\xi,z)$ and $u_{1,2V}(\xi,z)$ are particular solutions of the wave equations given by (5.A1) and (5.A2) except that the longitudinal wave number $q_0$ is replaced by $\xi$.

We accept that the introduced particular solutions satisfy the following initial conditions at the upper boundary $z=0$:

$$u_{1H}(\xi,0)=1,\ u'_{1H}(\xi,0)=0,\ u_{2H}(\xi,0)=0,\ u'_{2H}(\xi,0)=i\mu_1(0)w_0(\xi), \tag{5.26}$$

$$u_{1V}(\xi,0)=1,\ u'_{1V}(\xi,0)=0,\ u_{2V}(\xi,0)=0,\ u'_{2V}(\xi,0)=i\varepsilon_1(0)w_0(\xi)\,. \tag{5.27}$$

3) Fields in the Half-Space $z\le -d_n$

In the lower half-space the first-order fields can be represented as follows:

$$\mathbf{E}^{(1)}(\boldsymbol{\rho},z)=\frac{1}{(2\pi)^2}\iint\left\{v_H(\boldsymbol{\xi},z)\hat{\psi}+\frac{1}{ik_0\varepsilon(z)}v'_V(\boldsymbol{\xi},z)\hat{\xi}-\frac{\xi}{k_0\varepsilon(z)}v_V(\boldsymbol{\xi},z)\hat{z}\right\}\tilde{\zeta}_n(\boldsymbol{\xi}-\mathbf{q}_0)e^{i\boldsymbol{\xi}\cdot\boldsymbol{\rho}}d\boldsymbol{\xi}, \tag{5.28a}$$

$$\mathbf{H}^{(1)}(\boldsymbol{\rho},z)=\frac{1}{Z_0(2\pi)^2}\iint\left\{v_V(\boldsymbol{\xi},z)\hat{\psi}-\frac{1}{ik_0\mu(z)}v'_H(\boldsymbol{\xi},z)\hat{\xi}+\frac{\xi}{k_0\mu(z)}v_H(\boldsymbol{\xi},z)\hat{z}\right\}\tilde{\zeta}_n(\boldsymbol{\xi}-\mathbf{q}_0)e^{i\boldsymbol{\xi}\cdot\boldsymbol{\rho}}d\boldsymbol{\xi}, \tag{5.28b}$$

where $v_{H,V}(\boldsymbol{\xi},z)$ are solutions of wave equations (5.A1) and (5.A2) with the replacement of $q_0$ by $\xi$.

5.3.3. Spectral Magnitudes of the Scattered Field from the Rough Surface

Substituting the first-order fields into the boundary conditions (5.5) at the smooth interface $z = 0$ and taking into account (5.26) and (5.27), we obtain the following:

$$c^n_{1H,V}(\xi) = c^n_{2H,V}(\xi) = a^n_{H,V}(\xi). \tag{5.29}$$

Then plugging the first-order fields in boundary conditions (5.6) accounting for equations (5.20) and (5.21), and applying the Fourier transform to both sides of the obtained pair of equations we derive the following:

$$\begin{aligned}&\left[u_H(\xi,-d_n) - v_H(\xi,-d_n)\right]\hat{\psi} + \frac{1}{ik_0}\left[\frac{u'_V(\xi,-d_n)}{\varepsilon_n(-d_n)} - \frac{v'_V(\xi,-d_n)}{\varepsilon_{n+1}(-d_n)}\right]\hat{\xi} = \\ &= -ik_0\Delta\mu_{n+1}\left[-E_V\varepsilon_n(-d_n)L^n_V(q_0)\hat{\rho} + E_H M^n_H(q_0)\hat{\phi}\right] + i\Delta\varepsilon_{n+1}E_V\xi\frac{q_0 L^n_V(q_0)}{k_0\varepsilon_{n+1}(-d_n)}\hat{\xi}\end{aligned}, \tag{5.30}$$

$$\begin{aligned}&\left[u_V(\xi,-d_n) - v_V(\xi,-d_n)\right]\hat{\psi} - \frac{1}{ik_0}\left[\frac{u'_H(\xi,-d_n)}{\mu_n(-d_n)} - \frac{v'_H(\xi,-d_n)}{\mu_{n+1}(-d_n)}\right]\hat{\xi} = \\ &= -ik_0\Delta\varepsilon_{n+1}\left[E_H\mu_n(-d_n)L^n_H(q_0)\hat{\rho} - E_V M^n_V(q_0)\hat{\phi}\right] - i\Delta\mu_{n+1}E_H\xi\frac{q_0 L^n_H(q_0)}{k_0\mu_{n+1}(-d_n)}\hat{\xi}\end{aligned}. \tag{5.31}$$

Multiplying both sides of these equations by unit vectors $\hat{\psi}$ and $\hat{\xi}$, and taking into account (5.29), we obtain:

$$\left.\begin{aligned} &a_H^n(\xi)[u_{1H}(\xi,-d_n)+u_{2H}(\xi,-d_n)]-v_H(\xi,-d_n)= \\ &=-ik_0\Delta\mu_{n+1}\left[E_V\varepsilon_n L_V^n(q_0)\sin(\psi-\Phi_0)+E_H M_H^n(q_0)\cos(\psi-\Phi_0)\right] \\ &a_H^n(\xi)\frac{\mu_{n+1}(-d_n)}{\mu_n(-d_n)}\left[u'_{1H}(\xi,-d_n)+u'_{2H}(\xi,-d_n)\right]-v'_H(\xi,-d_n)= \\ &=-k_0^2\Delta\varepsilon_{n+1}\mu_{n+1}(-d_n)\left[E_H\mu_n L_H^n(q_0)\cos(\psi-\Phi_0)+E_V M_V^n(q_0)\sin(\psi-\Phi_0)\right]-\Delta\mu_{n+1}E_H\xi q_0 L_H^n(q_0) \end{aligned}\right\}, \quad (5.32)$$

$$\left.\begin{aligned} &a_V^n(\xi)[u_{1V}(\xi,-d_n)+u_{2V}(\xi,-d_n)]-v_V(\xi,-d_n)= \\ &=ik_0\Delta\varepsilon_{n+1}\left[E_H\mu_n L_H^n(q_0)\sin(\psi-\Phi_0)-E_V M_V^n(q_0)\cos(\psi-\Phi_0)\right] \\ &a_V^n(\xi)\frac{\varepsilon_{n+1}(-d_n)}{\varepsilon_n(-d_n)}\left[u'_{1V}(\xi,-d_n)+u'_{2V}(\xi,-d_n)\right]-v'_V(\xi,-d_n)= \\ &=-k_0^2\Delta\mu_{n+1}\varepsilon_{n+1}(-d_n)\left[E_V\varepsilon_n L_V^n(q_0)\cos(\psi-\Phi_0)-E_H M_H^n(q_0)\sin(\psi-\Phi_0)\right]-\Delta\varepsilon_{n+1}E_V\xi q_0 L_V^n(q_0) \end{aligned}\right\}. \quad (5.33)$$

Systems of equations (5.32) and (5.33) can be resolved with respect to spectral magnitudes $a_{H,V}^n(\xi)$ of the scattered field in the air. Similar to zero-order approximation (Appendices 5.A and 5.B) we introduced coefficients $L_{H,V}^n(\xi)$, $M_{H,V}^n(\xi)$. Then, the following relationships for the magnitudes $a_{H,V}^n(\xi)$ in the air can be derived:

$$a_H^n(\xi)=\frac{E_H\mu_n(-d_n)k_0^2}{2iw_0(\xi)}\left[-\Delta\varepsilon_{n+1}\mu_n(-d_n)L_H^n(q_0)L_H^n(\xi)\cos(\psi-\Phi_0)-\frac{\Delta\mu_{n+1}\xi q_0}{\mu_{n+1}(-d_n)k_0^2}L_H^n(q_0)L_H^n(\xi)+\frac{\Delta\mu_{n+1}}{\mu_n(-d_n)}M_H^n(q_0)M_H^n(\xi)\cos(\psi-\Phi_0)\right], \quad (5.34)$$
$$-\frac{E_V\mu_n(-d_n)k_0^2}{2iw_0(\xi)}\left[\Delta\varepsilon_{n+1}M_V^n(q_0)L_H^n(\xi)-\frac{\Delta\mu_{n+1}\varepsilon_n(-d_n)}{\mu_n(-d_n)}L_V^n(q_0)M_H^n(\xi)\right]\sin(\psi-\Phi_0)$$

$$a_V^n(\xi)=-\frac{E_V\varepsilon_n(-d_n)k_0^2}{2iw_0(\xi)}\left[\Delta\mu_{n+1}\varepsilon_n(-d_n)L_V^n(q_0)L_V^n(\xi)\cos(\psi-\Phi_0)+\frac{\Delta\varepsilon_{n+1}\xi q_0}{\varepsilon_{n+1}(-d_n)k_0^2}L_V^n(q_0)L_V^n(\xi)-\frac{\Delta\varepsilon_{n+1}}{\varepsilon_n(-d_n)}M_V^n(q_0)M_V^n(\xi)\cos(\psi-\Phi_0)\right]. \quad (5.35)$$
$$+\frac{E_H\varepsilon_n(-d_n)k_0^2}{2iw_0(\xi)}\left[\Delta\mu_{n+1}M_H^n(q_0)L_V^n(\xi)-\frac{\Delta\varepsilon_{n+1}\mu_n(-d_n)}{\varepsilon_n(-d_n)}L_H^n(q_0)M_V^n(\xi)\right]\sin(\psi-\Phi_0)$$

### 5.3.4. Normalized Radar Cross-Sections

First-order fields in far zone are estimated using the method of stationary phase [74]. Then, radar cross-sections are calculated through the Poynting vector of electromagnetic field in far zone. We

omit details of this part and present the derived radar cross-sections for co- and cross-polarized components at the observation point $(\theta,\varphi)$:

$$\sigma^n_{\alpha\beta}(\theta,\varphi)=\frac{k_0^4}{4\pi}\,|\,a^n_{\alpha\beta}(\theta,\varphi)\,|^2\;\tilde{K}_n(\mathbf{q}-\mathbf{q}_0)\,, \tag{5.36}$$

where subscripts $\alpha=H,V$ and $\beta=H,V$ denote polarizations of the incident ($\alpha$) and the scattered ($\beta$) waves respectively. In (5.36) we have:

$$a^n_{HH}(\theta,\varphi)=\frac{2w_0(q)}{k_0^2E_H}\,a^n_H(\mathbf{q})\Big|_{E_V=0} \qquad a^n_{VV}(\theta,\varphi)=\frac{2w_0(q)}{k_0^2E_V}\,a^n_V(\mathbf{q})\Big|_{E_H=0}\,, \tag{5.37}$$

$$a^n_{HV}(\theta,\varphi)=\frac{2w_0(q)}{k_0^2E_H}\,a^n_V(\mathbf{q})\Big|_{E_V=0} \qquad a^n_{VH}(\theta,\varphi)=\frac{2w_0(q)}{k_0^2E_V}\,a^n_H(\mathbf{q})\Big|_{E_H=0}\,. \tag{5.38}$$

Also, $\mathbf{q}=k_0\sin\theta\big(\hat{x}\cos\varphi+\hat{y}\sin\varphi\big)$; $\tilde{K}_n(\mathbf{q}-\mathbf{q}_0)$ is the spatial power spectral density of the roughness linked with the autocorrelation function $K_n(\boldsymbol{\rho})=\big\langle\zeta_n(\boldsymbol{\rho}+\boldsymbol{\rho}')\zeta_n(\boldsymbol{\rho}')\big\rangle$ at interface $z=-d_n$ as follows:

$$\tilde{K}_n(\mathbf{q}-\mathbf{q_0})=\iint K_n(\boldsymbol{\rho})e^{-i(\mathbf{q}-\mathbf{q_0})\boldsymbol{\rho}}d\boldsymbol{\rho}\,. \tag{5.39}$$

Magnitudes of the scattered field in the direction of observation $(\theta,\varphi)$ are the following:

$$a_{HH}^{n}(\theta,\varphi)=i\left[\Delta\varepsilon_{n+1}\mu_{n}^{2}(-d_{n})L_{H}^{n}(q_{0})L_{H}^{n}(q)\cos(\varphi-\Phi_{0})+\Delta\mu_{n+1}\frac{\mu_{n}(-d_{n})qq_{0}}{\mu_{n+1}(-d_{n})k_{0}^{2}}L_{H}^{n}(q_{0})L_{H}^{n}(q)-\Delta\mu_{n+1}M_{H}^{n}(q_{0})M_{H}^{n}(q)\cos(\varphi-\Phi_{0})\right], \quad (5.40)$$

$$a_{VV}^{n}(\theta,\varphi)=i\left[\Delta\mu_{n+1}\varepsilon_{n}^{2}(-d_{n})L_{V}^{n}(q_{0})L_{V}^{n}(q)\cos(\varphi-\Phi_{0})+\Delta\varepsilon_{n+1}\frac{\varepsilon_{n}(-d_{n})qq_{0}}{\varepsilon_{n+1}(-d_{n})k_{0}^{2}}L_{V}^{n}(q_{0})L_{V}^{n}(q)-\Delta\varepsilon_{n+1}M_{V}^{n}(q_{0})M_{V}^{n}(q)\cos(\varphi-\Phi_{0})\right], \quad (5.41)$$

$$a_{HV}^{n}(\theta,\varphi)=-i\left[\Delta\mu_{n+1}\varepsilon_{n}(-d_{n})M_{H}^{n}(q_{0})L_{V}^{n}(q)-\Delta\varepsilon_{n+1}\mu_{n}(-d_{n})L_{H}^{n}(q_{0})M_{V}^{n}(q)\right]\sin(\varphi-\Phi_{0}), \quad (5.42)$$

$$a_{VH}^{n}(\theta,\varphi)=i\left[\Delta\varepsilon_{n+1}\mu_{n}(-d_{n})M_{V}^{n}(q_{0})L_{H}^{n}(q)-\Delta\mu_{n+1}\varepsilon_{n}(-d_{n})L_{V}^{n}(q_{0})M_{H}^{n}(q)\right]\sin(\varphi-\Phi_{0}). \quad (5.43)$$

Thus, the general formulations for NRCS of the initial problem displayed in Figure 5.1 can be written as follows:

$$\sigma_{\alpha\beta}(\theta,\varphi)=\frac{k_{0}^{4}}{4\pi}\sum_{n=0}^{N-1}\left\{|\,a_{\alpha\beta}^{n}(\theta,\varphi)\,|^{2}\;\tilde{K}_{n}(\mathbf{q}-\mathbf{q}_{0})+\sum_{m\neq n}\mathrm{Re}\left[a_{\alpha\beta}^{m}(\theta,\varphi)a_{\alpha\beta}^{n*}(\theta,\varphi)\right]\tilde{K}_{mn}(\mathbf{q}-\mathbf{q}_{0})\right\}, \quad (5.44)$$

where the asterisk denotes the complex conjugate and the cross power spectral density between interfaces $m$ and $n$ is defined as follows:

$$\tilde{K}_{mn}(\mathbf{q}-\mathbf{q_{0}})=\iint K_{mn}(\boldsymbol{\rho})e^{-i(\mathbf{q}-\mathbf{q_{0}})\boldsymbol{\rho}}d\boldsymbol{\rho}, \quad (5.45)$$

In the last equation the cross-correlation function between interfaces $m$ and $n$ $K_{mn}(\boldsymbol{\rho})=\langle\zeta_{m}(\boldsymbol{\rho}+\boldsymbol{\rho}')\zeta_{n}(\boldsymbol{\rho}')\rangle$.

If all rough surfaces are statistically independent, then the second term in equation (5.44) disappears and the total radar cross-section is a sum of radar cross-sections from each of the rough interfaces:

$$\sigma_{\alpha\beta}(\theta,\varphi)=\sum_{n=0}^{N-1}\sigma_{\alpha\beta}^{n}(\theta,\varphi). \tag{5.46}$$

It is worthwhile to note that for grazing elevation angles the accuracy of the SPM theory becomes lower. At grazing elevation angles the shadowing effects (which are negligible at other angles) start dominating [91]. These phenomena are not taken into account by the SPM theory. In the literature there are attempts to introduce additional factors accounting for the shadowing effects in the second-order approximation of the SPM theory for the cross-polarized signal [91]. In general, it is assumed that the SPM theory is valid within the range from 20 to 80 degrees of incidence and observation elevation angles. At the elevation angles close to nadir the mirror reflection appears. We would like to note that elevation angles of currently operational radar systems fall within the range of validity of the SPM theory. For example, incidence angles of Canadian RADARSAT-2 vary from 20 to 60 degrees [9].

### 5.3.5. Monostatic Scattering

In the monostatic case the receiver elevation and azimuth angles are $\theta=\Theta_0$ and $\varphi=\pi+\Phi_0$ respectively. Therefore, general equations from the previous section can be reduced to the following:

$$\sigma_{\alpha\alpha}^{0}=\frac{k_0^4}{4\pi}\sum_{n=0}^{N-1}\left\{|\,a_{\alpha\alpha}^{n0}\,|^2\;\tilde{K}_n(-2\mathbf{q}_0)+\sum_{m\neq n}\mathrm{Re}\left[a_{\alpha\alpha}^{m0}a_{\alpha\alpha}^{n0*}\right]\tilde{K}_{mn}(-2\mathbf{q}_0)\right\},\ \alpha=H,V \tag{5.47}$$

where

$$a_{HH}^{n0} = i\left[\Delta\mu_{n+1}\frac{\mu_n(-d_n)q_0^2}{\mu_{n+1}(-d_n)k_0^2}\left[L_H^n(q_0)\right]^2 + \Delta\mu_{n+1}\left[M_H^n(q_0)\right]^2 - \Delta\varepsilon_{n+1}\mu_n^2(-d_n)\left[L_H^n(q_0)\right]^2\right], \tag{5.48}$$

$$a_{VV}^{n0} = i\left[\Delta\varepsilon_{n+1}\frac{\varepsilon_n(-d_n)q_0^2}{\varepsilon_{n+1}(-d_n)k_0^2}\left[L_V^n(q_0)\right]^2 + \Delta\varepsilon_{n+1}\left[M_V^n(q_0)\right]^2 - \Delta\mu_{n+1}\varepsilon_n^2(-d_n)\left[L_V^n(q_0)\right]^2\right]. \tag{5.49}$$

The cross-polarization components of the fist-order solution for the monostatic case are zeros. However, we expect that the second-order solution would provide a non-zero result for backscatter coefficients. The derivation of such a second-order solution for wave scattering from a homogeneous rough half-space is presented in [122]. Derivation of the second-order solution for wave scattering from rough boundaries interfacing inhomogeneous media is an important topic of future research.

## 5.4. Validation of Solution

In this section we consider three special cases of the derived general solution. In all cases the permeability of all media is one. The obtained scattering characteristics for these cases are evaluated and compared with formulations available in the literature. Furthermore, we calculate bistatic scattering coefficients for a three-layered structure and compare the results with those available in the literature.

### 5.4.1. Scattering from a Rough Surface on Top of Homogeneous Half-Space

In the simplest case the wave is scattered by a rough surface $\zeta(\boldsymbol{\rho})$ on top of a homogeneous medium with CDC $\varepsilon_1$. Then $L_{H,V}^0(q_0) = 1 + \Re_{H,V}^0(q_0)$, $M_{H,V}^0(q_0) = \cos\Theta_0\left(1 - \Re_{H,V}^0(q_0)\right)$, where

$\Re^0_{H,V}(q_0)$ are ordinary Fresnel reflection coefficients from a homogeneous half-space with CDC $\varepsilon_1$ [123]:

$$\Re^0_H(q_0) = \frac{\cos\Theta_0 - \sqrt{\varepsilon_1 - \sin^2\Theta_0}}{\cos\Theta_0 + \sqrt{\varepsilon_1 - \sin^2\Theta_0}}, \tag{5.50}$$

$$\Re^0_V(q_0) = \frac{\varepsilon_1\cos\Theta_0 - \sqrt{\varepsilon_1 - \sin^2\Theta_0}}{\varepsilon_1\cos\Theta_0 + \sqrt{\varepsilon_1 - \sin^2\Theta_0}}. \tag{5.51}$$

It is not difficult to demonstrate that our general formulations for backscatter coefficients (5.47) - (5.49) are reduced to the following:

$$\sigma^0_{HH} = \frac{4k_0^4}{\pi}\left|\frac{\varepsilon_1 - 1}{\left[\cos\Theta_0 + \sqrt{\varepsilon_1 - \sin^2\Theta_0}\right]^2}\right|^2 \tilde{K}(-2\mathbf{q_0})\cos^4\Theta_0, \tag{5.52}$$

$$\sigma^0_{VV} = \frac{4k_0^4}{\pi}\left|(\varepsilon_1 - 1)\frac{(\varepsilon_1 - 1)\sin^2\Theta_0 + \varepsilon_1}{\left[\varepsilon_1\cos\Theta_0 + \sqrt{\varepsilon_1 - \sin^2\Theta_0}\right]^2}\right|^2 \tilde{K}(-2\mathbf{q_0})\cos^4\Theta_0, \tag{5.53}$$

where $\tilde{K}$ is the spatial power spectral density of the rough surface. The obtained results are identical to those presented among other sources in [49], [91], [121].

5.4.2. Scattering from a Rough Surface Embedded in a Three-Layered Structure

Consider wave scattering from a rough interface embedded in a three layered medium displayed in Figure 5.2. The original solution of this problem was derived by Yarovoy et al. in [92], and an alternative formulation in terms of reflection and transmission coefficients was proposed in [93]. In this case each medium is homogeneous i.e.:

$$\varepsilon_1(z)=\varepsilon_1,\ -d_1<z<0,\ \varepsilon_2(z)=\varepsilon_2,\ -d_2<z<-d_1,\ \varepsilon_3(z)=\varepsilon_3,\ z<-d_2,$$

and in equations (5.16), (5.17) $n=1$. Also it is possible to show that:

$$T_H^1(q_0)=\frac{w_1(q_0)}{w_0(q_0)}\tau_{01H}(q_0)e^{iw_1(q_0)d_1},\ \ T_V^1(q_0)=\frac{w_1(q_0)}{\varepsilon_1 w_0(q_0)}\tau_{01V}(q_0)e^{iw_1(q_0)d_1},$$

$$R_{H,V}^1(q_0)=-r_{01H,V}(q_0)e^{2iw_1(q_0)d_1}.$$

Here $w_1(q_0)=k_0\sqrt{\varepsilon_1-\sin^2\Theta_0}$, $\tau_{01H,V}(q_0)$ and $r_{01H,V}(q_0)$ are Fresnel transmission and reflection coefficients for the interface between air and medium 1 when wave is incident from the air. $r_{H,V}(q_0)\equiv r_{H,V}^1(q_0)$ are reflection coefficients from the two-layered structure (medium 2 and medium 3). Substituting equations (5.16) and (5.17) taken for $n=1$ into our general formulations for backscatter coefficients (5.47) - (5.49) we obtain:

$$\sigma_{HH}^0=\frac{k_0^4}{4\pi}\left|(\varepsilon_2-\varepsilon_1)\left(\frac{\tau_{01H}(q_0)e^{iw_1(q_0)d_1}}{1+r_H(q_0)r_{01H}(q_0)e^{2iw_1(q_0)d_1}}\right)^2[1+r_H(q_0)]^2\right|^2\tilde{K}(-2\mathbf{q_0}),\qquad(5.54)$$

$$\sigma_{VV}^{0} = \frac{k_0^4}{4\pi}\left|\frac{\varepsilon_2-\varepsilon_1}{\varepsilon_1}\left(\frac{\tau_{01V}(q_0)e^{iw_1(q_0)d_1}}{1+r_V(q_0)r_{01V}(q_0)e^{2iw_1(q_0)d_1}}\right)^2\left\{\frac{\sin^2\Theta_0}{\varepsilon_2}\left[1+r_V(q_0)\right]^2+\frac{\varepsilon_1-\sin^2\Theta_0}{\varepsilon_1}\left[1-r_V(q_0)\right]^2\right\}\right|^2 \tilde{K}(-2\mathbf{q_0}), \quad (5.55)$$

where $\tilde{K}$ is the spatial power spectral density of the rough surface. These formulations are identical to those presented in [93] for Yarovoy model [92].

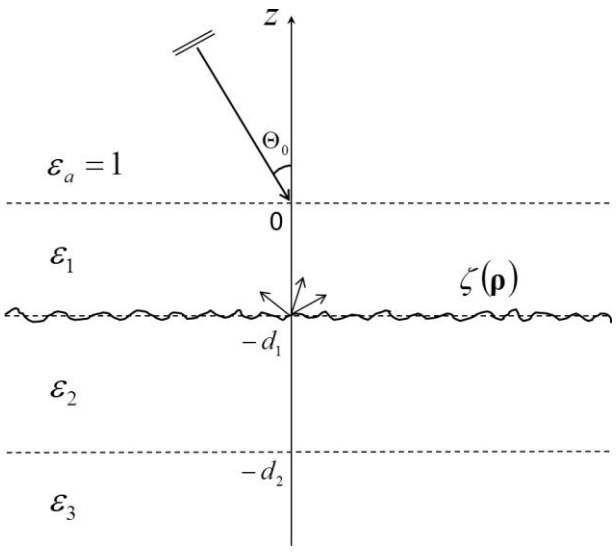


Figure 5.2. Geometry of scattering from a rough surface embedded in a three-layered medium. Reproduced courtesy of the Electromagnetics Academy.

5.4.3. Scattering from a Rough Surface Embedded in a Discretely Layered Medium

Consider a more general case when an electromagnetic wave is scattered by a rough surface embedded in a discretely layered medium shown in Figure 5.3.

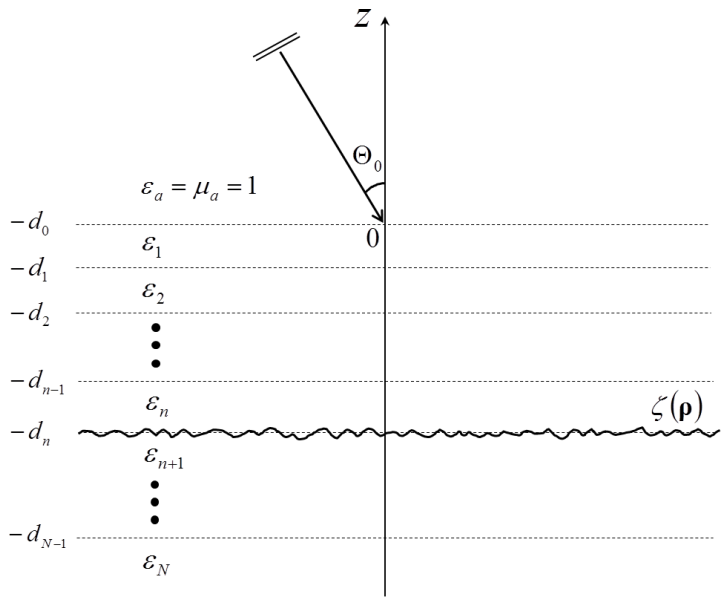


Figure 5.3. Geometry of scattering from a rough surface embedded in a layered medium. Reproduced courtesy of the Electromagnetics Academy.

Taking into account the phase change of the wave in layer $n$ we obtain:

$$L^n_{H,V}(q) = \frac{w_0(q)}{w_n(q)} \frac{T^{n-1}_{H,V}(q) e^{iw_n(q)\Delta_n}}{1 - r^n_{H,V}(q) R^{n-1}_{H,V}(q) e^{2iw_n(q)\Delta_n}} \left[1 + r^n_{H,V}(q)\right], \tag{5.56}$$

$$M^n_{H,V}(q) = \frac{w_0(q)}{k_0} \frac{T^{n-1}_{H,V}(q) e^{iw_n(q)\Delta_n}}{1 - r^n_{H,V}(q) R^{n-1}_{H,V}(q) e^{2iw_n(q)\Delta_n}} \left[1 - r^n_{H,V}(q)\right], \tag{5.57}$$

where $\Delta_n = d_n - d_{n-1}$ is the layer thickness over the rough surface; $T^{n-1}_{H,V}(q)$ are transmission coefficients through the upper $(n-1)$ layers when the wave is incident from the half-space with CDC $\varepsilon_n$; $R^{n-1}_{H,V}(q)$ are reflection coefficients from the upper $(n-1)$ layers when the wave is

incident from the half-space with CDC $\varepsilon_n$; $r^n_{H,V}(q)$ are reflection coefficients from the lower half-space when the wave is incident from the half-space with CDC $\varepsilon_n$.

Given (5.56), (5.57), our general solution (5.40) - (5.44) can be reduced to the formulations presented by Imperatore et al. in [96]. At the same time, our solution is more general and elegant than the solution obtained by [96]. Unlike [96] we do not discretize the medium to derive the solution. Instead, we use properties of particular solutions of wave equations in the continuously layered media. Our solution is expressed through physically meaningful reflection and transmission coefficients for inhomogeneous media.

### 5.4.4. Numerical Results for a Three-Layered Structure

To further validate our model we calculate bistatic scattering coefficients for a special case illustrated in Figure 5.4. To compare the numerical results with the literature data we chose exactly the same scattering geometry and parameters of the media as considered in [96]. All the three rough interfaces have the same root mean square (RMS) height and correlation length. Each rough surface is described by the Gaussian autocorrelation function. The spectrum of this function is given as follows:

$$\tilde{\tilde{K}}_m(\mathbf{q}-\mathbf{q_0}) = \tilde{\tilde{K}}_m(|\mathbf{q}-\mathbf{q_0}|) = \pi L_m^2 \sigma_m^2 \exp\left(-\frac{L_m^2|\mathbf{q}-\mathbf{q_0}|^2}{4}\right), \tag{5.58}$$

where $\sigma_m$, $L_m$ are RMS height and correlation length of the rough interface $m = 0,1,2$.

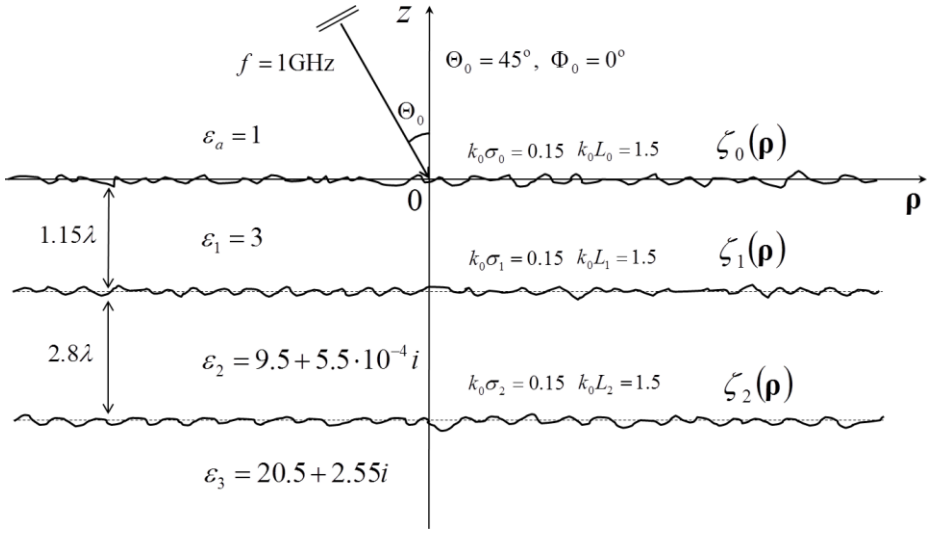


Figure 5.4. Three layered scattering geometry of the validation problem. Reproduced courtesy of the Electromagnetics Academy.

The incident elevation and azimuth angles were chosen to be $\Theta_0 = 45^\circ$ and $\Phi_0 = 0^\circ$ respectively. The observation azimuth angle is $\varphi = 45^\circ$ while the observation elevation angle has been varied. Figure 5.5 demonstrates numerically calculated bistatic scattering coefficients for all polarizations (HH, VH, HV, and VV) from each rough boundary and from the whole structure (as a sum). In order to compare our outputs with the results presented in literature we digitized 120 data points from Figure 4 of [96] and transferred them to our graphs. From Figure 5.5 one may observe a very good agreement between our numerical results and data from [96] for all polarizations. A small disparity can be attributed to the error coming from digitizing the low resolution graphs taken directly from the digital version of [96].

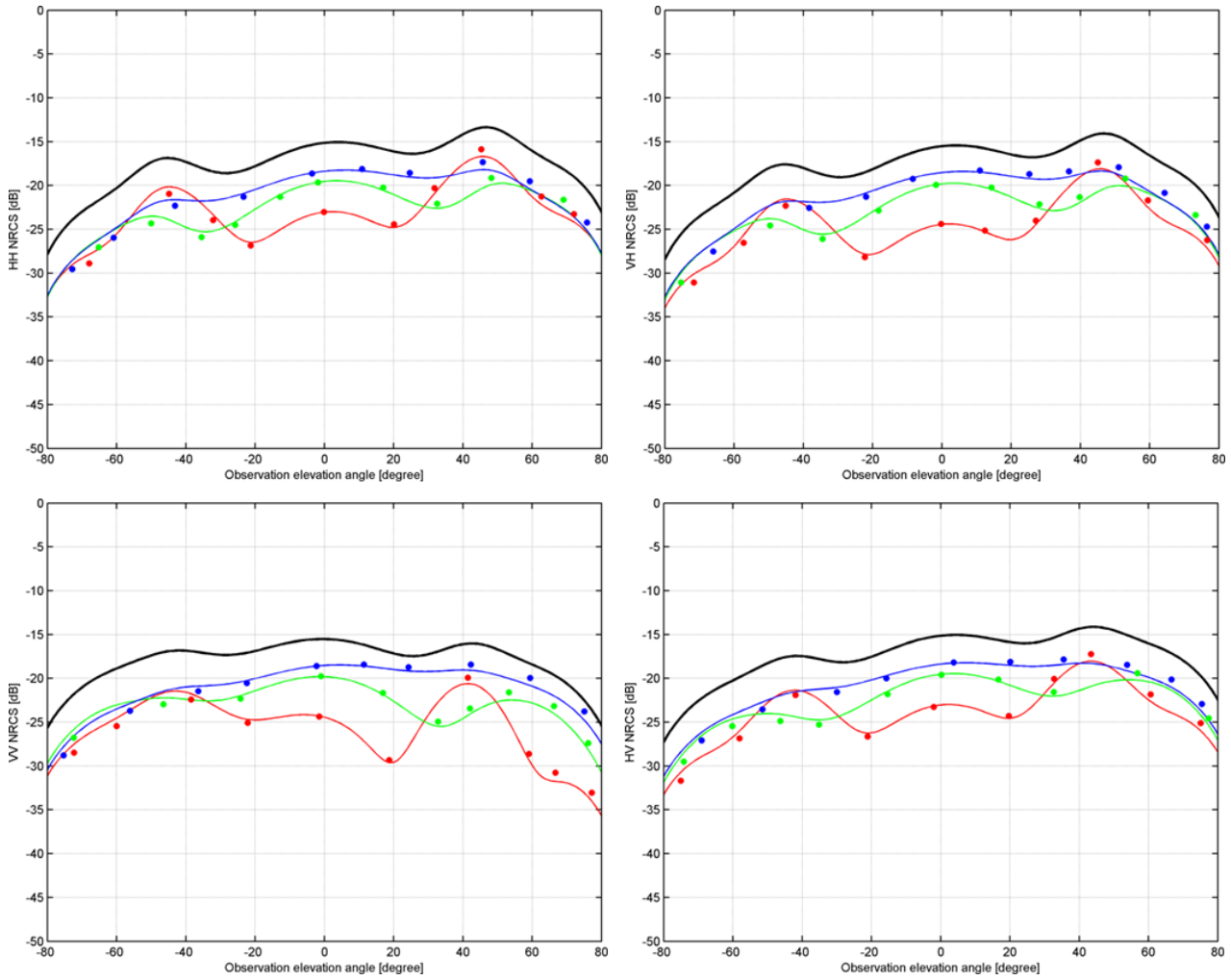


Figure 5.5. Comparison of numerical results computed according to our model (solid lines) against the (digitized) data presented in [96] (dots) for the geometry shown in Figure 5.4. Red: scattering from the upper boundary; green: scattering from the middle boundary; blue: scattering from the bottom boundary; black: total scattering. Reproduced courtesy of the Electromagnetics Academy.

## 5.5. Electromagnetic Wave Scattering by Snow-Covered Sea Ice

Electromagnetic wave scattering by snow-covered sea ice is an important special case of the general problem being considered. A plane electromagnetic wave is scattered by snow-covered sea

ice. Snow and sea ice are characterized as continuous or discrete layered media. CDC of snow and sea ice are known functions $\varepsilon_s(z)$ and $\varepsilon_i(z)$ of vertical coordinate $z$ as displayed in Figure 5.6.

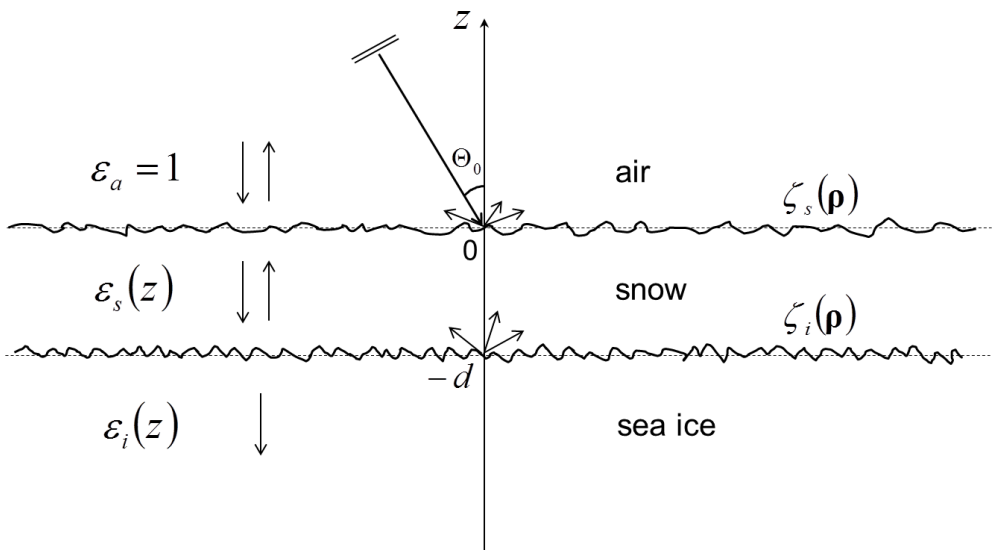


Figure 5.6. Wave scattering from sea ice covered by snow. Reproduced courtesy of the Electromagnetics Academy.

The roughness of the air-snow and snow-ice interfaces are described by stationary random functions $\zeta_s(\boldsymbol{\rho})$ and $\zeta_i(\boldsymbol{\rho})$ which define deviations from planes $z = 0$ and $z = -d$ respectively; $d$ is the snow thickness. The dominant scattering mechanism in this problem is the surface scattering at the air-snow and snow-ice interfaces.

The obtained general solution (5.40) - (5.44) can be reduced to the snow-covered sea ice case by setting the number of rough interfaces to two and permeability of all media to one. Thus, the scattering component from rough sea ice can be written as follows:

$$\sigma_{HH}^{ice}(\theta,\varphi)=\frac{k_0^4\left|\Delta\varepsilon_i\right|^2}{4\pi}\left|L_H(q_0)L_H(q)\right|^2\cos^2(\varphi-\Phi_0)\,\tilde{K}_i(\mathbf{q}-\mathbf{q_0}), \tag{5.59}$$

$$\sigma_{VV}^{ice}(\theta,\varphi)=\frac{k_0^4\left|\Delta\varepsilon_i\right|^2}{4\pi}\left|\frac{\varepsilon_s(-d)}{\varepsilon_i(-d)}\sin\Theta_0\sin\theta\,L_V(q_0)L_V(q)-M_V(q_0)M_V(q)\cos(\varphi-\Phi_0)\right|^2\tilde{K}_i(\mathbf{q}-\mathbf{q_0}), \tag{5.60}$$

$$\sigma_{HV}^{ice}(\theta,\varphi)=\frac{k_0^4\left|\Delta\varepsilon_i\right|^2}{4\pi}\left|L_H(q_0)M_V(q)\right|^2\sin^2(\varphi-\Phi_0)\tilde{K}_i(\mathbf{q}-\mathbf{q_0}), \tag{5.61}$$

$$\sigma_{VH}^{ice}(\theta,\varphi)=\frac{k_0^4\left|\Delta\varepsilon_i\right|^2}{4\pi}\left|L_H(q)M_V(q_0)\right|^2\sin^2(\varphi-\Phi_0)\tilde{K}_i(\mathbf{q}-\mathbf{q_0}), \tag{5.62}$$

where

$$L_{H,V}(q)=\frac{w_0(q)}{w_s(q)}\frac{T_{sH,V}(q)}{1-r_{iH,V}(q)R_{sH,V}(q)}\left[1+r_{iH,V}(q)\right], \tag{5.63}$$

$$M_{H,V}(q)=\frac{w_0(q)}{k_0}\frac{T_{sH,V}(q)}{1-r_{iH,V}(q)R_{sH,V}(q)}\left[1-r_{iH,V}(q)\right]. \tag{5.64}$$

In (5.59) – (5.62) $\Delta\varepsilon_i=\varepsilon_i(-d)-\varepsilon_s(-d)$ is the dielectric contrast between ice and snow at the rough interface. $\tilde{K}_i$ is the spatial power spectral density of the ice-snow surface. In (5.63) - (5.64) $w_s(q)=\sqrt{k_0^2\varepsilon_s(-d)-q^2}$, $w_0(q)=\sqrt{k_0^2-q^2}$; $T_{sH,V}$ and $R_{sH,V}$ are transmission and reflection coefficients for the inhomogeneous snow layer when the wave is incident from the half-space with CDC $\varepsilon_s(-d)$; $r_{iH,V}$ are reflection coefficients from the inhomogeneous sea ice when the wave is incident from the half-space with CDC $\varepsilon_s(-d)$.

The scattering components from the rough snow can be written as follows:

$$\sigma_{HH}^{snow}(\theta,\varphi)=\frac{k_0^4\left|\Delta\varepsilon_s\right|^2}{4\pi}\left|[1+\Re_H(q_0)][1+\Re_H(q)]\right|^2\cos^2(\varphi-\Phi_0)\tilde{K}_s(\mathbf{q}-\mathbf{q_0}), \tag{5.65}$$

$$\sigma_{VV}^{snow}(\theta,\varphi)=\frac{k_0^4\left|\Delta\varepsilon_s\right|^2}{4\pi}$$
$$\times\left|\frac{\sin\Theta_0\sin\theta}{\varepsilon_s(0)}[1+\Re_V(q_0)][1+\Re_V(q)]-[1-\Re_V(q_0)][1-\Re_V(q)]\cos(\varphi-\Phi_0)\cos\Theta_0\cos\theta\right|^2\tilde{K}_s(\mathbf{q}-\mathbf{q_0}) \tag{5.66}$$

$$\sigma_{HV}^{snow}(\theta,\varphi)=\frac{k_0^4\left|\Delta\varepsilon_s\right|^2}{4\pi}\left|[1+\Re_H(q_0)][1-\Re_V(q)]\sin(\varphi-\Phi_0)\cos\theta\right|^2\tilde{K}_s(\mathbf{q}-\mathbf{q_0}), \tag{5.67}$$

$$\sigma_{VH}^{snow}(\theta,\varphi)=\frac{k_0^4\left|\Delta\varepsilon_s\right|^2}{4\pi}\left|[1-\Re_V(q_0)][1+\Re_H(q)]\sin(\varphi-\Phi_0)\cos\Theta_0\right|^2\tilde{K}_s(\mathbf{q}-\mathbf{q_0}). \tag{5.68}$$

In (5.65) - (5.68) $\Delta\varepsilon_s=\varepsilon_s(0)-1$ is the dielectric contrast at the air-snow interface; $\tilde{K}_s$ is the spatial power spectral density of the snow surface; $\Re_{H,V}$ are reflection coefficients from the entire snow-covered sea ice structure at horizontal and vertical polarizations.

If the air-snow and snow-ice interfaces are statistically independent then the total NRCS is a sum of NRCS from the snow and sea ice:

$$\sigma_{\alpha\beta}(\theta,\varphi)=\sigma_{\alpha\beta}^{ice}(\theta,\varphi)+\sigma_{\alpha\beta}^{snow}(\theta,\varphi). \tag{5.69}$$

The last equation is a special case of the more general equation (5.44) for two rough interfaces i.e. $N = 2$. If the rough interfaces are correlated then according to (5.44) an additional correlation term should be introduced.

In the monostatic scattering case $\theta = \Theta_0$, $\varphi = \pi + \Phi_0$ and the cross-polarization component is zero. Therefore, the radar backscatter coefficients from sea ice can be presented as follows:

$$\sigma_{HH}^{0ice} = \frac{k_0^4 |\Delta\varepsilon_i|^2}{4\pi} |L_H(q_0)|^4 \tilde{K}_i(-2\mathbf{q_0}), \tag{5.70}$$

$$\sigma_{VV}^{0ice} = \frac{k_0^4 |\Delta\varepsilon_i|^2}{4\pi} \left| \frac{\varepsilon_s(-d)}{\varepsilon_i(-d)} \sin^2\Theta_0 L_V^2(q_0) + M_V^2(q_0) \right|^2 \tilde{K}_i(-2\mathbf{q_0}), \tag{5.71}$$

$$\sigma_{HV}^{0ice} = \sigma_{VH}^{0ice} = 0. \tag{5.72}$$

The radar backscatter coefficients from the rough snow surface can be written as follows:

$$\sigma_{HH}^{0snow} = \frac{k_0^4 |\Delta\varepsilon_s|^2}{4\pi} |[1 + \Re_H(q_0)]|^4 \tilde{K}_s(-2\mathbf{q_0}), \tag{5.73}$$

$$\sigma_{VV}^{0snow} = \frac{k_0^4 |\Delta\varepsilon_s|^2}{4\pi} \left| \frac{\sin^2\Theta_0}{\varepsilon_s(0)} [1 + \Re_V(q_0)]^2 + [1 - \Re_V(q_0)]^2 \cos^2\Theta_0 \right|^2 \tilde{K}_s(-2\mathbf{q_0}), \tag{5.74}$$

$$\sigma_{HV}^{0snow} = \sigma_{VH}^{0snow} = 0. \tag{5.75}$$

The total radar backscatter from snow-covered sea ice is a sum of the backscatter coefficients from snow and sea ice similar to (5.69) (if the rough interfaces are statistically independent).

Modeling of dielectric properties of snow-covered sea ice (as a function of depth) is a separate problem which will be discussed in more details in our future publication on numerical modeling and measurements of scattering characteristics from real snow-covered sea ice. Here we briefly describe how the CDC of snow and sea ice can be found as functions of the vertical coordinate.

Snow on sea ice is a mixture of pure ice, air and brine (wicked from the sea ice surface). CDC of brine in snow is estimated as a function of temperature using Stogryn and Desargant model [81]. CDC of pure ice is nearly a constant (~3.15) in a wide range of frequencies [80]. The brine volume content in snow can be found through sea ice surface temperature and salinity (according to [83]) as well as snow density (which is a function of depth). We use physical properties of snow and sea ice from our field campaigns in the Arctic Ocean. There are a few dielectric models for estimating the CDC of moist snow (such as [82], [124]). However, a reliable dielectric mixture model for estimating the CDC of brine wetted snow on top of sea ice has not been developed. At the same time it has been shown that the refractive mixture model (which is linear with respect to refractive indices) is effective for sea ice [76]. In addition, the refractive mixture model has been proven to be the most accurate for wet soils [125]. Using this mixture model with input physical parameters measured in the field we obtain the CDC of snow as a function of depth.

The CDC of sea ice is calculated using the refractive mixture model for an isotropic two-phase medium consisting of pure ice and brine inclusions. In the study by [76] it was found that the refractive dielectric mixture model agrees very well with the dielectric measurements of sea ice reported in [77]. The brine volume of sea ice can be estimated as a function of ice temperature and bulk salinity according to [78]. The CDC of brine in sea ice can be found through the Debye relaxation model with temperature dependent parameters empirically derived by [81]. In the field

campaigns we usually conduct measurements of temperature and bulk salinity as functions of sea ice depth (see e.g. [119]). Therefore, the CDC of sea ice is also derived as a function of depth.

We note that, if necessary, the sea water below the ice and the rough ice-water interface can be naturally included in the obtained formulation, but this is not the usual case as the penetration depth in natural FY sea ice is on the order of the wavelength (e.g. 5.5 cm in C-band and 21 cm in L-band) while FY ice grows to about 2 m thick by winters end. At the same time, if we model scattering characteristics from newly formed sea ice (with no snow cover) with the thickness around 10-20 cm then the sea water half-space below the ice must be introduced. In this case the CDC of sea water can be found using the Debye-based model by Stogryn [126].

## 5.6. Conclusion

In this study we presented a new analytical formulation for electromagnetic wave scattering from an arbitrary number of rough surfaces interfacing continuously layered media and derived a solution for wave scattering from snow-covered sea ice as a special case of the general problem. We solved Maxwell's equations within the first-order approximation of the SPM theory. First, we derived a solution for wave scattering from a single rough boundary while the other rough interfaces are absent. A key step in this solution is the introduction of two auxiliary problems on wave propagation in inhomogeneous media. In the first problem a plane wave is incident upon a piecewise continuously layered medium located above the rough interface from a medium with an arbitrary CDC $\varepsilon_\delta$ and CMC $\mu_\delta$. This problem allowed to link the reflection and transmission coefficients for the layered slab with the wave equations' particular solutions and their normal derivatives at the bottom of this slab. In the second problem a plane wave is incident upon a

piecewise continuously layered medium located below the rough surface from the same medium as in the first problem (CDC $\varepsilon_\delta$ and CMC $\mu_\delta$). In this problem reflection coefficients from this medium are linked with the wave equations' particular solutions and their normal derivatives at the mean level of the rough interface. The results obtained in these two problems in conjunction with the boundary conditions allowed us to derive necessary equations for zero-order fields and their normal derivatives at the mean level of the rough interface. According to the SPM theory, these equations for zero-order fields are substituted into the boundary conditions for first-order fields. The first-order fields are represented through the Fourier integral over the partial plane waves outgoing from the rough surface. The under integral functions are written analogously to the first-order fields using particular solutions of the wave equations. Similarly to the zero-order case we found a link between the particular solutions of wave equations at the rough interface with reflection and transmission coefficients. Boundary conditions for the first-order fields enabled to resolve magnitudes of the scattered fields in the air. Finally, the radar characteristics are derived through the analytical evaluation of the Fourier integrals in far zone.

In our formulation we avoided any discretization of the continuously layered media; instead, we introduced particular solutions of wave equations and associated with them reflection and transmission coefficients at the rough interface. Such an approach makes our solution compact and physically meaningful. For example, the symmetry of the bi-static solution with respect to transmitting and receiving points is straightforward. The solution obtained for a single rough interface is naturally expanded to an arbitrary number of rough boundaries interfacing continuously layered media.

To validate the derived general solution we considered three special cases of the scattering problem. We demonstrated that our solution can be reduced to the formulations available in the literature including the most recent solution [96]. Furthermore we showed that our numerical results for wave scattering from a three-layered structure well agree with those presented in [96].

We would like to point out that our formulation has been expressed through physically meaningful reflection and transmission coefficients associated with continuously layered media. To numerically implement the model, these coefficients must be estimated separately. For example, they can be computed using the following approaches: (1) invariant embedding method (where the inhomogeneous media are discretized) [127], (2) Runge Kutta method directly applied to one-dimensional wave equations (with non-constant coefficients), (3) analytical exact or analytical approximate approaches (applied in some cases) to solving the differential wave equations with non-constant coefficients. In practice, we use the invariant embedding approach [127].

The novelty of our model can be outlined as follows:

1. The obtained formulation is user-oriented and convenient for practical geophysical remote sensing applications. Our solution operates with physically meaningful reflection and transmission coefficients associated with certain geophysical media (e.g. snow, ice, soil, etc.).
2. Our solution is fairly flexible because the numerical implementation can be split into two separate algorithmic units: (a) estimation of the reflection and transmission coefficients for inhomogeneous media using the approach that is best suited to a given structure of the inhomogeneous media; (b) calculation of scattering characteristics by plugging in these coefficients in the general solution.

3. If the complex reflection and transmission coefficients (for layered media) can be directly measured in the field (using, for example, a portable vector network analyzer), then the obtained values (at a given frequency) can be plugged in our model. In this case step (a) from the previous point is not required.
4. It appears that our analytical formulation is the only solution for wave scattering from layered media where both the complex dielectric and complex magnetic constants are continuous functions of depth.
5. Mathematical derivation and final formulation of our model is quite compact and at the same time general and physically meaningful compared to the previous solutions.

As the final step of this study, we presented an important special case of our formulation for wave scattering from snow-covered sea ice where both air-snow and snow-ice interfaces are rough and snow and ice are continuously layered media. The developed theory could be beneficial for the interpretation of sequential SAR signatures over snow-covered sea ice and inverse modeling. Beyond polar applications, the obtained theoretical formulation could be useful in remote sensing of various environmental media (e.g. snow-covered soil).

In our ongoing work we are currently validating this theory against in-situ C-band scatterometer measurements collected over natural snow-covered sea ice in the Canadian Arctic.

# Appendix 5.A. Reflection Coefficients from Inhomogeneous Slab

A plane wave with horizontal (or vertical) polarization with magnitude $A_H$ (or $A_V$) propagates from the half-space $z \le -d_n$ with $\varepsilon_\delta, \mu_\delta$ and transmits through the inhomogeneous layer $-d_n \le z \le 0$ with CDC $\varepsilon(z)$ and CMC $\mu(z)$ as shown in Figure 5.A1.

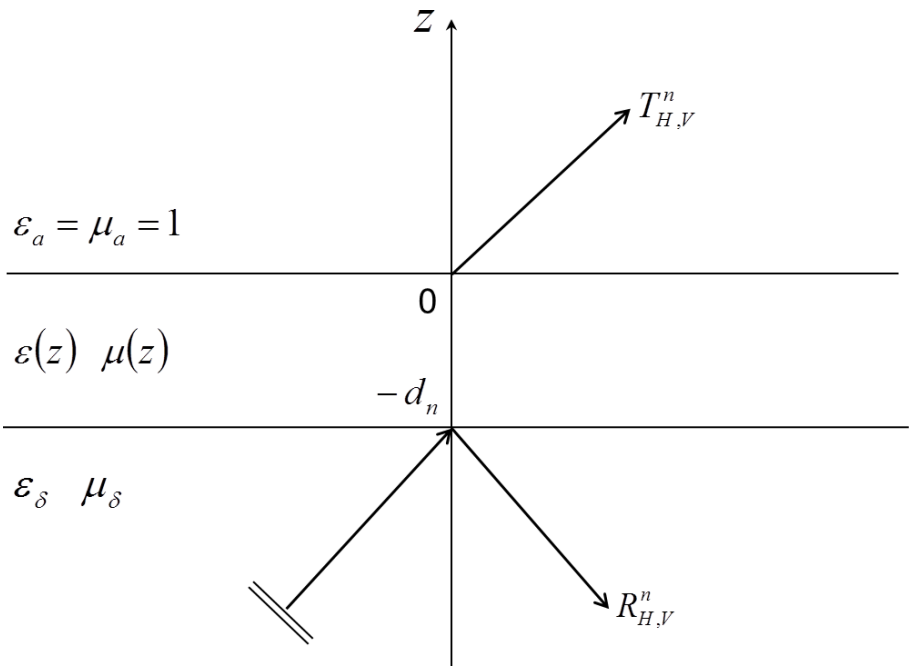


Figure 5.A1. Transmission of a plane wave through the inhomogeneous slab.

Particular solutions in the inhomogeneous medium $-d_n \le z \le 0$ satisfy the following wave equations written for horizontal and vertical polarizations:

$$\mu(z)\frac{d}{dz}\left[\frac{1}{\mu(z)}\frac{dU_{1,2H}(z)}{dz}\right] + \left[k^2(z) - q_0^2\right]U_{1,2H}(z) = 0, \qquad (5.A1)$$

$$\varepsilon(z)\frac{d}{dz}\left[\frac{1}{\varepsilon(z)}\frac{dU_{1,2V}(z)}{dz}\right]+\left[k^2(z)-q_0^2\right]U_{1,2V}(z)=0, \tag{5.A2}$$

where $k^2(z)=k_0^2\varepsilon(z)\mu(z)$. Below we express complex reflection and transmission coefficients through a solution of the wave equation in the inhomogeneous medium for both horizontal and vertical polarizations.

5.A.1. Horizontal Polarization

Tangential components of electric and magnetic fields are derived in region $z\le -d_n$:

$$\begin{aligned}\mathbf{E}_t(\boldsymbol{\rho},z)&=A_H\left[e^{iw_\delta(z+d_n)}+R_H^n(q_0)e^{-iw_\delta(z+d_n)}\right]e^{i\mathbf{q}_0\cdot\boldsymbol{\rho}}\hat{\phi}\\ \mathbf{H}_t(\boldsymbol{\rho},z)&=-\frac{w_\delta}{Z_0k_0\mu_\delta}A_H\left[e^{iw_\delta(z+d_n)}-R_H^n(q_0)e^{-iw_\delta(z+d_n)}\right]e^{i\mathbf{q}_0\cdot\boldsymbol{\rho}}\hat{\rho},\end{aligned} \tag{5.A3}$$

where $R_H^n$ is the reflection coefficient from the layer at horizontal polarization.

$-d_n\le z\le 0$:

$$\begin{aligned}\mathbf{E}_t(\boldsymbol{\rho},z)&=\left[C_{1H}U_{1H}(z)+C_{2H}U_{2H}(z)\right]e^{i\mathbf{q}_0\cdot\boldsymbol{\rho}}\hat{\phi}\\ \mathbf{H}_t(\boldsymbol{\rho},z)&=-\frac{1}{Z_0ik_0\mu(z)}\left[C_{1H}U'_{1H}(z)+C_{2H}U'_{2H}(z)\right]e^{i\mathbf{q}_0\cdot\boldsymbol{\rho}}\hat{\rho},\end{aligned} \tag{5.A4}$$

$z \geq 0$:

$$\begin{aligned}
\mathbf{E}_t(\boldsymbol{\rho}, z) &= A_H T_H^n(q_0) e^{iw_0 z + i\mathbf{q}_0 \cdot \boldsymbol{\rho}} \hat{\phi} \\
\mathbf{H}_t(\boldsymbol{\rho}, z) &= -\frac{w_0}{k_0 Z_0} A_H T_H^n(q_0) e^{iw_0 z + i\mathbf{q}_0 \cdot \boldsymbol{\rho}} \hat{\rho},
\end{aligned} \tag{5.A5}$$

where $T_H^n$ is the transmission coefficient through the inhomogeneous layer at horizontal polarization. Taking into account initial conditions (5.10) and boundary conditions at the interfaces $z = 0$ and $z = -d_n$ we obtain:

$$\left.\begin{aligned}
&A_H\left[1 + R_H^n\right] = C_{1H}U_{1H}(-d_n) + C_{2H}U_{2H}(-d_n) \\
&\frac{iw_\delta(q_0)}{\mu_\delta} A_H\left[1 - R_H^n\right] = \frac{1}{\mu_n(-d_n)}\left[C_{1H}U'_{1H}(-d_n) + C_{2H}U'_{2H}(-d_n)\right] \\
&C_{1H}U_{1H}(0) + C_{2H}U_{2H}(0) = C_{1H} = A_H T_H^n(q_0) \\
&\frac{1}{\mu_1(0)}\left[C_{1H}U'_{1H}(0) + C_{2H}U'_{2H}(0)\right] = C_{2H} iw_0(q_0) = iw_0(q_0) A_H T_H^n
\end{aligned}\right\}, \tag{5.A6}$$

The last system of equations helps to derive the transmission and reflection coefficients:

$$\begin{aligned}
T_H^n(q_0) &= \frac{2iw_\delta(q_0)\mu_n(-d_n)}{iw_\delta(q_0)\mu_n(-d_n)p_H^n + \mu_\delta p_H'^n} \\
R_H^n(q_0) &= \frac{iw_\delta(q_0)\mu_n(-d_n)p_H^n - \mu_\delta p_H'^n}{iw_\delta(q_0)\mu_n(-d_n)p_H^n + \mu_\delta p_H'^n},
\end{aligned} \tag{5.A7}$$

where

$$\begin{aligned} p_H^n &= U_{1H}(-d_n) + U_{2H}(-d_n) \\ p_H'^n &= U'_{1H}(-d_n) + U'_{2H}(-d_n) \end{aligned}. \tag{5.A8}$$

5.A.2. Vertical Polarization

Analogous to the horizontal polarization case we find tangential components of electric and magnetic fields in the regions $z \le -d_n$, $-d_n \le z \le 0$ and $z \ge 0$. Substituting these fields into the boundary conditions at the interfaces $z = -d_n$, $z = 0$ and using initial conditions (5.11) we obtain expressions for the reflection and transmission coefficients with respect to tangential magnetic field at vertical polarization:

$$\begin{aligned} T_V^n(q_0) &= \frac{2iw_\delta(q_0)\varepsilon_n(-d_n)}{iw_\delta(q_0)\varepsilon_n(-d_n)p_V^n + \varepsilon_\delta p_V'^n} \\ R_V^n(q_0) &= \frac{iw_\delta(q_0)\varepsilon_n(-d_n)p_V^n - \varepsilon_\delta p_V'^n}{iw_\delta(q_0)\varepsilon_n(-d_n)p_V^n + \varepsilon_\delta p_V'^n}, \end{aligned} \tag{5.A9}$$

where

$$\begin{aligned} p_V^n &= U_{1V}(-d_n) + U_{2V}(-d_n) \\ p_V'^n &= U'_{1V}(-d_n) + U'_{2V}(-d_n). \end{aligned} \tag{5.A10}$$

Values $\varepsilon_\delta$ and $\mu_\delta$ can be arbitrary selected; however, to simplify our formulations we accept that $\varepsilon_\delta = \varepsilon_n(-d_n),\ \mu_\delta = \mu_n(-d_n),\ w_\delta(q_0) = w_n(q_0) = \sqrt{k_0^2\varepsilon_n(-d_n)\mu_n(-d_n) - q_0^2}$. Therefore, we obtain:

$$T_{H,V}^{n}(q_0) = \frac{2iw_n(q_0)}{iw_n(q_0)p_{H,V}^{n} + p'^{n}_{H,V}}, \tag{5.A11}$$

$$R_{H,V}^{n}(q_0) = \frac{iw_n(q_0)p_{H,V}^{n} - p'^{n}_{H,V}}{iw_n(q_0)p_{H,V}^{n} + p'^{n}_{H,V}}. \tag{5.A12}$$

# Appendix 5.B. Reflection Coefficients from Inhomogeneous Half-Space $z < -d_n$

Consider a boundary between two media $\varepsilon_\delta, \mu_\delta$ and $\varepsilon(z), \mu(z)$ respectively. A plane monochromatic wave is incident upon this interface from the upper half-space $z > -d_n$ as shown in Figure 5.B1. Magnitudes $V_{H,V}(z)$ in the inhomogeneous area $z < -d_n$ satisfy differential equations given by (5.A1) and (5.A2).

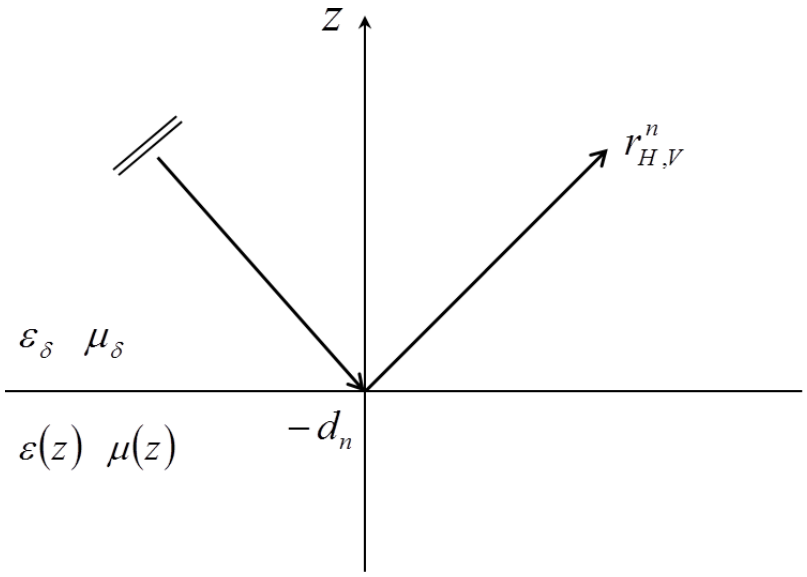


Figure 5.B1. Reflection of a plane wave from the inhomogeneous half-space.

## 5.B.1. Horizontal Polarization

From Maxwell's equations the tangential components of the fields are given as follows.

In the upper half-space $z \geq -d_n$:

$$\mathbf{E}_t(\boldsymbol{\rho}, z) = A_H \left[ e^{-iw_\delta (z+d_n)} + r_H^n e^{iw_\delta (z+d_n)} \right] e^{i\mathbf{q}_0 \cdot \boldsymbol{\rho}} \hat{\phi}$$
$$\mathbf{H}_t(\boldsymbol{\rho}, z) = \frac{w_\delta}{k_0 Z_0 \mu_\delta} A_H \left[ e^{-iw_\delta (z+d_n)} - r_H^n e^{iw_\delta (z+d_n)} \right] e^{i\mathbf{q}_0 \cdot \boldsymbol{\rho}} \hat{\rho}, \tag{5.B1}$$

where $w_\delta = \sqrt{k_0^2 \varepsilon_\delta \mu_\delta - q_0^{\,2}}$ is the transverse wave number in $z > -d_n$; $r_H^n$ is the reflection coefficient with respect to the tangential electric field.

In the lower half-space $z \le -d_n$:

$$\mathbf{E}_t(\boldsymbol{\rho}, z) = V_H(z) e^{i\mathbf{q}_0 \cdot \boldsymbol{\rho}} \hat{\phi}$$
$$\mathbf{H}_t(\boldsymbol{\rho}, z) = -\frac{1}{ik_0 Z_0 \mu(z)} V_H'(z) e^{i\mathbf{q}_0 \cdot \boldsymbol{\rho}} \hat{\rho}. \tag{5.B2}$$

From the boundary conditions for electric and magnetic fields at $z = -d_n$ we obtain the following relationships:

$$\left.\begin{aligned} A_H[1 + r_H^n] &= V_H(-d_n) \\ \frac{iw_\delta}{\mu_\delta} A_H[1 - r_H^n] &= -\frac{1}{\mu_{n+1}(-d_n)} V_H'(-d_n) \end{aligned}\right\}, \tag{5.B3}$$

$$\frac{V_H'(-d_n)}{V_H(-d_n)} = -iw_\delta \frac{\mu_{n+1}(-d_n)}{\mu_\delta} \left( \frac{1 - r_H^n}{1 + r_H^n} \right). \tag{5.B4}$$

B.2. Vertical Polarization

Similar to the horizontal polarization case the tangential fields are found in the upper and lower half-spaces. Substituting them into the boundary conditions at $z = -d_n$ we derive:

$$\frac{V_V'(-d_n)}{V_V(-d_n)} = -iw_\delta \frac{\varepsilon_{n+1}(-d_n)}{\varepsilon_\delta}\left(\frac{1-r_V^n}{1+r_V^n}\right). \tag{5.B5}$$

Finally, the following relationships are obtained by setting $\varepsilon_\delta = \varepsilon_n(-d_n)$ and $\mu_\delta = \mu_n(-d_n)$:

$$\frac{V_H'(-d_n)}{V_H(-d_n)} = -iw_n \frac{\mu_{n+1}(-d_n)}{\mu_n(-d_n)}\left(\frac{1-r_H^n}{1+r_H^n}\right), \tag{5.B6}$$

$$\frac{V_V'(-d_n)}{V_V(-d_n)} = -iw_n \frac{\varepsilon_{n+1}(-d_n)}{\varepsilon_n(-d_n)}\left(\frac{1-r_V^n}{1+r_V^n}\right). \tag{5.B7}$$

# Appendix 5.C. Wronskians of Particular Solutions of Wave Equations

## 5.C.1. Horizontal Polarization

Particular solutions $U_{1H}(z)$ and $U_{2H}(z)$ satisfy the following wave equations in region $-d_n \le z \le 0$:

$$\begin{aligned} \mu(z)\frac{d}{dz}\left[\frac{1}{\mu(z)}\frac{dU_{1H}}{dz}\right]+\left[k^2(z)-q_0^2\right]U_{1H}=0 \\ \mu(z)\frac{d}{dz}\left[\frac{1}{\mu(z)}\frac{dU_{2H}}{dz}\right]+\left[k^2(z)-q_0^2\right]U_{2H}=0. \end{aligned} \tag{5.C1}$$

The particular solutions also satisfy initial conditions (5.10) at the upper boundary $z=0$. Multiplying the first equation of system (5.C1) by $U_{2H}$ and the second equation by $U_{1H}$ and subtracting the second equation from the first one we obtain:

$$\frac{d}{dz}\left\{\frac{1}{\mu(z)}W_H(z)\right\}=0, \tag{5.C2}$$

where $W_H(z)=U_{1H}(z)U'_{2H}(z)-U_{2H}(z)U'_{1H}(z)$ is the Wronskian at horizontal polarization. Taking into account (5.C2) and (5.10), we obtain:

$$\frac{1}{\mu(z)}W_H(z)=const=iw_0(q_0). \tag{5.C3}$$

From (5.C3) we obtain $W_H(z)$ at $z = -d_n$:

$$W_H(-d_n) = i\mu_n(-d_n)w_0(q_0). \tag{5.C4}$$

5.C.2. Vertical Polarization

Analogous to the horizontal polarization case we derive the Wronskian at vertical polarization:

$$W_V(-d_n) = i\varepsilon_n(-d_n)w_0(q_0). \tag{5.C5}$$

# CHAPTER 6. MODELING AND MEASUREMENT OF C-BAND RADAR BACKSCATTER FROM SNOW-COVERED FIRST-YEAR SEA ICE

**A. S. Komarov**, D. Isleifson, D. G. Barber, and L. Shafai, "Modeling and measurement of C-band radar backscatter from snow-covered first-year sea ice," *IEEE Transactions on Geoscience and Remote Sensing*, in press, 2015.

## 6.1. Introduction

Arctic sea ice extent has been drastically declining over the past three decades [1], [6]. The low record minimum in summer sea ice extent of $3.41 \cdot 10^6\,\mathrm{km}^2$ (which is 49% less than 1979 to 2000 average) was recorded by spaceborne microwave radiometers in September 2012 [2]. Correspondingly, there is strong evidence that the Arctic Ocean multiyear (MY) sea ice has been rapidly disappearing at a rate of 15.1% per decade [3], [4]. During this, the MY sea ice is being replaced by seasonal first-year (FY) sea ice as the maximum extent (in winter) has not changed appreciably [5]. These changes significantly impact physical, chemical and biological processes in the Arctic marine ecosystem while facilitating industrial developments in the Arctic Ocean. Therefore, detection of thermodynamic state in snow-covered FY sea ice is becoming increasingly important.

Active microwave remote sensing has been proven to be an efficient tool to characterize the thermodynamic state of snow-covered sea ice [121] where the snow cover plays an important role in wave propagation and scattering within the system [63], [128].

The influence of snow cover on C-band radar signatures in spring was investigated by Barber and Nghiem in [63]. In [63] two experimental sites were located on 1.7 m thick landfast smooth snow-covered FY sea ice in the Canadian Arctic Archipelago near Resolute Bay. The physical data were collected at these two sites (with snow thickness of 12 cm and 24 cm respectively) on May 6 (cold conditions) and May 9 (warm conditions) in 1993. Thus, the following four modeling case studies were considered: a) Thin (12 cm), cold (-13.7 $^{o}$C) snow cover; b) Thin (12 cm), warm (-5.8 $^{o}$C) snow cover; c) Thick (24 cm), cold (-11.5$^{o}$C) snow cover; d) Thick (24 cm), warm (-8.8 $^{o}$C) snow cover where the temperature of basal snow is displayed in brackets.

In [63] the following scattering contributions were analyzed: (1) volume scattering from snow grains within the snow basal layer, (2) volume scattering from brine inclusions within the snow basal layer, (3) scattering from brine pockets within the surface layer of ice, and (4) scattering from the rough snow-ice interface. Scattering from the air-snow interface and wave propagation through the layer of snow lying above the basal layer were neglected. In [63] it was demonstrated that volume scattering (from snow grains and brine inclusions within the basal layer of snow) dominated in both cold and warm cases while the surface scattering (from the snow-ice interface) contributes the least to the total scattering. In the cold case removing the snow grain scattering reduced VV backscatter by 3.6 dB; the rest of the total backscatter was from the brine in snow and ice and the rough snow-ice interface. In the warm case the situation was reversed, i.e. removing the brine inclusions from snow reduced VV backscatter by 3.6 dB and the rest of the total backscatter was primarily from snow grains, brine inclusions in ice and the rough snow-ice interface.

In [63] temperature changes within the basal layer substantially controlled the volume scattering. Over the thin snow cover an increase in VV backscatter (at $23^o$ incidence angle) was 3.5 dB while over the thick snow cover a significantly lower increase was observed (0.7 dB). Therefore, a larger change in scattering is detected between a warm and cold condition surface for a thin snow cover relative to a thick snow cover [63]. This is explained by the fact that an increase in air temperature caused an increase in the brine volume in the basal layer of snow and consequently the volume scattering from ice grains and brine inclusions [63]. In the same study an increase in snow thickness under cold conditions caused an increase in VV backscatter (by 2.4 dB), while an increase in snow thickness under warm conditions caused a substantially smaller increase in VV backscatter (by 0.7 dB). Based on these results, variations in snow water equivalent from synthetic aperture radar (SAR) data can be detected according to [129].

As an expansion of the theory described in [63] there are times when we expect volume scattering to be minimal from snow covered sea ice. This can occur for thin snow covers, when the snow is quite new on the sea ice, resulting in smaller kinetic growth grains in the basal layer of the snow [130]. If the volume scattering within snow-covered sea ice is negligible, as often is the case in mid winter, then the surface scattering at the air-snow and snow-ice rough interfaces dominates. In this case we expect that the snow cover may affect radar signatures differently than in [63].

To investigate the effect of snow cover on radar signatures and to quantify thermodynamic changes in the snow-covered sea ice reliable modeling techniques linking geophysical parameters of snow and sea ice and radar response are required. Analytical and numerical approaches for modelling electromagnetic wave scattering from snow-covered sea ice can be found in literature. Carlström and Ulander [131] implemented a radiative transfer model (RTM) taking into account

surface scattering from air-snow and snow-ice interfaces as well as volume scattering within the ice. The volume scattering component within the snow was neglected. The surface scattering components of the RTM were modelled using the single scattering term of the integral equation model (IEM) [132]. In [131] it was also shown that the surface scattering at the snow-ice interface dominated over the volume scattering within sea ice in C-band. Dierking et al. in [133] demonstrated this effect for incidence angles below $45^{o}$ (for HH-polarization) and the incidence angles below $55^{o}$ (for VV-polarization) using the same RTM model (in conjunction with the IEM). We note that the IEM scattering model [132] does not account for the layered structure of snow and ice (i.e. the dependence of the dielectric properties on the vertical coordinate). Therefore, in [131] and [133] the dielectric of snow and ice were constants with respect to depth. Another modeling approach presented in the recent study by Fuller et al. [134] is based on the RTM modified for several layers and accounting for surface and volume scattering. The surface scattering contribution is calculated through the Kirchhoff physical optics method and the volume scattering component is estimated on the basis of the number density and effective size of ice-particles in snow.

Numerical finite-difference time-domain (FDTD) [88] and finite-volume time-domain (FVTD) [89] scattering models solve Maxwell's equations directly for complex media, but they require significant computational resources. The computational constrains make the numerical models difficult to apply to practical remote sensing problems.

The small perturbation theory has been extensively used for modelling of electromagnetic wave scattering from slightly rough natural surfaces [91]. Our new theoretical approach proposed in [13] provides an analytical solution (within the first–order approximation of the small

perturbation theory) for a general scattering geometry where an electromagnetic wave is scattered by an arbitrary number of rough surfaces interfacing arbitrary layered media. In [13] the snow-covered sea ice was considered as a special case of the general scattering geometry where both snow and ice were treated as continuously layered media separated by a slightly rough interface (in C- and L- bands). In our study a medium is defined as continuously layered if the dielectric profile of this medium represents a continuous function of the vertical coordinate. Note that the scattering theory described in [13] is valid for arbitrary layered media (i.e. multi-layered or continuously layered) as the solution for NRCS is expressed through generalized reflection and transmission coefficients associated with layered media. This means that snow and ice could be represented as discretely-layered media as well.

As mentioned above, the small perturbation scattering theory presented in [13] accounts for arbitrary layered structures (i.e. continuously layered or multi-layered media located above and/or beneath a rough interface) while the IEM model [133] is applied to a rough surface on top of a homogeneous half space. Meanwhile, the IEM model is valid for a wider range of roughness parameters compared to the small perturbation theory. The model proposed in [13] is also computationally efficient (compared to FDTD and FVTD) which allows to simulate backscatter coefficients for numerous input parameters (e.g. snow and ice surface roughness). Nevertheless, comparisons of theoretical model results with experimental data for snow-covered sea ice have not been performed.

In this paper we pursue the following objectives: (1) to model normalized radar cross-sections (NRCS) (equivalent to backscattering coefficients) in C-band from snow-covered FY sea ice for different snow thickness conditions over smooth first-year sea ice using the theory presented in

[13], (2) to validate the numerical results against winter ship-based scatterometer observations of snow-covered FY sea ice collected in the Canadian Arctic, and (3) Investigate the influence of snow cover on radar signatures using model and experimental data.

## 6.2. Methods

### 6.2.1. Identification of Scattering Mechanisms

In order to identify the dominant scattering mechanism in our modelling study we use a three component decomposition model developed by Freeman and Durden [135]. The model quantifies contributions of three scattering mechanisms: (1) surface scattering, (2) volume scattering, and (3) double-bounce scattering from a pair of orthogonal surfaces. Given the fact, that the Freeman-Durden decomposition was originally developed for forest targets, it may not be fully suited for sea ice and snow applications, but it can provide rough estimations of fractions of surface and volume scattering contributions. This decomposition has also been successfully used for quantifying surface, volume, and double-bounce scattering contributions from sea ice and for identifying various ice types from polarimetric SAR images [136]-[140].

In our study we deal with smooth FY sea ice with thickness exceeding 1 m (see more details in Section 6.3); therefore, there is no need to consider scattering contributions from large-scale ice deformations (i.e. double-bounce scattering). Thus, decomposition model [135] can be considered for two scattering components. The contributions of surface and volume scattering for a given incidence angle can be determined as follows (see Appendix 6.A):

$$\frac{P_s}{P} = \frac{\sigma^0_{VV} + \sigma^0_{HH} - 6\sigma^0_{HV}}{\sigma^0_{VV} + \sigma^0_{HH} + 2\sigma^0_{HV}}, \tag{6.1}$$

$$\frac{P_v}{P} = 1 - \frac{P_s}{P}, \tag{6.2}$$

where $\sigma^0_{HH}$, $\sigma^0_{VV}$, and $\sigma^0_{HV}$ are observed HH, VV, and HV backscattering coefficients. In the last two equations $P_s$ is the power of the received signal due to surface scattering, $P_v$ is the power of the received signal due to volume scattering, and $P = P_s + P_v$ is the total power. Numerical results for surface and volume scattering contributions (demonstrating a negligible level of volume scattering) in our case studies are presented in Section 6.5.1.

### 6.2.2. Microwave Scattering Model

A plane electromagnetic monochromatic wave with angular frequency $\omega$ and time dependence $e^{-i\omega t}$ is incident upon the snow-covered sea ice as illustrated in Figure 6.1. Dielectric properties of snow and ice are represented by continuous functions $\varepsilon_s(z)$ and $\varepsilon_i(z)$ respectively (where $z$ is a vertical coordinate). The snow layer thickness on top of sea ice is $d$. Roughness of the air-snow and snow-sea ice interfaces is described by stationary random functions $\zeta_s(\boldsymbol{\rho})$ and $\zeta_i(\boldsymbol{\rho})$ which define deviations of the rough surfaces from planes at $z = 0$ and $z = -d$ respectively (where $\boldsymbol{\rho}$ is the position vector at the horizontal plane).

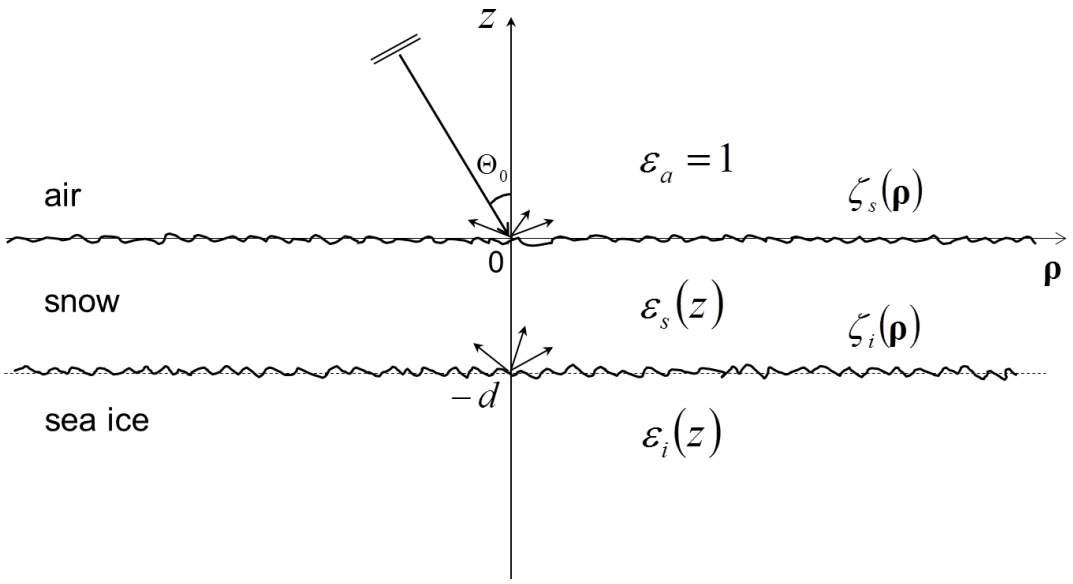


Figure 6.1. Illustration of wave scattering from snow-covered sea ice.

An analytical formulation for NRCS at both horizontal (H) and vertical (V) polarizations within the first-order approximation of small perturbation theory was derived in [13]. According to [13], the NRCS from the air-snow and snow-sea ice interfaces in the monostatic case can be written as follows.

Air-snow interface:

$$\sigma_{HH}^{0snow} = \frac{k_0^4 |\Delta\varepsilon_s|^2}{4\pi} \left|[1+\Re_H(q_0)]\right|^4 \tilde{K}_s(-2\mathbf{q_0}), \tag{6.3}$$

$$\sigma_{VV}^{0snow} = \frac{k_0^4 |\Delta\varepsilon_s|^2}{4\pi} \left| \frac{\sin^2\Theta_0}{\varepsilon_s(0)} [1+\Re_V(q_0)]^2 + [1-\Re_V(q_0)]^2 \cos^2\Theta_0 \right|^2 \tilde{K}_s(-2\mathbf{q_0}), \tag{6.4}$$

$$\sigma_{HV}^{0snow} = \sigma_{VH}^{0snow} = 0. \tag{6.5}$$

Snow-ice interface:

$$\sigma_{HH}^{0ice} = \frac{k_0^4 \left|\Delta\varepsilon_i\right|^2}{4\pi} \left|L_H(q_0)\right|^4 \tilde{K}_i(-2\mathbf{q_0}), \tag{6.6}$$

$$\sigma_{VV}^{0ice} = \frac{k_0^4 \left|\Delta\varepsilon_i\right|^2}{4\pi} \left|\frac{\varepsilon_s(-d)}{\varepsilon_i(-d)} \sin^2\Theta_0 L_V^2(q_0) + M_V^2(q_0)\right|^2 \tilde{K}_i(-2\mathbf{q_0}), \tag{6.7}$$

$$\sigma_{HV}^{0ice} = \sigma_{VH}^{0ice} = 0. \tag{6.8}$$

If both rough interfaces are not correlated then the total radar backscatter from snow-covered sea ice is a sum of backscattering coefficients from rough snow and sea ice:

$$\sigma_{pp}^{0} = \sigma_{pp}^{0ice} + \sigma_{pp}^{0snow}, \ p = H,V. \tag{6.9}$$

If the rough interfaces are correlated then an additional correlation term should be included in (6.9) according to [13]. Also, the rough ice-water interface could be included in this formulation; however, in our study we deal with FY ice thicker than 1 m.

In (6.3), (6.4), (6.6), and (6.7) $\Theta_0$ is the incidence angle; $k_0$ is the wave number in vacuum; $\varepsilon_s(-d)$ is the complex dielectric constant (CDC) of snow at the snow-ice interface $z = -d$; $\varepsilon_i(-d)$ is the CDC of ice at the snow-ice interface; $\Delta\varepsilon_i = \varepsilon_i(-d) - \varepsilon_s(-d)$ is the dielectric contrast between ice and snow at the snow-ice interface; $\Delta\varepsilon_s = \varepsilon_s(0) - 1$ is the dielectric contrast between snow and air at the air-snow interface; $\mathbf{q_0} = k_0 \sin\Theta_0 (\hat{x}\cos\Phi_0 + \hat{y}\sin\Phi_0)$ is a projection

of the wave vector in the air onto the horizontal plane (where $\Phi_0$ is the azimuth angle of the incident wave, and $\hat{x}$, $\hat{y}$ are Cartesian unit vectors in the horizontal plane).

Also, $\Re_{H,V}$ in (6.3) and (6.4) are complex reflection coefficients from the entire snow-covered sea ice structure at horizontal and vertical polarizations. In (6.6) and (6.7) the auxiliary variables $L_{H,V}$ and $M_{H,V}$ are defined as follows:

$$L_{H,V}(q_0) = \frac{w_0(q_0)}{w_s(q_0)} \frac{T_{sH,V}(q_0)}{1 - r_{iH,V}(q_0) R_{sH,V}(q_0)} \left[1 + r_{iH,V}(q_0)\right], \tag{6.10}$$

$$M_{H,V}(q_0) = \frac{w_0(q_0)}{k_0} \frac{T_{sH,V}(q_0)}{1 - r_{iH,V}(q_0) R_{sH,V}(q_0)} \left[1 - r_{iH,V}(q_0)\right], \tag{6.11}$$

where $w_s(q_0) = \sqrt{k_0^2 \varepsilon_s(-d) - q_0^2}$, $w_0(q_0) = \sqrt{k_0^2 - q_0^2}$; $T_{sH,V}$ and $R_{sH,V}$ are complex transmission and reflection coefficients for the inhomogeneous snow layer when the wave is incident from the half-space with CDC $\varepsilon_s(-d)$ at horizontal and vertical polarizations; $r_{iH,V}$ are reflection coefficients from the inhomogeneous sea ice when the wave is incident from the half-space with CDC $\varepsilon_s(-d)$ at horizontal and vertical polarizations.

All the transmission and reflection coefficients for inhomogeneous media can be numerically calculated using the invariant embedding approach [127], [141]. A numerical recursive scheme for this method is presented in Appendix 6.B. The dielectric profiles of snow and sea ice serve as inputs to calculate the reflection and transmission coefficients. There is no need to calculate reflection coefficients for the entire ice thickness (more than 1 m) as (in C-band) the wave

attenuates significantly within sea ice. Thus, to calculate the reflection coefficients for sea ice we used a dielectric profile of the upper 40 cm layer of ice.

In equations (6.3), (6.4), (6.6), and (6.7) $\tilde{K}_s$ and $\tilde{K}_i$ are the spatial power spectral densities of the air-snow and snow-ice rough interfaces given by:

$$\tilde{K}_{s,i}(\mathbf{q}) = \iint K_{s,i}(\boldsymbol{\rho}) e^{-i\mathbf{q}\boldsymbol{\rho}} d\boldsymbol{\rho}\,, \tag{6.12}$$

where $K_s(\boldsymbol{\rho})$ and $K_i(\boldsymbol{\rho})$ are autocorrelation functions of the rough air-snow and snow-ice interfaces respectively:

$$K_{s,i}(\boldsymbol{\rho}) = \left\langle \zeta_{s,i}(\boldsymbol{\rho}+\boldsymbol{\rho}')\zeta_{s,i}(\boldsymbol{\rho}') \right\rangle. \tag{6.13}$$

In our study we assume that both rough surfaces are isotropic, i.e. $K_s$ and $K_i$ are independent of the azimuth angle. However, anisotropic rough interfaces can be utilized in this model as well. The exponential function was found to provide best fit to the autocorrelation functions of snow and ice surfaces derived from terrestrial LiDAR data [142]. Therefore, we accept that the autocorrelation functions of both rough interfaces are described by exponential dependences i.e.:

$$K_{s,i}(\rho) = \sigma_{s,i}^2 \exp\left(-\frac{\rho}{L_{s,i}}\right), \tag{6.14}$$

where $\sigma_s$ and $L_s$ are root-mean square (RMS) height and correlation length of the air-snow rough interface, $\sigma_i$ and $L_i$ are RMS height and correlation length of the snow-ice rough interface. From (6.12) the corresponding spectrum can be found as follows [91]:

$$\tilde{K}_{s,i}(q) = \frac{2\pi L_{s,i}^2 \sigma_{s,i}^2}{\left(1 + q^2 L_{s,i}^2\right)^{1.5}}. \tag{6.15}$$

Roughness parameters of snow $\sigma_s$, $L_s$, and ice $\sigma_i$, $L_i$ were not measured during the field experiment. Therefore, they varied in our simulations as discussed in Section 6.5.

## 6.3. Experimental Data

Scatterometer and physical data for our study were collected in the southern Beaufort Sea in winter 2008 from the research icebreaker CCGS Amundsen as part of the Circumpolar Flow Lead (CFL) system study [143]. Three sites (case studies) represented mobile snow-covered FY sea ice (1.2 m, 1.2 m, and 1.1 m thick respectively) were selected for our analysis (as shown in Table 6.1). The ice concentration in the sampling area exceeded 9/10. The first site (March 8, 16 cm of snow) and the second site (March 10, 4 cm of snow) were located on different sides of the same floe. The third site (February 26, 3 cm of snow) was located around 12 km to the southwest from this floe. The sampling time of day 15:30 pm (local time) was similar for all three sites for consistency.

### 6.3.1. Scatterometer Data

Fully-polarimetric C-band (5.5 GHz) scatterometer measurements of snow-covered sea ice were collected at different incidence angles (with respect to nadir) in the elevation from $20^o$ to $60^o$ with $5^o$ step. At each incidence angle the effective NRCS for $-30^o$ to $30^o$ swath in the azimuth direction was computed, where $0^o$ azimuth corresponds to the direction perpendicular to the side of the ship. At a given sampling station, typically 5 to 10 scatterometer scans were performed, and from them the average angular dependences (and standard deviations) of NRCS at HH, VV, and VH polarizations were calculated. More details on this scatterometer system and field measurement techniques can be found in [119], [144].

Table 6.1. Three sites selected for analysis.

| **Case Study** | **Location Latitude/Longitude** | **Local Time** | **Air Temperature [$^o$C]** | **Snow Thickness [cm]** | **Ice Thickness [cm]** |
|---|---|---|---|---|---|
| 1 | 71.0163 $^o$N<br>123.8163 $^o$W | March 8, 2008, 15:30 | -17.5 | 16 | 120 |
| 2 | 71.0385 $^o$N<br>123.9103 $^o$W | March 10, 2008, 15:30 | -23.1 | 4 | 120 |
| 3 | 70.9203 $^o$N<br>123.9883 $^o$W | February 26, 2008, 15:30 | -19.3 | 3 | 110 |

### 6.3.2. Physical Data

In-situ physical sampling of snow and sea ice was conducted in support of the scatterometer observations. Snow density profiles were measured with 2 cm resolution using a snow density cutter and a gravimetric approach. Salinity of each melted snow sample was also measured using HACH SENSION5 portable conductivity meter (accuracy of ±0.01 ppt). The temperature profile

of a snow pit was captured with 2 cm resolution using a temperature probe (Traceable Digital Thermometer, Control Company, accuracy of ±0.05 °C). Measured snow density, salinity and temperature profiles were used to estimate volumetric contents of brine and pure ice as shown in Section 6.4.1.

Vertical profiles of temperature and salinity in sea ice were captured by analysing an ice core. The temperature profile of the extracted ice core was measured by drilling a hole at 5 cm increments and inserting a temperature probe. To register the bulk salinity profile, the ice core was cut into 5 cm lengths placing them in sealed buckets and melting them and equilibrating to room temperature. Salinity of each melted piece was measured in a lab using the conductivity meter.

The physical properties of snow and sea ice served as input parameters to dielectric modeling of these media.

## 6.4. Dielectric Modeling

### 6.4.1. Snow

Snow on FY sea ice is a mixture of pure ice, air and brine (wicked from the sea ice surface). There are a few dielectric mixture models for estimating CDC of fresh water snow (such as [82]). However, a reliable mixture model for estimating CDC of brine wetted snow on top of sea ice based on direct measurements of snow CDC in microwave band has not been developed. We implement the power dielectric mixture model, formulated as follows:

$$\varepsilon_s^{\gamma} = \varepsilon_{ds}^{\gamma} + \left(\varepsilon_{bs}^{\gamma} - 1\right) W_b \,. \tag{6.16}$$

In the last equation $\varepsilon_{ds}$ is the CDC of dry snow (where the brine volume is replaced with air) is given as follows:

$$\varepsilon_{ds}^{\gamma} = 1 + \left(\varepsilon_{pi}^{\gamma} - 1\right) W_{pi}. \tag{6.17}$$

In equations (6.16) and (6.17) $W_b$ is the volumetric fraction of brine, $W_{pi}$ is the volumetric fraction of ice, $\varepsilon_{pi} = 3.15$ is the dielectric constant of pure ice [80], $\varepsilon_{bs}$ is the dielectric constant of brine which can be estimated as a function of temperature and frequency according to Stogryn and Desargant [81]. If in a special case of (6.16) and (6.17) we put $\gamma = 1$ then the dielectric mixture model becomes linear; if $\gamma = 0.5$ then the dielectric mixture model becomes refractive (which is linear with respect to the complex refractive indices). It has been shown that the refractive mixture model is effective for sea ice [76]. Furthermore, the refractive mixture model has been proven to be the most applicable for wet soils [125]. It is interesting to note that dielectric properties of pure ice and soil particles (rocks) are close to each other and the values of porosity in snow and soil are comparable as well. This indicates that the refractive dielectric mixture model could be applied to the brine wetted snow.

The volumetric content of brine $W_b$ and the volumetric content of pure ice $W_{pi}$ in the snow cover as function of the vertical coordinate $z$ can be estimated according to the formulation provided by Drinkwater and Crocker [83]:

$$W_b = \frac{\rho_s v_b}{(1 - v_b)\rho_{pi} + v_b \rho_b}, \tag{6.18}$$

where $\rho_s$ is the measured snow density, $\rho_b$ is the brine density and $\rho_{pi}$ is the density of pure ice.

In (6.18) $v_b$ is the ratio between the volume of brine and the volume of ice plus the volume of brine i.e.:

$$v_b = \frac{W_b}{W_b + W_{pi}}. \tag{6.19}$$

Following [83], this ratio can be estimated according to Frankenstein and Garner equations [78] through measured snow temperature $t_s$ ($^{o}$C) and snow bulk salinity $S_s$ (ppt) as follows:

$$v_b = \begin{cases} 10^{-3} S_s \left( -\frac{52.56}{t_s} - 2.28 \right), & -2.06^{o}\,\mathrm{C} \le t_s \le -0.5^{o}\,\mathrm{C} \\ 10^{-3} S_s \left( -\frac{45.917}{t_s} + 0.93 \right), & -8.2^{o}\,\mathrm{C} \le t_s \le -2.06^{o}\,\mathrm{C} \\ 10^{-3} S_s \left( -\frac{43.795}{t_s} + 1.189 \right), & -22.9^{o}\,\mathrm{C} \le t_s \le -8.2^{o}\,\mathrm{C} \end{cases}. \tag{6.20}$$

The ice volume fraction in snow $W_{pi}$ can be expressed as follows:

$$W_{pi} = \frac{\rho_s(1-v_b)}{(1-v_b)\rho_{pi} + v_b\rho_b}, \tag{6.21}$$

Substituting volumetric fractions of brine and pure ice given by equations (6.18) and (6.21) respectively into the dielectric mixture model (6.16) and (6.17) for the refractive case ($\gamma = 0.5$) it is possible to estimate the CDC of snow $\varepsilon_s$ as a function of depth.

6.4.2. Sea Ice

Sea ice consists of pure ice, brine inclusions and air bubbles. Unfortunately, size and distribution of air bubbles were not measured. Generally, air bubbles in FY sea ice have radius between 0.01 and 2 mm and number densities of 0.03 per $mm^3$ [145], whereas average brine inclusion number densities range from 1.0 to 4.5 per $mm^3$ [146]. Therefore, we assume that air bubbles do not affect the dielectric constant of FY sea ice significantly compared to the brine inclusions which have two orders of magnitude higher number densities and also have very high dielectric constant.

The CDC of sea ice was estimated using the power mixture model for an isotropic two-phase medium consisting of pure ice and brine inclusions. According to this model, the CDC of sea ice can be estimated as follows:

$$\varepsilon_i^{\gamma} = \varepsilon_{pi}^{\gamma}(1-V_b) + \varepsilon_{bi}^{\gamma}V_b, \tag{6.22}$$

where $\varepsilon_{pi} = 3.15$ is the dielectric constant of pure ice, $\varepsilon_{bi}$ is the CDC of brine inclusions in ice, $V_b$ is the volume fraction of brine inclusions. CDC of brine in sea ice $\varepsilon_{bi}$ can be found through the

Debye relaxation model with temperature dependent parameters empirically derived by Stogryn and Desargant in [81].

Brine volume content $V_b$ can be estimated using Frankenstein and Garner empirical equations as a function of temperature and bulk salinity of sea ice [78]. Note that the Frankenstein and Garner equations [78] assume constant sea ice density of 0.926 g/cm$^3$. The newer equation by Cox and Weeks [147] would be more accurate, but it requires sea ice density. According to the equation by [147] the brine volume estimated from [78] should be multiplied by the factor $\rho_{si}/0.926$ where $\rho_{si}$ is the density of sea ice. Assuming that the bulk density of FY sea ice typically ranges between 0.89 and 0.93 g/cm$^3$ [148] the relative error falls within the range between -0.04% and 4%. In our case studies the maximum brine volume content in sea ice was 4.2% (as shown in Section 6.5). Therefore, the maximum possible absolute error of sea ice brine volume content associated with assuming the constant sea ice density would be around 0.17%.

In the study by [76] it was shown that the refractive dielectric mixture model ($\gamma = 0.5$) agrees very well with dielectric measurements of sea ice reported in [77]. Therefore, we use the refractive model for estimating CDC of sea ice.

## 6.5. Results: Model versus Experiment

In this section we present numerically calculated HH and VV backscattering coefficients compared against ship based C-band scatterometer data for three cases of snow-covered FY sea ice. Prior to numerical simulations, in all case studies, snow temperature, salinity, and density profiles measured at 2 cm resolution were interpolated to 1 mm resolution using a shape-

preserving piecewise cubic interpolation. The obtained profiles were used to calculate the brine content and CDC of snow. In a similar way measured temperature and salinity profiles of sea ice with 5 cm resolution were interpolated to 1 mm resolution. The brine content and CDC of sea ice were calculated based on the interpolated profiles. The interpolated dielectric profiles of snow and sea ice served as inputs for calculating reflection and transmission coefficients in our scattering model.

### 6.5.1. Surface and Volume Scattering Contributions

For each case study we calculated average values of $\frac{P_s}{P}$ and $\frac{P_v}{P}$ (using (6.1) and (6.2)) for all incidence angles in the scatterometer observations. We demonstrated that the surface scattering contribution was 95%, 96%, and 91%, and the volume scattering contribution around 5%, 4%, and 9% for case studies 1, 2, and 3 respectively. This indicates that the dominant scattering mechanism in our case is surface scattering. This result is supported by the observation that the measured cross-polarized return $\sigma^0_{HV}$ was very low in all three cases (around or below the noise floor of the instrument which is -40 dB).

We note that in the Freeman-Durden decomposition the HV signal is explained by the volume scattering effect only. At the same time, in our case studies the measured cross-polarization (HV) signal is likely explained by the combination of both volume and surface scattering mechanisms. This indicates that the derived values for volume scattering contributions (through the Freeman-Durden decomposition) could be overestimated. Given the fact, that the obtained values for volume scattering contributions were 4%, 5% and 9% in Case Studies 1, 2, and 3 respectively, the actual volume scattering contributions would be even less than these values.

We would like to point out that our situation is substantially different from the case studied by Barber and Nghiem in [63], where the volume scattering from snow grains and brine inclusions in the basal layer prevailed over the surface scattering. For the cold snow case in [63] the ice grain size in the basal layer of snow was around 11.8 $mm^2$. In our case the estimated snow grain size at the bottom of the snowpack was smaller (around 7.8 $mm^2$). Also, in our study the temperature of the snow-ice interface was considerably lower than in [63] (where in-situ measurements were collected later in May). Therefore, the brine volume content at the snow-ice interface ( $z = 0$ ) was lower than in [63]. More specifically, in our three case studies (described below) the brine volume content at the snow-ice interface was 2.0% (in Case Study 1), 1.4% (in Case Study 2) and 0.7% (in Case Study 3). In [63] this value was 2.4% and 5.6% for thin (12 cm) cold and warm snow cases respectively, and 2.6% and 3.6% for thick (24 cm) cold and warm snow cases respectively. Thus, the smaller grain size in the basal layer of snow and the smaller brine volume content is snow in our case (in comparison to [63]) prevented volume scattering within the snow pack.

### 6.5.2. Roughness Parameters

Direct measurements of snow and sea ice roughness parameters (RMS height and correlation length) are quite rare in the literature. Measuring roughness of sea ice surface covered by snow is especially challenging as snow removal may substantially affect the ice surface. Generally, based on the published measurements, we expect that the RMS height of snow and ice is on the order of millimeters, whereas the correlation length is on the order of centimeters [111], [142]. Since the roughness parameters of snow and sea ice were not captured during the field campaign we varied these parameters within the ranges presented in Table 6.2.

Table 6.2. Ranges of snow and sea ice surface roughness parameters.

| Parameter | Min | Step | Max |
|---|---|---|---|
| RMS height of snow surface $\sigma_s$ [cm] | 0.01 | 0.02 | 0.31 |
| Correlation length of snow surface $L_s$ [cm] | 0.1 | 0.1 | 3 |
| RMS height of ice surface $\sigma_i$ [cm] | 0.01 | 0.02 | 0.31 |
| Correlation length of ice surface $L_i$ [cm] | 0.1 | 0.1 | 3 |

From this table only those parameters which satisfy the validity range of the small perturbation theory (with respect to the wavelength) formulated in [91] are used. We note that for the snow-ice rough interface the validity range is probably more strict compared to the air-snow interface (as the wave length in snow is smaller than in the air); however, there is no precise criterion accounting for this effect (especially in a layered medium). Therefore, for the snow-ice interface we use the same criterion as for the air-snow interface. For each set of four roughness parameters the cost function between the experimental and numerical NRCS at both VV and HH polarization was calculated. The roughness parameters $\sigma_s$, $L_s$, $\sigma_i$, $L_i$ minimizing the cost function were accepted as "true" values. The optimum roughness parameters derived for each case study are summarized in Table 6.3.

Table 6.3. Optimum parameters of snow and sea ice surface roughness for the three case studies for the high resolution of layers in snow and ice ($\Delta z_{snow} = \Delta z_{ice} = 1\text{mm}$).

| Case Study | $\sigma_s$ [cm] | $L_s$ [cm] | $\sigma_i$ [cm] | $L_i$ [cm] |
|---|---|---|---|---|
| 1 | 0.19 | 0.9 | 0.25 | 0.9 |
| 2 | 0.25 | 1.9 | 0.25 | 1.7 |
| 3 | 0.25 | 1.9 | 0.25 | 1.7 |

In the recent study by Landy et al. [142] roughness parameters for different ice types (including newly formed, first- and multiyear ice) derived from LiDAR measurements are presented. In [142] for FY ice of 1 m thick (with no snow cover) RMS height was 0.2 cm, and correlation length was 1.68 ± 0.21 cm. These values are close to our values obtained for Case Study 2 and Case Study 3 and shown in Table 6.3. In [142] no measurements of roughness parameters for dry snow were presented as in this case volume scattering may bias the ranging estimate of the LiDAR and, therefore, more research is required to evaluate the suitability of using LiDAR over dry snow. However, in the same study, RMS height for wet snow was 0.18 cm, and correlation length was 0.96 ± 0.18 cm. In another study by [111] roughness measurements of different ice types are presented. For congelation smooth FY sea ice (1.5 m thick) the RMS height was 0.053 cm and correlation length was 1.736 cm. The roughness values presented in [142] and [111] fall within the validity range of the small perturbation theory formulated in [91].

To explore how the derived roughness values change in response to the resolution of layers in snow and ice we reduced resolution of layers for snow to $\Delta z_{snow} = 1\,\text{cm}$ and for sea ice to $\Delta z_{ice} = 2.5\,\text{cm}$ and conducted the numerical simulations for all three case studies. The obtained results of optimum roughness parameters are summarized in Table 6.4. This table indicates that the RMS heights did not change compared to the results presented in Table 6.3 for $\Delta z_{snow} = \Delta z_{ice} = 1\text{mm}$, whereas the correlation length of snow has slightly changed in all case studies and correlation length of ice has slightly changed in case studies 1 and 2. The largest relative change is observed for case study 1 where the gradient of dielectric properties of snow was the largest (in comparison to the other case studies). The NRCS curves (as functions of incidence angle) for the low resolution ($\Delta z_{snow} = 1\,\text{cm}$ and $\Delta z_{ice} = 2.5\text{cm}$) did not change substantially

compared to the high resolution ($\Delta z_{snow} = \Delta z_{ice} = 1\,\text{mm}$). The cost function (between model and experimental NRCS values) has changed by 0.6%, 3.4% and 0.2% in case studies 1, 2, and 3 respectively (which are discussed below). Thus, our modeling results are not significantly affected by the resolution of layers in snow and ice.

Table 6.4. Optimum parameters of snow and sea ice surface roughness for the three case studies for the low resolution of layers in snow and ice ($\Delta z_{snow} = 1\,\text{cm}$ and $\Delta z_{ice} = 2.5\,\text{cm}$).

| Case Study | $\sigma_s$ [cm] | $L_s$ [cm] | $\sigma_i$ [cm] | $L_i$ [cm] |
|---|---|---|---|---|
| 1 | 0.19 | 0.7 | 0.25 | 1.0 |
| 2 | 0.25 | 1.8 | 0.25 | 1.6 |
| 3 | 0.25 | 2.1 | 0.25 | 1.7 |

The model has been run with the use of the roughness parameters obtained for 1 mm resolution (shown in Table 6.3); the obtained results for the three case studies are presented below.

### 6.5.3. Case Study 1: Snow Thickness 16 cm

In this case study the snow thickness was 16 cm which is the highest among the other cases. Snow temperature and salinity profiles are displayed in Figure 6.2(c). The salinity has the maximum value at the snow bottom and it rapidly decreases when approaching the air-snow interface. The temperature gradually decreases from the top to the bottom in the snow cover. Figure 6.2(d) shows the measured density and the estimated brine volume content (through density, temperature, and salinity) according to (6.18) in the snow cover. The brine volumetric content has the maximum value in the vicinity of the ice surface and it decreases when approaching the snow surface. One may observe that the brine volume content is substantially controlled by the salinity profile in

snow. Snow density and brine content directly affect the CDC of snow and therefore the wave attenuation within the snow pack. The estimated real and imaginary parts of snow CDC as functions of depth are displayed in Figure 6.2(e).

Measured temperature and bulk salinity profiles of the upper 40 cm layer of sea ice are shown in Figure 6.2(f). The surface layers of sea ice are colder and more saline compared to the deeper layers. The higher bulk salinity in the upper layers (compared to the lower layers) cause the higher values of brine volume content in ice (shown in Figure 6.2(g)). Therefore, both real and imaginary parts of sea ice CDC are higher at the ice surface (as displayed in Figure 6.2(h)).

The modelled and measured NRCS as functions of incidence angle are shown in Figure 6.2(a) and (b). The HH NRCS from the air-snow (given by (6.3)) and snow-ice (given by (6.6)) rough interfaces were computed separately. The VV NRCS from these two interfaces were calculated according to (6.4) and (6.7) respectively. Figure 6.2(a) and (b) show that the snow-ice interface has a larger impact on the total backscatter compared to the snow-air interface.

Good agreement between the model and experimental data for both VV and HH radar backscatter coefficients can be observed. One may also observe a wavy pattern in modelled HH NRCS curve shown in Figure 6.2(b). We attribute this effect to the interference of the coherent component of the field within the snow layer (which is thick enough relative to the wavelength). The same effect also takes place for VV polarization (Figure 6.2(a)); however, it is significantly less pronounced compared to the HH polarization.

The model result for the cross-polarization (HV) radar backscatter is zero (i.e. $-\infty$ dB). At the same time the experimental HV NRCS is approximately equal to or below the noise floor of the

instrument (which is -40 dB). This indicates that the small perturbation theory is appropriate for modeling scattering characteristics from winter snow-covered FY sea ice.

The estimated noise floor of the instrument (-40 dB) was provided by the manufacturer (ProSensing) based on their calibration experiment. We emphasize that the data was carefully analyzed to ensure that an adequate signal to noise ratio (typically 10 dB) was maintained throughout processing in a similar way to [119].

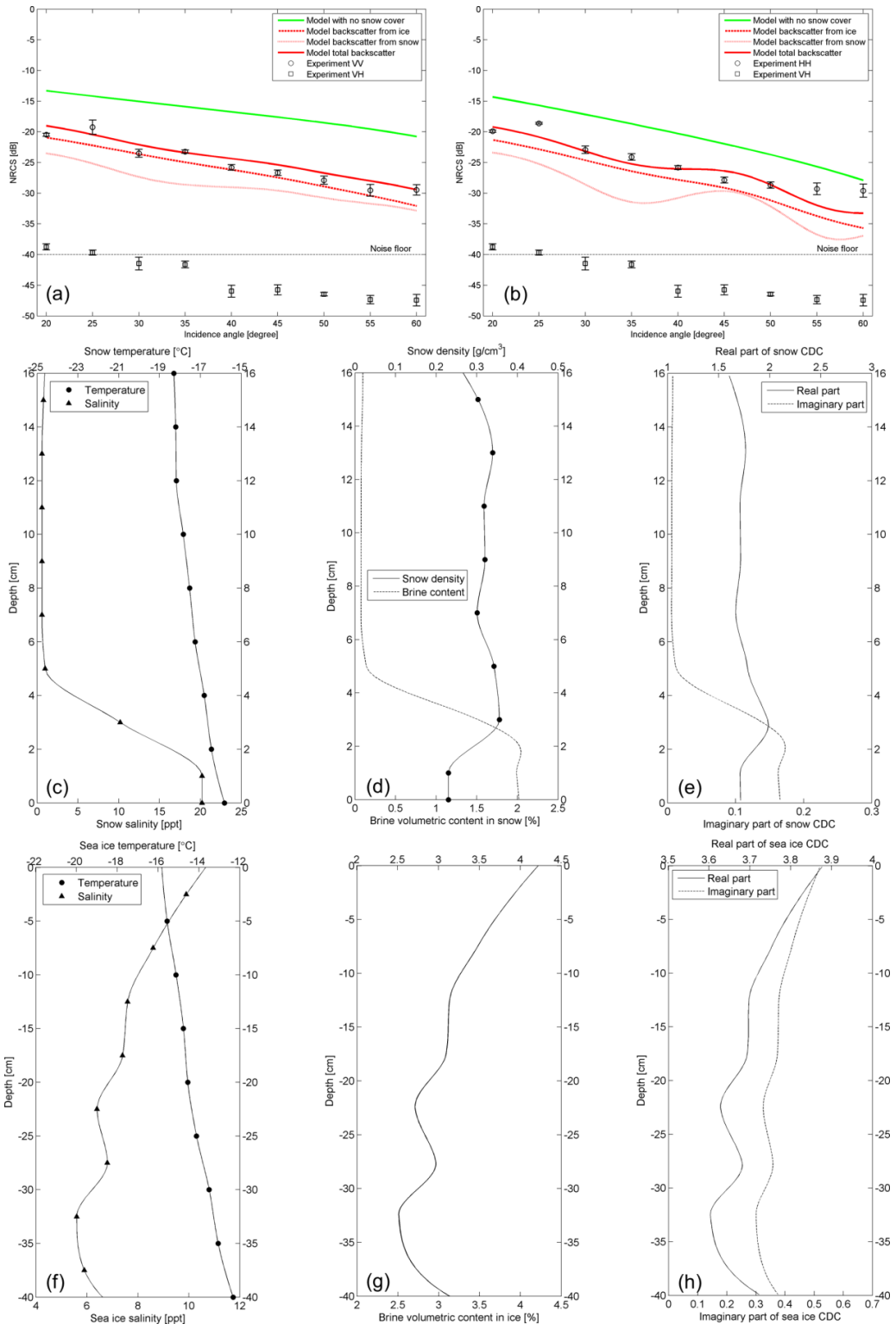


Figure 6.2. NRCS and physical properties of snow-covered sea ice for Case Study 1 (16 cm of snow). (a) Model and experimental VV NRCS along with experimental VH NRCS; (b) Model and

experimental HH NRCS along with experimental VH NRCS; (c) Snow temperature and salinity; (d) Snow density and brine content as functions of depth; (e) Real and imaginary parts of snow CDC; (f) Temperature and salinity of sea ice; (g) Brine content in sea ice; (h) Real and imaginary parts of sea ice CDC. All variables in snow and sea ice are functions of the vertical coordinate.

In Figure 6.2(a) and (b) we also presented a model result for the case with no snow cover (i.e. where the snow is replaced by air). It is seen that neglecting the snow layer leads to the increased values of NRCS compared to the observations. We explain it by the fact that the snow layer (containing brine) significantly attenuates the incident wave and the scattered wave travelling from the snow-ice rough interface.

### 6.5.4. Case Study 2: Snow Thickness 4 cm

Model and observation results for this case study are presented in Figure 6.3. Measured temperature and salinity profiles in sea ice are given in Figure 6.3(f). Estimated brine volume content in ice is shown in Figure 6.3(g), and the corresponding real and imaginary parts of sea ice CDC as functions of depth are displayed in Figure 6.3(h). The frazil ice layer is substantially colder than in the previous case due to the thinner snow cover. This leads to the lower values of brine volume in the ice surface layer, and as a result to the lower values of both real and imaginary parts of sea ice CDC.

Measured snow temperature and salinity profiles are shown in Figure 6.3(f) and measured snow density and estimated brine volume content in snow are displayed in Figure 6.3(g). The brine volume content at the snow-ice interface is slightly lower than in the Case Study 1. The corresponding real and imaginary parts of snow CDC are shown in Figure 6.3(h).

Figure 6.3(a) and (b) demonstrate model and measured VV and HH NRCS as functions of the incidence angle. In this figure the NRCS from the air-snow and ice-snow interfaces are plotted separately. The results indicate that the dominant scattering occurs at the snow-ice rough interface, except for the incidence angles at $37^{o}$ and higher at HH polarization. Neglecting the snow cover leads to overestimating the backscatter for VV polarization; however, at HH polarization neglecting this does not affect the model result significantly. The model NRCS agrees well with measurements for both VV and HH polarizations. Similar to the previous case, the observed cross-polarization NRCS signal is equal to or below the instrument noise floor.

### 6.5.5. Case Study 3: Snow Thickness 3 cm

Figure 6.4 displays model and observation results obtained for this case study. Using physical properties of snow (Figure 6.4(c) and Figure 6.4(d)) and sea ice (Figure 6.4(f) and Figure 6.4(g)) we estimated the CDC of snow (Figure 6.4(e)) and sea ice (Figure 6.4(h)). The ice-snow interface was the coldest (among the other cases) and therefore the brine volume content in snow was the lowest (0.7 %). The model results presented in Figure 6.4(a) and (b) show a good agreement between model and measured NRCS for both VV and HH polarization. In this case the dominance of the surface scattering at the snow-ice interface (over the surface scattering at the air-snow interface) is especially pronounced compared to the other cases (due to the low amount of brine in the snow). Neglecting the snow cover considerably impacts both the VV and HH NRCS signals. In this case the observed cross-polarization signal is also close to or lower than the instrument noise floor.

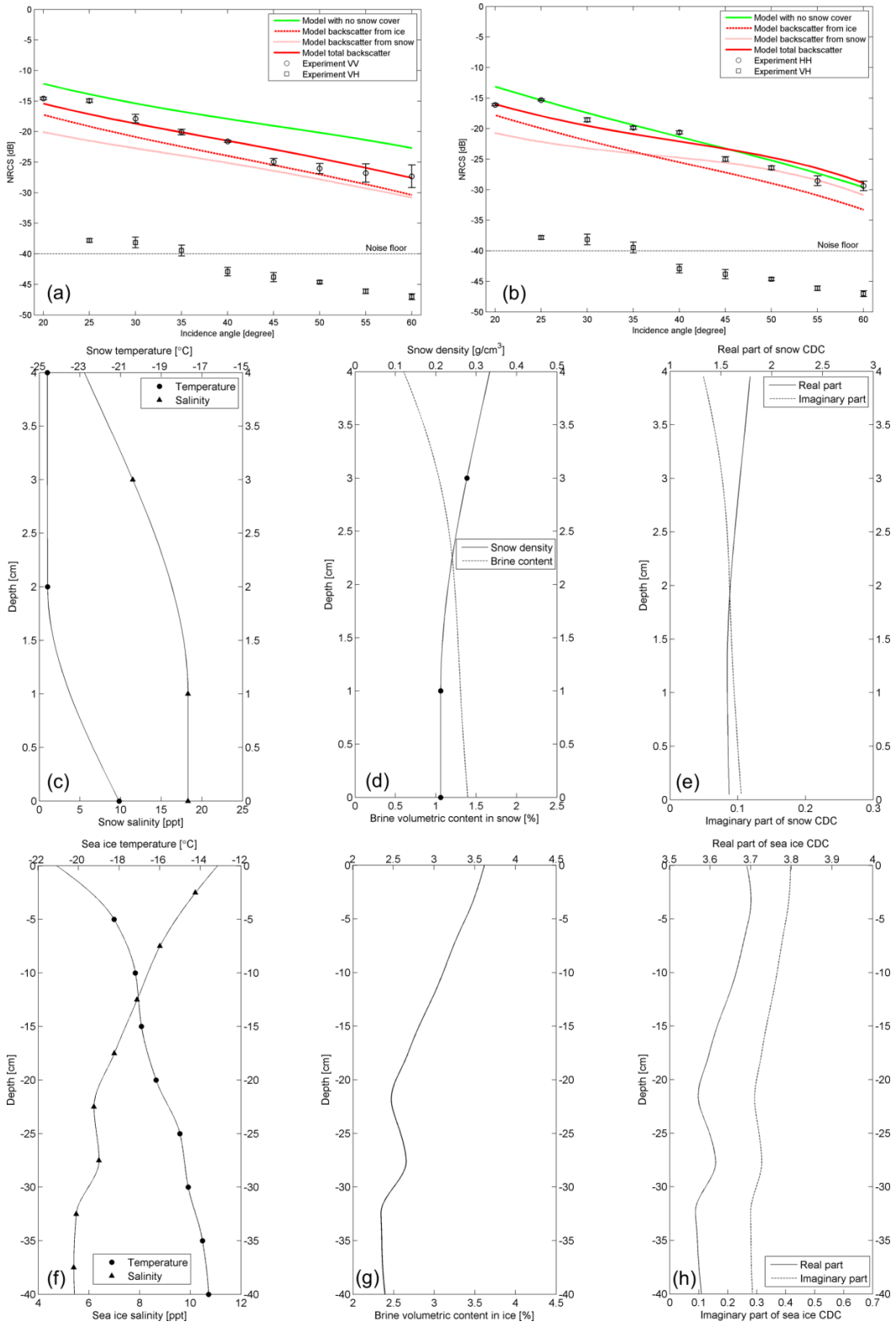


Figure 6.3. Same as Figure 6.2, but for Case Study 2 (4 cm of snow).

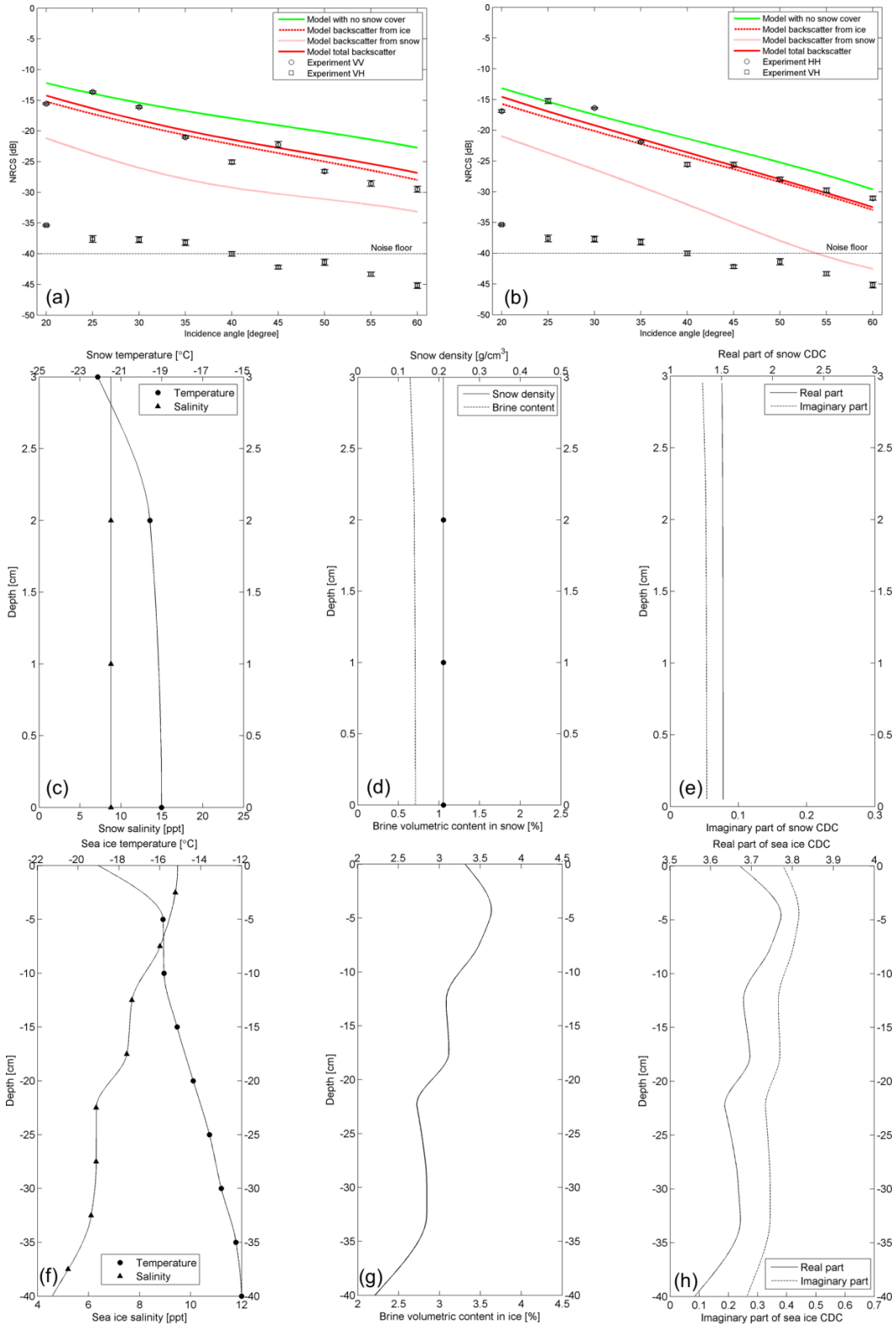


Figure 6.4. Same as Figure 6.2, but for Case Study 3 (3 cm of snow).

6.5.6. Backscattering Coefficients for Thick (16 cm) versus Thin (4 cm) Snow Cover

The thickness of the snow layer (containing brine) substantially controls the attenuation of the incident wave and the wave scattered by the snow-ice rough interface. Generally, a thick snow layer absorbs more microwave energy than a thin snow layer.

We note that in the case of the thick snow cover there is more brine at the snow-ice interface (i.e. at the ice surface layer and at the snow bottom layer). This means that the dielectric constants of both ice and snow at the snow-ice interface are greater for the thick snow cover case compared to the thin snow cover case. However, the dielectric contrast $|\Delta\varepsilon_i|$ (in equations (6.6) and (6.7)) at the snow-ice interface are found to be close for both cases (i.e. $|\Delta\varepsilon_i| = 2.19$ for 16 cm of snow and $|\Delta\varepsilon_i| = 2.13$ for 4 cm of snow). This indicates that the thermodynamic effect of the warmer ice surface does not significantly increase the dielectric contrast at the snow-ice interface.

Figure 6.5(a) and (b) demonstrate that modeled and observed NRCS (for both VV and HH polarizations) are considerably lower for the thick snow cover (16 cm) compared to the thin snow cover (4 cm). This result confirms that the effect of wave attenuation in the thick snow substantially controls the total NRCS from the snow-covered sea ice system. Our results presented in Figure 6.5 suggest a physical basis for winter snow thickness retrieval from radar observations under the specific geophysical and thermodynamic conditions represented in our three case studies.

We point out that Barber and Nghiem in [63] demonstrated an increase in backscatter between thin and thick snow cases. This was associated with a higher level of volume scattering in the basal layer of the thick snow cover compared to the thin snow. At the same time, in [63] the volume

scattering dominated over surface scattering, while in our study the volume scattering was negligible compared to the surface scattering as shown in Section 6.5.1.

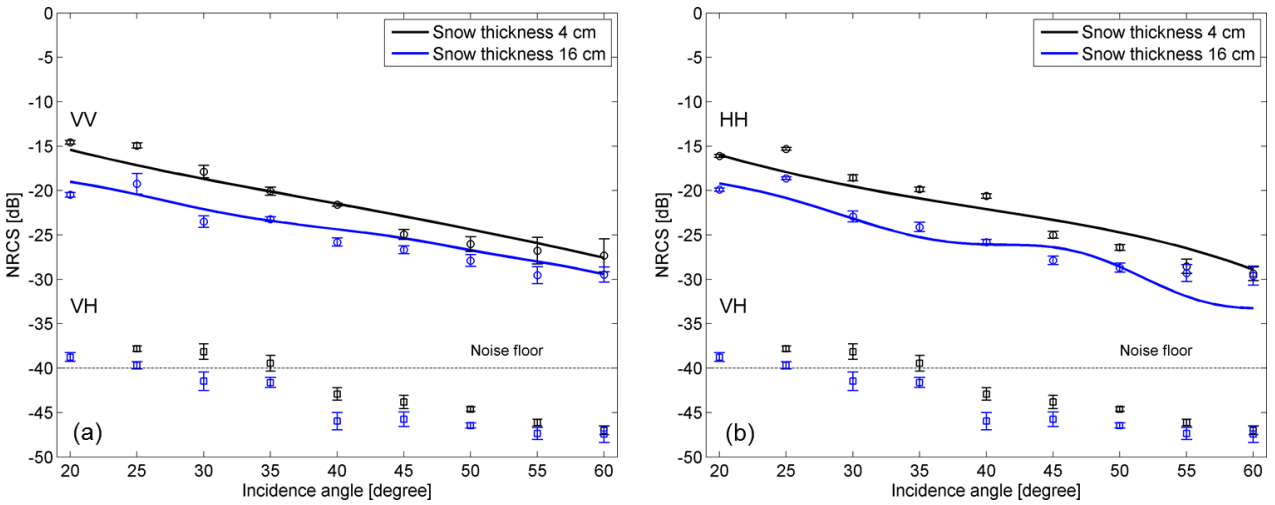


Figure 6.5. NRCS for thin (4 cm) versus thick (16 cm) snow cover. (a) Model (solid line) and experimental (circles) VV NRCS along with experimental VH NRCS (squares) for thin and thick snow covers; (b) Model (solid line) and experimental (circles) HH NRCS along with experimental VH NRCS (squares) for thin and thick snow covers.

### 6.5.7. Backscattering Coefficients for Thin Snow Covers with Different Brine Contents

To investigate the influence of brine content in snow on radar backscatter in more detail we compare model and experimental results for Case Study 2 (4 cm of snow) and Case Study 3 (3 cm of snow) shown in Figure 6.6. The average brine volume content in Case Study 3 was lower than in Case Study 2 (i.e. 0.7% and 1.1 % respectively) because the snow cover was less saline in Case Study 3 compared to Case Study 2. Therefore, the dielectric contrast at the air-snow interface is higher for Case Study 2 ($|\Delta\varepsilon_s| = 0.79$) compared to Case Study 3 ($|\Delta\varepsilon_s| = 0.51$), and, consequently, the backscatter component from the air-snow interface is higher in Case Study 2

compared to Case Study 3. At the same time, the dielectric contrast at the snow-ice interface in Case Study 2 ($|\Delta\varepsilon_i| = 2.13$) and Case Study 3 ($|\Delta\varepsilon_i| = 2.18$) are close to each other (which means that the thermodynamic effect does not influence the dielectric contrast between the snow and ice). But the backscatter component from the snow-ice interface is lower for Case Study 2 compared to Case Study 3, because the wave attenuation is higher in Case Study 2 (where the brine content in snow is higher) in comparison to Case Study 3. These two opposite effects result in almost similar total backscatter (i.e. sum from the air-snow and snow-ice interfaces) for VV polarization at all incidence angles. For the HH polarization the backscatter coefficients in Case Studies 2 and 3 are close to each other up to 35°, while at 35°-60° the backscatter coefficients for Case Study 2 are substantially higher compared to Case Study 3 as shown in Figure 6.6.

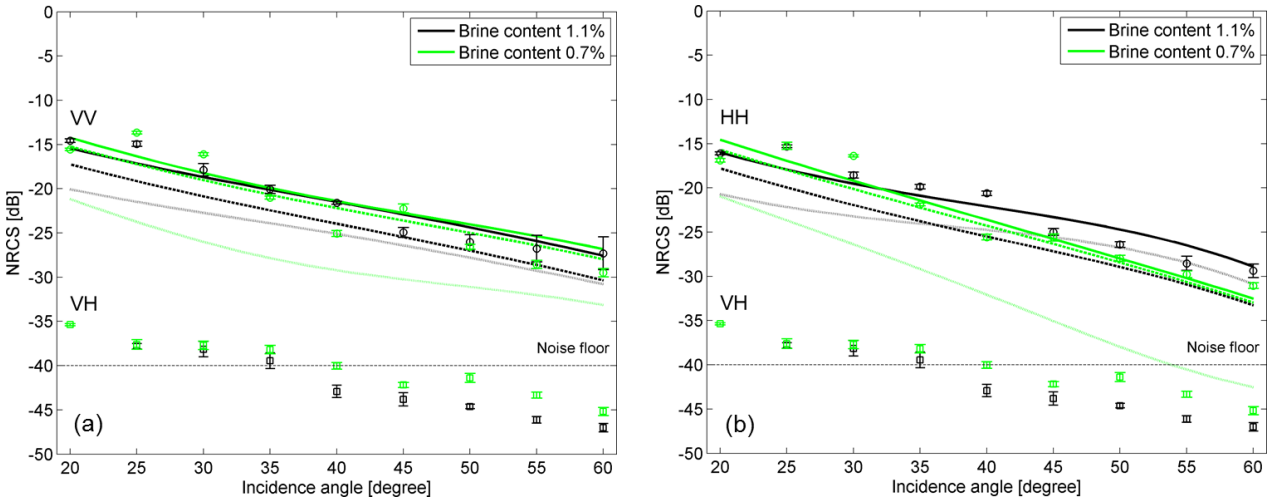


Figure 6.6. NRCS for thin snow covers with average brine volume contents of 1.1% and 0.7%. (a) Model total VV NRCS (solid line), model VV NRCS from the air-snow interface (dotted line), model VV NRCS from the snow-ice interface (dashed line) and experimental VV NRCS (circles) along with experimental VH NRCS (squares); (b) Model total HH NRCS (solid line), model HH NRCS from the air-snow interface (dotted line), model HH NRCS from the snow-ice interface (dashed line) and experimental (circles) VV NRCS along with experimental VH NRCS (squares).

Our results suggest that a situation where different brine volume contents in snow layers with similar thicknesses do not affect the total backscatter is possible. However, more case studies (including experimental physical and scatterometer data) for snow covers with similar thicknesses, but different brine volume contents are required to investigate the observed effect in greater detail.

## 6.6. Conclusion

In this paper we present model and experimental results for C-band radar backscatter from snow covered FY sea ice with average snow thicknesses of 16 cm, 4 cm, and 3 cm representing three case studies. Using experimental data we demonstrated that surface scattering from the air-snow and snow-ice rough interfaces dominated, while the volume scattering contribution was negligible. To model scattering processes we used a first-order approximation of the small perturbation theory for electromagnetic wave scattering from rough boundaries interfacing inhomogeneous media proposed in [13]. The autocorrelation functions of the air-snow and snow-ice rough interfaces were chosen to be exponential [142]. The CDC of both snow and sea ice are functions of the vertical coordinate.

Experimental microwave and snow and sea ice physical data were collected in winter 2008 onboard the CCGS research icebreaker Amundsen as part of the large CFL International Polar Year (IPY) project. The observed physical characteristics of snow and ice served as inputs to estimate the CDC of these media using the refractive dielectric mixture model. The RMS height and correlation length of the air-snow and snow-ice interfaces were not available during the field measurements. Therefore, we varied these input parameters in the model. The sets of roughness

parameters minimizing the error between the experimental and model NRCS were accepted as representative values.

The modeled NRCS values for the three case studies agree well with experimentally collected data for both HH and VV polarizations. We found that surface scattering at the snow-ice rough interface is usually stronger than at the air-snow interface. Furthermore, the model NRCS is considerably lower for thick snow cover compared to the thin snow cover. This effect is in agreement with experimental data. We attribute it to the higher attenuation of the propagated wave within the thicker snow pack. Also, we demonstrated that different brine volume content in snow with similar thicknesses may not influence the backscatter coefficients. These modeled and observed effects provide a physical basis for the retrieval of snow thickness from radar measurements in winter when the snow and sea ice geophysics and thermodynamics are similar to those represented by this case study.

The observed and modelled VV and HH C-band radar backscatter change between thin and thick snow covers is detectable if the following conditions are met: (1) kinetic growth snow grains at the bottom of the snow pack are too small in size to cause volume scattering, (2) low brine content in snow allowing wave penetration and interaction with the snow-ice interface, and (3) surface geometry of sea ice has no large-scale deformations. This situation can be typically observed for smooth FY snow-covered sea ice (over 1 m thick) in the mid of winter (under cold conditions). We note that further investigation of backscatter response from winter snow-covered sea ice with similar snow thicknesses, but different brine volume content in snow is required.

Our situation is quite different from the case described in [63] where the snow grains and brine inclusions in snow were large enough to become scattering centers (in C-band) which is

typical for spring (May). In fact, the opposite effect in [63] was observed (i.e. the backscatter decreases when the snow thickness increases). Also, further research is required to investigate the backscatter response from snow on top of thinner (less than 1 m) sea ice where the brine content may vary considerably.

Fully-polarimetric modes of current (e.g. RADARSAT-2) and future (e.g. Canadian RADARSAT Constellation, European Sentinel-1) SAR spaceborne platforms would allow to quantify contributions of different scattering mechanisms over snow-covered sea ice [136]. This information would allow to identify areas where the scattering conditions (i.e. the low level of volume and double-bounce scattering) described in our study take place and to infer snow thickness for these areas accordingly.

# Appendix 6.A. Application of Freeman-Durden Decomposition Model

In this appendix we derive equation (6.1) from the following Freeman-Durden decomposition equations given on page 965 of paper [135]:

$$\left\langle \left|S_{HH}\right|^2 \right\rangle = f_s \left|\beta\right|^2 + f_d \left|\alpha\right|^2 + f_v , \tag{6.A1}$$

$$\left\langle \left|S_{VV}\right|^2 \right\rangle = f_s + f_d + f_v , \tag{6.A2}$$

$$\left\langle \left|S_{HV}\right|^2 \right\rangle = \frac{f_v}{3} . \tag{6.A3}$$

where $f_s$, $f_d$ and $f_v$ are the surface, double-bounce, and volume scattering contributions respectively to the VV cross-section, $S_{HH}$, $S_{VV}$, $S_{HV}$ are components of the scattering matrix. $\alpha = \left\langle S_{HH} S_{VV}^* \right\rangle$ (in the case where surface and volume scattering are absent). $\beta = \left\langle S_{HH} S_{VV}^* \right\rangle$ (in the case where volume and double-bounce scattering are absent). For more details see [135].

Since in our case the double-bounce scattering component is absent (i.e. $f_d = 0$) then equations (6.A1)-(6.A3) can be rewritten as follows:

$$\left\langle \left|S_{HH}\right|^2 \right\rangle = f_s \left|\beta\right|^2 + f_v , \tag{6.A4}$$

$$\left\langle \left|S_{VV}\right|^2 \right\rangle = f_s + f_v , \tag{6.A5}$$

$$\left\langle \left|S_{HV}\right|^2 \right\rangle = \frac{f_v}{3} . \tag{6.A6}$$

Then, the total power can be found as follows:

$$P = P_s + P_v = \left\langle |S_{HH}|^2 \right\rangle + \left\langle |S_{VV}|^2 \right\rangle + 2\left\langle |S_{HV}|^2 \right\rangle = f_s\left(1 + |\beta|^2\right) + \frac{8}{3} f_v, \tag{6.A7}$$

where $P_s$ and $P_v$ are contributions of surface and volume scattering mechanisms to the total power $P$.

From equations (6.A1), (6.A2), and (6.A3) we obtain:

$$P_s = f_s\left(1 + |\beta|^2\right) = \left\langle |S_{HH}|^2 \right\rangle + \left\langle |S_{VV}|^2 \right\rangle - 6\left\langle |S_{HV}|^2 \right\rangle. \tag{6.A8}$$

Therefore, contribution from the surface scattering to the total power can be found as follows:

$$\frac{P_s}{P} = \frac{\left\langle |S_{HH}|^2 \right\rangle + \left\langle |S_{VV}|^2 \right\rangle - 6\left\langle |S_{HV}|^2 \right\rangle}{\left\langle |S_{HH}|^2 \right\rangle + \left\langle |S_{VV}|^2 \right\rangle + 2\left\langle |S_{HV}|^2 \right\rangle} = \frac{\sigma^0_{HH} + \sigma^0_{VV} - 6\sigma^0_{HV}}{\sigma^0_{HH} + \sigma^0_{VV} + 2\sigma^0_{HV}}. \tag{6.A9}$$

The last equation is equivalent to (6.1).

# Appendix 6.B. Invariant Embedding Approach for Wave Propagation in Layered Media

A plane electromagnetic wave with angular frequency $\omega$ and time dependence $e^{-i\omega t}$ is incident upon a continuously layered finite slab with CDC profile $\varepsilon(z)$ from a homogeneous half space with CDC $\varepsilon_\delta$ as shown in Figure 6.B1. CDC of the medium located beneath the inhomogeneous slab is $\varepsilon_l$. In this appendix we present a recursive numerical scheme to determine complex reflection and transmission coefficients for this slab at both horizontal and vertical polarizations.

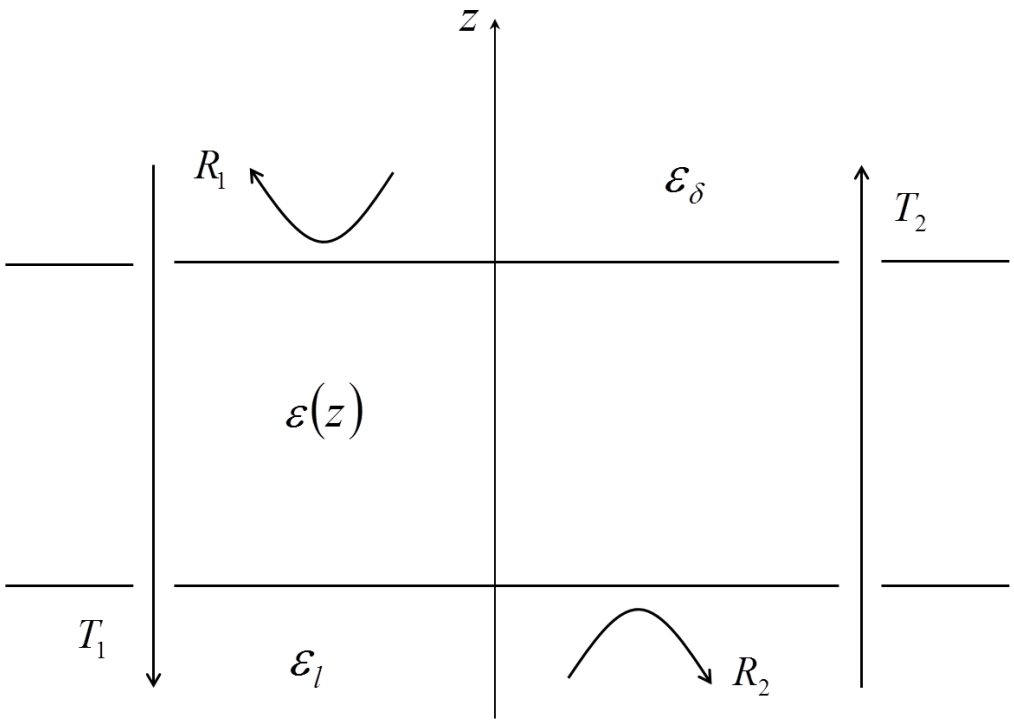


Figure 6.B1. Wave propagation through a slab with a continuous profile of CDC.

The slab with continuous profile of CDC $\varepsilon(z)$ is divided into $n$ layers with constant CDCs $\varepsilon(1)$, $\varepsilon(2)$, …, $\varepsilon(n)$ and equal thicknesses $\Delta z$ as illustrated in Figure 6.B2. First, we introduce a scattering matrix for the first $(j-1)$ layers at vertical or horizontal polarizations as follows:

$$\hat{S}(j-1)=\begin{pmatrix} T_1(j-1) & R_2(j-1) \\ R_1(j-1) & T_2(j-1) \end{pmatrix}, \tag{6.B1}$$

where $T_1(j-1)$ is the transmission coefficient through $(j-1)$ layers when the wave propagates downwards, $R_1(j-1)$ is the reflection coefficient from $(j-1)$ layers when the wave is incident from the upper half space $\varepsilon_\delta$, $T_2(j-1)$ is the transmission coefficient through $(j-1)$ layers when the wave propagates upwards, $R_2(j-1)$ is the reflection coefficient from the slab when the wave is incident from the lower layer with CDC $\varepsilon(j)$.

For each interface between layers $j$ and $j+1$ the partial scattering matrix can be written as follows:

$$\hat{s}(j,j+1)=\begin{pmatrix} t_1(j,j+1) & r_2(j,j+1) \\ r_1(j,j+1) & t_2(j,j+1) \end{pmatrix}, \tag{6.B2}$$

where $t_1(j,j+1)$, $r_1(j,j+1)$ are ordinary Fresnel transmission and reflection coefficients at the boundary between layers $j$ and $j+1$ when the wave propagates downwards. $t_2(j,j+1)$, $r_2(j,j+1)$ are ordinary Fresnel transmission and reflection coefficients at the same boundary

when the wave propagates upwards. The following relationships for these coefficients must hold: $t_1 = 1 + r_1$, $t_2 = 1 + r_2$, and $r_2 = -r_1$.

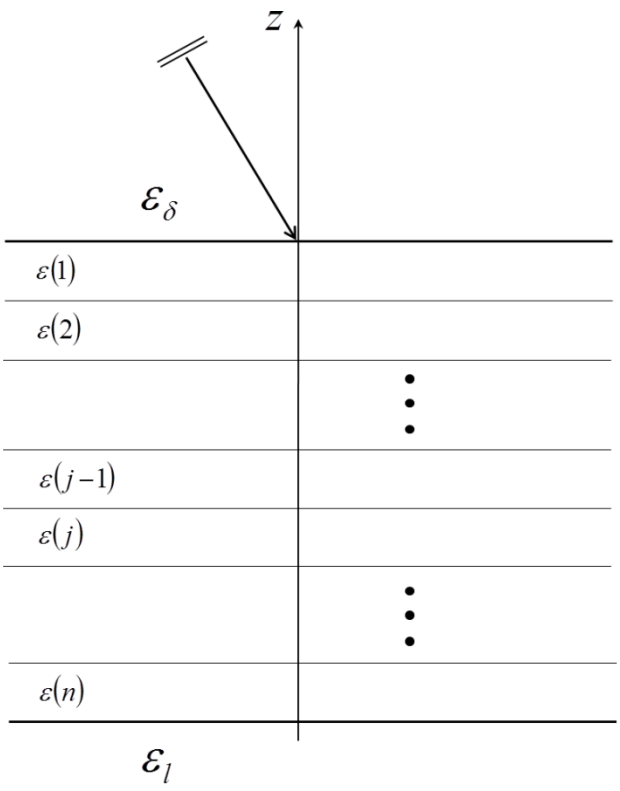


Figure 6.B2. Discrete representation of a continuously layered medium.

Suppose that scattering matrix $\hat{S}(j-1)$ for the first $j-1$ layers is known. Then, the scattering matrix for the first $j$ layers $\hat{S}(j)$ is formed by addition layer $j$ with CDC $\varepsilon(j)$. Scattering matrix $\hat{S}(j)$ can be found in a recursive manner as a function of matrices $\hat{S}(j-1)$ (known from the previous iteration step) and $\hat{s}(j, j+1)$ (found at the interface between layers $j$ and $j+1$) as follows:

$$T_1(j)=\frac{T_1(j-1)t_1(j,j+1)u(j)}{1-R_2(j-1)r_1(j,j+1)u^2(j)}, \tag{6.B3}$$

$$R_1(j)=R_1(j-1)+\frac{T_1(j-1)T_2(j-1)r_1(j,j+1)u^2(j)}{1-R_2(j-1)r_1(j,j+1)u^2(j)}, \tag{6.B4}$$

$$T_2(j)=\frac{T_2(j-1)t_2(j,j+1)u(j)}{1-R_2(j-1)\,r_1(j,j+1)u^2(j)}, \tag{6.B5}$$

$$R_2(j)=r_2(j,j+1)+\frac{t_1(j,j+1)t_2(j,j+1)R_2(j-1)u^2(j)}{1-R_2(j-1)r_1(j,j+1)u^2(j)}, \tag{6.B6}$$

where factor $u(j)=\exp[iw(j)\Delta z]$ represents phase change in layer $j$. $w(j)=k_0\sqrt{\varepsilon(j)-\sin^2\Theta_0}$ is the projection of wave vector onto axis $z$ in layer $j$. In the recursive scheme (6.B3) - (6.B6) at the zeroth iteration $j=0$ we put $\varepsilon(j)=\varepsilon_\delta$ (the upper half space) and initial values for transmission and reflection coefficients $T_1(j)=T_2(j)=1$, $R_1(j)=R_2(j)=0$. At the last iteration $j=n$, we put $\varepsilon(j+1)=\varepsilon_l$ (the lower half space).

In the case of horizontally polarized incident wave the Fresnel reflection coefficient $r_1$ between layers with CDC $\varepsilon(j)$ and $\varepsilon(j+1)$ with respect to the electric field is defined as follows:

$$r_{1H}(j,j+1)=\frac{w(j)-w(j+1)}{w(j)+w(j+1)}. \tag{6.B7}$$

In the case of vertical polarization, the reflection coefficient $r_1$ with respect to the magnetic field is expressed as follows:

$$r_{1V}(j, j+1) = \frac{\varepsilon(j+1)w(j) - \varepsilon(j)w(j+1)}{\varepsilon(j+1)w(j) + \varepsilon(j)w(j+1)}. \qquad \text{(6.B8)}$$

The recursive numerical scheme given by (6.B3) - (6.B8) should be run separately for horizontally and vertically polarized incident waves.

# CHAPTER 7. CONCLUSION

## 7.1. Summary of Major Results

In this section we summarize major scientific results and contributions of this dissertation which address our objectives stated in Chapter 1.

**Result 1. New sea ice motion tracking system operating with SAR images.**

In Chapter 3 we present a new sea ice motion tracking algorithm that operates with two sequential SAR images. Even though, SAR-based ice motion detection algorithms had been developed in the past (e.g. [34], [36]), our technique contains several new components which significantly increased the system's robustness and accuracy. These components include:

1) new feature tracking approach based on the combination of phase-correlation and cross-correlation matching techniques;
2) new algorithm for selecting control points;
3) an approach for filtering out error ice drift vectors by comparing vectors derived from the forward pass (tracking from the first image to the second one) and the backward pass (tracking from the second image to the first one);
4) confidence level setting for output drift vectors.

The accuracy of the system was thoroughly examined based on the visual detection of similar ice features in sequential SAR images and ground truth GPS beacon data for various ice conditions. We demonstrate a very good agreement between the SAR derived vectors and ice

drifting beacon trajectories located in close proximity (less than 3 km) to the nearest SAR ice motion vectors. The RMSE is 0.43 km for 36 comparison points.

In Chapter 3 we also draw special attention to ice motion detection from the cross-polarization (HV) channel which was not available (in ScanSAR mode) before launching RADARSAT-2 in 2007. In particular, we formulated the following condition where the HV channel is more reliable than the HH channel for ice tracking: if $\sigma^0_{HV} - \sigma^0_{NE} > 0.003$ (linear units), then for ice tracking HV is preferable to HH; otherwise, the HH channel is preferable to HV for ice tracking.

In Chapter 3 we also propose a novel technique for filtering noise floor stripes in HV imagery, which allowed us to demonstrate that the ice motion tracking algorithm is not sensitive to the noise floor stripes along the satellite track.

The developed sea ice motion tracking system has been implemented for operational use at the Canadian Ice Service, Environment Canada. It was successfully used to quantify recent changes in the exchange of sea ice between the Arctic Ocean and the Canadian Arctic Archipelago [46], [149], [150]. It has been also proven to be an instrumental tool for verifying sea ice forecasting models, and supporting field work in the Arctic Ocean conducted in compliance with the United Nations Convention on the Law of the Sea (UNCLOS).

**Result 2. New models for ocean surface wind speed retrieval from SAR imagery.**

Surface wind is one of the major factors affecting sea ice dynamics. In Chapter 4 we present two new models for ocean surface wind speed retrieval from C-band SAR imagery based on a large body of statistics on buoy observations collocated and coincided with RADARSAT-1 and -2 ScanSAR images. The conventionally used C-band geophysical model functions (CMODs) (e.g.

[56], [59]) require input wind direction which are normally provided by numerical weather prediction (NWP) models. However, these models are often not accurate (especially in the Arctic Ocean).

As opposed to CMOD, our proposed models do not require input wind direction. The first model's independent variables are co-polarization (HH), normalized radar cross-section (NRCS), and antenna beam incidence angle. The second model's predictors are co-polarization (HH), cross-polarization (HV) NRCS, instrument noise floor, and incidence angle. The latter model has a better accuracy than the first, due to using an additional cross-polarization variable. Furthermore, we found that the proposed models without wind direction input demonstrate a better accuracy than CMOD_IFR2 and CMOD5.N models in combination with the SAD co-polarization ratio (VV/HH), which require wind direction input. For example, RMSE for our HH-HV wind speed retrieval model is 1.59 m/s while RMSE of CMOD5.N+SAD model (which requires wind direction) is 2.19 m/s. These results were confirmed on a large independent subset of collected data. The developed models have been integrated into a quasi-operational system at the Meteorological Service of Canada.

It was interesting to note that sea ice motion and wind speed can be extracted from the same RADARSAT-2 ScanSAR datasets. In the areas where open water is present (such as marginal ice zone, leads, or polynyas) the wind speed can be calculated using the developed models. Therefore, in Chapter 4 we also present a new SAR-based ice motion-wind speed product which combines our methods for wind speed and ice motion retrieval from SAR. The developed product can be a useful tool for studying sea ice dynamics processes in sea ice.

**Result 3. New analytical solution for electromagnetic wave scattering from rough surfaces interfacing layered media (including snow-covered sea ice).**

Advanced electromagnetic modeling techniques are required to assess the thermodynamic state of sea ice from radar remote sensing. In Chapter 5 a new analytical formulation for electromagnetic wave scattering from rough boundaries interfacing inhomogeneous media is derived based on the first-order approximation of the small perturbation theory. First, we considered a scattering problem for a single rough boundary embedded in a piecewise continuously layered medium. As a key (and novel) step, we introduced auxiliary wave propagation problems that are aimed to link reflection and transmission coefficients in the layered media with particular solutions of one-dimensional wave equations at the mean level of the rough interface. This approach enabled us to express the final solution in a closed form avoiding a prior discretization of the inhomogeneous medium. Second, we naturally extended the obtained solution to an arbitrary number of rough interfaces separating continuously layered media.

We think that the obtained formulation is user-oriented and convenient for practical geophysical remote sensing applications as it operates with physically meaningful reflection and transmission coefficients associated with certain geophysical media (e.g. snow and ice). Furthermore, the derived solution is fairly flexible because the numerical implementation can be split into two separate algorithmic units: (1) estimation of the reflection and transmission coefficients for layered media; (2) calculation of scattering characteristics by plugging in these coefficients in the general solution.

As a validation step, we demonstrated that available SPM solutions in the literature (including the most recent [96]) represent special cases of our general solution. Furthermore, we showed that our numerical results agree well with published data for a special case from [96].

In Chapter 5, we also present a formulation for inhomogeneous snow-covered sea ice when the dominant scattering occurs at the snow-ice and air-snow interfaces as a particular special case of the general solution.

**Result 4. Good agreement between model and experimental C-band backscatter from snow-covered first-year sea ice and a possibility for winter snow thickness retrieval from SAR.**

In Chapter 6 we validate the theory presented in Chapter 5 by comparing model and measurement results for C-band HH and VV NRCS from winter snow-covered first-year sea ice with average snow thicknesses of 16 cm, 4 cm, and 3 cm. The experimental data were collected during the Circumpolar Flaw Lead system study in winter 2008 in the southern Beaufort Sea from the research icebreaker Amundsen. The brine content in snow pack was low in all three case studies which is typical for cold winter conditions. First, using experimental data, we showed that surface scattering dominated, whereas volume scattering was negligible which is opposite to the previous study by [63] conducted for spring. Therefore, our model accounted for surface scattering from the air-snow and snow-ice rough interfaces and continuously layered snow and sea ice was applied. By comparing model and experimental data for the three case studies we revealed the following:

1) Good agreement between the model and experimental data were observed for all three case studies suggesting that our model is well applicable to winter snow-covered sea ice.
2) The scattering at the snow-ice rough interface is usually stronger than at the air-snow interface.

3) Both model and experimental NRCS values were considerably higher for thin snow cover compared to the thick snow cover case. We associate this effect with the lower attenuation of the propagated wave within the thin snow in comparison to the thick snow pack.
4) Different brine content in snow covers with close thicknesses (4 cm and 3 cm) significantly affected the backscatter components from the air-snow and snow-ice interfaces; however, the total backscattering coefficients for VV polarization (at all incidence angles) and HH polarization (at incidence angles below $35^{o}$) did not change considerably.

We believe that these findings provide the physical basis for, and suggest that, winter snow thickness retrieval may be possible from radar observations under particular scattering conditions.

## 7.2. Future Work

In this dissertation we considered various methods for detecting dynamic and thermodynamic parameters of sea ice from radar remote sensing. We emphasize that retrieval of dynamic characteristics of sea ice can be conducted from spaceborne SAR platforms for large geographical areas with very high resolution and accuracy at the operational level. With the launch of Canadian RCM and European Sentinel-1 constellation SAR missions the temporal resolution of retrieved characteristics from space will drastically increase. At the same time, detection of thermodynamic parameters of sea ice from SAR platforms (in the operational mode) remains challenging due to the complexity and variability of snow and sea ice properties and geometry and, therefore, the difficulty in accurate modeling dielectric constant of the media and modeling scattering characteristics. However, sensitivity of model and experimental backscatter coefficients to certain geophysical parameters (e.g. snow thickness, brine content in snow and ice) is well observed. Therefore, from the operational point of view, an important general challenge that needs to be addressed is bringing the methods for assessing thermodynamic state of sea ice (developed for small scales) to the satellite (large) scale. We note, however, that it may not be fully possible for the current satellite systems due to their technical limitations for this task including (1) single frequency, (2) monostatic capability, (3) single incidence angle for a given pixel in the image.

We also recommend the following specific directions of possible future research:

<u>Detection of sea ice dynamics</u>

- Generally, there are some challenges of detecting similar features in two SAR images during melt season, when surface physical properties of snow-covered sea ice may vary significantly

over a short period of time. Furthermore, during advanced melt there is a lack of distinctive ice features in SAR imagery. These reasons complicate automated ice tracking in summer time. The most efficient solution is decreasing the time interval between sequential SAR images (which will be provided by the upcoming constellation SAR mission). On the other hand, using L-band SAR imagery (e.g. Japanese ALOS-2) instead of C-band may be more efficient as longer wavelengths are less sensitive to the moisture in snow and penetrate deeper. Therefore, identification of most suitable wavelengths for sea ice motion detection (in different seasons) is required.

- To further improve ocean surface wind retrieval from SAR more observations of high speed wind events (coincided and collocated with dual-polarization imagery) are needed.
- It is also highly desirable to retrieve wind direction as well. This may be possible by combining CMOD and the proposed wind retrieval models with no input wind direction.
- To improve our SAR-based ice motion-wind speed product a reliable automated ice/water separation algorithm (from SAR) is required.

<u>Detection of sea ice thermodynamics</u>

- The developed theory for modeling wave scattering from layered media relies on the first-order approximation of the small perturbation theory. We believe that the introduced concept can be extended to the second-order solution. Unlike the first-order solution, the second-order solution would give a non-zero cross-polarization backscattering coefficients. Furthermore, the second-order solution can be applied to rough surfaces with a wider range of roughness parameters.

- The developed scattering theory should be extended to the two-scale geometry where the small-scale roughness is modulated by large-scale changes in ice topography.
- Improvement of existing dielectric mixture models for snow and ice is very important as any scattering model substantially relies on the accuracy of the dielectric modeling.
- Our scattering theory should be also validated for other bands (most importantly L- and P-bands). In these bands the validity range of roughness parameters is wider (compared to C-band) due to the larger wave lengths.

# APPENDIX A. CONTRIBUTIONS OF AUTHORS TO THESIS CHAPTERS

## Chapter 3

I developed, validated and optimized the entire algorithm for sea ice motion detection from SAR imagery. I developed an algorithm for noise floor stripes removal from cross-polarization SAR images. I also conducted the detailed analysis of ice motion tracking from HH and HV images. David Barber provided ice beacon data for validation of the system and comments of the manuscript drafts.

## Chapter 4

I developed and validated the ocean surface wind speed retrieval models. I also developed the SAR-based ice motion-wind speed product. Vladimir Zabeline contributed the basic idea for the wind retrieval models and provided valuable directions. David Barber provided his comments on the manuscript.

## Chapter 5

I developed analytical formulations for electromagnetic wave scattering from rough surfaces interfacing inhomogeneous media. I also conducted comparisons with special cases from the literature. Lotfollah Shafai and David Barber provided reviews of the manuscript drafts.

# Chapter 6

I conducted modeling of backscattering coefficients from winter snow-covered FY sea ice and detailed analysis of the obtained results. Dustin Isleifson collected experimental data and provided comments and reviews of the manuscript drafts. David Barber contributed valuable comments and suggestions on manuscript drafts. Lotfollah Shafai provided comments on the obtained results.

# APPENDIX B. ADDITIONAL CONTRIBUTIONS TO THE PEER REVIEWED LITERATURE

In addition to the four journal publications contained in the body of this thesis, I also co-authored eleven peer-reviewed papers. Titles of these articles and my contributions are presented below:

N. Firoozy, **A. S. Komarov**, P. Mojabi, D. G. Barber, J. Landy, and R. Scharien, "Retrieval of snow-covered sea ice temperature and salinity evolution through radar cross section inversion," *IEEE Transactions on Geoscience and Remote Sensing*, in review, 2014.

In this paper, I collected (with the lead author) time-series C-band scatterometer and physical measurements of sea ice at the Sea Ice Environmental Research Facility (SERF) at the University of Manitoba in winter 2014. I also provided comments and suggestions on manuscript drafts.

J. Landy, **A. S. Komarov**, and D. G. Barber, "Numerical and experimental evaluation of terrestrial LiDAR for parameterizing centimeter-scale sea ice surface roughness," *IEEE Transactions on Geoscience and Remote Sensing*, in review, 2014.

In this paper I derived mathematical formulations for simulation of rough surfaces with known statistical properties (i.e. root-mean square height and autocorrelation function). I also provided comments and suggestions on manuscript drafts.

N. Firoozy, **A. S. Komarov**, J. Landy, D. G. Barber, P. Mojabi, and R. Scharien, Inversion-based sensitivity analysis of snow-covered sea ice electromagnetic profiles, *IEEE Journal of Selected Topics in Applied Earth Observations and Remote Sensing*, in review, 2014.

In this paper, I collected (with the lead author) C-band scatterometer and physical measurements of sea ice at SERF, University of Manitoba in winter 2014. I also provided comments and suggestions on manuscript drafts.

J. Landy, D. Isleifson, **A. S. Komarov**, and D. G. Barber, "Parameterization of sea ice surface roughness using LiDAR," *IEEE Transactions on Geoscience and Remote Sensing,* in press, 2015.

In this paper, I provided expertise regarding the role of roughness in microwave scattering models. I also provided mathematical formulations for roughness parameters of two-dimensional rough surfaces as well as comments and suggestions on manuscript drafts at various stages of its preparation.

K. Warner, R. Scharien, D. Isleifson, **A. S. Komarov**, J. Landy, and D. G. Barber, "Diurnal variability of C-band backscatter signatures from multiyear ice during advanced melt," *International Journal of Remote Sensing,* in review, 2014.

In this paper, I assisted the lead author with physical and scatterometer data collection on board the CCGS Amundsen in summer 2011. I also provided comments and suggestions on manuscript drafts.

D. G. Barber, G. McCullough, D. Babb, **A. S. Komarov**, L. M. Candlish, J. V. Lukovich, M. Asplin, S. Prinsenberg, I. Dmitrenko and S. Rysgaard, "Climate change and ice hazards in the Beaufort Sea," *Elementa-Oceans.* Elem. Sci. Anth. 2: 000025, 2014.

In this paper, I run the ice motion tracking algorithm and wind speed retrieval models for a few SAR images acquired over the study area. I created two figures illustrating sea ice motion and winds in the area of interest. I also provided comments and suggestions on manuscript drafts.

D. Isleifson, R. J. Galley, D. G. Barber, J. C. Landy, **A. S. Komarov**, L. Shafai, "A study on the C-band polarimetric scattering and physical characteristics of frost flowers on experimental sea ice," *IEEE Transactions on Geoscience and Remote Sensing*, vol. 52, no. 3, pp. 1787-1798, Mar. 2014.

In this paper, I assisted the lead author with data collection at SERF, University of Manitoba and I helped with data analysis. I also provided comments and suggestions on manuscript drafts at various stages of its preparation.

S.E.L. Howell, T. Wohlleben, M. Dabboor, C. Dersken, **A. S. Komarov**, L. Pizzolato, "Recent changes in the exchange of sea ice between the Arctic Ocean and the Canadian Arctic Archipelago," *Journal of Geophysical Research, ,* vol. 118, no. 7, pp. 3595-3607, July 2013.

In this paper, the sea ice motion tracking system I developed was employed for quantifying sea ice fluxes between the Arctic Ocean and the Canadian Arctic Archipelago. I also provided comments and suggestions on manuscript drafts.

S.E.L. Howell, T. Wohlleben, **A. S. Komarov**, L. Pizzolato, and C. Derksen, "Recent extreme light sea ice years in the Canadian Arctic Archipelago: 2011 and 2012 eclipse 1998 and 2007," *The Cryosphere*, 2013, DOI:10.5194/tcd-7-1313-2013.

In this paper, the sea ice motion tracking system I developed was employed for quantifying sea ice fluxes between the Arctic Ocean and the Canadian Arctic Archipelago. I also provided comments and suggestions on manuscript drafts.

T. Wohlleben, S. Howell, T. Agnew, and **A. S. Komarov**. Sea ice motion and flux within the Prince Gustaf Adolf Sea, Queen Elizabeth Islands, Canada during 2010, *Atmosphere-Ocean*, 2012, DOI:10.1080/07055900.2012.750232.

In this paper, the sea ice motion tracking system I developed was employed for quantifying sea ice fluxes between the Arctic Ocean and the Canadian Arctic Archipelago. I also provided comments and suggestions on manuscript drafts.

S. A. Komarov, **A. S. Komarov**, and V. Zabeline. "Marine wind speed retrieval from RADARSAT-2 dual-polarization imagery," *Canadian Journal of Remote Sensing*, vol. 37, no. 5, pp. 520-528, 2011.

In this paper, I provided an algorithm and software for automated selection of ocean buoy observations collocated and coincided with SAR images. I also provided comments and suggestions on manuscript drafts at various stages of its preparation.

# REFERENCES


[1] J. Comiso, C. Parkinson, R. Gersten, and L. Stock, "Accelerated decline in the Arctic sea ice cover," *Geophys. Res. Lett.*, vol. 35, p. L01703, Jan. 2008.

[2] [Online] NSIDC web site. Available: http://nsidc.org/arcticseaicenews/2012/09/arctic-sea-ice-extent-settles-at-record-seasonal-minimum/.

[3] J. C. Comiso, "Large decadal decline of the Arctic multiyear ice cover." *J. Climate*, vol. 25, pp. 1176–1193, 2012.

[4] D. G. Barber, R. Galley, M. G. Asplin, R. De Abreu, K.-A. Warner, M. Pucko, M. Gupta, S. Prinsenberg, and S. Julien, "Perennial pack ice in the southern Beaufort Sea was not as it appeared in the summer of 2009," Geophys. Res. Lett., vol. 36, p. L24501, Oct. 2009.

[5] J. Cavalieri and C. L. Parkinson. "Arctic sea ice variability and trends, 1979–2010," *The Cryosphere*, vol. 6, pp. 881–889, 2012.

[6] R. Kwok, and D. Rothrock, "Decline in Arctic sea ice thickness from submarine and ICESat records: 1958 – 2008," *Geophys. Res. Lett*., vol. 36, p. L15501, Aug. 2009.

[7] G. Spreen, R. Kwok, and D. Menemenlis, "Trends in Arctic sea ice drift and role of wind forcing: 1992–2009," *Geophys. Res. Lett.*, vol. 38, pp. L19501, Oct. 2011.

[8] D.G. Barber, G. McCullough, D. Babb, A. S. Komarov, L.M. Candlish, J.V. Lukovich, M. Asplin, S. Prinsenberg, I. Dmitrenko and S. Rysgaard. "Climate change and ice hazards in the Beaufort Sea," *Elementa-Oceans.* Elem. Sci. Anth. 2: 000025, 2014.

[9] *RADARSAT-2 Product Description RN-SP-52-1238*. Richmond (BC): MacDonald, Dettwiler and Associates Ltd., 2009.

[10] [Online]. RADARSAT Constellation Mission description. Available: http://www.asc-csa.gc.ca/eng/satellites/radarsat/.

[11] A. S. Komarov and D. G. Barber, "Sea ice motion tracking from sequential dual-polarization RADARSAT-2 images," *IEEE Trans. Geosci. Remote Sens.*, vol. 52, no. 1, pp. 121-136, Jan. 2014.

[12] A. S. Komarov, V. Zabeline, and D. G. Barber, "Ocean surface wind speed retrieval from C-band SAR images without wind direction input," *IEEE Trans. Geosci. Remote Sens.*, vol. 52, no. 2, pp. 980-990, Feb. 2014.

[13] A. S. Komarov, L. Shafai, and D. G. Barber, "Electromagnetic wave scattering from rough boundaries interfacing inhomogeneous media and application to snow-covered sea ice," *Progress in Electromagnetic Research,* vol. 144, pp. 201-219, 2014.

[14] A. S. Komarov, D. Isleifson, D. G. Barber, and L. Shafai, "Modeling and measurement of C-band radar backscatter from snow-covered first-year sea ice," *IEEE Trans. Geosci. Remote Sens.*, in press, 2015.

[15] P. Wadhams. *Sea Ice in the Ocean*. Gordon and Breach Science Publishers. UK, 2000.

[16] W. D. III Hibler, "A dynamic thermodynamic sea ice model." *J. Phys. Oceanogr.*, vol. 9, no. 4, pp. 815-846, 1979.

[17] W. F. Weeks. *On Sea Ice*. University of Alaska Press, Fairbanks, 2010.

[18] R. A. Brown. "Planetary boundary layer modeling for AIDJEX," *Sea ice processes and models*, Univ. Washington Press, Seattle, pp. 387-401, 1980.

[19] M. G. McPhee, "Sea ice drag laws and simple boundary layer concepts, including application to rapid melting," Rept. 82-4, US Army Cold Regions Res. & Engng. Lab., Hanover N.H., 1982.

[20] P. S. Guest, and K. L. Davidson, "The aerodynamic roughness of different types of sea ice," *J. Geophys. Res.*, vol. 96, pp. 4709–4721, 1991.

[21] J. E. Overland, "Atmospheric boundary layer structure and drag coefficients over sea ice," *J. Geophys. Res.*, vol. 90, pp. 9029–9049, 1985.

[22] E. G. Banke, S. D. Smith, and J. Anderson, "Drag coefficients at AIDJEX from sonic anemometer measurements," *Sea ice processes and models*, Univ. Washington Press, Seattle, pp. 430-442, 1980.

[23] N. N. Zubov, *Arctic Ice*. (Translation, U.S. Naval Electronics Laboratory, 1963), 1945.

[24] R. Colony, and A. S. Thorndike, "An estimate of the mean field of Arctic sea ice motion," *J. Geophys. Res.*, vol. 89, no. C6, pp. 10623–10629, 1984.

[25] M. Leppäranta, *The Drift of Sea Ice.* Chichester, UK: Springer Praxis Publishing Ltd, 2005.

[26] W. D. III Hibler, "Arctic ice-ocean dynamics," In *The Arctic seas. Climatology, oceanography, geology, and biology.* (Y. Herman, ed.). Van Nostrand Reinold, New York, pp. 47-91, 1989.

[27] P. Wadhams, "A comparison of sonar and laser profiles along corresponding tracks in the Arctic Ocean," *Sea ice processes and models,* Univ. Washington Press, Seattle, pp. 283-299, 1980.

[28] M. Sturm, J. Holmgren and D. K. Perovich, "Winter snow cover on the sea ice of the Arctic Ocean at the Surface Heat Budget of the Arctic Ocean (SHEBA): temporal evolution and spatial variability," *J. Geophys. Res.*, vol. 107, no. C10, 2002.

[29] J. Iacozza, and D. G. Barber, "An examination of the distribution of snow on sea ice," *Atmosphere-Ocean,* vol. 37, no. 1, 1999.

[30] J. Comiso. *Polar Oceans from Space.* Springler New York Dordrecht Heidelberg London, 2010.

[31] M. Fily and D. Rothrock, "Sea ice tracking by nested correlations," *IEEE Trans. Geosci. Remote Sens.*, vol. GE-25, no. 5, pp. 570-580, Sep. 1987.

[32] J. Karvonen, M. Simila, and J. Lehtiranta, "SAR-based estimation of the Baltic sea ice motion," in Proc. of the International *Geoscience and Remote Sensing Symposium 2007 (IGARSS-07).* IEEE, 2007, pp. 2605-2608.

[33] *T.* Heacock*, T. Hirose, F. Lee, M. Manore and B. Ramsay*, "Sea-ice tracking on the east coast of Canada using NOAA AVHRR imagery," *Ann. Glaciol.*, vol. 17, pp. 405-413, 1993.

[34] R. Kwok, J. Curlander, R. McConnell, and S. Pang, "An ice-motion tracking system at the Alaska SAR facility," *IEEE J. Ocean. Eng.*, vol. 15, no. 1, pp. 44-54, Jan. 1990.

[35] R. Vincent, R. Marsden, and A. McDonald, "Short time-span ice tracking using sequential AVHRR imagery," *Atmosphere-Ocean,* vol. 39, no. 3, pp. 279-288, Mar. 2001.

[36] M. Thomas, C. Geiger, and C. Kambhamettu. "High resolution (400m) motion characterization of sea ice using ERS-1 SAR imagery," *J. Cold Regions Science and Technology*, vol. 52, pp. 207-223, 2008.

[37] R. N. Bracewell, K. Y. Chang, A. K. Jha, and Y. H. Wang, "Affine theorem for two-dimensional Fourier transform," *Elec. Letters*, vol. 29, no. 3, p. 304, Feb. 1993.

[38] S. Reddy and B. Chatterji, "An FFT-based technique for translation, rotation, and scale-invariant image registration," *IEEE Trans. Image Proc.*, vol. 5, no. 8, pp. 1266-1271, Aug. 1996.

[39] A. Liu, S. Martin, and R. Kwok, "Tracking of ice edges and ice floes by wavelet analysis of SAR images," *J. Atmos. Oceanic Tech.*, vol. 14, pp. 1187–1198, 1997.

[40] R. McConnell, R. Kwok, J. Curlander, S. Pang and W. Kobe, "Ψ-S correlation and dynamic time warping: two methods for tracking ice floes in SAR images," *IEEE Trans. Geosci. Remote Sens.*, vol. 29, no. 6, pp. 1004-1012, 1991.

[41] M. Fily and D. Rothrock, "Opening and closing of sea ice leads: digital measurement from Synthetic Aperture Radar," *J. Geophys. Res.,* vol. 95, no. C1, pp. 789-796, Jan. 1990.

[42] J. Yu, Y. Yang, A. Liu, and Y. Zhao, "Analysis of sea ice motion and deformation in the marginal ice zone of the Bering Sea using SAR data," *Int. J. Remote Sens.*, vol. 30, no. 14, pp. 3603–3611, Jul. 2009.

[43] R. Kwok. "Baffin Bay ice drift and export: 2002–2007," *Geophys. Res. Lett.*, vol. 34, pp. L19501, 2007.

[44] R. Kwok, and G. F. Cunningham, "Seasonal ice area and volume production of the Arctic Ocean: November 1996 through April 1997," *J. Geophys. Res.*, vol. 107, no. C10, pp. 8038, 2002.

[45] R. Kwok, "Exchange of sea ice between the Arctic Ocean and the Canadian Arctic Archipelago," *Geophys. Res. Lett*., vol. 33, pp. L16501, Aug. 2006.

[46] T. Wohlleben, S. Howell, T. Agnew, and A. Komarov. "Sea ice motion and flux within the Prince Gustaf Adolf Sea, Queen Elizabeth Islands, Canada during 2010," *Atmosphere-Ocean,* DOI:10.1080/07055900.2012.750232, 2012.

[47] B. R. Furevik, O. M. Johannessen, and A. D. Sandvik, "SAR-retrieved wind in polar regions - comparison with in situ data and atmospheric model output," *IEEE Trans. Geosci. Remote Sens.*, vol. 40, no. 8, pp.1720-1732, Aug. 2002.

[48] G. R. Valenzuela, "Theories for the interactions of electromagnetic and oceanic waves: A review," *Boundary Layer Meteorol.*, vol. 13, pp. 61-85, 1978.

[49] F. T. Ulaby, R. K. Moore, and A. K. Fung, *Microwave Remote Sensing: Active and Passive,* vol. 2. Norwood, MA: Artech House, 1990.

[50] A. K. Fung, *Microwave Scattering and Emission Models and Their Applications*. Boston (MA): Artech House, 1994.

[51] A. G. Voronovich, *Wave Scattering from Rough Surfaces*. Berlin (DE): Springer-Verlag, 1994.

[52] C. C. Wackerman, P. Clemente-Colon, W. G. Pichel, X. Li, "A two-scale model to predict C-band VV and HH normalized radar cross section values over the ocean," *Can. J. Remote Sens*., vol. 28, no. 3, pp. 367-384, Mar. 2002.

[53] A. G. Voronovich and V. U. Zavorotny, "Depolarization of microwave backscattering from a rough sea surface: modelling with small-slope approximation," in Proc. of the International *Geoscience and Remote Sensing Symposium 2011 (IGARSS-11).* IEEE, 2011, pp. 2033-2036.

[54] Y. Quilfen, B. Chapron, T. Elfouhaily, K. Katsaros, and J. Tournadre, "Observation of tropical cyclones by high-resolution scatterometry," *J. Geophys. Res.*, vol. 103, no. C4, pp. 7767-7786, Apr. 1998.

[55] H. Hersbach, A. Stoffelen, and S. de Haan, "An improved C-band scatterometer ocean geophysical mode function: CMOD5," *J. Geophys. Res.*, vol. 112, no. C3, p. C03 006, Mar. 2007.

[56] H. Hersbach, "Comparison of C-band scatterometer CMOD5.N equivalent neutral winds with ECMWF," *J. Atmos. Ocean. Technol.*, vol. 27, no. 4, pp. 721–736, Apr. 2010.

[57] A. B. Wilson, D. H. Bromwich, and K. M. Hines, "Evaluation of Polar WRF forecasts on the Arctic system reanalysis domain: Surface and upper air analysis," *J. Geophys. Res.*, vol. 116, D11112, Jun. 2011.

[58] J. Horstmann, W. Koch, S. Lehner, and R. Tonboe, "Wind retrieval over the ocean using synthetic aperture radar with C-band HH polarization," *IEEE Trans. Geosci. Remote Sens.*, vol. 38, no. 5, pp. 2122-2131, Sep. 2000.

[59] P. W. Vachon and F. W. Dobson, "Wind retrieval from RADARSAT SAR images: Selection of a suitable C-band HH polarization wind retrieval model," *Can. J. Remote Sens.*, vol. 26, no. 4, pp. 306-313, Apr. 2000.

[60] H. Shen, Y. He, and W. Perrie, "Speed ambiguity in hurricane wind retrieval from SAR imagery," *Int. J. Remote Sens.*, vol. 30, no. 11, pp. 2827-2836, Jun. 2009.

[61] P. W. Vachon and J. Wolfe, "C-Band cross-polarization wind speed retrieval," *IEEE Geosc. Remote Sens. Lett.*, vol. 8, no. 3, pp. 456-459, May 2011.

[62] W. F. Weeks and S. F. Ackley, "The growth, structure, and properties of sea ice," CRREL, Hanover, NH, Monograph 82-1, 1982.

[63] D. G. Barber and S. V. Nghiem, "The role of snow on the thermal dependence of microwave backscatter over sea ice," *J. Geophys. Res.*, vol. 104, no. C11, pp. 25789-25803, Nov. 1999.

[64] S. C. Colbeck, "An overview of seasonal snow metamorphism," *Reviews of Geophysics and Space Physics*, vol. 20, no. 1, pp. 45-61, Feb. 1982.

[65] G. A. Maykut and N. Untersteiner, "Some results from a time-dependent thermodynamic model of sea ice," *J. Geophys. Res.*, vol. 76, no. 6, pp. 1550-1575, 1971.

[66] E.E. Ebert, and J.A. Curry "An intermediate one-dimensional thermodynamic sea-ice model for investigating ice-atmosphere interaction," *J. Geophys. Res.*, vol. 98, no. C6, pp. 10085-10109, 1993.

[67] N. Untersteiner. "On the mass and heat budget of Arctic sea-ice," *Arch. Meteorol. Geophys. Bioklimatol.*, vol. 12, no. 2, pp. 151-182, 1961.

[68] Y. C. Yen, *Review of Thermal Properties of Snow, Ice and Sea Ice.* CRREL Report 81-10, Cold Regions Research and Engineering Laboratory. New Hampshire, 1981.

[69] N. Ono. "Thermal properties of sea ice: IV; Thermal constants of sea ice," *Low Temp. Sci.*, vol. 26, pp. 249-258., 1968.

[70] J. Launiainen, and B. Cheng, "Modelling of ice thermodynamics in natural water bodies," *Cold Regions Science and Tech.*, vol. 27, pp. 153-178, 1998.

[71] D. K. Perovich, and B. Elder. "Estimates of ocean heat flux at SHEBA," *Geophys. Res. Lett.*, vol. 29, no. 9, pp. 1344, 2002.

[72] D. K. Perovich, W. B. Tucker III, and R. A. Krishfield. "Oceanic heat flux in the Fram Strait measured by a drifting buoy," *Geophys. Res. Lett.*, vol. *16*, no. 9, pp. 995–998, 1989.

[73] D. G. Barber, "Microwave remote sensing, sea ice and arctic climate," *Phys. Can.*, vol. 61, pp. 105-111, 2005.

[74] R. E. Collin, *Antennas and Radio Wave Propagation*. New York: McGraw-Hill, 1985.

[75] S. J. Ofranidis, *Electromagnetic waves and antennas.* 2008. Available: http://www.ece.rutgers.edu/~orfanidi/ewa/.

[76] P. Gloersen, and J. K. Larabee, *An Optical Model for the Microwave Properties of Sea Ice*, NASA TM-83865, NASA Goddard Space Flight Center, Greenbelt, Maryland, 1981.

[77] M. R. Vant, R. B. Gray, R. O. Ramseier, and V. Makios, "Dielectric properties of fresh and sea ice at 10 and 35 GHz," *J. Appl. Phys.*, vol. 45, no. 11, pp. 4712-4717, 1974.

[78] G. Frankenstein and R. Garner, "Equations for determining the brine volume of sea ice from $-0.5^{\circ}C$ to $-22.9\ ^{\circ}C$," *J. Glaciol.*, vol. 6, no. 48, pp. 943–944, 1967.

[79] C. Matzler and U. Wegmuller, "Dielectric properties of fresh-water ice at microwave frequencies," *J.Phys. D: Appl. Phys.*, vol. 20, pp. 1623-1630, 1987.

[80] F. T. Ulaby, R. K. Moore, and A. K. Fung, *Microwave Remote Sensing: Active and Passive*, vol. 3. Norwood, MA: Artech House, 1986.

[81] A. Stogryn and G. D. Desargant, "The dielectric properties of brine in sea ice at microwave frequencies," *IEEE Trans. Antennas Propag.*, vol. AP-33, no. 5, pp. 523–532, 1985.

[82] M. Hallikainen, F. Ulaby, M. Abdelrazik, "Dielectric properties of snow in the 3 to 37 GHz range," *IEEE Trans. Antennas Propag.*, vol. 34, no. 11, pp. 1329-1340, Nov. 1986.

[83] M. R. Drinkwater and G. B. Crocker, "Modeling changes in the dielectric and scattering properties of young snow covered sea ice at GHz frequencies." *J. Glaciology*, vol. 34, no. 118, pp. 274–282, 1988.

[84] D. P. Winebrenner et al., "Microwave Sea Ice Signature Modeling," in *Microwave Remote Sensing of Sea Ice*, F. D. Carsey, Ed. Washington, DC: American Geophysical Union, 1992, vol. 68, ch. 8.

[85] Y. S. Kim, R. Onstott, R. Moore, "Effect of a snow cover on microwave backscatter from sea ice," *IEEE J. Ocean. Eng.*, vol. 9, no. 5, pp. 383- 388, Dec. 1984.

[86] A. Ishimaru, *Wave Propagation and Scattering in Random Media*, vol. 1/2. New York: Academic, 1978.

[87] F. D. Hastings, J. B. Schneider, S. L. Broschat, "A Monte-Carlo FDTD technique for rough surface scattering," *IEEE Trans. Antennas Propag*, vol. 43, no. 11, pp.1183-1191, Nov. 1995.

[88] E. M. Nassar, J. T. Johnson, R. Lee, "A numerical model for electromagnetic scattering from sea ice," *IEEE Trans. Geosci. Remote Sens.*, vol.38, no. 3, pp. 1309-1319, May 2000.

[89] D. Isleifson, I. Jeffrey, L. Shafai, J. LoVetri, D. G. Barber, "A Monte Carlo method for simulating scattering from sea ice using FVTD," *IEEE Trans. Geosci. Remote Sens*, vol. 50, no. 7, pp. 2658-2668, Jul. 2012.

[90] S. O. Rice (1951, Aug.). Reflection of electromagnetic waves from slightly rough surfaces. *Commun. Pure Appl. Math.* [Online]. *4(2/3),* pp. 351–378. Available: http://dx.doi.org/10.1002/cpa.3160040206.

[91] A. K. Fung and K.S. Chen, *Microwave Scattering and Emission Models for Users*. Boston (MA): Artech House, 2010.

[92] A. G. Yarovoy, R. V. de Jongh, and L. P. Ligthard, "Scattering properties of a statistically rough interface inside a multilayered medium," *Radio Sci.*, vol. 35, no. 2, pp. 455–462, 2000.

[93] G. Franceschetti, P. Imperatore, A. Iodice, D. Riccio, and G. Ruello, "Scattering from layered structures with one rough interface: A unified formulation of perturbative solutions," *IEEE Trans. Geosci. Remote Sens.*, vol. 46, no. 6, Jun. 2008.

[94] I. M. Fuks, "Wave diffraction by a rough boundary of an arbitrary plane-layered medium," *IEEE Trans. Antennas Propag.*, vol. 49, no. 4, pp. 630–639, Apr. 2001.

[95] A. Tabatabaeenejad and M. Moghaddam, "Bistatic scattering from dielectric structures with two rough boundaries using the small perturbation method," *IEEE Trans. Geosci. Remote Sens.*, vol. 44, no. 8, Aug. 2006.

[96] P. Imperatore, A. Iodice, and D. Riccio, "Electromagnetic wave scattering from layered structures with an arbitrary number of rough interfaces," *IEEE Trans. Geosci. Remote Sens.*, vol. 47, no. 4, pp. 1056–1072, Apr. 2009.

[97] R. Kwok and N. Untersteiner, "The thinning of Arctic sea ice," *Physics Today*, vol. 64, issue 4, pp. 36-41, Apr. 2011.

[98] K. Wilson, D. King, and D. Barber, "A case-study in tracking 1998 spring ice dynamics in the smith sound, North Water Polynya region, Canadian Arctic, using RADARSAT-1 data," *Ann. Glaciol.*, vol. 33, pp. 413 - 418, 2001.

[99] R. Vincent, R. Marsden and A. McDonald, "Short time-span ice tracking using sequential AVHRR imagery," *Atmosphere-Ocean*, vol. 39, no. 3, pp. 279-288, Mar. 2001.

[100] M. Arkett, R. De Abreu, D. Flett, G. Langlois, T. Zagon, A. April, D. Crosbie, Z. Ou, and C. Fabi. "Transitioning CIS ice operations to dual-channel RADARSAT-2 - a cost-benefit analysis," *Canadian Ice Service, Ottawa,* 2009.

[101] M. Arkett, D. Flett, and R. De Abreu. "C-band multiple polarization SAR for sea ice monitoring – what can it do for the Canadian Ice Service," in *Proc of Envisat Simposium*, 2007.

[102] J. Snyder, *Map projections – a working manual.* U.S. Geological Survey Professional Paper 1395. U.S. Government Printing Office. Washington, D.C., 1987.

[103] K. Khlopenkov and A. Trishchenko, "Implementation and evaluation of concurrent gradient search method for reprojection of MODIS Level 1B imagery," *IEEE Trans. Geosci. Remote Sens.*, vol. 46, no. 7, pp. 2016-2027, Jul. 2008.

[104] M. Thomas, C. Kambhamettu, and C. Geiger, "Motion tracking of discontinuous sea ice," *IEEE Trans. Geosci. Remote Sens.*, vol. 49, no. 12, pp. 5064-5079, Dec. 2011.

[105] S. Peddada and R. McDevitt. “Least average residual algorithm (LARA) for tracking the motion of Arctic sea ice,” *IEEE Trans. Geosci. Remote Sens.,* vol. 34, no. 4, pp. 915-926, Jul. 1996.

[106] B. G. T. Else, T. N. Papakyriakou, M. G. Asplin, D. G. Barber, R. J. Galley, L. A. Miller, and A. Mucci, “Annual cycle of air-sea CO2 exchange in an Arctic polynya region,” *Glob. Biogeochem. Cycles,* vol. 27, no. 2, pp. 388-398, June 2013.

[107] I. R. Young, S. Zieger, and A. V. Babanin, “Global trends in wind speed and wave height,” *Science,* vol. 332, no. 6028, pp. 451-455, Apr. 2011.

[108] F. J. Wentz and L. Ricciardulli, “Comment on “Global trends in wind speed and wave height,”” *Science,* vol. 334, no. 6028, p. 905, Nov. 2011.

[109] B. Zhang, W. Perrie, and Y. He, “Wind speed retrieval from RADARSAT-2 quad-polarization images using a new polarization ratio model,” *J. Geophys. Res.,* vol. 116, no. C8, p. C08 008, 2011.

[110] S. Komarov, A. Komarov, and V. Zabeline, “Marine wind speed retrieval from RADARSAT-2 dual-polarization imagery,” *Can. J. Remote Sens.*, vol. 37, no. 5, pp. 520-528, Oct. 2011.

[111] R. G. Onstott, “Chapter 5: SAR and scatterometer signatures of sea ice,” in *Microwave Remote Sensing of Sea Ice*, vol. 68, F. D. Carsey, Ed. Washington, DC: AGU, 1992.

[112] RADARSAT-1 user guide, Richmond (BC): MacDonald, Dettwiler and Associates Ltd., 1999.

[113] [Online]. Available through Environment Canada domain: http://thetis.pyr.ec.gc.ca/.

[114] W. T. Liu, and W. Tang, “Equivalent neutral wind,” *JPL Publ., 96–17*, 8 p., 1996.

[115] J. Cote, S. Gravel, A. Methot, A. Patoine, M. Roch, and A. Staniforth, “The operational CMC-MRB Global Environmental Multiscale (GEM) model. Part I: Design considerations and formulation,” *Monthly Weather Review*, vol. 126, no. 6, pp. 1373-1395, Jun. 1998.

[116] E. Korsbakken, J. A. Johannessen, and O.M. Johannessen, “Coastal wind field retrievals from ERS synthetic aperture radar images,” *J. Geophys. Res.*, vol. 103, no. C4, pp. 7857-7874, Apr. 1998.

[117] D. K. Perovich, B. Light, H. Eicken, K. F. Jones, K. Runciman, and S. V. Nghiem, “Increasing solar heating of the Arctic Ocean and adjacent seas, 1979–2005: Attribution and role in the ice-albedo feedback,” *Geophys. Res. Lett.,* vol. 34, pp. L19505, Oct. 2007.

[118] M. C. Serreze, M. M. Holland, and J. Stroeve, “Perspectives on the Arctic’s shrinking ice cover,” *Science*, vol. 315, pp. 1533–1536, Mar. 2007.

[119] D. Isleifson, B. Hwang, D. Barber, R. Scharien, and L. Shafai, "C-Band polarimetric backscattering signatures of newly formed sea ice during fall freeze-up," *IEEE Trans. Geosci. Remote Sens.*, vol. 48, no. 8, pp. 3256-3267, Aug. 2010.

[120] A. Moreira, P. Prats-Iraola, M. Younis, G. Kreiger, I. Hajnsek, and K. P. Papathanassiou, "A tutorial on synthetic aperture radar," *IEEE Geosci. and Remote Sens. Magazine*, vol. 1, no. 1, pp. 6-43, Mar. 2013.

[121] F. D. Carsey, *Microwave Remote Sensing of Sea Ice*, Geophysical Monograph 68, American Geophysical Union, 1992.

[122] L. Tsang and J.A. Kong, *Scattering of Electromagnetic Waves: Advanced Topics*, Wiley Interscience, 2001.

[123] F. T. Ulaby, R. K. Moore, and A. K. Fung, *Microwave Remote Sensing: Active and Passive*, vol. 1. Norwood, MA: Artech House, 1986.

[124] A. Khenchaf, "Bistatic reflection of electromagnetic waves from random rough surfaces. Application to the sea and snowy-covered surfaces," *Eur. Phys. J., Applied Physics*, vol. 14, pp. 45 - 62, 2001.

[125] V. L. Mironov, M. C. Dobson, V. H. Kaupp, S. A. Komarov, and V. N. Kleshchenko, "Generalized refractive mixing dielectric model for moist soils," *IEEE Trans. Geosci. Remote Sens.*, vol. 42, no. 4, pp. 773–785, Apr. 2004.

[126] A. Stogryn. "Equations for calculating the dielectric constant of saline water," *IEEE Trans. Microwave Theory Thech.*, Vol. MIT-19, pp. 733-736, 1971.

[127] R. Bellman and R. Vasudevan. *Wave Propagation – An Invariant Embedding Approach.* D. Reidel Publishing Company, 1986.

[128] S. V. Nghiem, R. Kwok, S. H. Yueh, and M. R. Drinkwater, "Polarimetric Signatures of Sea Ice. Part 2: Experimental Observations," *J. of Geophys. Res.*, vol. 100, no. C7, pp. 13681-13698, July 1995.

[129] J.J. Yackel, and D. G. Barber. "Observations of snow water equivalent change on landfast first-year sea ice in winter using synthetic aperture radar data *IEEE Trans. Geosci. Remote Sens.*, vol. 45, no. 4, pp. 1005–1015, Apr. 2007.

[130] D.G. Barber, S.P. Reddan, and E.F. LeDrew, "Statistical characterization of the geophysical and electrical properties of snow on landfast first-year sea ice," *J. Geophys. Res.*, vol. 100, no. C2, pp. 2673-2686, 1995.

[131] A. Carlström and L. M. H. Ulander, "Validation of backscatter models for level and deformed sea ice in ERS-1 SAR images," *Int. J. Remote Sens.*, vol. 16, no. 7, pp. 3245-3266, 1995.

[132] A.K. Fung, Z. Li, K.S. Chen, "Backscattering from a randomly rough dielectric surface," *IEEE Trans. Geosc. Rem. Sens.*, vol.30, no.2, pp. 356-369, Mar 1992.

[133] W. Dierking, M. I. Pettersson, and J. Askne, "Multifrequency scatterometer measurements of Baltic Sea ice during EMAC-95," *Int. J. Remote Sens.*, vol. 20, no. 2, pp. 349-372, 1999.

[134] M. C. Fuller, T. Geldsetzer, J.P.S. Gill, J.J. Yackel, and C. Derksen, "C-band backscatter from a complexly-layered snow cover on first-year sea ice," *Hydrol. Process.*, vol. 28, no. 16, pp. 4614-4625, 2014.

[135] A. Freeman and S. L. Durden, "A three-component scattering model for polarimetric SAR data," *IEEE Trans. Geosci. Remote Sens.*, vol. 36, no. 3, pp. 963-973, May 1998.

[136] M. Hossain, J. Yackel, M. Dabboor, and M. Chris Fuller, "Application of a three-component scattering model over snow-covered first-year sea ice using polarimetric C-band SAR data," *Int. J. Remote Sens.*, vol. 35, no. 5, pp. 1786–1803, 2014.

[137] B. Scheuchl, I. Cumming, and I. Hajnsek, "Classification of fully polarimetric single- and dual-frequency SAR data of sea ice using the Wishart statistics," *Can. J. Remote Sens.*, vol. 31, no. 1, pp. 61–72, 2005.

[138] B. Scheuchl, I. Hajnsek, and I. Cumming, "Model-based classification of polarimetric SAR sea ice data," in *Proc. of the International Geoscience and Remote Sensing Symposium 2002 (IGARSS-02).* IEEE, 2002, pp. 1521-1523.

[139] T. Eltoft, J. Grahn, A. Doulgeris, C. Brekke, L. Ferro-Famil, B. Holt, "Multi-frequency polarimetric analysis of sea ice," in *Proc. of the Asia-Pacific Conference on Synthetic Aperture Radar 2013 (APSAR-13), IEEE 2013,* pp.96-99.

[140] J. P.S. Gill, J. J. Yackel, "Evaluation of C-band SAR polarimetric parameters for discrimination of first-year sea ice types," *Can. J. Remote Sens*, vol. 38, no. 3, pp. 306-323, 2012.

[141] L. A. Brekhovskikh. *Waves in layered media*. New York, Academic Press, 1980.

[142] J. C. Landy, D. Isleifson, A. S. Komarov, and D. G. Barber, "Parameterization of centimeter-scale sea ice surface roughness using terrestrial LiDAR," *IEEE Trans. Geosci. Remote Sens.*, in press, 2015.

[143] D. Barber, M. Asplin, Y. Gratton, J. Lukovich, R. Galley, R. Raddatz, D. Leitch. "The International Polar Year (IPY) Circumpolar Flaw Lead (CFL) system study: introduction and physical system", Atmosphere-Ocean, vol. 48, no. 4, pp. 225-243, 2010.

[144] T. Geldsetzer, J. B. Mead, J. J. Yackel, R. K. Scharien, and S. E. L. Howell, "Surface-based polarimetric C-band scatterometer for field measurements of sea ice," *IEEE Trans. Geosci. Remote Sens.*, vol. 45, no. 11, pp. 3405–3416, Nov. 2007.

[145] T. C. Grenfell, "A theoretical model of the optical properties of sea ice in the visible and near infrared," *J. Geoph. Res.*, vol. 88, no. C14, pp. 9723-9735, 1983.

[146] D. K. Perovich, and A. J. Gow, "A quantitative description of sea ice inclusions," *J. Geophys. Res.*, vol. 101, no. C8 , pp. 18327–18243, 1996.

[147] G. F. N. Cox and W. F. Weeks, "Equations for determining the gas and brine volumes in sea-ice samples," *J. Glaciol.*, vol. 29, no. 102, pp. 306–316, 1983.

[148] B. Light, G. A. Maykut, and T. C. Grenfell, "Effects of temperature on the microstructure of first-year Arctic sea ice," *J. Geoph. Res.*, vol. 108, no. C2, pp. 3051, 2003.

[149] S.E.L. Howell, T. Wohlleben, A. S. Komarov, L. Pizzolato, and C. Derksen, "Recent extreme light sea ice years in the Canadian Arctic Archipelago: 2011 and 2012 eclipse 1998 and 2007," *The Cryosphere*, 2013, DOI:10.5194/tcd-7-1313-2013.

[150] S.E.L. Howell, T. Wohlleben, M. Dabboor, C. Dersken, A. S. Komarov, L. Pizzolato, "Recent changes in the exchange of sea ice between the Arctic Ocean and the Canadian Arctic Archipelago," *J. Geoph. Res.*, vol. 118, no. 7, pp. 3595-3607, July 2013.